Imperial College London

Department of Earth Science and Engineering

Constraining Nonequilibrium Isotopic Effects in Carbonates: Through Clumped Isotopes, Trace Metal Analysis, and Numerical Modelling

Xuan Cao

Submitted in part fulfilment of the requirements for the degree of Doctor of Philosophy in

October 2024

Abstract

Calcium carbonates are important sedimentary rocks that are not only volumetrically important reservoir rocks but also pivotal paleoenvironment archives. The clumped isotope thermometer (Δ_{47}) is the most advanced paleo-thermometer for carbonates and a powerful tool in related research. However, the kinetic effects on clumped isotopes are ambiguous and controversial. The pairing of clumped isotope and trace metal concentration found in natural calcite cement was recently suggested as a promising tool to identify kinetic effects in clumped isotopes but needs to be further confirmed via experiments. This PhD work breaks down the knowledge gap into three linked research questions: [1] Key controls on polymorphism, [2] Mathematical description of trace metal incorporation, and [3] Potential causes of kinetic effects on clumped isotopes.

To address the gap, I synthesised $CaCO_3$ under controlled laboratory conditions. The obtained precipitates were analysed for various properties. Based on the results, I concluded: [1] Temperature and the combination of temperature > 25°C with rapid precipitation rates are primary controls on polymorphism, with ionic impurities and precipitation rate as secondary and tertiary controls. [2] The partitioning of Fe^{3+} and Mn^{2+} in $CaCO_3$ is independent in the polymorph and exhibited strong correlations with the precipitation rates and temperatures. [3] The examined parameters didn't solely cause kinetic effects on the clumped isotope. However, the elevated dehydration of cation impurities can lead to kinetic effects. I interpret this as the shift in the crystal growth mechanism. I extended the Δ_{47}-T calibration to cryogenic temperatures with a range of -15 to 250°C.

This PhD work provides a laboratory framework for the research of carbonate clumped isotope kinetic effects and suggests that the pairing of clumped isotope and trace metal concentration may not be a widely applicable tool.

Acknowledgements

I would like to express my thanks to my supervisors Professor Cedric John and Professor Dominik Weiss, who made it possible for me to complete the research. They not only provide me with state-of-the-art lab environments and enough research funds but also mentally guide me through tough scientific questions with patience and kindness. I learnt a lot under their supervision.

I want to also thank the lab support from my lab colleagues Fatimah Alfadel, Simon Davis, Sarah Robinson, Qi Adlan, Trevor Ferris, Katharina Kreissig, Jonathan Watson, Claudia Rocco, Jay Bullen, Juy Saleesongsom, Congying Chen, and Md Hanif. I am grateful for the group discussion with my colleagues Harriet Dawson, Mahmoud ElYamani, Saira Bannu Baharuddin, Zayad AlZayer, Waleed AlGharbi, and Robert Platt.

I would like to thank my flatmates Hui Xu and Lianjun Li, and my friends Yifan Du, Yuxin Hao, Weiyue Liu, Linfeng Li, Xinyu Dong and other friends not yet mentioned here who made my PhD student life at Imperial College London so enjoyable and fruitful.

Special thanks to my partner Lijun Hu who is here with me and warmly supporting me all the time. Thanks to my family who stand by me firmly as always. Because of their support, I can complete this long and tough journey bravely.

Finally, I would like to acknowledge the funding support from the China Scholarship Council and the lab support from Imperial College London Agilent Measurement Suite.

Declarations of originality and copyright

I hereby confirm that the work in this thesis is my own and I give appropriate references and citations whenever I refer to, describe or quote from the work of others.

Xuan CAO

‘The copyright of this thesis rests with the author. Unless otherwise indicated, its contents are licensed under a Creative Commons Attribution-Non-Commercial 4.0 International Licence (CC BY-NC). Under this licence, you may copy and redistribute the material in any medium or format. You may also create and distribute modified versions of the work. This is on the condition that: you credit the author and do not use it, or any derivative works, for a commercial purpose. When reusing or sharing this work, ensure you make the licence terms clear to others by naming the licence and linking to the licence text. Where a work has been adapted, you should indicate that the work has been changed and describe those changes. Please seek permission from the copyright holder for uses of this work that are not included in this licence or permitted under UK Copyright Law.’

Table of Contents

Abstract ..... **I**

Acknowledgements ..... **II**

Declarations of originality and copyright ..... **III**

List of Tables ..... **i**

List of Figures ..... **ii**

Chapter 1 Introduction **1**

1.1 General introduction **1**

1.2 Aims **4**

1.3 Detailed objectives and approach **5**

1.4 Thesis outline and publications **6**

Chapter 2 Theoretical background and methodology **9**

2.1 Carbonate Clumped Isotope Paleothermometry **9**

2.1.1 The theory of multiply substituted isotopologues 9

2.1.2 Theory of carbonate clumped isotope thermometry 10

2.1.3 Experimental Protocol 12

2.1.4 Data Reduction 15

2.2 Calcium carbonate precipitation **22**

2.2.1 Calcium carbonate precipitation under 25-90°C-XC2024 22

2.2.2 Calcium carbonate precipitation under cryogenic temperatures-CS2024 25

2.2.3 Existing calcium precipitates-TK2015 26

2.3 X-ray diffraction (XRD) analysis 28

2.4 Microscopy observation and energy dispersive spectroscopy (EDS) 28

2.5 Elemental analysis 29

2.5.1 Inductively coupled plasma mass spectrometry (ICP-MS) 29

2.5.2 Trace metal distribution coefficient calculation 30

2.6 Calcium carbonate precipitation rate (rp) calculation 33

2.7 PHREEQC modelling 34

Chapter 3 Formation of carbonate polymorphs under controlled laboratory conditions: Relative control of temperature, precipitation rate and ionic impurities 35

3.1 Abstract 35

3.2 Introduction 36

3.3 Methods and materials 39

3.4 Results 39

3.4.1 Chemical evolution log of the solution 39

3.4.2 PHREEQC speciation calculations 43

3.4.3 Mineralogical characterization of precipitates 44

3.5 Discussions 48

3.5.1 Primary control of temperature (T_c) on $CaCO_3$ polymorphism 48

3.5.2 Delaying the vaterite-calcite transformation with the addition of Na^+ 52

3.5.3 Effects of precipitation rates (Log (rp)) on $CaCO_3$ polymorphism 53

3.5.4 Effects of ionic impurities on $CaCO_3$ polymorphism 54

3.5.5 The Aragonite-Vaterite problem: instability of vaterite under elevated temperature 59

3.6 Conclusions 61

Chapter 4 Quantification of trace metal partitioning into calcium carbonate ($CaCO_3$) during the CO_2 degassing 64

4.1 Abstract 64

4.2 Introduction 65

4.3 Methods and materials 67

4.4 Results 68

4.4.1 Chemical evolution of reactive fluids 68

4.4.2 Mineralogy characterization of the precipitated solids 69

4.4.3 Trace metal partitioning between $CaCO_3$ and the reactive fluid 71

4.5 Discussions 75

4.5.1 Comparison between different DMe: trace metal suitable for the research on deposits of $CaCO_3$ polymorph mixture 75

4.5.2 The role of precipitation rate in trace metal partitioning in $CaCO_3$ 79

4.5.3 The role of temperature in trace metal partitioning in $CaCO_3$ 82

4.5.4 Implications for the trace metal incorporation modelling and the use of Me/Ca in field samples 85

4.6 Conclusions 87

Chapter 5 Evaluating kinetic effects in carbonate clumped isotopes (Δ_{47}) under controlled laboratory environments and first laboratory calibration to cryogenic temperatures 89

5.1 Abstract 89

5.2 Introduction 90

5.3 Methods and materials 93

5.4 Results 93

5.4.1 Mineral description and ICP-MS results 93

5.4.2 Carbon and oxygen isotopic composition 95

5.5 Discussions 101

5.5.1 Effects of polymorphism on ^{13}C–^{18}O clumping 101

5.5.2 Effects of pH and Log (rp) on ^{13}C–^{18}O clumping 106

5.5.3 Effects of cation impurities on ^{13}C–^{18}O clumping 107

5.5.4 Extension of Δ_{47}-T calibration to cryogenic temperature 112

5.6 Conclusions 115

Chapter 6 Conclusions and future research directions 117

6.1 Conclusions 117

6.1.1 Overall findings 117

6.1.2 Main findings in research chapters 118

6.2 Further work 120

Appendices 122

Bibliography 138

List of Tables

Table 2.1 List of standards with their isotopic compositions following Bernasconi et al. (2013) 21

Table 2.2 Precipitation conditions of synthetic carbonate in the laboratory..... 27

Table 2.3 Agilent 8900 ICP-MS operating configuration 30

Table 2.4 Elements Measured in this study 31

Table 3.1 List of acronyms in the study..... 38

Table 3.2 Precipitation settings and mineralogy of synthetic calcium carbonates in the laboratory. 40

Table 3.3 Experimental studies of calcium carbonate synthesis with reported composition. 44

Table 4.1 Precipitation details and mineralogy of calcium carbonate precipitates in this study.. 71

Table 5.1 Isotopic composition and distribution coefficient of synthetic calcium carbonates in the laboratory. 95

List of Figures

Figure 1.1 The motivation map of the present study shows key ideas, experimental conditions, and literature. 4

Figure 2.1 Atomic structure of the calcite lattice, illustrating the homogeneous isotope exchange reaction between carbonate ion units on which carbonate clumped isotope thermometry is based. 11

Figure 2.2 Layout of IBEX main software window showing a schematic of the traps 13

Figure 2.3 Schematic illustration of the major components of the source, analyzer and detector array of the Thermo 253-Ultra. 15

Figure 2.4 Example of linear regression for drift correction. 19

Figure 2.5 Scans showing mass 47 intensities across acceleration voltages ranging from 9.36 to 9.39 kV (top) and the linear regression between the background signal and beam intensity. 20

Figure 2.6 ETF correction from the reference frame dated 23rd August 2023 using ETH1, ETH2 and ETH3. 22

Figure 2.7 Flowcharts show the synthetic calcite preparation procedure in the laboratory. 23

Figure 2.8 A schematic representation of the experimental setup devised for calcium carbonate precipitation. 26

Figure 3.1 The precipitation data logs consist of two typical patterns. 40

Figure 3.2 Plots show the PHRREQC model results. 43

Figure 3.3 Ternary diagrams show the $CaCO_3$ polymorph composition. 46

Figure 3.4 Morphology description of the XC2024 samples. 48

Figure 3.5 Column distribution plot showing the mineralogy composition of samples. 49

Figure 3.6 Plots showing the polymorph composition variation with precipitation rates, temperature and the trace metal addition. 52

Figure 3.7 A SEM photo of 25CuT shows the vaterites (V) transformation to calcites (C) is retarded by Na^{+}. 53
Figure 3.8 Illustration of two theories explaining the morphology variation. 55
Figure 3.9 Plots show the PHRREQC model results of ionic impurities speciation of Ba^{2+} under degassing setting and Zn^{2+} under mixing and degassing setting (only the three most abundant species are shown here). The total trace metal concentration of the degassing setting is 1×10^{-4} mol/L, whereas that of the mixing setting is 5×10^{-5} mol/L. 58
Figure 3.10 Illustration of two different calcium carbonate growth theories. 60
Figure 3.11 SEM photo of samples 70SrA and 90SrA. 62
Figure 4.1 Cathodoluminescence (CL) and SEM photos showing the characterization of calcite (C), aragonite (Ar), and vaterite (V) under microscopes. 70
Figure 4.2 Box plot showing the range of Log D_{Me} of the researched elements. 75
Figure 4.3 Scatter plot showing the dependence of Log D_{Me} on temperature and precipitation rate of the researched elements. 78
Figure 4.4 Scatter plot showing the dependence of Log D_{Me} on the precipitation rate of the researched elements. 80
Figure 4.5 Single polarization (-) and SEM photos showing the morphology of calcites (C) under microscopes. 83
Figure 4.6 Scatter plot showing the comparison between the Log D_{Mn2+} and Log D_{Fe3+} dependence on temperature and precipitation rates. 84
Figure 4.7 Scatter plot showing the saturation index variation with temperature increases for calcite, aragonite, and vaterite. 86
Figure 4.8 Scatter plot showing the Fe/Ca (A) and Mn/Ca (B) variation with temperature and precipitation rates. 88
Figure 5.1 Scanning electron microscope (SEM) photos show the morphology characterization of calcites and aragonite precipitated in this study. 94
Figure 5.2 Scatter plot shows the bulk isotope composition of the samples in this study. 99

Figure 5.3 Plots show the relative relation between the current community clumped isotope calibration and the samples in this study. 100
Figure 5.4 Scatter plot shows the correlation between the $\delta^{18}O_{Fluid}$ and the experimental temperature of XC2024 and CS2024. 102
Figure 5.5 Scatter plot shows the relation between clumped isotope (Δ_{47}) and the temperature of active degassing, passive degassing, and NaOH titration samples in this study. 103
Figure 5.6 Scatter plot shows the differences between measured Δ_{47} and the expected Δ_{47}, which vary with the Aragonite to calcite ratio. 104
Figure 5.7 A Scatter plot shows the Δ_{47}-T regression for samples exhibiting no kinetic effects and composed of only one phase. 105
Figure 5.8 Scatter plots show the differences between measured Δ_{47} and the expected Δ_{47} of XC2024. 107
Figure 5.9 Scatter plots show the differences between measured Δ_{47} and the expected Δ_{47} vary with the distribution coefficient. 108
Figure 5.10 Scatter plots show the differences between the measured Δ_{47} and the expected Δ_{47} vary with the Me/Ca. 109
Figure 5.11 Schematic of the calcium carbonate growth pathways and the cation impurities incorporation pathways which is inspired and modified from Putnis et al. (2021). 110
Figure 5.12 Deviations of the measured coral Δ_{47} and $\delta^{18}O_{Fluid}$ from the expected equilibrium values for different studies. 113
Figure 5.13 The scatter plot shows the relation between clumped isotope (Δ_{47}) and the temperature of isotopic equilibrated samples measured in this study. 115

Chapter 1

Introduction

1.1 General introduction

Calcium carbonates, chemically represented as $CaCO_3$, is an important sedimentary rock, extensively distributed across the Earth's surface and forming more than 40% of conventional reservoirs of oil, gas, and water. The oxygen isotopic composition ($\delta^{18}O$) of the natural calcium carbonate deposits, including inorganic limestone and calcifying marine organisms, is widely used to reconstruct the paleotemperature of ancient environments (O'Neil et al., 1969; Kim and O'Neil, 1997; Lear et al., 2000; Adkins et al., 2003; Kim et al., 2007). This conventional $\delta^{18}O$ thermometry, thereby, is a powerful tool in carbonates-related research. However, its application is considerably constrained by uncertainties in the $\delta^{18}O$ value of the parent fluid (Davies et al., 2021).

Over the past two decades, the advent of carbonate clumped isotope thermometry has revolutionized this field by allowing direct calculation of carbonate precipitation temperatures without prior knowledge of the parent fluid's isotopic composition. This method, which involves measuring the "clumping" of ^{13}C-^{18}O bonds within the carbonate lattice, is increasingly employed to infer the origins environments of calcium carbonate sediments (Ghosh et al., 2006; Eiler, 2007; Dennis et al., 2011; Eiler, 2011; Huntington et al., 2011).

Despite the advantage of independence from the parent fluid composition, carbonate clumped isotope thermometry, like conventional $\delta^{18}O$ thermometry, may be affected by kinetic

factors such as temperature, pH, precipitation rate, biological activity, and fluid composition (Tarutani et al., 1969; Kim and O'Neil, 1997; Adkins et al., 2003; Kim et al., 2006; Kim et al., 2007; Dietzel et al., 2009; Gabitov et al., 2012). The exact mechanisms underlying these non-equilibrium effects, however, remain largely elusive for both the $\delta^{18}O$ thermometry and the clumped isotope thermometry. For $\delta^{18}O$ thermometry, natural samples often show lower $\delta^{18}O$ values with rapid growth rates (De Villiers et al., 1995; Adkins et al., 2003), while synthetic samples exhibit variable relationships between $\delta^{18}O$ and precipitation rates—ranging from independence to inverse correlations (Kim et al., 2006). Furthermore, there is ongoing debate regarding the influence of pH on $\delta^{18}O$ (Zeebe, 1999; Jiménez-López et al., 2001; Adkins et al., 2003), with some studies suggesting higher pH leads to lower $\delta^{18}O$ (Dietzel et al., 2009), and others attributing observed effects to dissolution-recrystallization during calcite precipitation (Jiménez-López et al., 2001).

In contrast, the understanding of kinetic effects on clumped isotopes remains even more limited. While some studies argue that the clumped isotope is not the subject of the kinetic effects (Eiler, 2006; Tang et al., 2014), others have proposed various parameters, such as polymorphic composition (Schauble et al., 2006; Guo et al., 2009), pH (Falk et al., 2016; Holdsworth et al., 2022), trace metal incorporation (Kluge and John, 2015a; Tripati et al., 2015), precipitation rate (Herlambang and John, 2021), and biological influences-"vital effects" (Davies and John, 2017, 2019), as potential contributors to kinetic effects in clumped isotopes. Given that most natural carbonate minerals are believed to precipitate under non-equilibrium conditions (Daëron et al., 2019), it is meaningful to propose a proxy that can indicate and assess the clumped isotope non-equilibrium effects.

Bajnai et al. (2020) made a significant advancement by detecting clumped isotope non-equilibrium effects through a dual proxy approach combining Δ_{47} and Δ_{48}. This method represents the first proxy capable of indicating non-equilibrium effects in clumped isotopes. However, while Δ_{47} measurement techniques are well-established, Δ_{48} measurements remain technically

challenging and expensive, limiting their widespread application to only a few specialized laboratories. When studying naturally occurring fault-calcites in Oman, Herlambang and John (2021) proposed a novel combined proxy that integrates clumped isotope data (Δ_{47}) with trace metal concentrations. This new proxy builds on Dromgoole and Walter (1990b)'s finding that the incorporation of divalent Mn and Fe into carbonates correlates strongly with precipitation rate and temperature. Thanks to this paired approach, Herlambang and John (2021) found out that the natural calcite cement from Jebel Madar, Oman, was characterized by high precipitation rates that could induce clumped isotope non-equilibrium effects, resulting in higher apparent clumped isotope temperatures. Compared to Δ_{48} measurements, determining trace metal concentrations using techniques like ICP-MS is more cost-effective and accessible, making this proxy a promising tool for further exploration.

In my thesis, I am interested in further developing this new proxy. The study of Herlambang and John (2021) was limited to natural samples, where parent fluid compositions could not be directly measured, necessitating the assumption that the diagenetic fluid was similar to the fluids in the Dromgoole and Walter (1990b) experimental setup. This PhD thesis aims to refine and validate the potential of this new proxy by performing clumped isotope (Δ_{47}) and trace metal concentration analyses on synthetic carbonates precipitated under controlled laboratory conditions. With precise knowledge of both precipitation temperatures and parent fluid compositions, this research will assess the ability of a paired clumped isotope–trace metal approach to detect kinetic effects induced by factors such as calcium carbonate polymorphism, precipitation rate, pH, and trace metal incorporation. Figure 1.1 illustrates the conceptual framework and motivation for this PhD thesis. The three main research findings in this PhD work were written into three paper drafts that were submitted to journals and are under review.

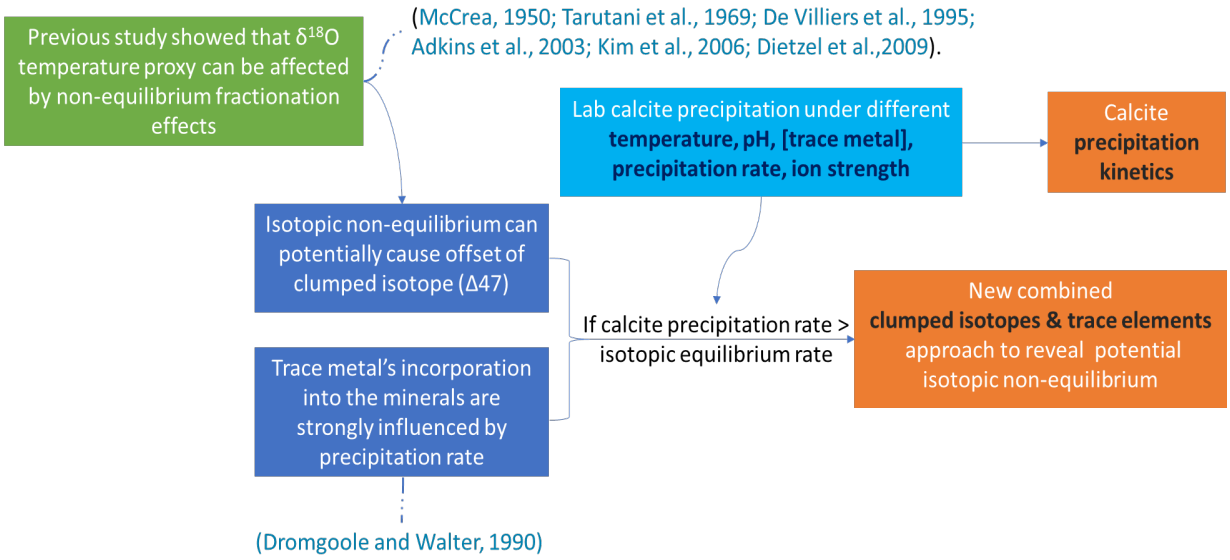


Figure 1.1 The motivation map of the present study shows key ideas, experimental conditions, and literature.

1.2 Aims

The main aim of this study is to test the usefulness of the combined proxy, the pairing of clumped isotope and trace metal concentration, in identifying and constraining the clumped isotope kinetic effects using calcium carbonates synthesised under controlled laboratory conditions. To achieve this aim, the following key questions will be addressed:

1. What are the key control parameters of calcium carbonate polymorphism? Would that influence the trace metal incorporation into calcium carbonate and the clumping of ^{13}C-^{18}O bonds?
2. Which trace metal is sensitive to the changes in fluid properties e.g. temperatures, and precipitation rates, and can we mathematically describe its incorporation into the calcium carbonate as a function of varied fluid properties?
3. What are the possible causes of kinetic effects in clumped isotope and is the combined proxy, clumped isotope and trace metal concentration, a valid proxy in identifying possible causes?

Understanding how kinetic effects would impact carbonate clumped isotopes is pivotal in constraining how this technique can be applied to the reconstruction of fluid environments in various geological settings.

1.3 Detailed objectives and approach

The following objectives were undertaken to answer the key questions above. These objectives are divided based on the research result chapters and associated with the key questions they help to address.

The first objective in general was to determine key control parameters of calcium carbonate polymorphism. Addressing this objective will require the following methodological approach:

1. Precipitation of calcium carbonates in controlled laboratory conditions including a range of temperatures, precipitation rates, pH, and the presence or absence of different trace metals;
2. Undertake experiments to characterize the mineralogy and morphology of the precipitates;
3. Compare the polymorphy composition and morphology characterization of precipitates and assess the relative control of the different parameters under examination, therefore providing a polymorphism background for the following objectives.

The second objective was to derive mathematical equations to describe the relation between trace metal partitioning into calcium carbonate and the initial fluid. This objective includes the following methodological approach:

1. Based on the precipitates obtained in the first objective, perform elemental analysis and calculate the distribution coefficients of trace metals

2. Analysis of the relationship between the controlled precipitation parameters and the calculated distribution coefficients, including a mathematical formulation of this relationship;
3. Understand the relative control of different analytical parameters on trace metal incorporation into calcium carbonate. This objective provides a trace metal incorporation background for the final objective.

The third objective was to identify the possible causes of kinetic effects in the precipitates and test the pairing of clumped isotope and trace metal concentration as a proxy. This objective includes the following methodological approach:

1. Based on the precipitates obtained in objective 1, perform isotopic composition characterization ($\delta^{13}C$, $\delta^{18}O$, and Δ_{47});
2. Identify and quantify the kinetic effects in the dataset given that the initial fluid temperature is known;
3. Evaluate the relative influences of polymorphism, pH, precipitation rate, and trace metal addition on clumped isotope kinetic effects.
4. Test the combined proxy, clumped isotope and trace metal concentration, in identifying and constraining the observed clumped isotope kinetic effects.
5. Derive a new clumped isotope-temperature calibration curve based on the precipitates at equilibrium in this study and the existing precipitates in the literature.

1.4 Thesis outline and publications

This thesis consists of 6 chapters, and is organized as follows:

Chapter 1: "Introduction ". This chapter provides a general introduction, study motivation, research background, aims and detailed objectives and approaches of the study.

Chapter 2: "Theoretical background and methodology". This chapter first presents how the calcium carbonates are synthesised in a controlled laboratory. Then it presents a literature review on the background of the clumped isotope measurement technique. The clumped isotope measurement in this chapter includes the carbon dioxide extraction, purification and data processing used in the John Lab at Imperial College London. This chapter also shows the mineralogy, morphology, and elemental characterization techniques and PHREEQC modelling I did at Imperial College London.

Chapter 3: "Formation of carbonate polymorphs under controlled laboratory conditions: Relative control of temperature, precipitation rate and ionic impurities". This is the first results chapter and is designed to address the first objective. By systematically analysing the role of temperature, pH, and precipitation rate, the relative control significance of each parameter on calcium carbonate polymorphism is evaluated.

This chapter was submitted to Geochemica et Cosmochemica Acta: Cao, X., Weiss, D. J., Alfadel, F., Ferris, T., & John, C. M. Formation of carbonate polymorphs under controlled laboratory conditions: Relative control of temperature, precipitation rate and ionic impurities.

Chapter 4: "Quantification of trace metal partitioning into calcium carbonate ($CaCO_3$) during the CO_2 degassing". This is the second results chapter and is designed to address the second objective. We systematically analysed the link between the trace metal partitioning into calcium carbonates and the environment's conditions. We observed that Fe^{3+}, Mn^{2+}, and Sr^{2+} partitioning in calcium carbonate are temperature and precipitation rate-dependent but not polymorph-dependent.

This chapter was submitted to Geochemica et Cosmochemica Acta: Cao, X., Weiss, D. J., Alfadel, F., Ferris, T., & John, C. M. Quantification of trace metal partitioning into calcium carbonate ($CaCO_3$) during the CO_2 degassing.

Chapter 5: "Evaluating kinetic effects in carbonate clumped isotopes (Δ_{47}) under controlled laboratory environments and first laboratory calibration to cryogenic temperatures". This is the third results chapter and is designed to address the third objective. We present the kinetic effects on clumped isotopes caused by the dehydration of impurity ions and this is the first time it has been observed. We also give the first clumped isotope-temperature calibration extended to the cryogenic temperature ranges (< 0 ℃).

This chapter was submitted to Geochemica et Cosmochemica Acta: Cao, X., Weiss, D. J., Alfadel, F., Ferris, T., & John, C. M. Carbonate clumped isotope (Δ_{47}): evaluation of kinetic effects and the extrapolation to cryogenic temperature under controlled laboratory environments.

Chapter 6: "Conclusions and future research directions". This chapter brings together the studies described in Chapters 3, 4, and 5 to discuss the kinetic effects on the clumped isotope in order to obtain a better understanding of its application under different geological settings.

Chapter 2

Theoretical background and methodology

2.1 Carbonate Clumped Isotope Paleothermometry

2.1.1 The theory of multiply substituted isotopologues

Isotopologues are distinct molecular forms, organic entities, or mineral structural units that share the same components but differ in their isotopic composition such as $^{12}C^{16}O^{16}O$ and $^{12}C^{17}O^{16}O$, and H_2 and D_2 (Eiler, 2006; Eiler, 2007). Multiple-substituted isotopologues incorporate two or more rare 'heavy' isotopes, such as $^{13}C^{18}O^{16}O$. Clumped isotope analysis focuses on the bonding or 'clumping' of these rare 'heavier' isotopes within a molecule (Eiler and Schauble, 2004; Ghosh et al., 2006; Schauble et al., 2006; Huntington and Petersen, 2023).

The primary interest lies in the tendency of these heavier isotopes to bond or 'clump' together within a molecule, rather than being randomly distributed (Schauble et al., 2006). This 'clumping' occurs due to the increased thermodynamic stability of heavy-heavy isotope bonds (e.g., ^{13}C-^{18}O) compared to bonds between light-light or heavy-light isotopes (e.g., ^{12}C-^{16}O or ^{13}C-^{16}O). Bonds between isotopes of greater mass have lower zero-point energy than those formed by the lighter isotopes or heavy-light pairs (Eiler, 2006; Eiler, 2007). Zero-point energy refers to the vibrational and rotational energy of molecules at an absolute zero kelvin (Wang et al., 2004; Eiler, 2007). The zero-point energy decreases with the substitution of a single heavy isotope and further decreases with an additional substitution for another heavier isotope (Urey, 1947; Bigeleisen, 1955; Eiler, 2007). The likelihood that clumped isotopes remain bonded at lower temperatures is higher,

which results in a deviation from a purely random distribution. This probability is counterbalanced by the system's entropy, which drives the distribution toward randomness as temperature rises (Eiler and Schauble, 2004; Ghosh et al., 2006; Schauble et al., 2006; Huntington and Petersen, 2023). Consequently, there is more 'clumping' of heavy isotopes at lower temperatures, and this clumping diminishes as the temperature increases.

2.1.2 Theory of carbonate clumped isotope thermometry

When synthetic inorganic calcite and natural biogenic aragonite are digested with phosphoric acid, the resulting CO_2 contains doubly substituted isotopologues ($^{13}C^{18}O^{16}O$). The abundance of these isotopologues is directly related to the presence of $^{13}C–^{18}O$ bonds in the digested carbonate material (Ghosh et al., 2006). In carbonates that have formed at lower temperatures, the occurrence of ^{13}C and ^{18}O isotope bonds in the CO_2 molecule (i.e., $^{13}C^{18}O^{16}O$) is higher than what would be expected based on probability alone (Ghosh et al., 2006). Therefore, the equilibrium constant of isotopic equilibrium reaction for carbonates like equation (2.1) is temperature-dependent and approaches 1.0 with the increase of temperature. Figure 2.1 shows the isotopic exchange among calcite ion units.

$$Ca^{13}C^{16}O_3 + Ca^{12}C^{18}O^{16}O_2 = Ca^{13}C^{18}O^{16}O_2 + Ca^{12}C^{16}O_3 \quad (2.1)$$

This means that the excess of this isotopologue, which has a mass of 47, can be quantified to estimate the temperature at which the carbonate mineral originally precipitated or re-precipitated. The temperature is determined by measuring the mass 47 isotopologue (Δ_{47}) and the oxygen isotopic composition ($\delta^{18}O$) of the CO_2 generated during acid digestion. This method, known as carbonate clumped isotope thermometry, allows for the direct determination of the carbonate mineral's precipitation temperature without needing to know the oxygen isotope composition ($\delta^{18}O_{fluid}$) of the fluid from which the carbonates formed (Eiler, 2007).

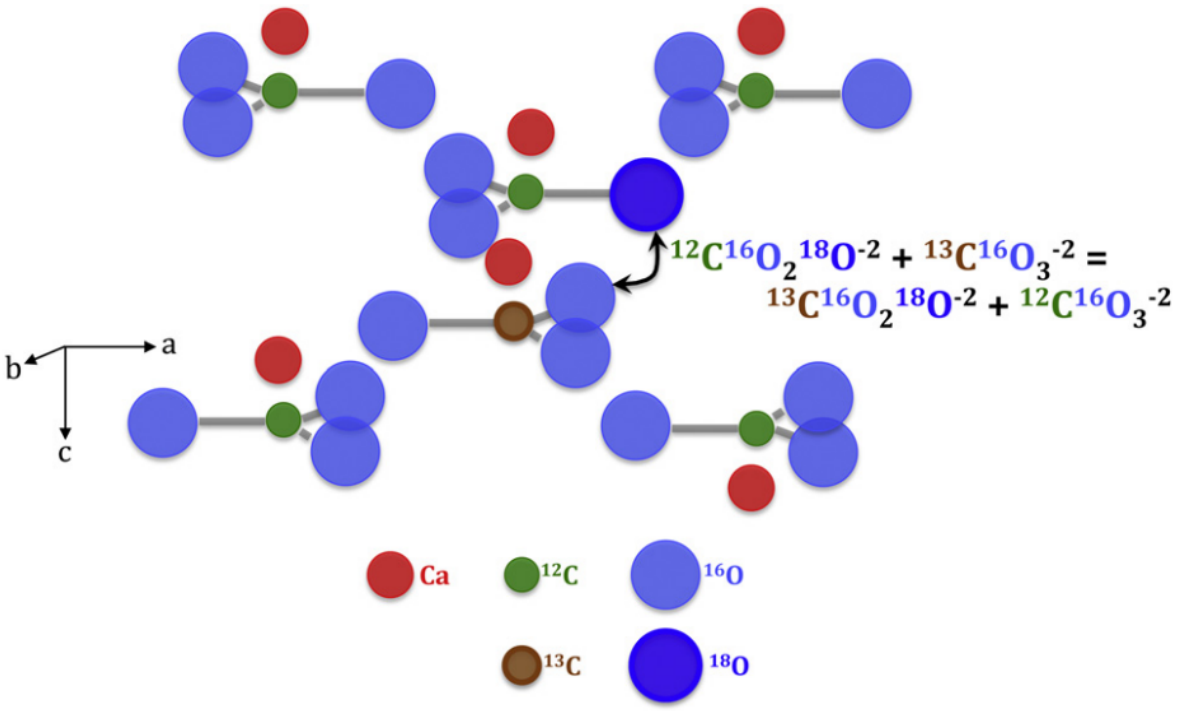


Figure 2.1 Atomic structure of the calcite lattice, illustrating the homogeneous isotope exchange reaction between carbonate ion units on which carbonate clumped isotope thermometry is based.

Analogous reactions exist among structural constituents of aragonite-structure solid carbonates and dissolved carbonate species (carbonic acid, carbonate, and bicarbonate ion). The figure is taken from Eiler (2011).

The Δ_{47} were converted to temperatures ($T_{\Delta47}$) through the current community Δ_{47}-temperature (Δ_{47}-T) calibration of Anderson et al. (2021) (Eqs (2.2)):

$$\Delta_{47} = 0.0391 \pm 0.0004 \times \frac{10^6}{T^2} + 0.154 \pm 0.004 \quad (2.2)$$

where T is the temperature in Kelvin (K). For natural samples, based on the clumped isotope temperature $T_{\Delta47}$ and the measured solid $\delta^{18}O$, the parent fluid $\delta^{18}O$ can be calculated by using the traditional $\delta^{18}O$-T calibration of Kim and O'Neil (1997) (in this study, this equation was applied to all phases including calcite, aragonite, and vaterite):

$$1000ln\alpha(Calcite - H_2O) = 18.03 \times \left(\frac{10^3}{T}\right) - 32.42 \quad (2.3)$$

in which α is calculated by Friedman and O'Neil (1977) as the following equation (2.4) and the conversion from PDB scale to VSMOW scale is calculated by Coplen et al. (1983) as equation (2.5):

$$\alpha = \frac{1000+\delta^{18}O_{Solid}}{1000+\delta^{18}O_{H_2O}} \quad (2.4)$$

$$\delta^{18}O_{VSMOW} = 1.03091 \times \delta^{18}O_{PDB} + 30.91 \quad (2.5)$$

2.1.3 Experimental Protocol

The extraction of clumped isotope values from carbonate rocks involves three essential stages, carried out in sequence: gas extraction, purification, and measurement using a mass spectrometer (Huntington et al., 2009). After these measurements are obtained, the resulting data undergo processing and correction before they can be interpreted.

2.1.3.1 CO_2 extraction and purification

At the John Lab at Imperial College London, measurements of clumped isotopes (Δ_{47}) and bulk isotopes ($\delta^{18}O$ and $\delta^{13}C$) were obtained from CO_2 that was extracted and purified using a fully automated system known as IBEX (Imperial Batch EXtraction) (Figure 2.2) (Davies et al., 2021). The IBEX (developed by the John Lab and sold by Protium) is the first fully automated sample digestion-purification system dedicated for Δ_{47} analysis. Compared with the traditional manual preparation lines, the IBEX enables time-saving, sample-saving, and highly repeatable Δ_{47} analysis (John and Davis, 2015). Typically, the IBEX is capable of loading 39 positions (16 standards and 23 samples) in one run with each position containing a vial of ~3.5 mg powdered sample (pure carbonate or sample with the equivalent carbonate weight). Each sample is subjected to acid digestion (Eq. 2.6) by being dropped into a vacuum-sealed common acid bath containing 105% orthophosphoric acid, heated to 90 °C, and reacted for 10 minutes for calcite and 20 minutes for dolomites (Dennis et al., 2011).

$$H_3PO_4 + XCO_3 \rightarrow CO_2 + H_2O + X^{2+} + HPO_4^{2-} \quad (2.6)$$

Then the gas products are transferred by helium flow to the three functional traps to remove water, sulphur, and hydrocarbon impurities step by step (Fig. 2.2):

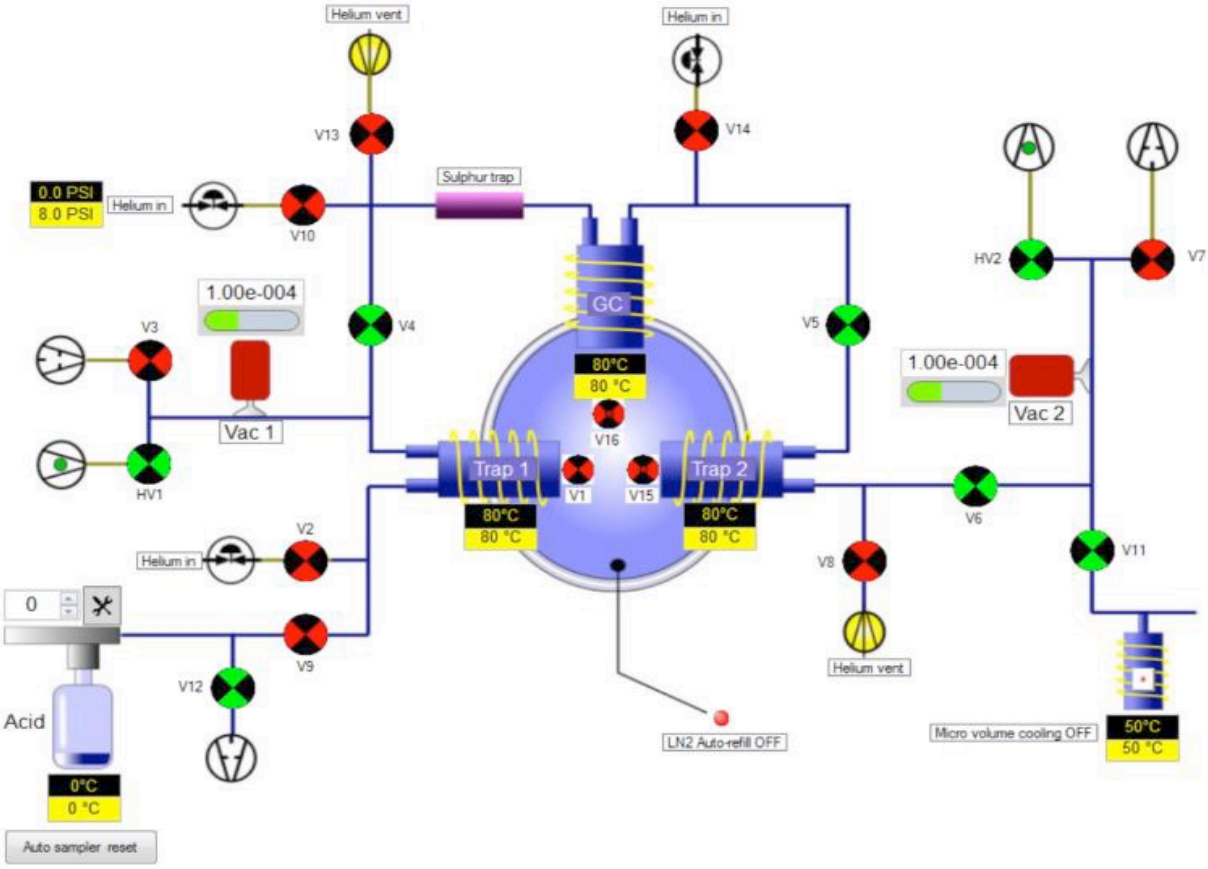


Figure 2.2 Layout of IBEX main software window showing a schematic of the traps

1. Trap 1 is cooled to -195.79 °C using liquid nitrogen (LN2) to trap the CO_2 after acid digestion has occurred.

2. Trap 1 is then heated to -80°C, which releases the CO_2 while other condensable gases, such as H_2O, remain trapped in Trap 1.

3. The released CO_2 is then transferred under helium flow through a sulphur trap containing silver wool, which removes any sulphur.

4. The CO_2 is moved under helium flow across a 2.5 mm gas chromatography (GC) column maintained at -35°C.

5. The CO_2 is then captured in Trap 2 at -195.79°C.

6. The microvolume temperature is lowered to -100°C, where the purified CO_2 is transfer by heating Trap 2.

7. Finally, the CO_2 is warmed to room temperature and transferred to the mass spectrometer via a transfer line, where it is ready for clumped isotope analysis in the mass spectrometry.

2.1.3.2 Mass Spectrometry

The John Lab operates a dual inlet gas source isotope ratio mass spectrometer (IRMS): MAT-253 (Figure 2.3, Thermo Scientific, US) with additional Faraday collectors registered for m/z 44–49 that permits clumped isotope (Δ_{47}) measurements. These mass spectrometers are equipped with dual inlet systems, enabling the determination of isotope ratios by alternately introducing the sample gas and a reference gas of known isotopic composition into the mass spectrometer under nearly identical pressure conditions (Huntington et al., 2009).

The bellow pressure was adjusted to approximately 45 mbar to produce an m/z 44 ion beam signal of roughly 15,000 mV after the sample was introduced into the mass spectrometer. The sample analysis in MAT-253 consists of 8 acquisitions each with 7 cycles with an integration time of ~25 seconds per cycle. Acquisitions are constrained by a CO_2 gas standard provided by BOC with fixed bulk isotope composition of $\delta^{13}C_{VPDB}$ = -36.8‰ and $\delta^{18}O_{VSMOW}$ = 8.6‰. The averaged precision for a normal run is 0.02‰ for Δ_{47} and 0.01‰ for both $\delta^{13}C_{VPDB}$ and $\delta^{18}O_{VSMOW}$. In the present study, at least 3 replicates for each sample were analysed on separate runs to obtain a realistic estimate of error and a typical acquisition time for one replicate was around 2.5 hours. Generally, a fully loaded IBEX run is finished in ~90 hours.

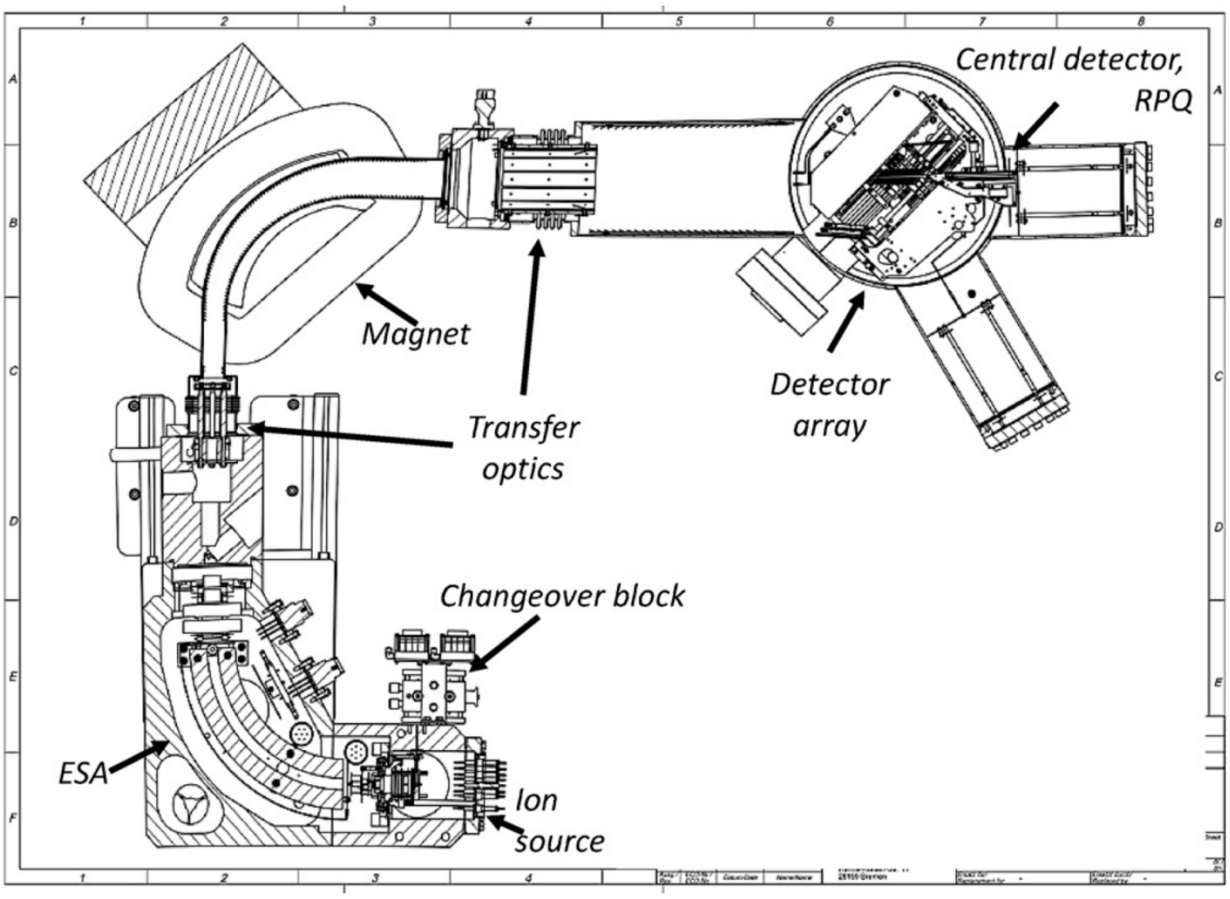


Figure 2.3 Schematic illustration of the major components of the source, analyzer and detector array of the Thermo 253-Ultra.

The changeover block is a set of pneumatic valves. Other major labelled components include the Nier-type electron impact ion source, the electrostatic analyzer (ESA), the magnet and the detector array. The figure is taken from Eiler et al. (2013)

2.1.4 Data Reduction

Following analysis, data processing was performed using the community software Easotope (John and Bowen, 2016).

2.1.4.1 Raw data processing

The process begins with the calculation of the relative abundance ratios R13 ($^{13}C/^{12}C$), R17 ($^{17}O/^{16}O$), and R18 ($^{18}O/^{16}O$) using the known $\delta^{18}O$ and $\delta^{13}C$ values of the working or reference

gas (WG). The relative abundances of $^{13}C/^{12}C$, $^{17}O/^{16}O$, and $^{18}O/^{16}O$ in the reference gas are defined as follows:

$$R_{REF}^{13} = \left(1 + \frac{\delta^{13}C_{REF}}{1000}\right) \times R_{VPDB}^{13} \quad (2.7)$$

$$R_{REF}^{18} = \left(1 + \frac{\delta^{18}O_{REF}}{1000}\right) \times R_{VSMOW}^{18} \quad (2.8)$$

$$R_{REF}^{17} = (1 + \frac{R_{REF}^{18}}{R_{VSMOW}^{18}})^{\lambda} \times R_{VSMOW}^{17} \quad (2.9)$$

The ratios R^{13}_{VPDB}, R^{18}_{VSMOW}, and R^{17}_{VSMOW} are given as 0.01118, 0.0020052, and 0.00038475, respectively (Brand et al., 2010). The value of λ is 0.528, according to Daëron et al. (2016). Subsequently, the abundances of ^{12}C, ^{13}C, ^{16}O, ^{17}O, and ^{18}O in the reference gas were calculated before determining its isotopologue composition for mass 44-49 (R^{44}_{REF} - R^{49}_{REF}), assuming a stochastic distribution (John and Bowen, 2016). Once the isotopologue composition of the reference gas was established, the isotopic composition of the sample gas ($\delta^{13}C_{SAMPLE}$ and $\delta^{18}O_{SAMPLE}$) was defined relative to the reference gas. The calculation involved:

1. Determining the abundance ratio (R^{i}_{SAMPLE}) for each m/z value (i = 44, 45, 46, 47, 48, 49) relative to m/z = 44 using the voltage (Vi) for each m/z value:

$$R_{Sample}^{i} = \frac{(Vi/V44)SAMPLE}{(Vi/V44)REF} \times R_{REF}^{i} \quad (2.10)$$

2. Compute the abundance ratio of the different masses (δ_i):

$$\delta_{SAMPLE}^{i} = \left(\frac{R_{SAMPLE}^{i}}{R_{REF}^{i}} - 1\right) \times 1000 \quad (2.11)$$

3. Compute the abundance ratio - R^{18}_{SAMPLE} (Assonov and Brenninkmeijer, 2003):

$$-3K^2(R_{SAMPLE}^{18})^{2\lambda} + 2K(R_{SAMPLE}^{45})(R_{SAMPLE}^{18})^{\lambda} + 2(R_{SAMPLE}^{18}) - R_{SAMPLE}^{46} = 0 \quad (2.12)$$

where

$$K = \frac{R_{REF}^{17}}{(R_{REF}^{18})^{\lambda}} \tag{2.13}$$

4. Compute the $\delta^{18}O_{SAMPLE}$:

$$\delta^{18}O_{SAMPLE} = (\frac{R_{SAMPLE}^{18}}{R_{VSMOW}^{18}} - 1) \times 1000 \tag{2.14}$$

5. Compute the $\delta^{13}C_{SAMPLE}$:

$$\delta^{13}C_{SAMPLE} = (\frac{R_{SAMPLE}^{13}}{R_{VPDB}^{13}} - 1) \times 1000 \tag{2.15}$$

where

$$R_{SAMPLE}^{13} = R_{SAMPLE}^{45} - 2(R_{SAMPLE}^{17}) \tag{2.16}$$

$$R_{SAMPLE}^{17} = K(R_{SAMPLE}^{18})^{\lambda} \tag{2.17}$$

6. Compute the ratio of isotopologues in $CO_{2\ SAMPLE}$ as a stochastic distribution, before calculating the abundance ratio for $CO_{2\ SAMPLE}$ as the stochastic distribution of m/z=45,46,47 (Rm/z*SAMPLE):

$$R45_{SAMPLE}^{*} = 45_{CO_2\ SAMPLE}/44_{CO_2\ SAMPLE} \tag{2.18}$$

$$R46_{SAMPLE}^{*} = 46_{CO_2\ SAMPLE}/44_{CO_2\ SAMPLE} \tag{2.19}$$

$$R47_{SAMPLE}^{*} = 47_{CO_2\ SAMPLE}/44_{CO_2\ SAMPLE} \tag{2.20}$$

The $\Delta_{47\ RAW}$ then can be calculated by using equation (2.21):

$$\Delta 47_{RAW} = \left[\left(\frac{R47_{SAMPLE}}{R47^{*}_{SAMPLE}} - 1\right) + \left(\frac{R46_{SAMPLE}}{R46^{*}_{SAMPLE}} - 1\right) + \left(\frac{R45_{SAMPLE}}{R45^{*}_{SAMPLE}} - 1\right)\right] * 1000 \quad (2.21)$$

where $R47_{SAMPLE}$, $R46_{SAMPLE}$, $R45_{SAMPLE}$ are abundance ratios of masses 47, 46, and 45 relatives to mass 44; i.e., the 47/44, 46/44, 45/44 ratios, respectively. $R47^{*}_{SAMPLE}$, $R46^{*}_{SAMPLE}$, $R45^{*}_{SAMPLE}$ are the corresponding ratios that would occur in the sample if it had a stochastic distribution (Eiler, 2006; Ghosh et al., 2006; Huntington et al., 2009)

2.1.4.2 Data corrections

Three corrections need to be applied to the raw data from previous calculations: drift correction, non-linearity correction, and reference frame projection. The drift correction was necessary because contaminants in the isotope-ratio mass spectrometer can cause signal instability related to the ion source performance, a phenomenon known as drift (D'Autry et al., 2010). The drift was corrected by plotting the raw $\delta^{18}O$ and $\delta^{13}C$ data against the isotopic values of inter-laboratory carbonate standards (ETH 1 to ETH 4) (Müller et al., 2017) and two internal standards: ICM and IOL. For more information on the isotopic composition of these standards, refer to Table 2.1. A linear regression model is fitted via the carbonate standards data (Figure 2.4). The corrected values for $\delta^{18}O$ and $\delta^{13}C$ ($\delta^{18}O_{CORRECTED}$ and $\delta^{13}C_{CORRECTED}$) were obtained by applying the resulting linear equation:

$$\delta^{18}O_{CORRECTED} = slope(\delta^{18}O_{CORRECTED}) + intercept \quad (2.22)$$

$$\delta^{13}C_{CORRECTED} = slope(\delta^{13}C_{CORRECTED}) + intercept \quad (2.23)$$

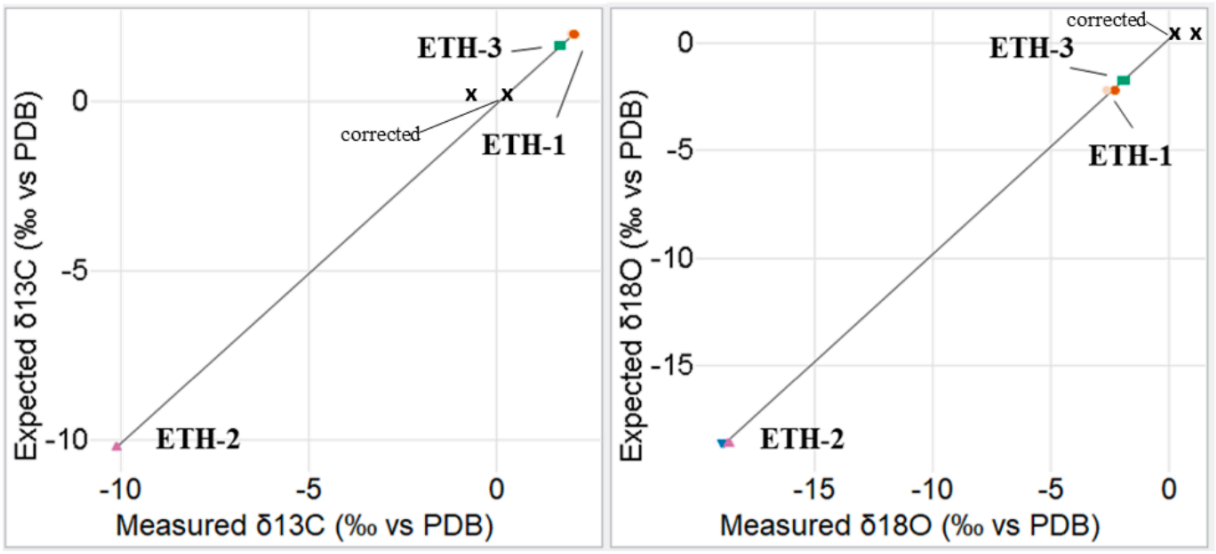


Figure 2.4 Example of linear regression for drift correction.

The next correction addresses the non-linearity in clumped isotopes inherent to all mass spectrometers, which varies depending on the machine and can change over time due to factors like cleanliness, filament condition, and tuning (Bernasconi et al., 2013). Two methods are commonly used to correct this effect: the "heated gas correction" (Huntington et al., 2009) and the "pressure baseline correction (PBL)" (Bernasconi et al., 2013). In this study, the "pressure baseline correction (PBL)" was used for samples processed with the auto-purification IBEX.

The pressure baseline (PBL) correction was applied to samples purified using the automated IBEX line to optimize the non-linearity adjustment (Bernasconi et al., 2013). This correction eliminates the influence of secondary electrons on the Faraday cup collectors, which generate a negative baseline signal inversely proportional to the beam intensity. Following Bernasconi et al. (2013), daily scans were conducted using the reference gas at varying intensities, from 12 kV to 17 kV in 1 kV increments, focusing on the m/z 44 beam. The negative background intensity was then plotted against the beam intensity, and the resulting regression was used to correct the sample intensity (Figure 2.5).

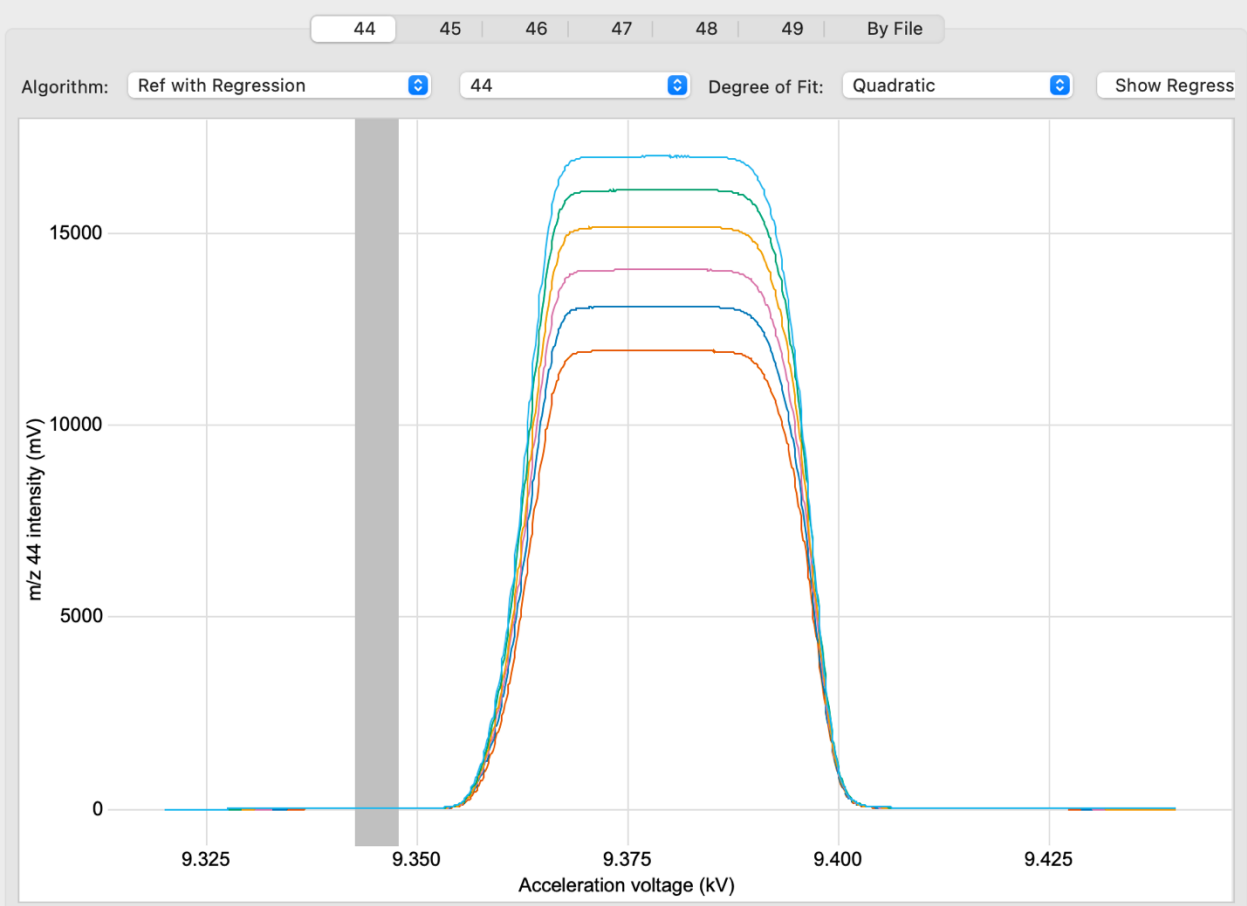


Figure 2.5 Scans showing mass 47 intensities across acceleration voltages ranging from 9.36 to 9.39 kV (top) and the linear regression between the background signal and beam intensity.

For the final correction, the raw data were projected onto the inter-laboratory absolute reference frame, also known as the Intercarb Carbon Dioxide Equilibrated Scale (I-CDES) (Bernasconi et al., 2021). This projection was based on routinely measured carbonate standards, including ETH1, ETH2, ETH3, ETH4, and our internal Carrara Marble (ICM) (Muller et al., 2017; Davies and John, 2019; Bernasconi et al., 2021). Previously referred to as the "carbon dioxide equilibrated scale (CDES)," when it was anchored on equilibrated CO_2 gases, this correction addresses scale compression by aligning measurement results of carbonate standards with the known reported value scale (Dennis et al., 2011; Bernasconi et al., 2021). The carbonate clumped isotope values of these standards are reported relative to an equilibrated gas reference frame

(Figure 2.6), giving absolute Δ_{47} values listed in Table 2.1 for ETH-1, ETH-2, and ETH-3, as per Bernasconi et al. (2021).

Table 2.1 List of standards with their isotopic compositions following Bernasconi et al. (2013) .

Carbonate Standards	Δ_{47} (‰, I-CDES)	$\delta^{13}C$ (‰,VPDB)	$\delta^{18}O$ (‰,VPDB)
ETH-1	0.2052	2	-2.19
ETH-2	0.2085	-10.2	-18.58
ETH-3	0.6132	1.67	-1.75
ETH-4	0.4505	-10.22	-18.67
ICM	0.291	2.02	-1.82
IOL	0.636	0.3	0.38

2.1.4.3 Metrics of contaminations

Contamination (e.g. organics and sulphur) can adversely impact clumped isotope precision, even at ppb level concentrations as this can cause a large Δ_{47} offset (Eiler, 2007). Therefore, it is crucial to monitor the contamination of analytes. Two parameters-$\Delta 48_{offset}$ and 49_{param} are calculated in Easotope to Monitor contamination. $\Delta 48_{offset}$ is calculated through equation (2.24) in which $\Delta 48$ of samples can be easily calculated in a similar equation like equation (2.21). If the $\Delta 48_{offset}$ is greater than 1‰, the replicate measurement is considered contaminated and not used for temperature calculations.

$$\Delta 48_{offset} = \Delta 48_{sample} - \frac{\sum_1^n \times \Delta 48_{standard}}{n} \quad (2.24)$$

If the 49_{param} (calculated through equation (2.25)) is greater than 0.2‰ the standard is considered as potentially contaminated. However, this metric is sample dependent and for unknown samples, a 49_{param} greater than 0.2‰ is sometimes acceptable.

$$49_{param} = \left[R^{49}_{sample} - R^{49}_{WG}\right] \times 10^4 \quad (2.25)$$

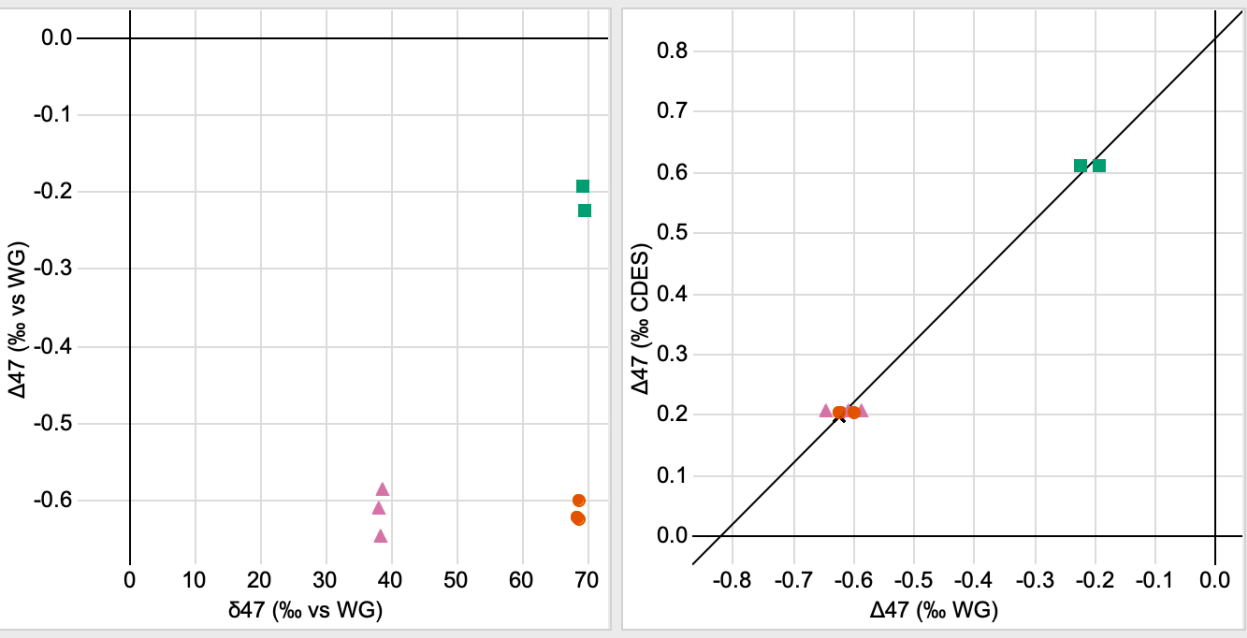


Figure 2.6 ETF correction from the reference frame dated 23rd August 2023 using ETH1, ETH2 and ETH3.

2.2 Calcium carbonate precipitation

Three different types of calcium carbonate precipitates-XC2024, CS2024, and TK2015-are used in this study and the synthesis process is summarized in Figure 2.7.

2.2.1 Calcium carbonate precipitation under 25-90°C-XC2024

To synthesise the $CaCO_3$, we initially dissolved 700 mg of $CaCO_3$ (99.95-100.05%, Sigma) in 1 L deionized water (18.2 MΩ•cm, Milli-Q) within a polycarbonate jar which was housed in a thermostat (Alpha RA 24, LAUDA), equipped with an overhead stirrer (Basic20, SciQuip). The dissolution of $CaCO_3$ was achieved through continuous bubbling of pure CO_2 (100%, BOC) at ~1 bar for nearly 10 hours (Figure 2.7A). Subsequently, the solution underwent filtration using double-layer filter papers (20-45 um pore size, VWR) to remove any undissolved solids. Following dissolution, the solution was maintained at the desired Tc (25, 50, 70, 90°C) for sufficient duration to reach isotopic equilibrium according to Beck et al. (2005) and Uchikawa and Zeebe (2012). The requirement for isotopic equilibrium came from further research plans. The isotopic equilibration

duration ranges from 2 hours at 90℃ to > 30 hours at 25℃ (Kluge et al., 2015). Throughout the equilibration period, CO_2 was continuously bubbled to avoid early precipitation.

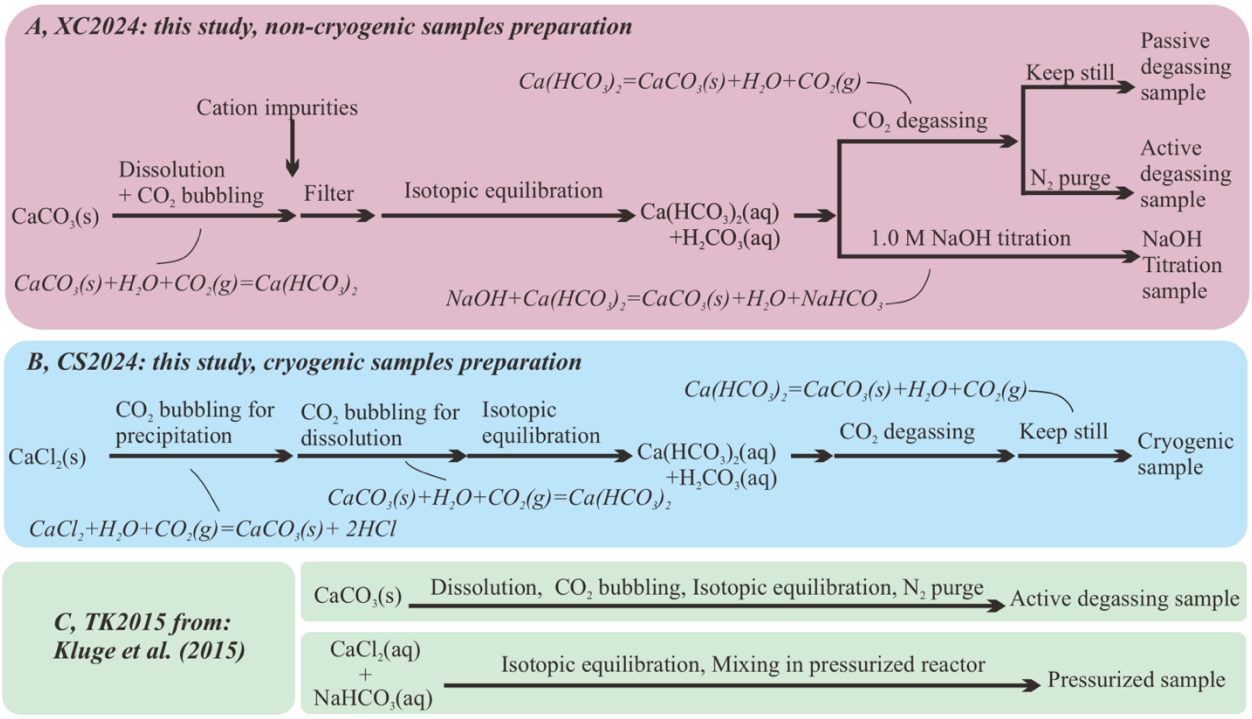


Figure 2.7 Flowcharts show the synthetic calcite preparation procedure in the laboratory.

A, Non-cryogenic samples (XC2024) prepared in this study by either CO_2 degassing or NaOH titration; B, Cryogenic samples (CS2024) precipitated by bubbling CO_2 through highly concentrated $CaCl_2$ solution and then degassing; and C, Samples from Kluge et al. (2015) (TK2015) by passive degassing or mixing in a pressurized vessel. The precipitation rate for A increases in the sequences of passive degassing, active degassing, and NaOH titration.

In experiments examining ionic impurities effects, the corresponding chloride salt ($CuCl_2$, $MgCl_2$, $MnCl_2$, $FeCl_3$, and $SrCl_2$ reagent grade, Sigma) was added before the equilibration step. In this project, the determination of trace metal concentrations in calcium carbonates is one of the most critical experiments. Given the constraints of time, only a select few trace metals will be investigated. Based on a comprehensive literature review, Mg, Mn, Fe, Cu, and Sr have been chosen as the primary research targets. The selection is justified as follows:

1. **Magnesium (Mg)**: As the second most abundant metal in typical seawater, Mg is more likely to be incorporated into calcite. Moreover, Mg is one of the key metals associated with carbonate minerals, alongside Ca and Fe.

2. **Mg/Ca Ratios**: The Mg/Ca ratio has been extensively reported as a reliable paleoenvironmental proxy for calcites found in speleothems, foraminifera, and molluscs (Elderfield et al., 2002; Immenhauser et al., 2005; Sadekov et al., 2010)

3. **Iron (Fe) and Manganese (Mn)**: Previous studies by Dromgoole and Walter (1990b) and Herlambang and John (2021) have demonstrated that the distribution coefficients of Fe and Mn are effective indicators for determining precipitation rates.

4. **Cathodoluminescence Analysis**: Cathodoluminescence is a vital technique for distinguishing carbonate minerals. The luminescence color and intensity are influenced by the ratio of activators to quenchers. In carbonates, Mn typically acts as the primary activator element, while Fe serves as the general quencher element (Dromgoole and Walter, 1990b).

5. **Strontium (Sr)**: Sr and its isotopes are frequently cited as significant paleoenvironmental indicators in carbonate research (Lorens, 1981; Gabitov and Watson, 2006; Tang et al., 2008).

To adjust and cover a wide Log (rp) range during the calcium carbonate precipitation, three different methods were implemented to induce precipitation:

(1) Passive degassing method ("P method"): the prepared solutions were covered with films, leaving several needle holes for gas exchange. Subsequently, the overhead stirrer was removed, allowing the solutions to stand still and degas by CO_2 exchange with the air above. This yields the low Log (rp).

(2) Active degassing method ("A method"): Pure N_2 (100%, BOC) was bubbled through the solution with the overhead stirrer operating at 90 rpm to expedite CO_2 stripping. The N_2 bubbling rate was regulated to ~ 1 bubble per second using a needle valve. This yields the intermediate Log (rp).

(3) Titration method ("T method"): A titrator (888 Titrando, Metrohm) was employed to induce precipitation by titrating 1.0 M NaOH into the solution at a rate of ~ 0.6 ml/min with the overhead stirrer speed maintained at 90 rpm. This yields the high Log (rp).

To mitigate the influence of evaporation, all gases were initially rinsed in a wash bottle filled with deionized water (Figure 2.8). The typical precipitation duration for the P, A, and T methods is within 20 days, 7 days, and 1 hour, respectively. In A and T method experiments, Tc and pH were monitored employing a data logger (OM-CP-PHTEMP2000, OMEGA) equipped with a thermometer (PR-10, OMEGA) and a pH electrode (HI-1131P, HANNA Instrument). Throughout the experiment, periodic sampling of the solution was performed using syringes with filters (45 um pore size, VWR). After precipitation, the solutions underwent filtration and the collected precipitates were air-dried at room temperature. The precipitation experiments here are similar to that in Kluge et al. (2015), but differ from Mavromatis (Mavromatis et al., 2013; Mavromatis et al., 2022) where aragonite or calcite seeds were used to control the mineralogy of precipitates.

2.2.2 Calcium carbonate precipitation under cryogenic temperatures-CS2024

Three cryogenic samples were precipitated separately at -10, -15, and -24°C and referred to as **CS2024**. The solution freezing point was lowered to nearly -50°C by adding 3.86 mol solid $CaCl_2$ to 1L deionised water (Ropp, 2013). The CO_2 was then bubbled through the solution for at least 7 days to induce $CaCO_3$ precipitation, dissolution, and reach isotopic equilibrium. The resulting solution of $Ca(HCO_3)_2$ was then passively degassed for up to 1 month for cryogenic

$CaCO_3$ precipitation (Figure 2.7B). Gases were first rinsed with deionized water before reaching the precipitation vessel to minimize evaporation influences. After precipitation, all precipitates were collected through filtering and then air-dried at room temperature.

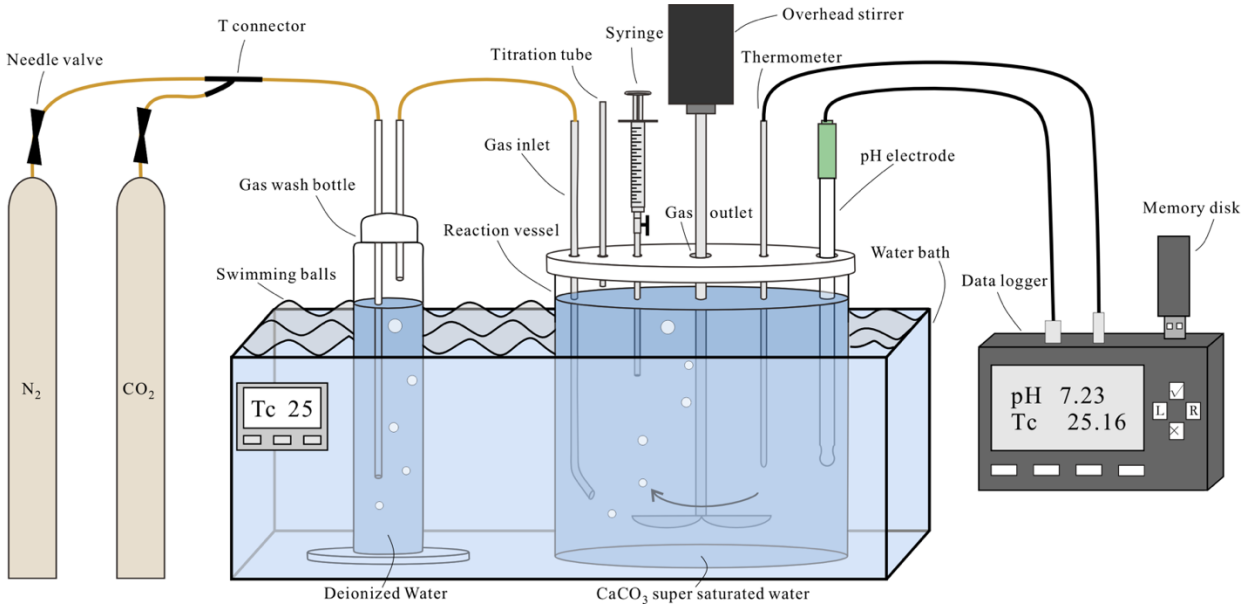


Figure 2.8 A schematic representation of the experimental setup devised for calcium carbonate precipitation.

The setup is adaptable, allowing for the conversion to three distinct precipitation methods: passive degassing (P), active degassing (A), and NaOH titration (T) through disassembly and recombination. This setup is also used for both the precipitation of XC2024 and CS2024.

2.2.3 Existing calcium precipitates-TK2015

Some existing isotopic equilibrium precipitates of Kluge et al. (2015) were remeasured in this study for three reasons: First, most Kluge et al. (2015) samples were precipitated using a method similar to the active degassing method (not exactly the same) without cation impurities so can be used to double-check the sample precipitated under the same temperature. Secondly, they were previously measured with the same mass spectrometer and anchored both the previous and the current Δ_{47}-T calibration curves (Kluge et al., 2015; Anderson et al., 2021), allowing us to check data reproducibility and mass spectrometer performance. Finally, some of the samples were precipitated in a pressurized vessel at up to 250°C (pressurized samples) by mixing $CaCl_2$ and $NaHCO_3$ (Figure 2.7 C), helping us to build a wider temperature range Δ_{47}-T calibration. The

remeasured samples were referred to as **TK2015**. See Table 2.2 and Figure 2.7C for sample preparation details

The TK2015 precipitated from 2012 to 2014 in the John Lab at Imperial College London and has been previously reported (Kluge and John, 2015a; Kluge et al., 2015). Two distinct precipitation methods were used to produce carbonate minerals at two different temperature ranges. For the low-pressure experiments (25-91°C), carbonates were precipitated through slow degassing of the $CaCO_3$ solution that was previously supersaturated with CO_2, which is in a similar setting as the precipitation conducted by Ghosh et al. (2006). The high-pressure precipitation (25-250 °C) was achieved by mixing 0.1 mol/L $CaCl_2$ and 0.18 mol/L $NaHCO_3$ in a heated and pressurized reaction vessel (~0.006 m^2 cross-sectional area, ~50 mL) to avoid the boiling of the fluid. Before each precipitation, all solutions were kept under the experimental temperature long enough to reach isotopic equilibrium according to the model of Beck et al. (2005) and Uchikawa and Zeebe (2012). X-ray diffraction (XRD, Kluge et al. (2015)) was conducted on all precipitates to characterize mineralogy. Most samples are pure calcite, few contain ~ 20% aragonite, and only two samples are composed of ~ 80% aragonite and ~20% calcite. Precipitation and mineral characterization details for each sample are summarized in Table 2.2.

Table 2.2 Precipitation conditions of synthetic carbonate in the laboratory.

Mineralogy of precipitates characterized by XRD. "No" samples are the degassed precipitates with no additional trace metal and "HT" samples are carbonates precipitated in the high-pressure vessel.

No.	Precipitation Temperature (°C)	Fluid Chemical Composition	Synthesis time (h)	Mineralogy
No-1	49.6 ± 0.5	$CaCO_3$ 0.74 g/L	195	Calcite
No-2	69.9 ± 0.5	$CaCO_3$ 0.76 g/L	25	Calcite (90%), aragonite (10%)
No-3	79.9 ± 0.5	$CaCO_3$ 0.70 g/L	20	Calcite (78%), aragonite (22%)
No-4	91.0 ± 0.5	$CaCO_3$ 0.74 g/L	138	Calcite (17%), aragonite (83%)
HT-1	25 ± 2	$NaHCO_3$ 0.17 M + $CaCl_2$ 0.1 M	281.5	Calcite
HT-2	50 ± 2	$NaHCO_3$ 0.18 M + $CaCl_2$ 0.1 M	221	Calcite

No.	Precipitation Temperature (°C)	Fluid Chemical Composition	Synthesis time (h)	Mineralogy
HT-3	80 ± 2	$NaHCO_3$ 0.18 M + $CaCl_2$ 0.1 M	144.75	Calcite (21%), aragonite (79%)
HT-4	125 ± 2	$NaHCO_3$ 0.18 M + $CaCl_2$ 0.1 M	113.5	Calcite
HT-5	125 ± 2	$NaHCO_3$ 0.18 M + $CaCl_2$ 0.1 M	113.5	Calcite
HT-6	175 ± 2	$NaHCO_3$ 0.18 M + $CaCl_2$ 0.1 M	59.5	Calcite
HT-7	250 ± 2	$NaHCO_3$ 0.18 M + $CaCl_2$ 0.1 M	41	Calcite

2.3 X-ray diffraction (XRD) analysis

Precipitated minerals were characterized for mineralogy at the Department of Materials at Imperial College London by using X-ray powder diffraction (XRD, PANalytical X'pert Pro MPD) with Cu Kα radiation. Each sample was scanned in continuous mode with 2θ from 15° to 85° and a step size of 0.0167. Subsequently, PANalytical HighScore version 5.2 was utilized for further data processing. The raw data underwent initial fitting via Default Profile Fit after peak selection, followed by Size-Strain Analysis. The Default Profile Fit and the Size-Strain Analys were all constrained by a LaB6 standard, before executing Expanded Rietveld for phase quantification. The resulting detection limit was ~1 wt%.

2.4 Microscopy observation and energy dispersive spectroscopy (EDS)

Precipitates were dispersed on thin sections by ethanol and further described under a transmitted light Zeiss Axioskop 40 microscope, followed by cathodoluminescence (CL) analysis with a Nikon Eclipse 50i equipped with an MK5-2 stage. The CL analysis was conducted with a current of 315 μA, an acceleration voltage of 15 kV, and a vacuum pressure of 0.003 mBar. This work was conducted at the John Lab at Imperial College London.

An aliquot of each sample was gold-coated with a coater (K575X, Emitech) and described under a scanning electron microscope (SEM, JSM-6010LA, JEOL) equipped with EDS (energy

dispersive X-ray spectroscopy) for morphology identification), operating at an accelerating voltage of 10-15 kV and a spot size of 22-45 nm. The SEM was executed at the Department of Materials at Imperial College London.

2.5 Elemental analysis

2.5.1 Inductively coupled plasma mass spectrometry (ICP-MS)

The measurement of element concentration in both the solids precipitates and the sampled solutions was conducted at the Agilent Measurement Suite (AMS) at Imperial College London using an inductively coupled plasma mass spectrometry (ICP-MS, 8900 ICP-QQQ, Agilent) equipped with an SPS4 autosampler and a MicroMist nebulizer. The instrument measurement configuration is listed in Table 2.3. The instrument was tuned using Agilent ICP/MS tuning solution 1 ug/L of Li, Mg, Y, Ce, Ti and Co. Around 3 mg of each sample was dissolved in 30 ml ICP grade 2% (w/w) nitric acid and then centrifuged with the help of a SIGMA 3-16L Centrifuge (Sigma, Germany) to separate any undissolved solids.

Similar calibration curves to Herlambang and John (2021) were prepared in this study: a multi-element ICP standard solution for trace metals (100 mg/L, 87047.18, VWR) was diluted to prepare a set of the calibration standards with 0, 1, 5, 10, 50, 100, 250, 500, 1000 ppb, whereas a mixture of Ca and Mg standard solution (1000 mg/L, 456692T and 456792W, VWR) was diluted into 0, 0.5, 1, 5, 10, 25, 50 ppm for the second set of calibration standards. For each sample and standard, at least five replicates were measured to obtain an average value. An internal standard of Re (50 ppb) was employed to ensure measurement accuracy (Table 2.4).

Each sample and standard underwent approximately five replicate measurements to determine average values. Calibration curves for all elements exhibited R^2 values exceeding 0.9979, with an averaged detection limits set at 0.9385 ppb for Mg, 39.770 ppb for Ca, 0.025 ppb for Mn, 0.021 ppb for Fe, 0.028 ppb for Cu, and 0.067 ppb for Sr.

Table 2.3 Agilent 8900 ICP-MS operating configuration

Configuration	**Type/Value**	**Unit**
Sampling Cone	Nickle	N/A
Skimmer Cone	Nickle	N/A
RF power	1550	W
Sampling Depth	8.0	mm
Nebulizer Gas	1.05	L/min
Plasma Gas	15.0	L/min
Extract 1	-10.8	V
Extract 2	-250.0	V
Omega Bias	-150.0	V
Omega Lens	6.6	V
Q1 Entrance	-50.0	V
He Flow rate	5.0	mL/min
Axial Acceleration	1	V
Energy Discrimination	3.0	V

2.5.2 Trace metal distribution coefficient calculation

Trace metals are widely used as tracers or constraints of natural processes. For carbonates, a wide range of research has shown that trace metals will partition into carbonates during precipitation (Meyer, 1984; Burton and Walter, 1991) and various metals have been studied including Na^+ (White, 1977), K^+ (White, 1977), Li^+ (Füger et al., 2019), Mg^{2+} (Mucci and Morse, 1983; Zhang and Dawe, 2000; Nielsen et al., 2016), Mn^{2+} (Lorens, 1981; Dromgoole and Walter, 1990b, a; Dietzel and Usdowski, 1996; Temmam et al., 2000), Fe^{2+} (Dromgoole and Walter, 1990b), Cu^{2+} (Parsiegla and Katz, 1999), Zn^{2+} (Temmam et al., 2000; Mavromatis et al., 2019),

Sr^{2+} (Lorens, 1981; Mucci and Morse, 1983; Tesoriero and Pankow, 1996; Dietzel et al., 2004; Gabitov and Watson, 2006), Ba^{2+} (Tesoriero and Pankow, 1996; Dietzel et al., 2004; Mavromatis et al., 2018), Ni^{2+} (Dietzel and Usdowski, 1996), Cd^{2+} (Lorens, 1981; Tesoriero and Pankow, 1996), Co^{2+} (Lorens, 1981; Dietzel and Usdowski, 1996), and U^{6+} (Weremeichik et al., 2017).

Table 2.4 Elements Measured in this study

Element	Mass Monitored (amu)
Ca	42
Cu	63
Cu	65
Fe	56
Fe	56-> 72 (MS/MS)
Mg	24
Mn	55
Sr	88
Re	185 (ISTD)

Divalent metals are the dominant impurity ions in natural carbonates. The partitioning of divalent cations into carbonate minerals depends on the cation radius and its coordination of metal ions to oxygen yielding in the specific crystal structure (Dietzel, 2011; Goetschl et al., 2019). Despite extensive research, a universal law governing the partitioning of trace metals into carbonates has not yet been established. Existing studies indicate that the incorporation of trace metals into carbonate minerals is influenced by a range of factors, including pH, temperature, solution composition, precipitation rate, and the crystal structure of the forming mineral (Füger et al., 2019).

The distribution coefficient -'$D_{Me/Ca}$' (Henderson and Kracek, 1927) is variously used by researchers in this domain and was employed here for trace metal data reduction. Morse and Bender (1990) modified the equation as:

$$D_{Me/Ca} = ([Me]_s/[Ca]_s)/(\alpha_{Me}/\alpha_{Ca}) \quad (2.26)$$

where $[Me]_s$ and α_{Me} denote the metal concentration in precipitates and the activity of the metal ion respectively. The activity is constrained by equation (2.27) and (2.28) (Lewis, 1907):

$$\alpha_{Me} = [Me] \times \gamma_{Me} \quad (2.27)$$

$$\alpha_{Me}/\alpha_{Ca} = ([Me]/[Ca]) \times (\gamma_{Me}/\gamma_{Ca}) \quad (2.28)$$

where [Me] is the trace metal concentration in the parent solution and the γ_{Me} is the activity coefficient of the ion.

Activity coefficient calculation is constrained for different ionic strengths (I) (Debye and Hückel, 1923; Guggenheim and Turgeon, 1955; Davies, 1962; Truesdell et al., 1973; Pitzer and Press, 1991). For instance, in high-pressure experiments, the mixture of 0.18 $NaHCO_3$ and 0.1 M $CaCl_2$ leads to ionic strength ~ 0.24 M. Therefore, Davies' equation (Davies, 1962) is employed for calculation:

$$Log\gamma_{Me} = -A \times Z^2 \times (\frac{\sqrt{I}}{1+\sqrt{I}} - 0.3 \times I) \quad (2.29)$$

where Z is the ionic charge (e.g. Z is 2 for Mg^{2+}), and A is a temperature-dependent parameter that is calculated through equation (5) (Bretti et al., 2004) in which T_K is the temperature in Kelvin:

$$A = 0.510 + 76.286 \times \left(\frac{1}{298.15} - \frac{1}{T_K}\right) + 1.4189 \times (\frac{298.15}{T_K} - 1 + Ln\frac{T_K}{298.15}) \quad (2.30)$$

2.6 Calcium carbonate precipitation rate (rp) calculation

The precipitation rate is calculated through the variation of calcium concentration with precipitation time. Obviously, the calcium concentration decreasing rate depends on the CO_2 degassing rate or the NaOH titration rate. Given that both the CO_2 stripping and NaOH addition processes resemble acid-base titration, the logistic model commonly employed for fitting titration data (Chuang, 1987; Friend et al., 2009; Simon et al., 2009; Stamou Jr et al., 2018) was performed here to derive the curve regression equation:

$$[Ca] = C_0/(1 + e^{k(t-t_0)}) + d \tag{2.31}$$

where [Ca] is the total Ca concentration in the sampled solution at time t, C_0 is the curve max value, k is the steepness of the curve, t_0 is the time of the sigmoid midpoint, and d is the compensation coefficient.

Subsequently, the average precipitation rate for each experiment was computed by integrating the differential function of the fitting curve over a specified time interval. Notably, the precipitation duration for the P and A methods exceeds that of the T method by at least 2 orders of magnitude. To derive a more representative precipitation rate and mitigate the influence of extended periods of low precipitation towards the end of the P and A methods, the integration time interval was defined from the initial Ca drop point to the point where 90% of precipitation occurred. Conversely, for the T method, the entire precipitation period was considered. It is important to emphasize that the average precipitation rates calculated here are not directly comparable to seeding precipitation experiments, such as those conducted by Mavromatis et al. (2022) as they calculated the average overgrowth rates on initial seed surfaces in the unit of $mol/m^2/s$.

2.7 PHREEQC modelling

PHREEQC is a C++-based computer program that is specially designed to perform aqueous geochemical calculations including batch-reaction, solid-solution calculations, mixing of solutions, etc. PHREEQC is often applied to the research of carbonate precipitation (Ruiz-Agudo et al., 2011; Mavromatis et al., 2015; Voigt et al., 2017; Goetschl et al., 2019). In this project, PHREEQC version 3 will be used to simulate aquatic chemical speciation and mineral saturation index in the carbonate solution system under different initial settings. In PHREEQC, the carbonate mineral saturation index is calculated through Eqs (2.32), proposed by Plummer and Busenberg (1982).

$$SI_{MeCO_3} = \log \frac{[Me^{2+}] \times [CO_3{}^{2-}]}{K_{sp}} \tag{2.32}$$

where K_{sp} is the solubility of the carbonate minerals, $[Me^{2+}]$ and $[CO_3^{2-}]$ respectively donate the activity of trace metal ion and carbonate.

At the same time, a PHREEQC reaction model was developed to simulate the $CaCO_3$ synthetic experiments and obtain species molalities and saturation states (Parkhurst and Appelo, 2013). Currently, PHREEQC operates 13 databases containing minerals with associated reactions and thermodynamic properties. The phreeqc.dat database was selected for this study as it contains the most carbonate minerals of interest with solid relations between the equilibrium constant and Tc. Key omissions such as vaterite, magnesite, and malachite were supplemented by literature data from Plummer and Busenberg (1982), Saldi et al. (2009), and the minteq.dat database respectively.

Chapter 3

Formation of carbonate polymorphs under controlled laboratory conditions: Relative control of temperature, precipitation rate and ionic impurities

3.1 Abstract

Calcium carbonate ($CaCO_3$) is a critical mineral to a wide range of research areas and manifests as three polymorphs: calcite, aragonite, and vaterite. The mechanisms controlling polymorph precipitation, however, are debated, particularly the role temperature (Tc), precipitation rates (Log (rp)), and ionic impurities play. The present study synthesized $CaCO_3$ under controlled laboratory conditions encompassing a spectrum of Tc (25 to 90°C), Log (rp) (-5.00 to -1.95 mol/m^3/s), and ionic impurities (Cu^{2+}, Mg^{2+}, Fe^{3+}, Mn^{2+}, Sr^{2+}), facilitating a detailed exploration of the parameters examined and the relative significance of them. The results highlight that Tc and the pair of high Tc and high Log (rp) (HTc- Log (rp)) emerge as the primary controlling factors with ionic impurities and Log (rp) as respectively secondary and tertiary controls. The precipitate morphology is dramatically influenced by ionic impurities, and we propose that morphology is a trade-off between kink site blocking and mineral dissolution. Under high Log (rp), morphology is more influenced by kink site blocking, whereas under low-intermediate Log (rp)

dissolution dominates. We also identify that environments rich in free ions prompt calcite formation, whereas environments poor in free ions lead to aragonite precipitation. We found that aragonite and vaterite do not occur independently of calcite as vaterite is prone to transform into calcite under elevated temperature, a process that can be retarded by the presence of Na^+ and Sr^{2+}. Our work sheds light on the relative control of physico-chemical parameters on polymorph precipitation, an essential first step in gaining a deeper understanding of chemical fractionation processes in carbonates.

3.2 Introduction

Calcium carbonate ($CaCO_3$) is ubiquitously distributed both on the Earth's surface and underground, exerting a significant influence on geochemical processes through its dissolution and precipitation dynamics (Molnár et al., 2021). In the natural environment, $CaCO_3$ occurs as three polymorphs each characterized by unique crystal systems: calcite (trigonal), aragonite (orthorhombic), and vaterite (hexagonal). Calcite stands as the thermodynamically most stable phase, constituting the predominant portion of the Earth's $CaCO_3$ reservoir, particularly in subsurface formations. Aragonite is a metastable phase primarily encountered on the Earth's surface, while vaterite's occurrence is rare owing to its lower metastability compared to calcite and aragonite (Jones, 2017).

Natural $CaCO_3$ deposits typically consist of varying proportions of calcite and aragonite, occasionally with minor quantities of vaterite. This poses the famous Aragonite-Calcite problem (Curl, 1962; Sun et al., 2015), as calcite, being the most thermodynamically stable phase, is expected to precipitate from supersaturated $CaCO_3$ solutions, rather than being supplanted or completely replaced by aragonite. The factors governing the formation of a single $CaCO_3$ phase thus are subject to intense debate (Rosa and Lundager Madsen, 2011; Molnár et al., 2021). Over the last two decades, an array of research employing diverse methodologies has been conducted to investigate this conundrum and temperature (Tc), precipitation rate (Log (rp)), and ionic impurities

emerged as prominent parameters influencing polymorphism (Rose, 1837, 1860; Curl, 1962; Rosa and Lundager Madsen, 2011; Weiss et al., 2014).

Rose (1837) first proposed that temperature (Tc) played a critical role in $CaCO_3$ polymorphism. Subsequent studies supported this assertion but debated the Tc thresholds for a singular $CaCO_3$ phase formation. Values such as 37 ℃ (Rosa and Lundager Madsen, 2011), 50 ℃ (Suganuma, 1928; Chen and Xiang, 2009), and 60 ℃ (Goto, 1961) have been suggested as necessary Tc values for aragonite precipitation. However, some studies suggested that Tc wasn't a control parameter in the $CaCO_3$ polymorphism (Siegel and Reams, 1966; Rowling, 2004). Another possible important control parameter is precipitation rate (Log (rp)), as it was suggested by Rose (1860) and Kitano (1962b) that the rapid CO_2 degassing prompted aragonite precipitation in line with the results of Yagi et al. (1984) and Matsumoto et al. (2010). Nevertheless, the extent of the Log (rp) effect remains unclear. Finally, Ionic impurities are also widely considered as an underlying control of aragonite versus calcite precipitation (Jones, 2017), for instance, the presence of Mg^{2+} has been thought to prompt aragonite precipitation (Curl, 1962; Kitano, 1962a) and Mn^{2+} may favour calcite formation (Tai and Chen, 1995; Rowling, 2004). However, the mechanism by which ionic impurities influence $CaCO_3$ polymorphism is debated. Some research proposed that Mg^{2+} coprecipitation delays calcite growth prompting aragonite formation (Fernández-Díaz et al., 1996; De Choudens-Sánchez and González, 2009), while others argue that Mg^{2+} is more readily incorporated into the aragonite lattice, thus not inhibiting its growth (Mucci and Morse, 1983; Jiménez-López et al., 2004).

Although all three parameters—Tc, Log (rp), and ionic impurities—have all been proposed as crucial in $CaCO_3$ polymorphism and investigated separately, it is challenging to forecast polymorph composition due to the difficulty in estimating the combined effects of these factors. Therefore, there are research gaps regarding $CaCO_3$ polymorphism, including (1) the exact role of Tc, Log (rp), and ionic impurities and (2) the relative significance of these parameters during precipitation. To address the research gaps, we conducted a series of laboratory $CaCO_3$ synthesis

experiments in which temperature (Tc, 25 to 90 ℃), precipitation rate (Log (rp), -5.00 to -1.95 mol/m^3/s), and ionic impurities (Cu^{2+}, Fe^{3+}, Mg^{2+}, Mn^{2+}, Sr^{2+}) were designed as primary control variables, with a Control group (no added ionic impurities) for comparative analysis. Based on the obtained precipitates, we aim to describe the role of the selected parameters and assess their relative importance, thus providing implications for the Aragonite-Calcite problem.

The acronyms in this chapter are summarized in Table 3.1

Table 3.1 List of acronyms in the study.

Acronyms	Defination
Tc	Precipitation Temperature
Log (rp)	Log value of precipitation rate
P method	Passive deagssing method-low precipitation rate
A method	Active degassing method-intermediate precipitation rate
T method	Titration method-high precipitation rate
C	Calcite
Ar	Aragonite
V	Vaterite
Tr1	Tc-aragonite relation 1
Tr2	Tc-aragonite relation 2
HTc- Log (rp)	The pair of high temperature (> 25 ℃) and high precipitation rate
F	Flat surfaces on crystal model
S	Stepped surfaces on crystal model
K	Kinded surfaces on crystal model
(Tc)+Ionic imprities/Control+Precipitation method	Experiments ID. For example, (1) 25CuT represents sample precipitated under 25 ℃, T method with Cu^{2+}, and (2) MgP indicates experiments dosed with Mg^{2+} udner the A method regardless of Tc

3.3 Methods and materials

In the current chapter, only XC2024 samples (a total of 68) were characterized which were precipitated under controlled laboratory conditions (Chapter 2 section 2.2.1) and all samples were characterized for mineralogy and morphology through XRD (Chapter 2 section 2.3) and SEM-EDS (Chapter 2 section 2.4). During the XC2024 precipitation, solutions were sampled from time to time to monitor the calcium concentration and these solution samples were characterized using the ICP-MS (Chapter 2 section 2.5.1).

3.4 Results

3.4.1 Chemical evolution log of the solution

Figure 3.1 illustrates two representative experimental logs during the precipitation, based on the results obtained from ICP-MS provided in Appendices Table 1, along with Tc and pH logs. The Ca concentration in the solution typically exhibits either a complete mirrored 'S' curve (Figure 3.1A) or a partial one (Figure 3.1B), depending on the presence of a plateau before the concentration decline. Table 3.2 shows the logistic model fitting R^2 values with the lowest R^2 of 0.96 validating the logistic model fitting. The calculated Log (rp) varies from -5.00 to -4.28, -4.27 to -3.78, and -2.68 to -1.95 mol/m^3/s for P, A, and T methods respectively (Table 3.2).

The calculated Log (rp) is not directly comparable to rates reported in seeding precipitation experiments such as Mavromatis et al. (2022), who calculated the overgrowth rates on seeds surface in mol/m^2/s. Eqs (2) provides a rough conversion equation：

$$Log\ (rp) = Log(rg \times S \times W/V) \tag{3.1}$$

where rg is the overgrowth rate in mol/m^2/s, S is the total seed reactive surface in m^2/g, W is the total seed mass in g, and V is the total fluid volume in L.

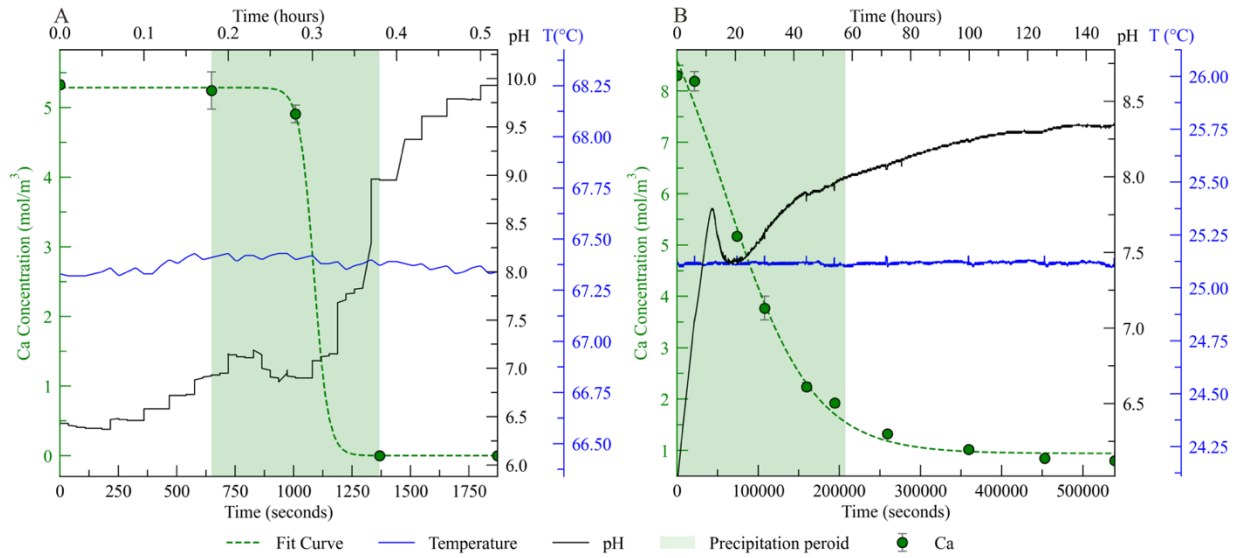


Figure 3.1 The precipitation data logs consist of two typical patterns.

A. The data log of 70ControlT represents precipitation experiments conducted using the T method, characterized by a Ca concentration decrease following a complete and mirrored 'S' curve. B. The data log of 70SrA represents most precipitation events conducted using the A method, where the Ca concentration decreases following half of a mirrored 'S' curve. In both scenarios, the green dashed curve denotes the logistic regression fit curve of the Ca concentration.

Throughout the precipitation, Tc remained stable with a standard error of ≤ 0.3°C. The average pH was calculated based on the specified time interval defined in the previous step. The average pH of the A method ranges from 7.0 ± 0.3 to 7.9 ± 0.4 and that of the T method is from 7.2 ± 0.7 to 9.1 ± 0.4 which is in line with the result of Kluge and John (2015a) (Table 3.2).

Table 3.2 Precipitation settings and mineralogy of synthetic calcium carbonates in the laboratory.

R^2 is the goodness of logistic model fitting. C,% Ar,% and V,% are the proportion of calcite, aragonite, and vaterite respectively. '-' indicates no measured data and '/' indicates no added ionic impurities. Average Tc, pH and Log (rp) are calculated based on the precipitation time interval specified in Section 2.5.

ID	Methods	Added Salt, mmoles/L	R^2	T, °C	pH	log (rp), mol/m^3/s	C,%	A,%	V,%
25ControlP	Passive degassing	/	0.99	25.1 ± 0.0	-	-5.00	100	0	0
50ControlP	Passive degassing	/	0.99	50.1 ± 0.0	-	-4.47	100	0	0
70ControlP	Passive degassing	/	0.98	70.5 ± 0.0	-	-4.37	12	88	0
90ControlP	Passive degassing	/	0.98	90.5 ± 0.1	-	-4.54	23	77	0
25ControlA	Active degassing	/	0.99	25.1 ± 0.0	7.6 ± 0.4	-4.47	85	0	15
50ControlA	Active degassing	/	1.00	49.4 ± 0.0	7.3 ± 0.4	-4.05	60	40	0

ID	Methods	Added Salt, mmoles/L	R^2	T, °C	pH	log (rp), mol/m^3/s	C,%	A,%	V,%
70ControlA	Active degassing	/	1.00	68.4 ± 0.0	7.2 ± 0.4	-4.03	4	96	0
90ControlA	Active degassing	/	1.00	87.1 ± 0.3	7.3 ± 0.3	-3.91	5	95	0
25ControlT	Titration	/	0.99	25.4 ± 0.0	8.2 ± 0.2	-2.68	48	0	52
50ControlT	Titration	/	1.00	49.1 ± 0.0	8.1 ± 0.2	-1.95	16	84	0
70ControlT	Titration	/	1.00	67.4 ± 0.0	7.3 ± 0.6	-2.13	9	91	0
90ControlT	Titration	/	1.00	84.8 ± 0.0	7.5 ± 0.8	-2.18	8	92	0
25CuP	Passive degassing	$CuCl_2$, 0.3	0.96	25.1 ± 0.0	-	-4.87	33	67	0
50CuP	Passive degassing	$CuCl_2$, 0.3	0.99	50.1 ± 0.0	-	-4.44	0	100	0
70CuP	Passive degassing	$CuCl_2$, 0.3	0.97	70.5 ± 0.0	-	-4.27	0	100	0
90CuP	Passive degassing	$CuCl_2$, 0.3	0.98	90.5 ± 0.1	-	-4.09	9	91	0
25CuA	Active degassing	$CuCl_2$, 0.3	0.97	25.3 ± 0.0	7.9 ± 0.4	-4.71	0	100	0
50CuA	Active degassing	$CuCl_2$, 0.3	1.00	50.8 ± 0.1	7.4 ± 0.4	-4.10	5	96	0
70CuA	Active degassing	$CuCl_2$, 0.3	0.98	70.6 ± 0.5	7.0 ± 0.3	-3.78	0	100	0
90CuA	Active degassing	$CuCl_2$, 0.3	0.98	87.0 ± 0.3	7.8 ± 0.5	-3.80	16	84	0
25CuT	Titration	$CuCl_2$, 0.3	1.00	25.3 ± 0.0	8.9 ± 0.6	-2.46	89	0	11
50CuT	Titration	$CuCl_2$, 0.3	1.00	48.9 ± 0.0	8.7 ± 0.8	-2.36	46	54	0
70CuT	Titration	$CuCl_2$, 0.3	1.00	66.7 ± 0.0	7.8 ± 0.7	-2.22	6	95	0
90CuT	Titration	$CuCl_2$, 0.3	1.00	83.7 ± 0.0	7.7 ± 1.1	-2.39	7	93	0
25FeP	Passive degassing	$FeCl_3$, 0.1	0.99	25.1 ± 0.0	-	-4.91	32	69	0
50FeP	Passive degassing	$FeCl_3$, 0.1	0.98	50.1 ± 0.0	-	-4.54	97	3	0
70FeP	Passive degassing	$FeCl_3$, 0.1	0.99	70.5 ± 0.0	-	-4.31	15	85	0
90FeP	Passive degassing	$FeCl_3$, 0.1	0.99	90.5 ± 0.1	-	-4.38	9	91	0
25FeA	Active degassing	$FeCl_3$, 0.1	0.99	25.1 ± 0.0	7.2 ± 0.4	-4.27	43	57	0
50FeA	Active degassing	$FeCl_3$, 0.1	0.99	49.4 ± 0.0	7.5 ± 0.4	-4.16	80	20	0
70FeA	Active degassing	$FeCl_3$, 0.1	1.00	68.5 ± 0.0	7.1 ± 0.3	-3.82	64	36	0
90FeA	Active degassing	$FeCl_3$, 0.1	1.00	87.0 ± 0.1	7.3 ± 0.3	-4.01	21	79	0
25FeT	Titration	$FeCl_3$, 0.1	1.00	25.4 ± 0.0	8.3 ± 0.7	-2.46	67	0	33
50FeT	Titration	$FeCl_3$, 0.1	1.00	49.1 ± 0.0	8.2 ± 1.0	-2.17	14	86	0
70FeT	Titration	$FeCl_3$, 0.1	1.00	66.4 ± 0.0	7.2 ± 0.6	-2.30	12	88	0

ID	Methods	Added Salt, mmoles/L	R^2	T, °C	pH	log (rp), mol/m^3/s	C,%	A,%	V,%
90FeT	Titration	$FeCl_3$, 0.1	1.00	82.6 ± 0.1	7.6 ± 0.6	-2.07	5	95	0
25MgP	Passive degassing	$MgCl_2$, 0.3	0.99	25.1 ± 0.0	-	-4.91	100	0	0
50MgP	Passive degassing	$MgCl_2$, 0.3	0.99	50.1 ± 0.0	-	-4.28	52	48	0
70MgP	Passive degassing	$MgCl_2$, 0.3	0.99	70.5 ± 0.0	-	-4.67	7	93	0
90MgP	Passive degassing	$MgCl_2$, 0.3	1.00	90.5 ± 0.1	-	-4.41	2	99	0
25MgA	Active degassing	$MgCl_2$, 0.3	0.99	25.3 ± 0.0	7.5 ± 0.5	-4.22	85	0	15
50MgA	Active degassing	$MgCl_2$, 0.3	0.99	50.8 ± 0.1	7.4 ± 0.4	-4.18	96	0	4
70MgA	Active degassing	$MgCl_2$, 0.3	0.99	70.6 ± 0.4	7.2 ± 0.3	-3.99	15	85	0
90MgA	Active degassing	$MgCl_2$, 0.3	0.99	87.1 ± 0.2	7.7 ± 0.5	-4.34	6	94	0
25MgT	Titration	$MgCl_2$, 0.3	1.00	25.3 ± 0.0	8.4 ± 0.9	-2.54	52	0	48
50MgT	Titration	$MgCl_2$, 0.3	1.00	48.8 ± 0.0	7.7 ± 0.7	-2.09	11	89	0
70MgT	Titration	$MgCl_2$, 0.3	1.00	67.7 ± 0.1	8.1 ± 1.0	-2.16	11	89	0
90MgT	Titration	$MgCl_2$, 0.3	1.00	83.0 ± 0.3	7.3 ± 0.6	-2.35	56	44	0
25MnP	Passive degassing	$MnCl_2$, 0.1	1.00	25.1 ± 0.0	-	-4.91	100	0	0
50MnP	Passive degassing	$MnCl_2$, 0.1	0.99	50.1 ± 0.0	-	-4.32	66	34	0
70MnP	Passive degassing	$MnCl_2$, 0.1	0.99	70.5 ± 0.0	-	-4.21	78	22	0
90MnP	Passive degassing	$MnCl_2$, 0.1	1.00	90.5 ± 0.1	-	-4.47	89	11	0
25MnA	Active degassing	$MnCl_2$, 0.1	0.99	25.1 ± 0.0	7.3 ± 0.3	-4.52	100	0	0
50MnA	Active degassing	$MnCl_2$, 0.1	1.00	49.4 ± 0.0	7.1 ± 0.4	-3.93	97	3	0
70MnA	Active degassing	$MnCl_2$, 0.1	1.00	68.5 ± 0.0	7.1 ± 0.3	-3.91	45	55	0
90MnA	Active degassing	$MnCl_2$, 0.1	1.00	87.0 ± 0.1	7.1 ± 0.2	-4.02	96	4	0
25MnT	Titration	$MnCl_2$, 0.1	0.99	25.3 ± 0.0	9.1 ± 0.4	-2.39	47	0	53
50MnT	Titration	$MnCl_2$, 0.1	1.00	49.2 ± 0.0	7.8 ± 1.0	-2.40	6	91	3
70MnT	Titration	$MnCl_2$, 0.1	1.00	67.0 ± 0.1	8.1 ± 1.0	-2.50	8	92	0
90MnT	Titration	$MnCl_2$, 0.1	1.00	83.3 ± 0.1	7.5 ± 0.8	-2.36	10	90	0
25SrA	Active degassing	$SrCl_2$, 0.1	0.98	25.1 ± 0.0	7.6 ± 0.4	-4.53	83	0	18
50SrA	Active degassing	$SrCl_2$, 0.1	0.99	49.4 ± 0.0	7.4 ± 0.4	-4.14	93	7	0
70SrA	Active degassing	$SrCl_2$, 0.1	0.99	68.4 ± 0.1	7.8 ± 0.5	-4.27	96	0	4
90SrA	Active degassing	$SrCl_2$, 0.1	1.00	86.6 ± 0.5	7.7 ± 0.4	-4.25	66	0	34

ID	Methods	Added Salt, mmoles/L	R^2	T, °C	pH	log (rp), mol/m^3/s	C,%	A,%	V,%
25SrT	Titration	$SrCl_2$, 0.1	1.00	25.5 ± 0.0	8.3 ± 0.4	-2.12	25	0	75
50SrT	Titration	$SrCl_2$, 0.1	1.00	49.2 ± 0.0	8.0 ± 0.6	-2.05	4	96	0
70SrT	Titration	$SrCl_2$, 0.1	1.00	67.4 ± 0.1	7.6 ± 0.5	-2.12	1	99	0
90SrT	Titration	$SrCl_2$, 0.1	1.00	82.9 ± 0.1	7.8 ± 1.1	-2.31	1	99	0

3.4.2 PHREEQC speciation calculations

The PHREEQC speciation results of the solution before precipitation are summarized in Figure 3.2. The model results suggest that the saturation index decreases in the order of calcite, aragonite, and vaterite, irrespective of the Tc and the ionic impurities, indicating that calcite is the most thermodynamically stable phase, with aragonite and vaterite being metastable phases. An example of the $CaCO_3$ polymorph saturation index under different Tc is provided in Figure 3.2A.

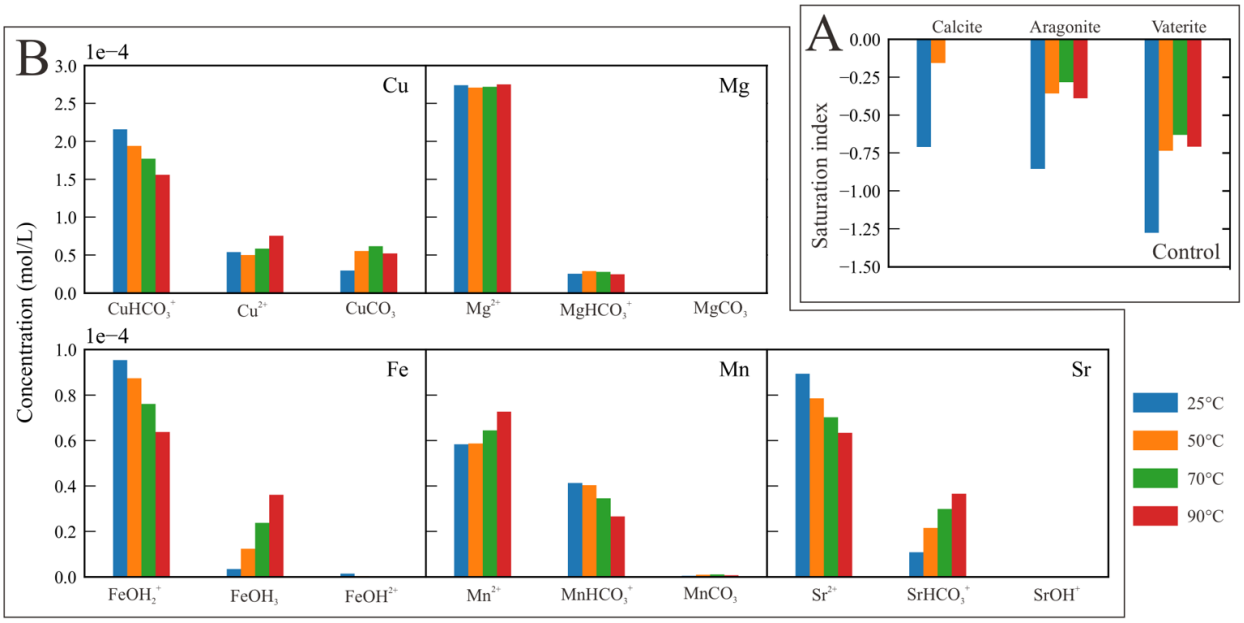


Figure 3.2 Plots show the PHRREQC model results.

A. The saturation index of three polymorphs in the solution under different temperatures. The blank experiment and impurity ion-dosed experiments exhibit negligible differences and B. The ion speciation results of each impurity ion in the solution (only the three most abundant species are shown here) and the total concentration of Mg and Cu is 3×10^{-4} mol/L respectively, whereas that of Fe, Mn, and Sr is 1×10^{-4} mol/L.

Figure 3.2B illustrates the speciation of Cu^{2+}, Mg^{2+}, Fe^{3+}, Mn^{2+}, and Sr^{2+} in solution and they mainly speciate as $CuHCO_3^+$, Mg^{2+}, $Fe(OH)_2^+$, Mn^{2+}, and Sr^{2+}, with averaged proportions of 62%, 91%, 81%, 64%, and 75%, respectively. This indicates that the speciation of Cu^{2+} and Fe^{3+} is complex-dominated whereas that of Mg^{2+}, Mn^{2+}, and Sr^{2+} is free ion-dominated.

3.4.3 Mineralogical characterization of precipitates

Table 3.2 lists XRD results of 68 precipitates collected and the literature data were summarized in Table 3.3 for comparison. All precipitates are $CaCO_3$ (Figure 3.3A) but the polymorph composition varies from sample to sample. Precipitates are generally composed of two phases in which calcite and aragonite are predominant in most cases with proportion up to 100%, and vaterite presents as a minor component up to 48%. However, vaterite emerges as the primary component in sample 25ControlT (52%), 25MnT(53%), and 25SrT (75%) (Table 3.2). The results here are similar to previous research but exhibit fewer samples containing three polymorphs than Kitano (1962b) and Wada et al. (1995) (Figure 3.3B).

Table 3.3 Experimental studies of calcium carbonate synthesis with reported composition.

C, Ar, and V are calcite, aragonite, and vaterite, respectively. Ca indicates the solution's initial Ca concentration before inducing precipitation. '-' indicates no data was reported and '/' indicates no added ionic impurities.

Reference	Synthesis method	Added Salt	Tc, ℃	pH	Log (rp)	Ca, M	Polymorph compsoition
Kitano (1962a)	CO_2 degasing	LiC, NaCl,KCl, NH_4Cl, RbCl, CSCl, $NaNO_3$	28	6.7-6.8	-	0.007	C, C+Ar
		$MgCl_2$, $MgSO_4$, $Mg(HCO_3)_2$	10	-	-	0.01	C, C+Ar
		$BaCl_2$, $Ba(HCO_3)_2$	12	-	-	0.006	C, V, C+V, C+Ar
Kitano (1962b)	CO_2 degasing	NaCl	30-100	-	-	0.02	C, C+Ar+V
	CO_2 degasing	$MgCl_2$	10-100	-	-	0.02	C+Ar

Reference	Synthesis method	Added Salt	Tc, °C	pH	Log (rp)	Ca, M	Polymorph compsoition
	CO_2 bubling through $CaCO_3$ saturated solution	NaCl, $MgCl_2$	70-80	-	-	0.02	C
Turnbull (1973)	CO_2 bubling through $CaCL_2$	NH_3	20	-	-	1	V, C+V
	Mix $CaCl_2$ and Na_2CO_3	/	20	-	-	1	C+V
Wada et al. (1995)	Mix $CaCl_2$ and Na_2CO_3	$Fe(NO_3)_2$, $Zn(NO_3)_2$, $MgCl_2$, $NiCl_2$, $CuCl_2$	15	-	-	0.1	C+Ar, C+Ar+V
Tai and Chen (1998)	Mix $CaCl_2$ and Na_2CO_3	$MnCl_2$, $MgCL_2$, KH_2PO_4	20-24	9.6-12.1	-	-	C, Ar, C+Ar, C+V, C+Ar+V
Jiménez-López et al. (2004)	Mix $CaCl_2$ and Na_2CO_3	$MgCl_2$	25	7.2-9.18	-	0.0023	MgC[*2]+V, MHC[*3], C+MHC, MgC+C+MHC+V, MHC+Ar C+MHC+Ar+V
Nishiyama et al. (2013)	Mix $CaCl_2$ and Na_2CO_3	$MgCl_2$	25	7.9-11.3	-	0.027-0.11	C+V, MHC, LMHC[*4], AM[*5]
Kluge and John (2015a)	CO_2 degasing	/	24-91	5-9	-4.27 to -3.78 in $mol/m^3/s$[*1]	0.0072	C, C+Ar
		NaCl	24-91	5.5-8.5	-4.27 to -3.78 in $mol/m^3/s$[*1]	0.0072	C, V, C+V, C+Ar+V
		$CaCl_2$	26-80	5-7.5	-4.27 to -3.78 in $mol/m^3/s$[*1]	0.0072	C
Kluge et al. (2015)	Mix $CaCl_2$ and $NaHCO_3$ (pressurized)	/	25-250	-	-	0.05	C, Ar
Goetschl et al. (2019)	Overgrowth on seeds by mixing	/	25	6.2-6.5	-7.56 to -6.92 in $mol/m^2/s$	0.01	C, C+Ar

Reference	Synthesis method	Added Salt	Tc, °C	pH	Log (rp)	Ca, M	Polymorph compsoition
	$CaCl_2$ and $NaHCO_3$						
This study	CO_2 degasing	$CuCl_2$, $FeCl_3$, $MgCl_2$, $MnCl_2$, $SrCl_2$	25-90	7.1-9.1	-5.00 to -1.95 in $mol/m^3/s$	0.007	C, Ar, V, C+Ar, C+V, C+Ar+V

*1 the estimated precipitation rate according to this study; *2 MgC: Mg-calcite; *3 MHC: Monohydrocalcite; *4 LMHC: low-crystalline MHC;*5 Am: Amorphous material.

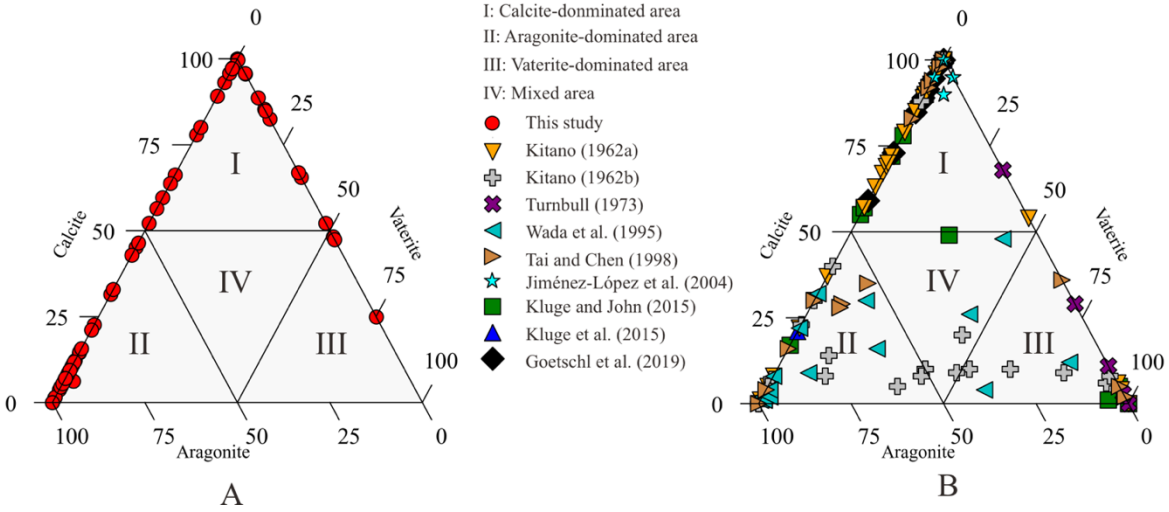
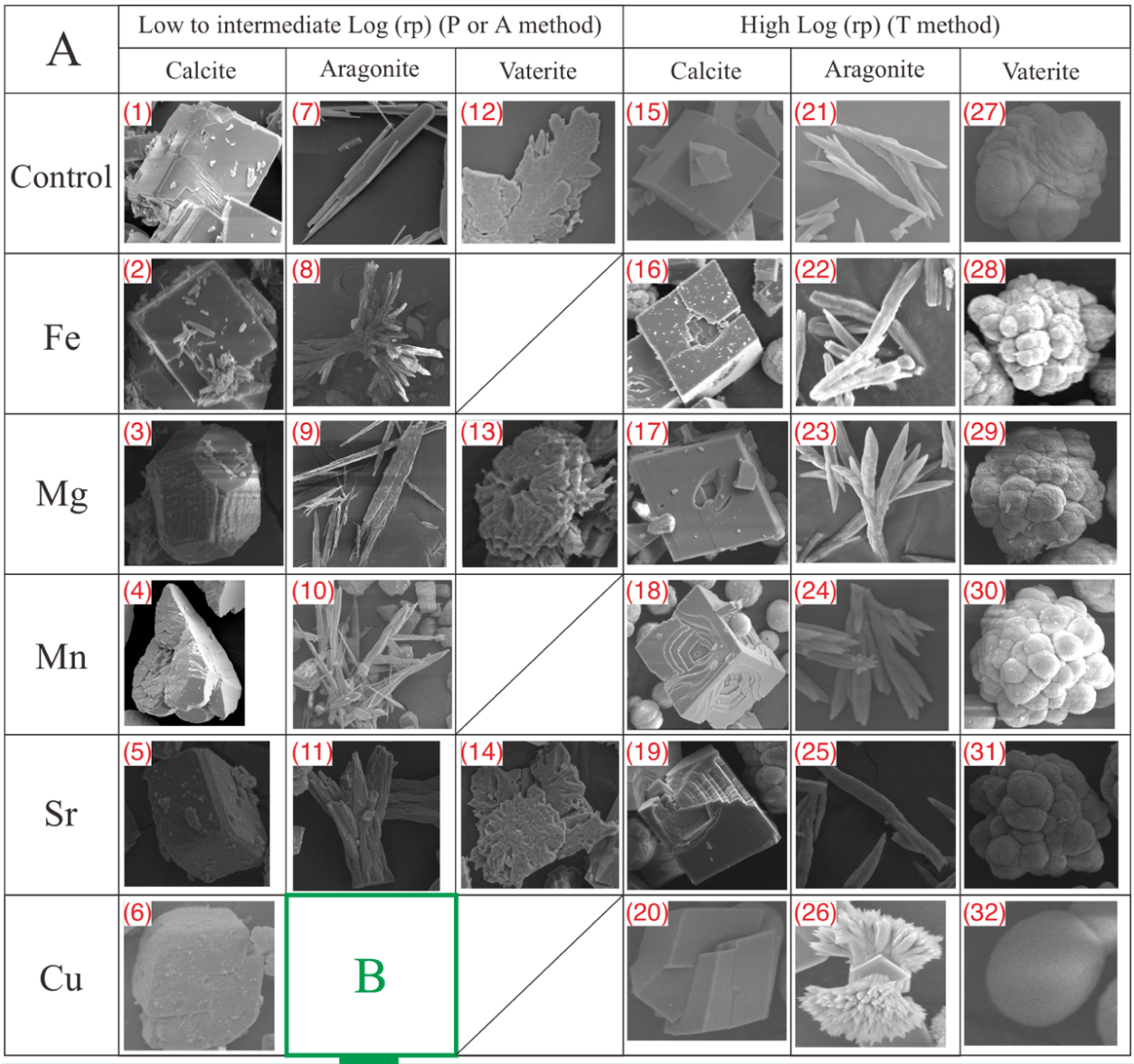


Figure 3.3 Ternary diagrams show the $CaCO_3$ polymorph composition.

A. this study and B. literature data (Kitano, 1962b, a; Turnbull, 1973; Wada et al., 1995; Tai and Chen, 1998; Jiménez-López et al., 2004; Kluge and John, 2015a; Kluge et al., 2015; Goetschl et al., 2019).

Figure 3.4 shows the morphology features of different experiments. The Control group's calcite and aragonite display predominantly rhombohedral (Figure 3.4 A(1)) and acicular (Figure 3.4 A(7)) habits respectively and show no relation to Log (rp). The vaterite morphology is Log (rp) dependent, with a laminar habit under low-intermediate Log (rp) (Figure 3.4 A(12)) and a botryoidal habit under high Log (rp) (Figure 3.4 A(27)).

For ionic impurities added experiments, calcites and aragonite morphology exhibit a strong dependence on Log (rp) and ionic impurities. Under the low-intermediate Log (rp), the calcite appears rhombohedral in experiments with Fe^{3+} or Sr^{2+} added (Figure 3.4A(2) and (5)) but exhibits


A
Low to intermediate Log (rp) (P or A method)
High Log (rp) (T method)
Calcite
Aragonite
Vaterite
Calcite
Aragonite
Vaterite
Control
Fe
Mg
Mn
Sr
Cu
(1)
(2)
(3)
(4)
(5)
(6)
(7)
(8)
(9)
(10)
(11)
(12)
(13)
(14)
(15)
(16)
(17)
(18)
(19)
(20)
(21)
(22)
(23)
(24)
(25)
(26)
(27)
(28)
(29)
(30)
(31)
(32)
B

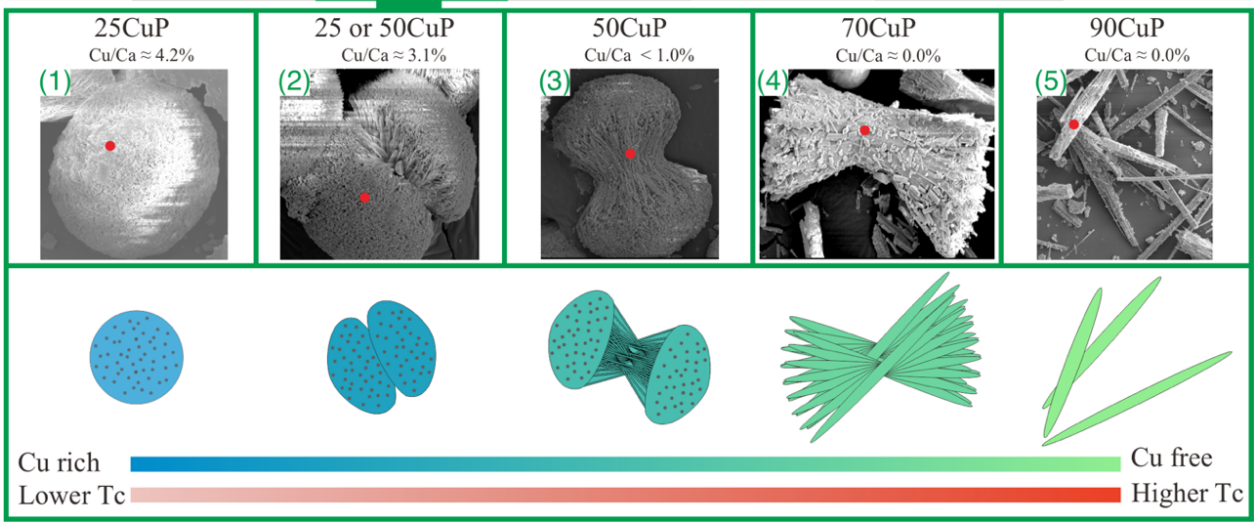

25CuP
Cu/Ca ≈ 4.2%
25 or 50CuP
Cu/Ca ≈ 3.1%
50CuP
Cu/Ca < 1.0%
70CuP
Cu/Ca ≈ 0.0%
90CuP
Cu/Ca ≈ 0.0%
(1)
(2)
(3)
(4)
(5)
Cu rich
Cu free
Lower Tc
Higher Tc

Figure 3.4 Morphology description of the XC2024 samples.

A. Scanning Electron Microscope (SEM) photo compilation illustrating the typical morphologies of $CaCO_3$ polymorphs observed in experiments varying with impurity ions and Log (rp). The slash (/) indicates that no corresponding morphology was observed. B. SEM photos and schematic diagram illustrating that in Cu added experiments, the aragonite morphology changes as the decreasing Cu/Ca and increasing Tc. The red point indicates EDS sample points.

prismatic and dodecahedron habits in experiments with Mn^{2+} or Mg^{2+} added (Figure 3.4A(3) and (4)). Aragonite displays a needle shape in Mg^{2+} added group (Figure 3.4A(9)) but shows clustered and radical shapes in experiments with Fe^{3+}, Mn^{2+}, or Sr^{2+} added (Figure 3.4A(8), (10), and (11)). Under the high Log (rp), except for with the addition of Cu^{2+}, all calcites exhibit rhombohedral habit but with hoppers on the surfaces (Figure 3.4 A(16)-(19)), and aragonites display needle shape but are curled and clustered (Figure 3.4A(22)-(25)).

The experiments with Cu^{2+} added exhibit distinct morphology from the other experiments. The calcite exhibits a rhombohedral shape but with rounded edges (Figure 3.4A(6)) under low-intermediate Log (rp) or nested together (Figure 3.4A(20)) under high (Log (rp)). The aragonite morphology is both Tc and Log (rp) dependent. Under low Log (rp), aragonite exhibits six different habits, including spherical, split spherical, dumbbell, firewood, and needle (Figure 3.4B(1)-(5)). The six different habits occur in sequence as the Tc increases from 25 to 90℃ and the Cu/Ca ratio (EDS) decreases from ca. 4.2% to below the detection limit. Aragonites exhibit a needle habit under the intermediate Log (rp) whereas under the high Log (rp) aragonites are highly clustered and grown on the calcite surfaces (Figure 3.4A(26)).

3.5 Discussions

3.5.1 Primary control of temperature (T_c) on $CaCO_3$ polymorphism

The polymorph composition of each sample varies with the Tc, Log (rp), and ionic impurities (Figure 3.5A). The results of the Control group exclude influences of ionic impurities effects and Tc on polymorphism, and display two end-member patterns:

(1) ***Pattern 1***: In pattern 1, calcites and vaterites predominate at 25℃ irrespective of Log (rp), while aragonite occurs at higher Tc (>25℃), suggesting 25-50℃ is the Tc threshold for aragonite occurrence.

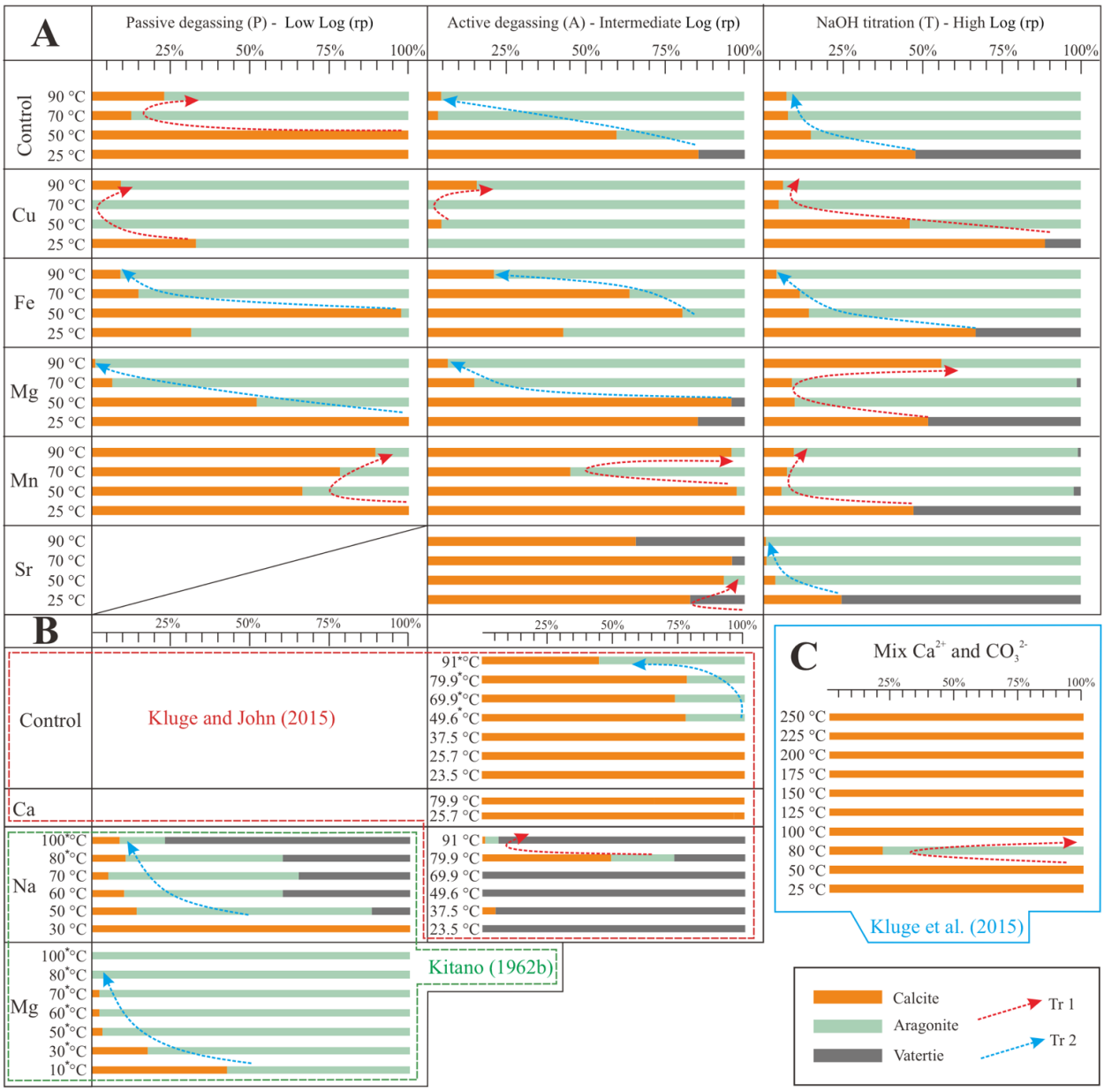


Figure 3.5 Column distribution plot showing the mineralogy composition of samples.

A. Samples in this study. B. Samples in the literature using P or A-like methods (Kitano, 1962b; Kluge and John, 2015a). C. Samples in the literature using the mix of solutions (Kluge et al., 2015). The red dashed arrow represents Tc-aragonite relation 1 (Tr1) with aragonite proportion decrease at higher Tc, and the blue dashed arrow Tc-aragonite relationship 2 (Tr2) with no rebounding.

(2) ***Pattern 2***: In pattern 2, there is a relation between Tc and aragonite proportion varying with Log (rp) including ***Tc-aragonite relation 1*** (Tr1) under low Log (rp) showing the aragonite proportion increases as Tc increases but reaches maximum at 70 ℃ and decreases at 90 ℃, and ***Tc-aragonite relation 2*** (Tr2) under intermediate-high Log (rp), where the aragonite proportion increases as Tc increases (Figure 3.5A).

Pattern 1 and ***Pattern 2*** are of significant importance as they reveal Tc can influence the polymorphism not only by governing the aragonite occurrence (***Pattern 1***) but also by interacting with Log (rp) to alter the aragonite optimum formation Tc (***Pattern 2***) which is ~70℃ in the Control group. The suggested Tc threshold range for aragonite is in line with previous research, such as the 37 ℃ threshold suggested by Rosa and Lundager Madsen (2011) and 50 ℃ by Suganuma (1928). Though this is the first time that ***Pattern 2*** has been proposed, previous research reported a Tr1-like relation where aragonite proportion reaches a maximum at 60 ℃ but starts to decrease as Tc further increases (Goto, 1961; Kitano, 1962b).

One may worry that Tc increment may lead to changes in reaction rate, thus the observed Tc effects could be caused by changes in Log (rp). Figure 3.6A compares the precipitates' dominant mineralogy, illustrating that (1) higher Tc tends to result in aragonite-dominant precipitates despite similar Log (rp), and (2) vaterite-dominant precipitates only exist at 25℃ with high Log (rp). This suggests that Tc itself is a strong control on polymorphism rather than influencing Log (rp).

Pattern 1 and ***Pattern 2*** can also help explain the role of ionic impurities (Figure 3.5A). ***Pattern 1*** is applicable in describing polymorphs prevailing at all Tc, except for FeP and FeA precipitates, where calcites prevail at 50℃. It is worth noting that ***Pattern 1*** points to the relative enrichment of aragonite at >25℃ rather than describing the predominant mineralogy. For instance, while MnA samples are always calcite-dominated, the aragonite proportion in >25℃ experiments is higher than in 25MnA, thus following ***Pattern 1***. However, obtaining ***Pattern 2*** requires changes

in aragonite optimum formation Tc or the correspondence of Tr1-low Log (rp) and Tr2-intermediate or high Log (rp). For example, the aragonite optimum formation Tc in SrA experiments is 50 ℃ and Tr1 corresponds to high Log (rp) in experiments with Mg^{2+} added. The lack of ***Pattern 1*** on FeP and FeA experiments, and the altered ***Pattern 2*** indicate that the Tc effects can further interact with ionic impurities and complicate the interpretation of $CaCO_3$ polymorphism.

At the same time, ***Pattern 1*** and ***Pattern 2*** can also be seen in the literature data (Figure 3.5B). Though their experiments differ in initial calcium and ionic impurities concentration, the MgP of Kitano (1962b) and ControlP of Kluge and John (2015a) exhibit Tr2 (***Pattern 2***, Figure 3.5B), in agreement with results obtained at similar experimental conditions in this study (Figure 3.5A). Most literature data in Figure 3.5B follows ***Pattern 1***, but aragonite in MgP starts to occur at 10 ℃. This stems from the extremely high Mg^{2+} concentration (at least 0.6 g/L) employed by Kitano (1962b), which is nearly 2 orders of magnitude larger than this study (0.007 g/L), greatly enhancing the Mg^{2+} aragonite-promoting effect (Davis et al., 2000a; Zhang and Dawe, 2000; Meldrum, 2003). Kluge et al. (2015) precipitated $CaCO_3$ by mixing two solutions, one containing Ca^{2+} and the other CO_3^{2-}, resulting in aragonite enriched at 80 ℃ and exhibited Tr1(Figure 3.5C), thus following both ***Pattern 1*** and ***Pattern 2***.

The use of ***Pattern 1*** and ***Pattern 2*** in describing the pattern of experiments with added ionic impurities and literature data highlights the primary critical role of Tc in $CaCO_3$ polymorphism. Our data indicates Tc acts as a higher-order control compared to the Log (rp) and ionic impurities, as the effects of Tc are always qualitatively traceable regardless of experiment settings.

3.5.2 Delaying the vaterite-calcite transformation with the addition of Na^+

The T method employed 1 M NaOH solution to achieve high Log (rp) but this also introduced Na^+ into the solution. Hence, it is imperative to examine Na^+ effects on polymorphism before analysing the effect of Log (rp). Precipitates under 25 ˚C and the T method generally exhibit a high proportion of vaterite regardless of the added ionic impurities and may even result in vaterite as the dominant phase (Figure 3.5A and 3.6). A temperature of 25 ˚C is necessary for vaterite occurrence as indicated by ***Pattern 1*** but itself can not explain vaterite presence because experiments under the same temperature but using the P or A method rarely lead to vaterite precipitation (Figure 3.5A). The T method, thereby accounts for vaterite enrichment and the key controlling factor is either Na^+ concentration or high Log (rp).

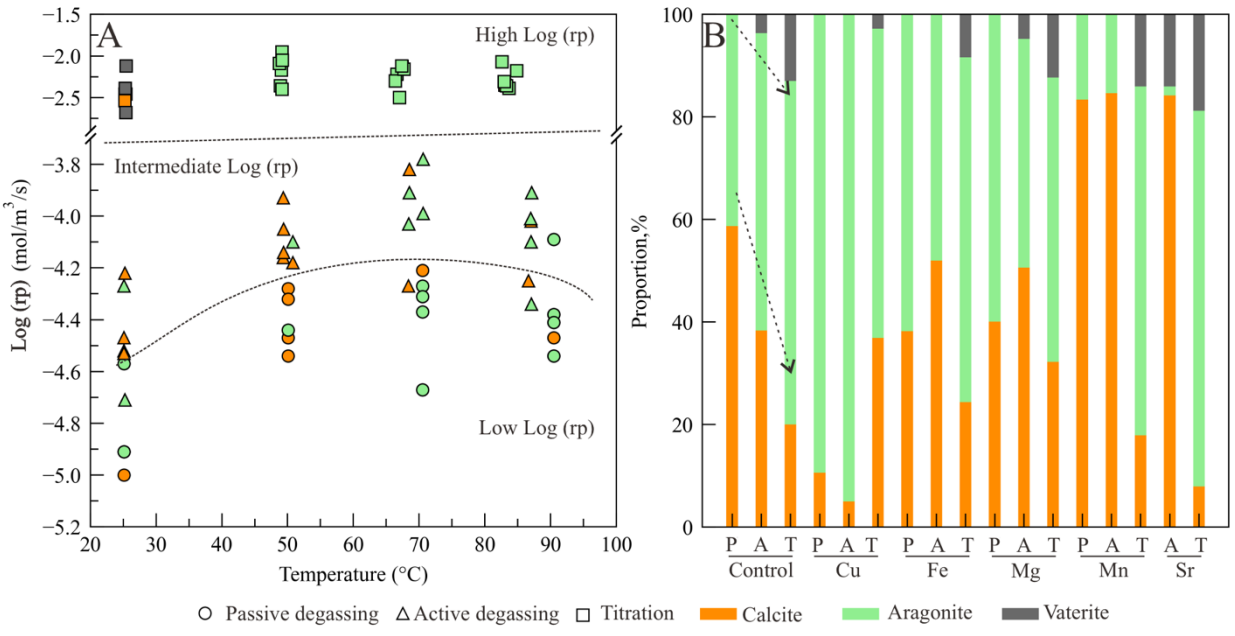


Figure 3.6 Plots showing the polymorph composition variation with precipitation rates, temperature and the trace metal addition.

A. Scatter plot showing the relation between dominant mineralogy, precipitation rate, and temperature. The marker shape indicates the precipitation method employed and the colour represents its dominant mineralogy. The black dashed line describes the rough boundary between different Log (rp) ranges. B. Column distribution plot showing the averaged polymorph composition under each precipitation method ignoring the Tc effects.

Kitano (1962b) and Kluge and John (2015a) obtained a high proportion of vaterite when using solutions containing Na^+ but under a low or intermediate Log (rp) (P or A method) and high Tc (up to 100℃. Figure 3.5B). Compared to the 0.69 g/L Na^+ concentration used in this study, the concentration of Na^+ in Kitano (1962b) and Kluge and John (2015a) is high (9.83 and 147.44 g/L, respectively). Correspondingly, the average vaterite proportion is 39%, 50%, and 86% suggesting that vaterite proportion is positively correlated with Na^+ concentration in the solution. Furthermore, direct evidence of a delayed transformation of vaterite into calcite is observed in sample 25CuT (Figure 3.7): high Na^+ solution concentration is likely to preserve the vaterite by inhibiting its transformation to calcite, explaining the positive correlation between vaterite content and Na^+ concentration.

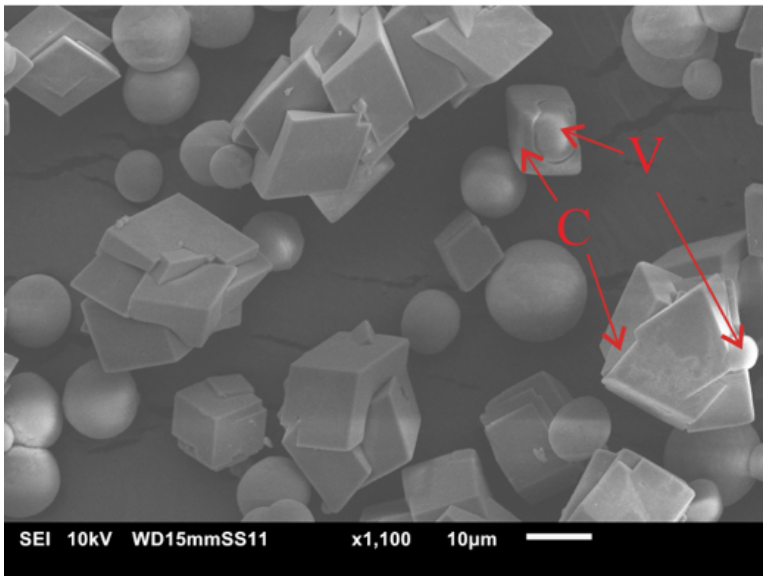


Figure 3.7 A SEM photo of 25CuT shows the vaterites (V) transformation to calcites (C) is retarded by Na^+.

3.5.3 Effects of precipitation rates (Log (rp)) on $CaCO_3$ polymorphism

By excluding the effects of Na^+, the role of log (rp) on polymorphism can be investigated. It appears that calcite-dominated samples are more frequent at low Log (rp) (Figure 3.6A), and one may be misled into considering a negative correlation between calcite proportion and Log (rp). However, this is only true if ionic impurities effects are ignored. Figure 3.6B exhibits the Log (rp)

effects on polymorph composition for each ionic impurities involving the group. The control group (i.e. no impurity added) displays a negative relation between the proportion of calcite and Log (rp), and a positive correlation between aragonite or vaterite proportion and Log (rp). However, these trends disappear when ionic impurities are added to the experiments. This observation suggests that the role of Log (rp) is greatly influenced or even overridden by ionic impurities effects. Compared to (1) Tc, the effects of which are always traceable and (2) ionic impurities which exhibit clear and distinct effects varying from ion to ion (Figure 3.5A and 3.6B), Log (rp) shows weaker control on $CaCO_3$ polymorphism and can thus be considered as a tertiary control.

Interestingly, under high Tc (> 25°C) and high Log (rp), all samples except for 90MgT exhibit a high proportion of aragonite (Figure 3.5), implying that the pair of high Tc (> 25°C) and high Log (rp) (HTc- Log (rp)) favours aragonite precipitation. Jones and Peng (2014) observed similar results with 97% aragonite in sediments of the Jifei hot spring (China), which they explain by temperatures of 40-60°C and fast CO_2 degassing. Though the high aragonite proportion (70-88%) in the Anraku hot spring (Japan) was attributed to the microbial mats by Kawano and Obokata (2007), given the high Tc and fast CO_2 degassing there, our results suggest that the HTc-Log (rp) pair could have induced the high aragonite proportion.

3.5.4 Effects of ionic impurities on $CaCO_3$ polymorphism

3.5.4.1 Effect of ionic impurities on morphology: a tradeoff between kink sites blocking and dissolution

As described in section 3.5.3 and Figure 3.4, compared to the control group, the samples with ionic impurities show dramatically altered $CaCO_3$ morphologies, and can be summarized as two Log (rp) related types: (1) Morphologies with defects under high Log (rp) including rhombohedral calcites with hoppers (Figure 3.4A: (16)-(19)) and nested calcites (Figure 3.4A: (20)), and (2) Morphologies with no defects but showing distinctive habit under low-intermediate Log (rp) including prismatic and dodecahedron calcites (Figure 3.4A: (3) and (4)), calcite with

rounded surfaces and edges (Figure 3.4A: (5) and (6)), and the unique aragonite observed in CuP experiments (Figure 3.4B: (1)-(4)).

Morphologies with defects under high Log (rp) indicate crystal growth is stopped by the ionic impurities attachment to active growing sites (kink sites) at the surface of the crystal that are in charge of the ion incorporation efficiency and the phase precipitation kinetics (Nielsen et al., 2013). Kink site distribution can be simplified as a model with three surfaces (Figure 3.8A): F(flat), S (stepped) and K (kinked) as kink site density decreases (Hartman, 1973; Zhang and Dawe, 2000). The F surface centre has the lowest kink site density and thus can more easily be blocked by ionic impurities than other sites. This blocking effect can be dramatically amplified under high Log (rp) when kink sites are competing for ion supply. This explains why, under high Log (rp), the F surfaces result in hoppers on the centre (Figure 3.4A: (16)-(19)). Similarly,Tai and Chen (1998) obtained calcite exhibiting a complete rhombohedron shape under low $CaCO_3$ supersaturation levels but displaying rhombohedrons with hoppers under high supersaturation levels with orthophosphate added. We suspect that the increased supersaturation level might have dramatically increased the Log (rp) in Tai and Chen (1998) and the orthophosphate blocked the kink sites. Rather than forming hoppers, Cu^{2+} blocking slightly rotates the crystal growth direction (C-axis direction) leading to nested calcites (Figure 3.4A (20) and Figure 3.7). This may be caused by the small radius of Cu^{2+} (0.57 Å) which is nearly half of Ca^{2+} (1.00 Å) forming ineffective blocking.

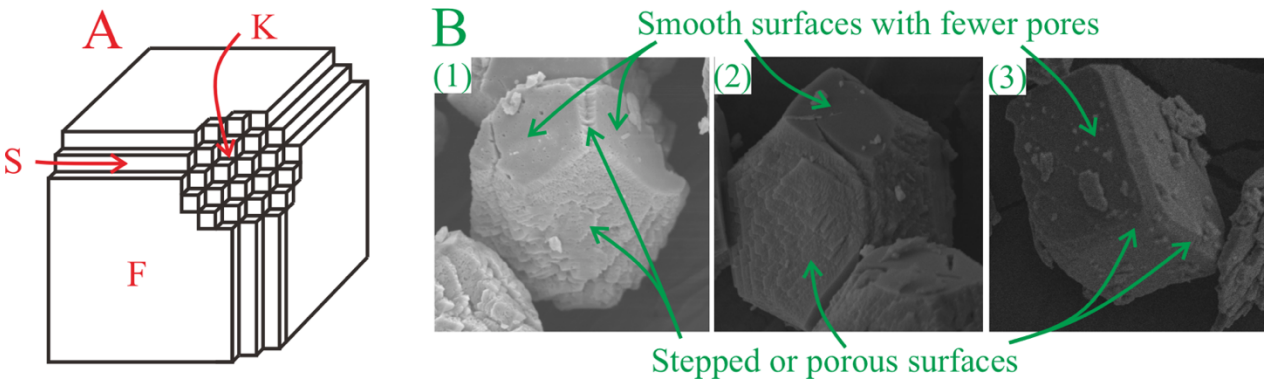


Figure 3.8 Illustration of two theories explaining the morphology variation.

A. Simplified model showing the kink site distribution on $CaCO_3$ crystal in which F, S, and K surfaces are flat,

stepped and kinked surfaces, respectively (Hartman, 1973; Zhang and Dawe, 2000). B, SEM photos showing two different surfaces on calcites from (1) 25MnA, (2) 25MgA, and (3) 25SrA.

The distinctive habits under low-intermediate Log (rp) may be governed by a different mechanism: distribution. Surfaces on these calcites (Figure 3.4A: (3)-(6)) are of two types: (1) Stepped and porous surfaces and (2) Smooth (fewer pores) surfaces (Figure 3.8B). The steps and pores on the surfaces indicate they suffer dissolution (Cao et al., 2020). Both the laboratory and model research proposed that ionic impurities incorporation could enhance mineral solubility (Davis et al., 2000a; Davis et al., 2000b; Nielsen et al., 2013). Stepped and porous surfaces (Figure 3.8B) are thereby probably equivalent to the K and S surfaces in Figure 3.8A, which theoretically absorb more ionic impurities and thus are preferentially dissolved (Paquette et al., 1996; Zhang and Dawe, 2000). The unique aragonite morphology in Figure 3.4B could also be explained by dissolution. The aragonite K surfaces are on lattice C-axis direction. Due to higher Cu concentration, the growth in the C-axis direction is severely inhibited due to dissolution. As the Cu concentration decreases, the inhibition effects fade gradually forming the morphologic evolution series from sphere, split spheres, dumbbell, firewood, to needle habit (Figure 3.4B).

Kink sites are blocked under high Log(rp) and dissolved under low to intermediate Log(rp). This suggests that the $CaCO_3$ morphology likely results from a trade-off between the rate of ion attachment (construction) and detachment (dissolution) (Zhang and Nancollas, 1998; Elhadj et al., 2006; Nielsen et al., 2013). It is crucial to note that the ionic impurities concentration-related dissolution effect is constrained by Log (rp), meaning the concentration doesn't directly control morphology. For instance, Mg^{2+} incorporation into calcite is positively correlated to Log (rp) (Mavromatis et al., 2013), so the Mg^{2+} concentration in 25MgT precipitates is higher than that of 25MgA precipitates. With no constraint from Log (rp), the 25MgT calcite should experience heavier dissolution leading to dodecahedron habit rather than rhombohedron habit with hoppers.

3.5.4.2 Ion speciation effects on polymorphism: free ions prompt calcite precipitation

Figure 3.5A indicates that the $CaCO_3$ polymorphism is significantly influenced by ionic impurities. When compared to the control group, their effects can be summarized as (1) Control-similar: Fe^{3+} and Mg^{2+} groups exhibit similar average calcite and aragonite proportion than the control group, (2) Aragonite-promoting: when Cu^{2+} is added higher aragonite proportion exists, and (3) Calcite-promoting: with the addition of Mn^{2+} or Sr^{2+} the experiments show higher calcite proportion. Except for the experiments where Mg^{2+} was added, a relation exists between the ionic impurities effects and the ion speciation results: the Control-similar and Aragonite-promoting groups correspond to complex-dominated speciation ions (Cu^{2+} and Fe^{3+}) whereas the Calcite-promoting group is associated with free ion-dominated speciation ions (Mn^{2+} and Sr^{2+}) (Figure 3.2B). This suggests that ion speciation is critical in polymorphism and free ion-dominated speciation favors calcite precipitation.

We hypothesise that the observed relation may stem from the larger radius of the complex compared to the free ions, a known controlling parameter on polymorph precipitation (Knight et al., 2023). Unlike free ions that can be easily incorporated into the interstitial position of the lattice or substitute for Ca^{2+} (Mason, 1966; Veizer, 1983), the large complex incorporation may inhibit lattice construction of which the inhibition effect may be heavier on calcite than on aragonite. This finding is crucial as previous research only focuses on free ion radius ignoring ion speciation.

Theoretically, the large cell of orthorhombic aragonite is closely related to larger ions (e.g., Ba^{2+}, Sr^{2+}), while smaller ions (e.g., Zn^{2+}) show a strong affinity to the smaller cell of trigonal calcite (Veizer, 1983; Dietzel, 2011). However, laboratory results suggest that Ba^{2+} and Sr^{2+} favour calcite precipitation in experiments of Kitano (1962a) and this study through CO_2 degassing, and Zn^{2+} promotes aragonite precipitation in Wada et al. (1995)'s synthesis experiments through the mixing of $CaCl_2$ and Na_2CO_3. These experimental results are in good agreement with the ion speciation effect proposed: Ba^{2+} and Sr^{2+} mainly speciate as free ions under a degassing setting

whereas Zn^{2+} mainly speciates as complexes under a mixing setting (Figure 3.2B and 3.9). Different experimental settings may result in different speciation effects: under a degassing setting ~ 50% Zn^{2+} speciates as free ions and thus may favour calcite precipitation (Figure 3.9). The ionic impurities speciation effect probably is constrained by concentration as several research showed that calcite proportion decreases as the total trace metal concentration increases (Kitano, 1962a; Wada et al., 1995).

Though the speciation of Mg^{2+} is characterised by a high proportion of free ions (Figure 3.2B), it didn't promote calcite precipitation (Figure 3.5A). Unlike other ionic impurities, Mg^{2+} speciation and its incorporation into $CaCO_3$ is a debated and complex topic. To date, growing evidence indicates that the high binding and hydration energies of Mg^{2+} play a crucial role in its speciation, leading to strong bonds with water molecules (Meldrum, 2003; Knight et al., 2023). This is not accounted for in PHREEQC explaining why our numerical results exhibit no calcite-promoting effect.

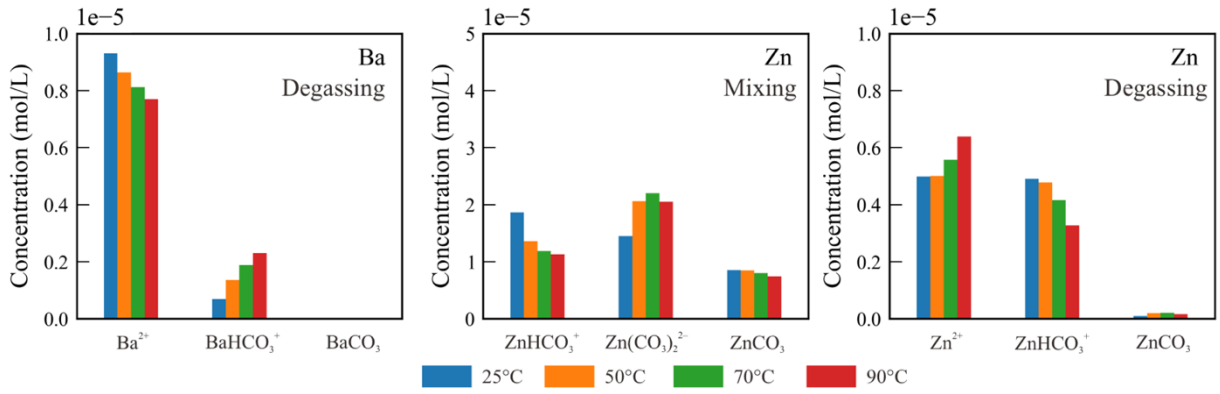


Figure 3.9 Plots show the PHRREQC model results of ionic impurities speciation of Ba^{2+} under degassing setting and Zn^{2+} under mixing and degassing setting (only the three most abundant species are shown here). The total trace metal concentration of the degassing setting is 1×10^{-4} mol/L, whereas that of the mixing setting is 5×10^{-5} mol/L.

3.5.5 The Aragonite-Vaterite problem: instability of vaterite under elevated temperature

All (n=302) samples from the literature (Kitano, 1962b, a; Turnbull, 1973; Wada et al., 1995; Tai and Chen, 1998; Jiménez-López et al., 2004; Kluge and John, 2015a; Kluge et al., 2015; Goetschl et al., 2019) and our samples (Figure 3.3) show that three $CaCO_3$ polymorphs may occur in any combination except as Aragonite and Vaterite together (Ar+V). This observation is in agreement with sample description in other literature (Lam et al., 2007; Rodriguez-Blanco et al., 2012; Zhang et al., 2012; Blue et al., 2017) suggesting that the Ar+V is exceedingly rare, which we propose here for the first time as the "Aragonite-Vaterite problem".

Classical $CaCO_3$ mineralization theory (Figure 3.10) tells that when a solution reaches supersaturation, ions become activated to form metastable ion clusters and nuclei, which then grow and crystallize as either amorphous calcium carbonate (ACC) or polymorphs through Ostwald ripening. Polymorphs can transform into each other (Becker and Döring, 1935; Horn and Rieger, 2001; Navrotsky, 2004). At the same time, some research argues that thermodynamically stable ion clusters exist in the solution (Gebauer et al., 2008) that would form different ACC ($ACC_{vaterite}$, $ACC_{calcite}$, and $ACC_{aragonite}$) transforming into the corresponding polymorph (Hasse et al., 2000; Politi et al., 2006; Lam et al., 2007) (Figure 3.10). Consequently, two models may explain the Aragonite-Vaterite problem: (1) the thermodynamically stable clusters tend to form $ACC_{calcite}$ leading to calcite formation or (2) vaterite tends to transform into the other two phases.

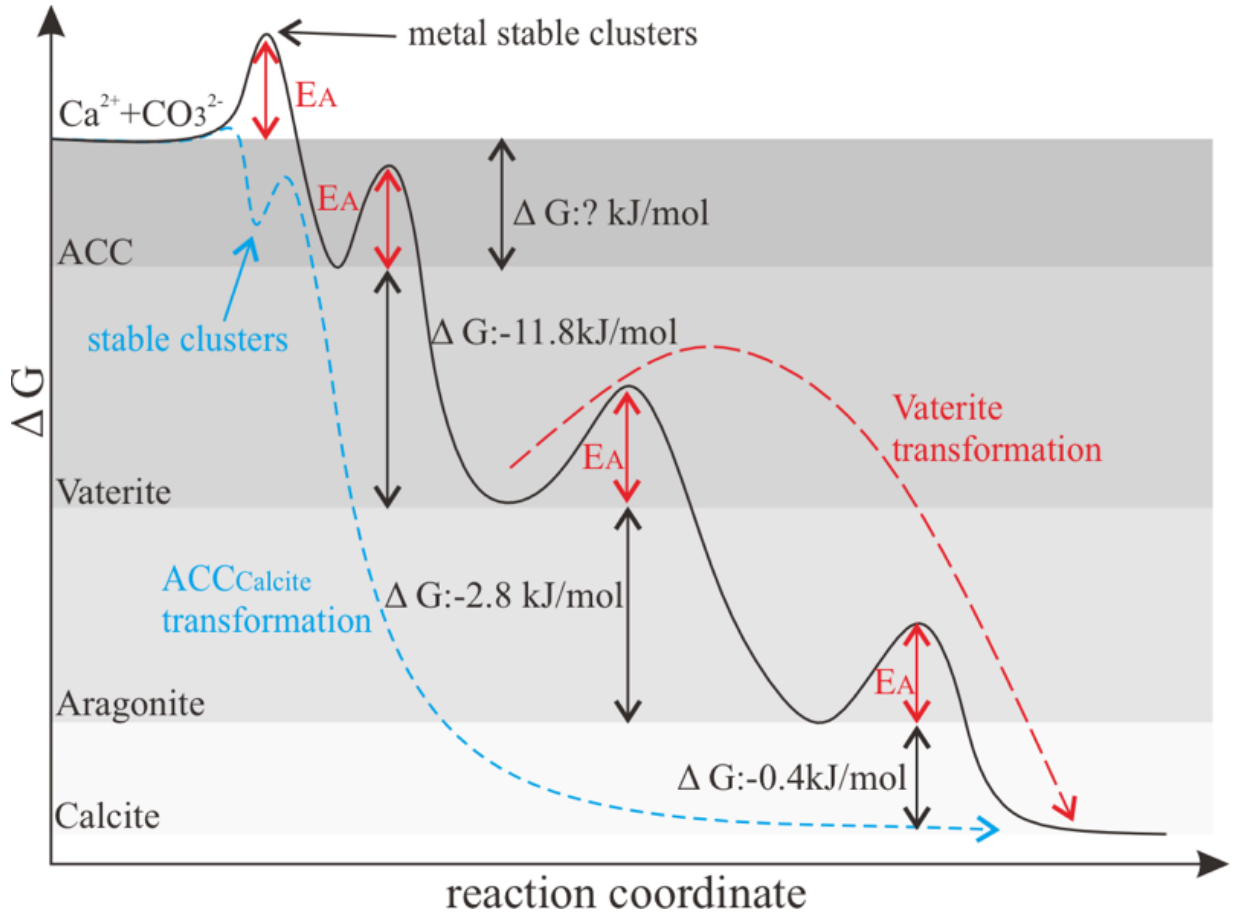


Figure 3.10 Illustration of two different calcium carbonate growth theories.

The black line illustrates the classic $CaCO_3$ mineralization theory transformation in which the amorphous calcium carbonate, vaterite, aragonite, and calcite form along the gradient of decrease in Gibbs free energy but are blocked due to the activation energy barriers (EA). The red and the blue dash lines represent the vaterite-calcite and the $ACC_{calcite}$ transformation respectively. Gibbs free energy data are from Wang et al. (2014) and Müller et al. (2015).

Except for 2 calcite dominated samples (C ≥ 50%), all the other C+Ar+V data are distributed in non-calcite-dominated areas (Figure 3.3) with an averaged proportion of 13.2% for calcite, 49.3% for aragonite, and 37.4% for vaterite. Assuming the parent fluid tends to form $ACC_{calcite}$ rather than the other two species, given that calcite is the most stable phase with the highest saturation index, then calcite would be likely to be a major phase of the mineral mixture rather than forming only 13.2% of the sample. On this basis, we discard the $ACC_{calcite}$ theory and contend that the vaterite transformation model is more likely. The vaterite transformation is a fluid-dependent process in which solution with ions favours the transformation into calcite, whereas

deionized water supports the transformation into aragonite (Sarkar and Mahapatra, 2010; Cherkas et al., 2018). As the vaterites in this study are synthesised in parent fluids containing ions, transformation into calcite is more likely and direct evidence of this is provided by the Sr^{2+} group.

The Sr^{2+} group not only promotes calcite precipitation due to the free ion-rich environment but also preserves the most vaterite compared to the other experiments (Figure 3.5A and 3.6B). Figure 3.10 exhibits that in Sr^{2+} dosed experiments, the laminar vaterite exhibits numerous particles on the surface (Figure 3.11A) that grow into wrinkled and sharp calcites (Figure 3.11B) as the Tc increases from 70 to 90 ˚C and Sr/Ca decrease from 1.2% to 0.7%. This suggests that Sr^{2+} (like Na^{+}) can retard the vaterite transformation preserving vaterite (Ogino et al., 1990). Thermodynamically, vaterite transformation is a process minimizing the Gibbs energy and activating the dissolution-recrystallization process (Cherkas et al., 2018). As concluded in section 4.1, vaterite mostly occurs under 25 ˚C and aragonite prevails at elevated Tc (>25 ˚C). We propose that the Aragonite-Vaterite problem is likely caused by vaterite's low Gibbs energy under elevated Tc leading to its rapid transformation into calcite.

3.6 Conclusions

We conducted $CaCO_3$ synthetic precipitation experiments under a range of temperatures and precipitation rates and the presence of different ionic impurities. The observations in this study suggest that:

1. Temperature and the coupling of high temperature and high precipitation rate (HTc- Log (rp)) are the first-order control on $CaCO_3$ polymorph formation, followed by ionic impurities as second-order, and precipitation rates as third-order control.

2. Temperature influences polymorphism following two distinct patterns. In ***Pattern 1*** calcite prevails at 25 ℃, while aragonite becomes relatively enriched at >25 ℃. In ***Pattern 2*** the relationship between temperature and aragonite proportion can exhibit two trends: one where

aragonite proportion increases with temperature (Tr1), and another where aragonite proportion rebounds at higher temperatures (Tr2).

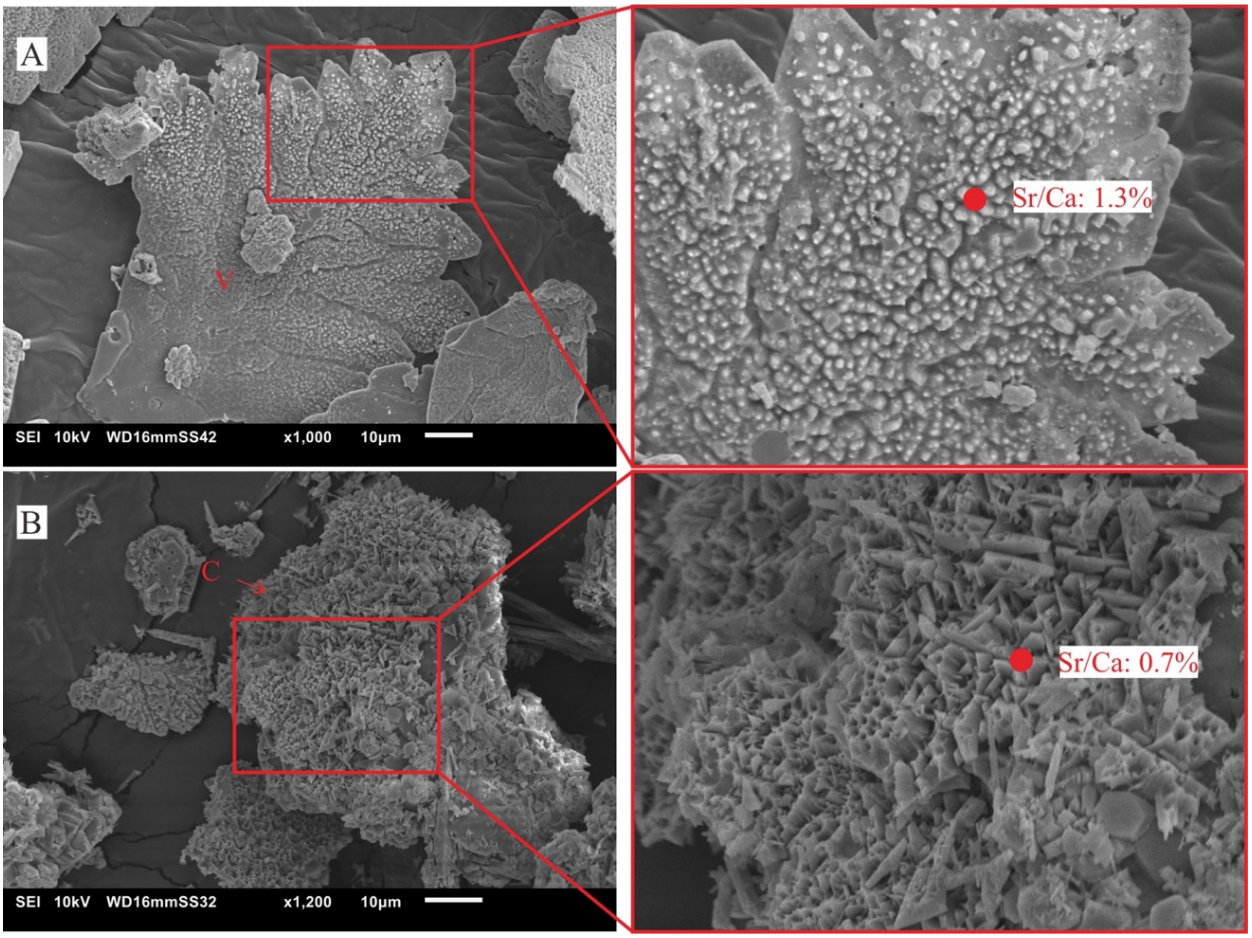


Figure 3.11 SEM photo of samples 70SrA and 90SrA.

A.70SrA shows the laminar vaterites with particles on the surface and B. 90SrA shows calcite with wrinkled and sharp surfaces in which the red dots are EDS points.

3. The presence of Na^+ may retard the transformation of vaterite into calcite thus increasing the relative proportion of vaterite. This retardation effect is positively correlated to Na^+ concentration.

4. The ionic impurities influence the $CaCO_3$ morphologies through two different mechanisms: kink site blocking (ion attachment) and dissolution (ion detachment) constrained by

precipitation rate. Under high precipitation rates, kink site blocking is the major mechanism whereas under lower precipitation rates, dissolution takes the role.

5. Ionic impurities speciation plays a key role in polymorph precipitation: free ion-dominated speciation (Mn^{2+}, Sr^{2+}) favours calcite precipitation. This effect is probably modulated by the concentration of ionic impurities.

6. The Ar+V system is thermodynamically unstable under > 25°C which favours vaterite transformation into calcite. Sr^{2+} exhibit a similar retardation effect to Na^{+} thus preserving the most vaterite in the samples.

These observations point out that the controls on polymorphism are complex, but can be predictable. This has implications for further scientific research, for instance on isotopic effects of cations incorporation. But it also is important for industrial processes where polymorphs need to be controlled. Future research should look into the impact of adding different metal ions together into the same solution.

Chapter 4

Quantification of trace metal partitioning into calcium carbonate ($CaCO_3$) during the CO_2 degassing

4.1 Abstract

Trace metal's presence in natural carbonates is a powerful and widely used paleo-environmental reconstruction proxy. However, its partitioning in a natural environment with a mix of calcium carbonate polymorphs is a research gap. In this study, the partitioning of trace metals (Cu^{2+}, Fe^{3+}, Mg^{2+}, Mn^{2+}, Sr^{2+}) during calcium carbonate precipitation was experimentally investigated by synthesizing $CaCO_3$ via CO_2 degassing method under a wider range of temperatures and precipitation rates. We observe that distribution coefficients ($D_{Me} = (Me/Ca)_{solid}/(Me/Ca)_{solution}$) of Fe^{3+} ($D_{Fe^{3+}}$) and Mn^{2+} ($D_{Mn^{2+}}$) were found to be independent in $CaCO_3$ polymorph and exhibited strong correlations with the average precipitation rates and temperatures. This is of significant importance as Fe^{3+} and Mn^{2+} are common impurities in natural carbonate occurring as the quencher and the activator in cathodoluminescence respectively. The observation suggests that $D_{Fe^{3+}}$ and $D_{Mn^{2+}}$ may be more suitable indicators than distribution coefficients of Cu^{2+}, Mg^{2+}, and Sr^{2+} for naturally deposited $CaCO_3$ polymorph mixture and their dependency on temperatures and precipitation rates can be summarized as follows:

$$\text{Log } D_{Fe^{3+}} = 0.363 \pm 0.010 \times \text{Log}(r_p) - 0.015 \pm 0.0004 \times Tc + 1.885 \pm 0.048$$

$$\text{Log } D_{Mn^{2+}} = -0.077 \pm 0.004 \times \text{Log}(r_p) + 0.001 \pm 0.0001 \times Tc - 0.285 \pm 0.016$$

where Tc is the temperature in degrees Celsius and Log (rp) is in mol/m^3/s.

$D_{Fe^{3+}}$ increases with increasing precipitation rate but decreases with decreasing temperature, while $D_{Mn^{2+}}$ exhibits the opposite trends. The control exerted by precipitation rate on D_{Me} is more pronounced compared to that by the temperature, particularly for $D_{Mn^{2+}}$, where the influence of temperature is minor and the $D_{Mn^{2+}}$ vs precipitation rate relation could be expressed as:

$$\text{Log } D_{Mn^{2+}} = -0.073 \pm 0.004 \times \text{Log}(r_p) - 0.217 \pm 0.013$$

Due to the challenge of obtaining the parent fluid composition for field samples, the application of D_{Me} in natural samples is inhibited and the use of Fe/Ca and Mn/Ca ratios may hold more significance but requires further investigation to mathematically confirm its correlation with precipitation rates and temperatures.

4.2 Introduction

Carbonate rocks made of calcium carbonate ($CaCO_3$) are valuable repositories of various resources (e.g. water) and serve widely as a crucial geological archive of past environmental conditions, thereby holding significant importance in geosciences. The precipitation of calcium carbonate is the result of a complex interplay between ionic species within the aquatic environment, leading to the incorporation of impurity elements (Watson, 2004; Nielsen et al., 2013) of which the process is highly related to the fluid conditions during precipitation such as the temperature and precipitation rate. The trace metal content within $CaCO_3$, thereby, has long been recognized and used as an important proxy for paleoclimate and environmental reconstruction. Notably,

magnesium (Mg), the most prevalent impurity, is successfully used as a proxy for precipitation temperature such as the use of Mg/Ca and Mg/Li ratios (Montagna et al., 2014; Mavromatis et al., 2022). Furthermore, the incorporation of trace metals can alter the optical and electromagnetic properties of $CaCO_3$, offering direct insights into environmental conditions when examined under microscopes. Specifically, the incorporation of iron (Fe) and manganese (Mn) into carbonates significantly influences cathodoluminescence (CL), a technique extensively employed in reconstructing the history of carbonate diagenesis (GÖTte and Richter, 2009; Cao et al., 2020).

$CaCO_3$ exists in three distinct polymorphs in nature—calcite, aragonite, and vaterite—with trigonal, orthorhombic, and hexagonal crystal systems respectively. Due to variations in crystal structures, different polymorphs of $CaCO_3$ display different abilities to incorporate trace metals. Extensive research endeavours have focused on experimentally determining the trace metal to calcium ratio (Me/Ca or D_{Me}) for a specific polymorph under diverse environmental conditions. For instance, in the laboratory synthesis experiment, the Mg partitioning in calcite and aragonite are both proven to be precipitation rate dependent and the Mg portioning in calcite is several orders larger than that in aragonite at similar precipitation rate (Mavromatis et al., 2013; Mavromatis et al., 2022). These measured relationships offer valuable mathematical descriptions of how trace metal partitioning in a specific $CaCO_3$ phase would vary with the precipitation rate and the temperature. However, such research faces three main limitations:

(1) These studies typically involve $CaCO_3$ precipitation by mixing of a Ca^{2+} solution and a CO_3^{2-} solution (e.g. $CaCl_2$ and Na_2CO_3) within a controlled reactor environment and a constant pH. This artificial setting deviates from natural conditions, where $CaCO_3$ precipitation occurs due to CO_2 degassing from $CaCO_3$ supersaturated solution (e.g. in springs), leading to continuously changing pH and ion concentrations.

(2) Calcite or aragonite seeds are introduced to control the mineralogy of overgrowths on seeds' surfaces. However, the precipitation of a singular $CaCO_3$ phase without seeds remains a

subject of ongoing debate, as polymorph precipitation is influenced not only by thermodynamic properties (Jones, 2017). Thus, previous studies' results are hard to be applied to predict trace metal concentrations in $CaCO_3$ polymorph mixtures formed naturally.

(3) These relations are generally limited by a low-temperature range such as 10-50℃ in Dromgoole and Walter (1990b) which does not capture the range of temperatures for subsurface carbonate precipitation.

Hence, there is a pressing need for studies mimicking natural $CaCO_3$ precipitation at a range of geologic temperatures to establish relationships between trace metal incorporation in $CaCO_3$ and environmental conditions and explore the correlation with a mix of $CaCO_3$ polymorphs. To address this gap, the present study syntheses $CaCO_3$ by degassing CO_2 from $CaCO_3$ supersaturated solution with or without five different trace metals Fe^{3+}, Mn^{2+}, Mg^{2+}, Cu^{2+}, and Sr^{2+}. Precipitation experiments are conducted across a range of temperatures (25 to 90℃) and precipitation rates. Subsequently, the precipitates are characterized for polymorph composition and morphology. Additionally, both the precipitates and the solution sampled during precipitation are analyzed for major and trace element concentrations. Through these efforts, our objectives are to: (1) Identify the trace metals that are suitable for investigating natural $CaCO_3$ polymorph mixture. (2) Investigate the influence of precipitation rate and temperature on trace metal incorporation into $CaCO_3$. (3) Provide insights for future modelling efforts and real-world applications of Me/Ca ratios.

4.3 Methods and materials

In the current chapter, only XC2024 samples (a total of 68) were characterized for solid elemental composition through ICP-MS (Chapter 2 section 2.5.1). The detailed sample preparation procedure (Chapter 2 section 2.2.1) and the methodology of the experimental techniques can be found in Chapter 2 along with the distribution coefficient calculation (Chapter 2 section 2.5.2).

The mineralogy and morphology characterization, and precipitation rate calculation (Chapter 3 section 3.4.1) of XC2024 are described in detail in Chapter 3 but will be briefly reviewed here.

4.4 Results

4.4.1 Chemical evolution of reactive fluids

The experimental conditions for each sample preparation are summarized in Chapter 3 Table 3.2, and a representative plot showing the chemical evolution of the solution is presented in Chapter 3 Figure 3.1. Throughout the precipitation process, the data logger recorded a consistently stable experimental temperature, with an average low standard error of ≤ 0.3°C. Initially, the solution was enriched with calcium and trace metals at a pH of approximately 6.5. As CO_2 was stripped from the solution, the pH gradually increased to a maximum before experiencing a slight decline, followed by either a gradual increase until reaching a plateau (P or A method, Chapter 3 Figure 3.1) or a continued increase until the end of the NaOH titration (T method). The fluctuations in solution calcium concentration exhibited either a full or part of a mirrored "S" curve (Chapter 3 Figure 3.1), contingent upon the presence of a relatively stable plateau at the onset. The trends observed in trace metal concentrations mirrored those of calcium fluctuations.

The temporal evolution of ion concentrations, coupled with the underlying reaction principle, suggests that CO_2 degassing essentially mimics an acid-base titration-like process. Consequently, the logistic model (Chapter 2 Eqs (2.31)), commonly utilized in titration regression fitting (Chuang, 1987; Stamou Jr et al., 2018), was employed to obtain the fitting curve describing calcium fluctuation.

Based on the fitting results, the average absolute precipitation rates for each experiment were calculated by integrating the differential function of the fitting curve within the precipitation window (Chapter 3 Figure 3.1). Table 3.2 shows the precipitation durations for the P, A, and T methods. They ranged between approximately 20 days, 7 days, and 1 hour, respectively, indicating

that the P and A methods required at least two orders of magnitude more time than the T method. Consequently, to derive a more representative precipitation rate, the precipitation window for the T method was defined from the point of calcium drop until the conclusion of precipitation, whereas for the A and P methods, it extended to the point where 90% of precipitation was achieved.

The Log value of integrated absolute precipitation rates, denoted as Log (rp), ranged from -5.00 to -4.28, -4.27 to -3.78, and -2.68 to -1.95 mol/m^3/s for the P, A, and T methods, respectively. It's noteworthy that the precipitation rates in this study are not directly comparable to the growth rates defined in seeding research but should be theoretically positively correlated. For example, Mavromatis et al. (2013) calculated crystal growth rates on the initial seed surfaces, expressed in units of mol/m^2/s.

4.4.2 Mineralogy characterization of the precipitated solids

X-ray diffraction (XRD) analysis revealed that all 68 precipitated samples in this study exhibited characteristic peaks indicative of $CaCO_3$, with traces of trace metal carbonates. Table 3.2 illustrates the $CaCO_3$ polymorph composition of the synthesized samples. The samples predominantly comprised a mixture of calcite and aragonite, with vaterite present as a minor component. In rare instances, vaterite emerged as the major component. Figure 3.5 demonstrates a strong correlation between polymorph composition and experimental precipitation rates or temperatures. Generally, calcite predominated at temperatures of 25 and 50 ℃, while aragonite prevailed at 70 and 90 ℃. Vaterite was more prominent at 25 ℃, particularly associated with faster precipitation rates. These findings align with previous research (Rosa and Lundager Madsen, 2011; Jones, 2017).

Observations under the microscope show grain sizes ranging from 8 μm to 200 μm. Cathodoluminescence (CL) microscopy revealed that calcite and vaterite typically exhibited dark orange luminescence (Figure 4.1A), while aragonite showed no luminescence.

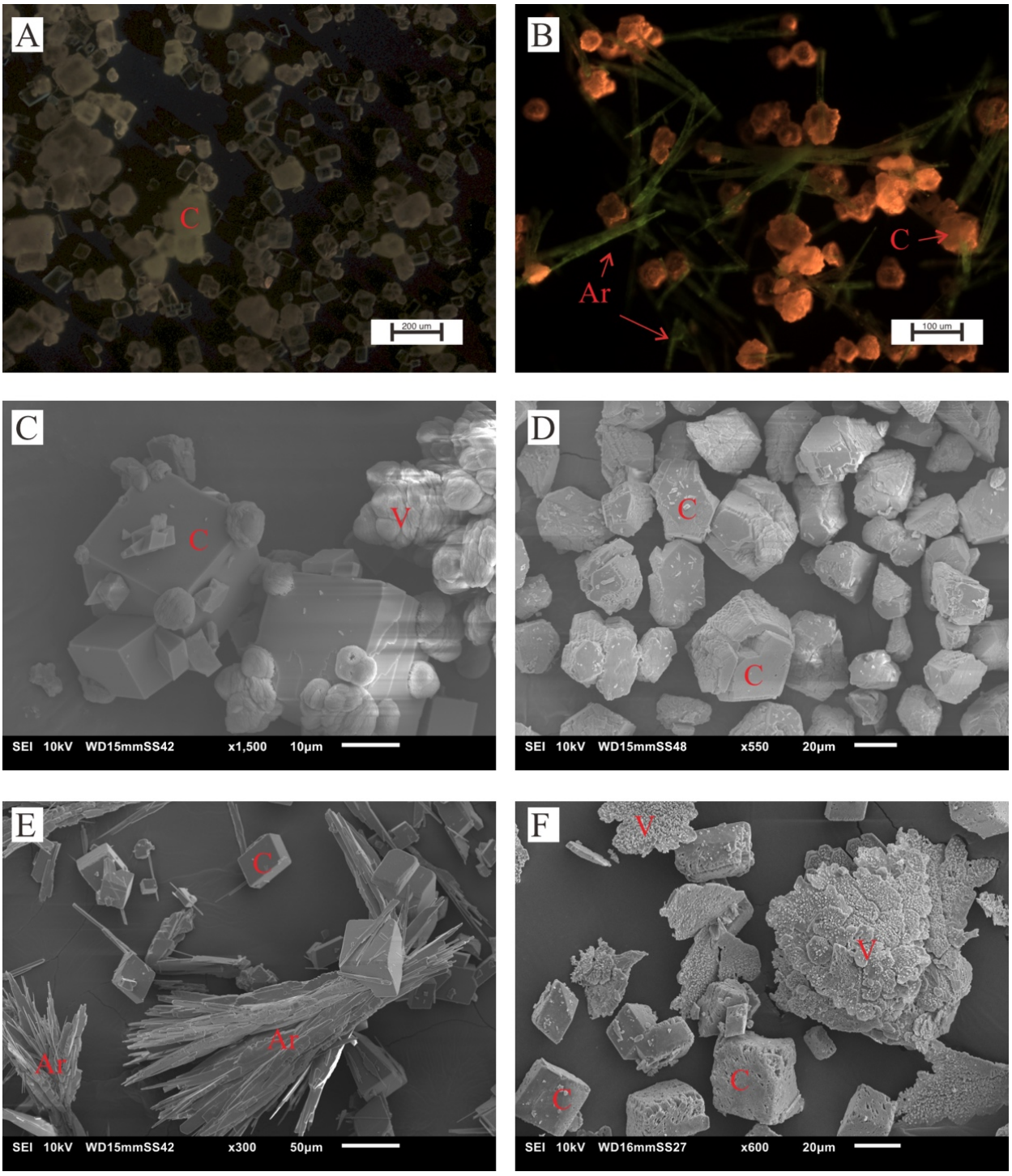


Figure 4.1 Cathodoluminescence (CL) and SEM photos showing the characterization of calcite (C), aragonite (Ar), and vaterite (V) under microscopes.

A.25P calcites show dark orange light under CL. B. 70MnA calcites and aragonites are bright orange and green respectively. Under CL C. 25T SEM photo shows the rhombohedral calcite and botryoidal vaterite. D. 25MnP SEM photo displays the prismatic and scalenohedral calcites. E. 50MgA SEM photo shows the radical habit aragonites. F. 70SrP SEM photo displays the laminar habit vaterite.

However, the presence of Mn^{2+} and Fe^{3+} resulted in distinct phenomena (GÖTte and Richter, 2009), with Mn-bearing calcites and aragonites displaying bright orange and green luminescence, respectively (Figure 4.1B), while Fe-bearing samples exhibited no luminescence under CL. Calcite typically exhibited a rhombohedral habit, occasionally displaying prismatic and scalenohedral habits (Figure 4.1C and D). Aragonite primarily exhibited a needle or radial shape (Figure 4.1B and E), while vaterite appeared in botryoidal or laminar formats (Figure 4.1C and F).

4.4.3 Trace metal partitioning between $CaCO_3$ and the reactive fluid

To elucidate the distribution of trace metals between the solution and solids, the distribution coefficient (D_{Me}), introduced by (Henderson and Kracek, 1927) is employed for trace metal data reduction which is wildly used by researchers in this field. Morse and Bender (1990) modified the equation as illustrated in Chapter 2 Eqs (2.26). The detailed calculation of activities is provided in Chapter 2 Eqs (2.27)-(2.30).

Table 4.1 Precipitation details and mineralogy of calcium carbonate precipitates in this study.

The Me/Ca (solids) is the trace metal to Ca ratio in solids and the $D_{Me/Ca}$ is the distribution coefficient of trace metal. The sample ID here are correlated to Table 3.2 in Chapter 3.

ID	Me/Ca	$D_{Me/Ca}$
25ControlP	-	-
50ControlP	-	-
70ControlP	-	-
90ControlP	-	-
25ControlA	-	-
50ControlA	-	-
70ControlA	-	-
90ControlA	-	-
25ControlT	-	-

ID	Me/Ca	$D_{Me/Ca}$
50ControlT	-	-
70ControlT	-	-
90ControlT	-	-
25CuP	0.061 ± 0.002	1.411 ± 0.067
50CuP	0.037 ± 0.001	0.969 ± 0.053
70CuP	0.110 ± 0.005	1.728 ± 0.099
90CuP	0.066 ± 0.003	0.731 ± 0.052
25CuA	0.068 ± 0.004	1.552 ± 0.148
50CuA	0.081 ± 0.004	1.532 ± 0.356
70CuA	0.091 ± 0.004	2.048 ± 0.419
90CuA	0.161 ± 0.007	1.927 ± 0.208
25CuT	0.056 ± 0.003	1.211 ± 0.091
50CuT	0.068 ± 0.004	1.237 ± 0.135
70CuT	0.064 ± 0.003	1.105 ± 0.188
90CuT	0.122 ± 0.005	1.105 ± 0.069
25FeP	0.009 ± 0.000	0.653 ± 0.126
50FeP	0.004 ± 0.000	0.303 ± 0.046
70FeP	0.003 ± 0.000	0.158 ± 0.018
90FeP	0.003 ± 0.000	0.095 ± 0.012
25FeA	0.016 ± 0.001	1.352 ± 0.151
50FeA	0.005 ± 0.000	0.402 ± 0.060
70FeA	0.003 ± 0.000	0.309 ± 0.039
90FeA	0.004 ± 0.000	0.134 ± 0.016
25FeT	0.021 ± 0.001	2.935 ± 0.232

ID	Me/Ca	$D_{Me/Ca}$
50FeT	0.026 ± 0.001	2.178 ± 0.214
70FeT	0.021 ± 0.001	1.375 ± 0.076
90FeT	0.013 ± 0.001	1.232 ± 0.133
25MgP	0.005 ± 0.000	0.115 ± 0.008
50MgP	0.005 ± 0.000	0.114 ± 0.009
70MgP	0.000 ± 0.000	0.005 ± 0.000
90MgP	0.003 ± 0.000	0.025 ± 0.002
25MgA	0.006 ± 0.000	0.108 ± 0.024
50MgA	0.007 ± 0.000	0.103 ± 0.010
70MgA	0.004 ± 0.000	0.061 ± 0.019
90MgA	0.045 ± 0.001	0.320 ± 0.017
25MgT	0.012 ± 0.000	0.250 ± 0.016
50MgT	0.002 ± 0.000	0.025 ± 0.002
70MgT	0.004 ± 0.000	0.055 ± 0.004
90MgT	0.119 ± 0.002	0.893 ± 0.031
25MnP	0.025 ± 0.001	1.298 ± 0.096
50MnP	0.024 ± 0.001	1.274 ± 0.092
70MnP	0.033 ± 0.001	1.075 ± 0.067
90MnP	0.073 ± 0.004	1.389 ± 0.117
25MnA	0.028 ± 0.001	1.235 ± 0.093
50MnA	0.032 ± 0.002	1.205 ± 0.127
70MnA	0.029 ± 0.001	0.905 ± 0.081
90MnA	0.074 ± 0.004	1.319 ± 0.127
25MnT	0.017 ± 0.001	0.835 ± 0.078

ID	Me/Ca	$D_{Me/Ca}$
50MnT	0.022 ± 0.001	0.898 ± 0.086
70MnT	0.032 ± 0.002	0.942 ± 0.084
90MnT	0.048 ± 0.002	0.954 ± 0.081
25SrA	0.006 ± 0.000	0.363 ± 0.035
50SrA	0.007 ± 0.000	0.445 ± 0.040
70SrA	0.008 ± 0.001	0.337 ± 0.036
90SrA	0.011 ± 0.001	0.371 ± 0.048
25SrT	0.011 ± 0.001	0.770 ± 0.087
50SrT	0.016 ± 0.001	0.925 ± 0.114
70SrT	0.021 ± 0.002	0.917 ± 0.096
90SrT	0.029 ± 0.002	0.945 ± 0.093

Among the five different trace metals, Log $D_{Fe^{3+}}$ exhibited the widest range and most evenly distributed data, varying from -1.023 to 0.468 (Figure 4.2 and Table 4.1). Conversely, Log $D_{Mn^{2+}}$ represented the most clustered data, varying from -0.078 to 0.143. Although Log $D_{Mg^{2+}}$ ranged from -2.290 to -0.049, the majority fell within the range of -1.601 to -0.495, excluding two apparent outliers (Figure 4.2 and Table 4.1). The distribution coefficient range of Cu^{2+} and Sr^{2+} was $-0.014 \leq \text{Log } D_{Cu^{2+}} \leq 0.311$ and $-0.472 \leq \text{Log } D_{Sr^{2+}} \leq -0.025$, respectively.

Furthermore, under the experimental settings of this study, Cu^{2+} and Mn^{2+} incorporation into $CaCO_3$ appears relatively easier, with the highest median Log D_{Me} of 0.121 and 0.086, respectively. Fe^{3+} incorporation was slightly lower, with a median Log $D_{Fe^{3+}}$ of -0.290, which is similar to the median of Log $D_{Sr^{2+}}$: -0.232. In contrast, Mg^{2+} incorporation was more challenging than other trace metals, with the lowest median Log $D_{Mg^{2+}}$ = -0.977, nearly one magnitude lower than that of other metals (Figure 4.2).

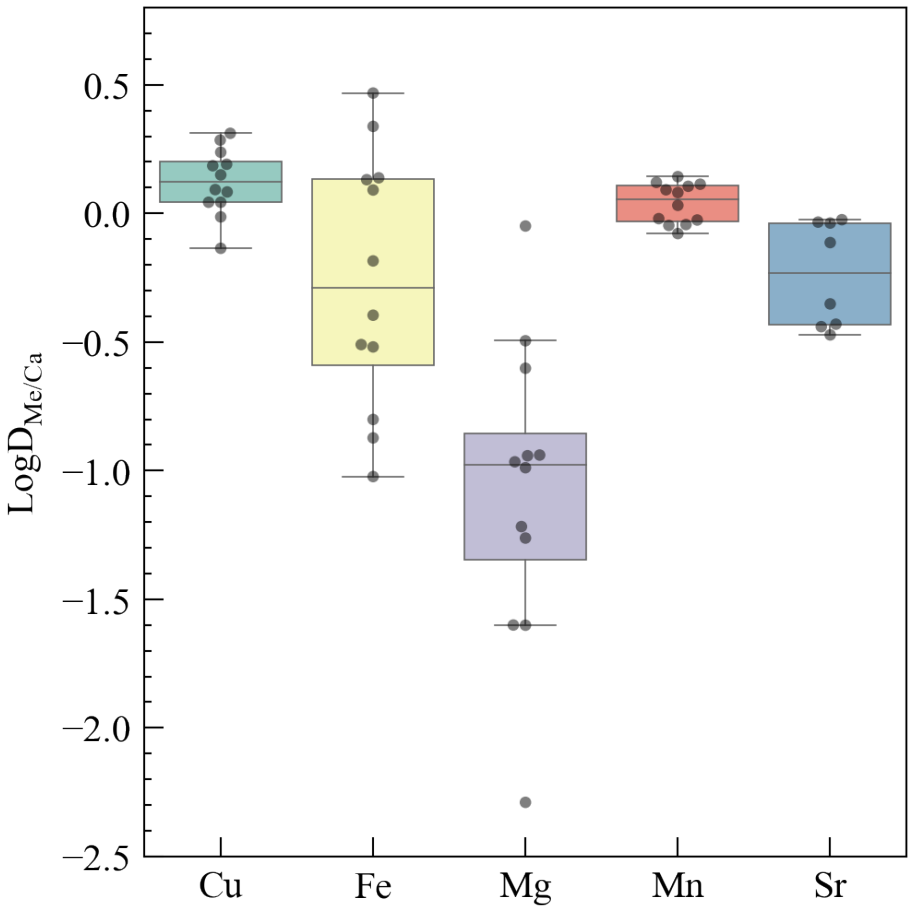


Figure 4.2 Box plot showing the range of Log D_{Me} of the researched elements.

The Log D_{Me} of Fe^{3+} exhibit the widest range and that of Cu^{2+} and Mn^{2+} displays the highest median value.

4.5 Discussions

4.5.1 Comparison between different D_{Me}: trace metal suitable for the research on deposits of $CaCO_3$ polymorph mixture

Among the five different trace metals investigated in this study, Log $D_{Fe^{3+}}$ and Log $D_{Mn^{2+}}$ exhibit strong correlations to changes in both the average precipitation rate and the temperature (Figure 4.3B and 4.3D). Fe^{3+} uptake at each temperature demonstrates a positive correlation with precipitation rate, with slopes at each temperature identical within uncertainty, suggesting a consistent mechanism governing Fe^{3+} partitioning in $CaCO_3$. Although sample 70MnP and

70MnA seem to deviate from the trend of Log $D_{Mn^{2+}}$ (Figure 4.3D)-a negative relation to precipitation rates but a positive relation to the temperature, their 1 SD overlap with the trend and sample 70MnT aligns well with this trend (Figure 4.3D). Linear regressions in log space indicate that Fe^{3+} and Mn^{2+} partitioning can be expressed as Eqs (4.1) and (4.2), respectively:

$$\text{Log } D_{Fe^{3+}} = 0.363 \pm 0.010 \times \text{Log}(r_p) - 0.015 \pm 0.0004 \times Tc + 1.885 \pm 0.048 \quad (4.1)$$

$$\text{Log } D_{Mn^{2+}} = -0.077 \pm 0.004 \times \text{Log}(r_p) + 0.001 \pm 0.0001 \times Tc - 0.285 \pm 0.016 \quad (4.2)$$

Unlike the previously proposed equations for a single $CaCO_3$ phase like the Log $D_{Fe^{2+}}$ and Log $D_{Mn^{2+}}$ for calcites (Dromgoole and Walter, 1990b), Eqs (4.1) and (4.2) are built on the fact that both the Fe-bearing samples and Mn-bearing samples are a mixture of different $CaCO_3$ polymorphs with different dominant (>50%) polymorphs (Figure 4.3B and 4.3D). Specifically, the polymorph composition of Fe-bearing samples is correlated with precipitation rate and temperature (Figure 4.3B and Table 4.1) with aragonite emerging as the predominant polymorph at high precipitation rates (T method), while calcite predominates at 50 ℃ at lower precipitation rates (P and A methods). The Mn-bearing samples polymorphism appears to be primarily related to precipitation rate, with calcite predominating under low precipitation rates (P and A methods) and aragonite or vaterite predominant under high precipitation rates (T method) (Figure 4.3D and Table 4.1). Under such circumstances, the relationship between Fe^{3+} and Mn^{2+} partitioning and precipitation rate at different temperatures exhibits similar slopes (Eqs (4.1)-(4.2)). This strongly suggests that Fe^{3+} and Mn^{2+} incorporation into $CaCO_3$ is not only sensitive to changes in temperature and precipitation rate but also not observable polymorph-dependent or alternatively their partitioning extent in different polymorphs is similar.

Despite magnesium being the most abundant divalent ionic impurity ion in both carbonates and the ocean, no systematic correlation is observed between Log $D_{Mg^{2+}}$ and either Tc or Log (rp) in our study. This lack of correlation may stem from the high dependence of Mg^{2+} incorporation

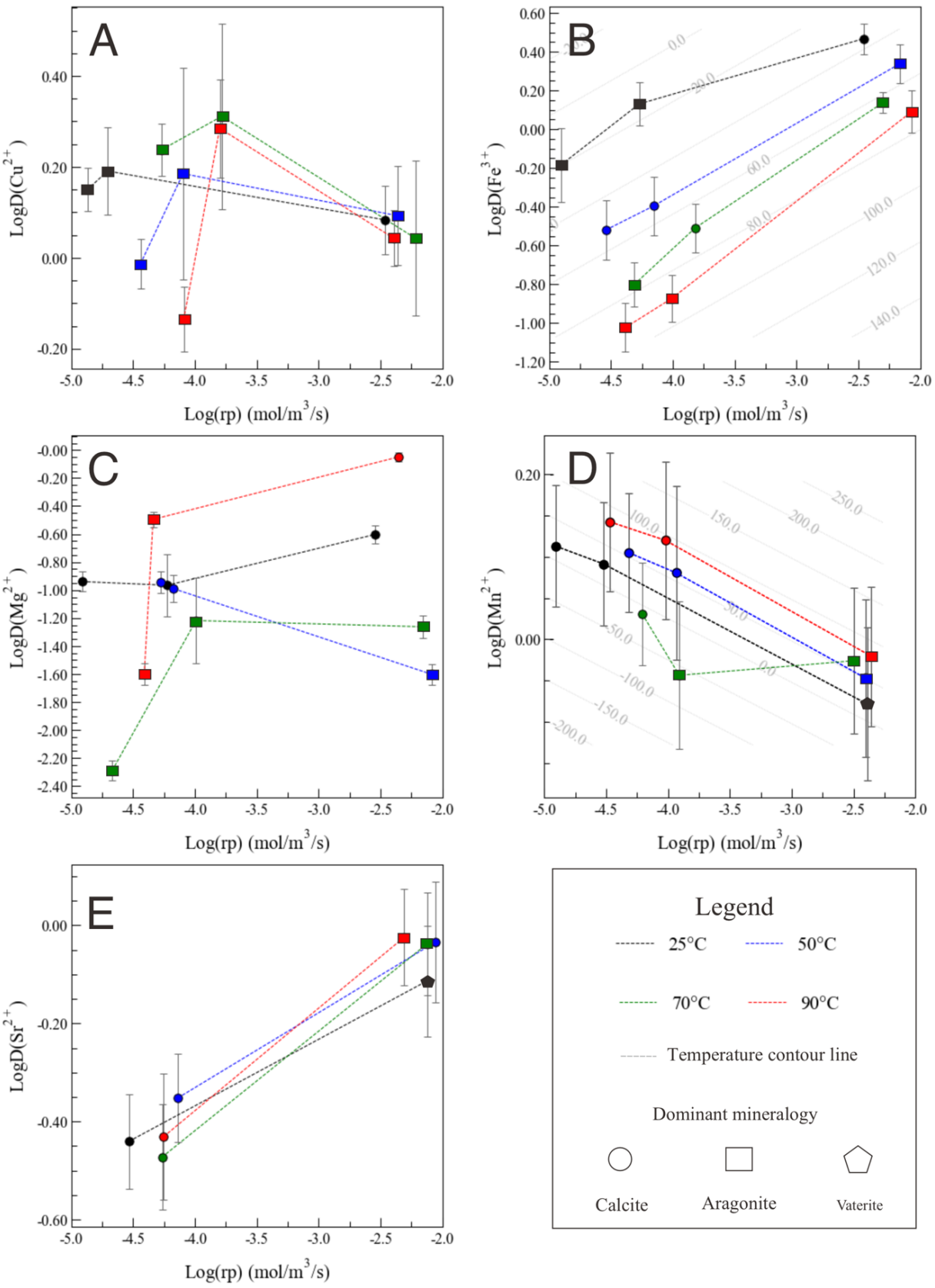

A
B
C
D
E
LogD(Cu2+)
LogD(Fe3+)
LogD(Mg2+)
LogD(Mn2+)
LogD(Sr2+)
Log(rp) (mol/m3/s)
Legend
25°C
50°C
70°C
90°C
Temperature contour line
Dominant mineralogy
Calcite
Aragonite
Vaterite

Figure 4.3 Scatter plot showing the dependence of Log D_{Me} on temperature and precipitation rate of the researched elements.

The Log D_{Me} of Fe^{3+} and Mn^{2+} displays good correlations with temperature and precipitation rate and can be summarized as Eqs (4.1)-(4.2). The dot shape indicates the dominant mineralogy of the sample. The contour lines in B and D donate the calculated temperature based on Eqs (4.1) and (4.2).

into $CaCO_3$ on the polymorph structure (Figure 4.3C). Indeed, compared to calcites, Mg^{2+} partitioning in aragonites is reported to be less dependent on precipitation rate (Goetschl et al., 2019). Published values of Log $D_{Mg^{2+}_{(Calcite)}}$ under similar experimental settings typically higher than Log $D_{Mg^{2+}_{(Atragonie)}}$ by 2-3 at similar temperatures and precipitation rates (Gabitov et al., 2008; Mavromatis et al., 2022). For example, at 25 °C and a Log (rp) of ~ -7 mol/m^2/s, Log $D_{Mg^{2+}}$ for aragonite and calcite range from -4.77 to -3.88 and from -2 to -1.40, respectively (Oomori et al., 1987; Huang and Fairchild, 2001; Mavromatis et al., 2022).

Copper ions (Cu^{2+}) may play a role in promoting aragonite formation as except for one calcite-dominated sample, all the other samples precipitated with Cu^{2+} are dominated by aragonite with an average proportion of 89% (Table 3.2 and Figure 4.3A). The relatively uniform polymorph composition potentially implies a functional relationship. However, the relationship between Log $D_{Cu^{2+}}$, Tc, and Log (rp) rejected this hypothesis (Figure 4.3A): at each temperature, a non-monotonic correlation exists between Log $D_{Cu^{2+}}$ and precipitation rate, and temperature correlations intersect with each other. Sr-bearing samples face similar challenges. The crossed regression lines at each temperature indicate that Log $D_{Sr^{2+}}$ is not sensitive to temperature in the current experimental setting (Figure 4.3E). Although the limited number of points makes it difficult to assess the dependence of Log $D_{Sr^{2+}}$ on precipitation rate, a strong correlation between Log $D_{Sr^{2+}}$ and precipitation rates exist ignoring temperature differences (Figure 4.3E).

In comparison to Mg^{2+} and Cu^{2+}, Fe^{3+} and Mn^{2+} partitioning in $CaCO_3$ are potential good proxies for precipitation rates and temperature. They exhibit strong correlations with these parameters over a wide range and show no, or at least no obvious, dependence on polymorph type.

Sr^{2+} partitioning may be a promising indication for precipitation rates but needs further investigation with more data. Although the trace metal incorporation rate may also be polymorph-specific, it is also related to calcium and trace metal concentration in the solution (Dromgoole and Walter, 1990b), we hereby argue that these influences and other potential influences may compensate for each other in the dynamic precipitation process leading to the capability of Eqs (4.1) and (4.2) in describing the overall precipitates.

4.5.2 The role of precipitation rate in trace metal partitioning in $CaCO_3$

We further investigate the role of precipitation rate. Figure 4.4 show that precipitation rate is pivotal in controlling the incorporation of trace metals in $CaCO_3$, where Log $D_{Mn^{2+}}$ and Log $D_{Sr^{2+}}$ exhibit a positive correlation with precipitation rate, whereas Log $D_{Fe^{3+}}$ displays the opposite trend. At the same temperature, 1 mol/m^3/s increase in precipitation rate (Log (rp)) leads to an increase of approximately 0.2 in Log $D_{Fe^{3+}}$ and a decrease of 0.05 in Log $D_{Mn^{2+}}$. From this perspective, the sensitivity of Log $D_{Fe^{3+}}$ to precipitation rates is approximately four times greater than that of Log $D_{Mn^{2+}}$.

Previous studies investigating Log D_{Me} vs precipitation such as Mg^{2+}, Fe^{2+}, Sr^{2+}, Co^{2+}, and Zn^{2+} (Lorens, 1981; Mucci and Morse, 1983; Dromgoole and Walter, 1990b; Rimstidt et al., 1998; Mavromatis et al., 2022) observe that under near-equilibrium conditions, trace metals with Log D_{Me} <0 show a positive correlation with precipitation rate, while those with Log D_{Me} >0 exhibits a reversed correlation. The partitioning of Fe^{3+} and Mn^{2+} observed in our study is in line with these observations: under low precipitation rates (P and A methods) approaching equilibrium conditions, Log $D_{Fe^{3+}}$ is negative and Log $D_{Mn^{2+}}$ is positive (Figure 4.4). However, under the T method with high precipitation rates, both Log $D_{Fe^{3+}}$ and Log $D_{Mn^{2+}}$ deviate from these observations by exhibiting more positive and negative values, respectively. Additionally, an overall trend between Log D_{Me} is observed in Figure 4.4: all samples exhibit a wide range of Log D_{Me} under lower precipitation rates, but Log D_{Me} tends to approach zero under high precipitation rates except for

the Mg-bearing samples. These observations suggest that the trace metal partitioning in calcium carbonate is directly governed by the precipitation rate under rapid precipitation by approaching the parent solution composition (Log D_{Me} = 0), but under relatively low precipitation rate other thermodynamic parameters may play a greater role (Mavromatis et al., 2022). We interpret the abnormal behaviour of Log $D_{Mg^{2+}}$ as probably related to the high binding and hydration energy of Mg^{2+} (Rodriguez-Cruz et al., 1999; Knight et al., 2023) that inhibits its incorporation as the ion needs to be dehydrated before the incorporation (Marriott et al., 2004; Alvarez et al., 2021).

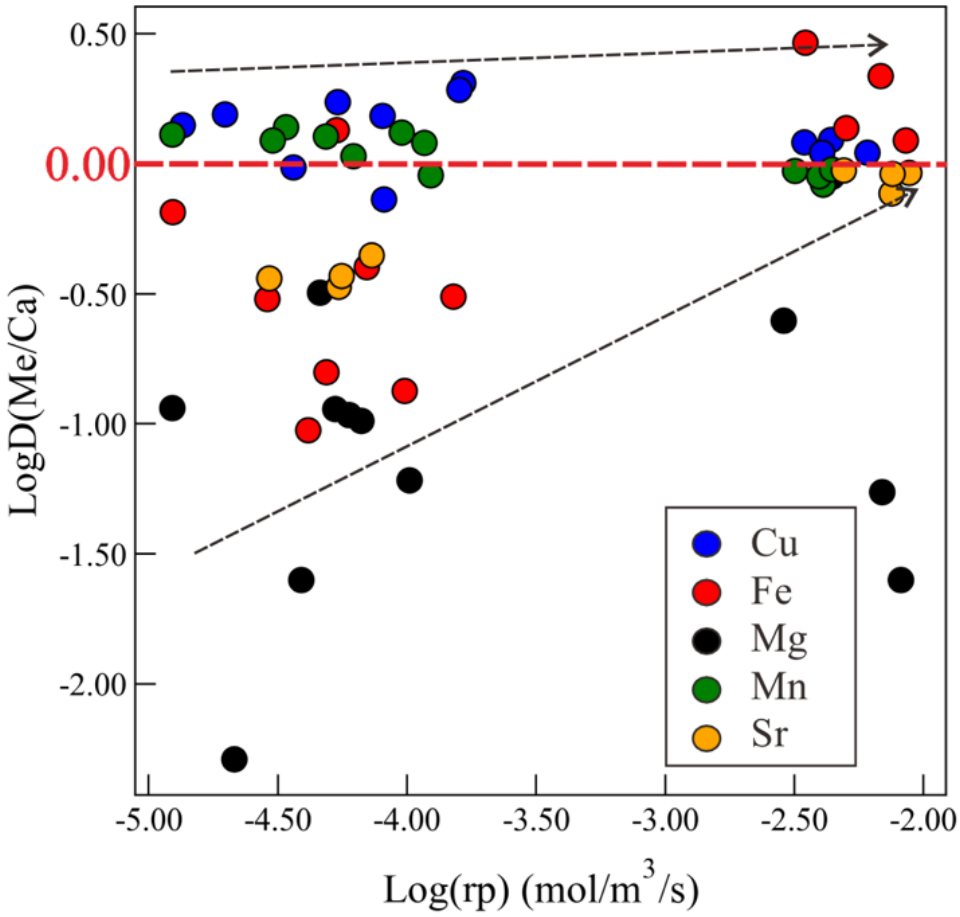


Figure 4.4 Scatter plot showing the dependence of Log D_{Me} on the precipitation rate of the researched elements. Except for the Mg-bearing samples, all the other Log D_{Me} are centralized at nearly 0.00 under the highest precipitation rate.

4.5.2.1 Control of precipitation rates on Fe^{3+} incorporation

Most previous research has primarily focused on the partitioning of divalent ions in $CaCO_3$, leading to a scarcity of literature on trivalent ions partitioning such as Fe^{3+}. Consequently, this study represents the first documentation of a positive correlation between Fe^{3+} incorporation and precipitation rate in $CaCO_3$. Unlike divalent ions, which can readily replace Ca^{2+} in the structure, the incorporation of non-divalent ions can lead to a charge imbalance necessitating compensation by other ions (Voigt et al., 2017; Füger et al., 2019). For instance, Voigt et al. (2017) suggested that the partitioning of trivalent rare earth elements (REE^{3+}) requires the incorporation of Na^{+}, while Busenberg and Niel Plummer (1985) proposed a model in which one Ca^{2+} ion is replaced by two Na^{+} ions. The positive charge imbalance caused by Fe^{3+} partitioning may directly influence Ca^{2+} absorption and impede crystal growth. This influence is observed directly under the microscope: Calcites in the blank group (no dosed trace metal) and exhibit complete rhombohedral shapes (Figure 4.1A and 4.1C) and Fe-bearing calcite precipitated under the P or A method are similar (Figure 4.5A and B), but Fe-bearing calcite synthesized under the T method display large hoppers on the calcite surfaces (Figure 4.5C and D). The presence of hoppers suggests that rapid precipitation increases Fe^{3+} attachment to growing mineral surfaces, the charge imbalance thereby blocking crystal surface active growing sites (kink sites) (Nielsen et al., 2013) and resulting in larger area of defect sites (Busenberg and Niel Plummer, 1985; Teng et al., 2000).

4.5.2.2 Control of precipitation rates on Mn^{2+} incorporation

In contrast to Fe^{3+} partitioning, the incorporation of Mn^{2+} into calcium carbonate has been extensively studied with more available literature data. Log $D_{Mn^{2+}}$ is reported to be negatively correlated with growth rate (Lorens, 1981; Dromgoole and Walter, 1990b), consistent with the findings in this study (Figure 4.3D). Lorens (1981) reported Log $D_{Mn^{2+}}$ decreasing from 1.7 to 0.7 as the growth rate increased from -1.5 to 2.2 nmol/mg/min, while Dromgoole and Walter (1990b) reported Log $D_{Mn^{2+}}$ decreasing from 1.40 to 0.41 as the growth rate increased from -6.903 to -

4.903 mol/m^2/s. Similar trends were observed by Pingitore et al. (1988) and Mills et al. (2022). Compared to the literature range of Log $D_{Mn^{2+}}$ (0.4 to 1.7), the values reported in this study are nearly one order of magnitude lower, ranging from -0.078 to 0.143. This discrepancy may be attributed to differences in experimental setups, as previous studies carefully maintained Mn^{2+} concentration in the solution with an infinite Mn^{2+} supply throughout the precipitation process.

Mn^{2+} partitioning varies with precipitation rate and can also be observed under SEM. Under low precipitation rates (A or P method), the Mn-bearing calcite morphology is dodecahedral and prismatic (Figure 4.5E), while under high precipitation rates Mn-bearing calcite exhibits rhombohedral habit with hoppers (Figure 4.5F) similar to that in Fe^{3+} precipitates (Figure 4.5D). Unlike Fe^{3+}, Mn^{2+} incorporation does not cause charge imbalance but can still block kink sites and impede mineral construction (Nielsen et al., 2013). Our interpretation of the unique morphology-precipitation relation for Mn-bearing calcite is that Mn^{2+} partitioning may preferentially slow down crystal growth rates by dissolution in specific directions, such as edges or corners (Paquette et al., 1996; Zhang and Dawe, 2000). Thus, under low precipitation rates, high Mn^{2+} partitioning results in dodecahedral or prismatic morphologies, while under high precipitation rates, low Mn^{2+} blocking on kink sites leads to the formation of hoppers. This observation gives the insight that trace metals with Log D_{Me} <0 under a relatively low precipitation rate can change the calcite morphology habit by high partitioning whereas under a high precipitation rate calcium carbonate sticks to the rhombohedron for calcite but may cause crystal defects (hoppers) on it.

4.5.3 The role of temperature in trace metal partitioning in $CaCO_3$

The role temperature plays in trace metal partitioning is minor compared to the precipitation rate discussed in section 4.5.2. For every 10 ℃ increase, there is only a 0.15 decrease and 0.001 increase in Log $D_{Fe^{3+}}$ and Log $D_{Mn^{2+}}$, respectively (Eqs (4.1)-(4.2)) which also indicates that the Log $D_{Fe^{3+}}$ variation with temperature is 150 times larger than that of Log $D_{Mn^{2+}}$.

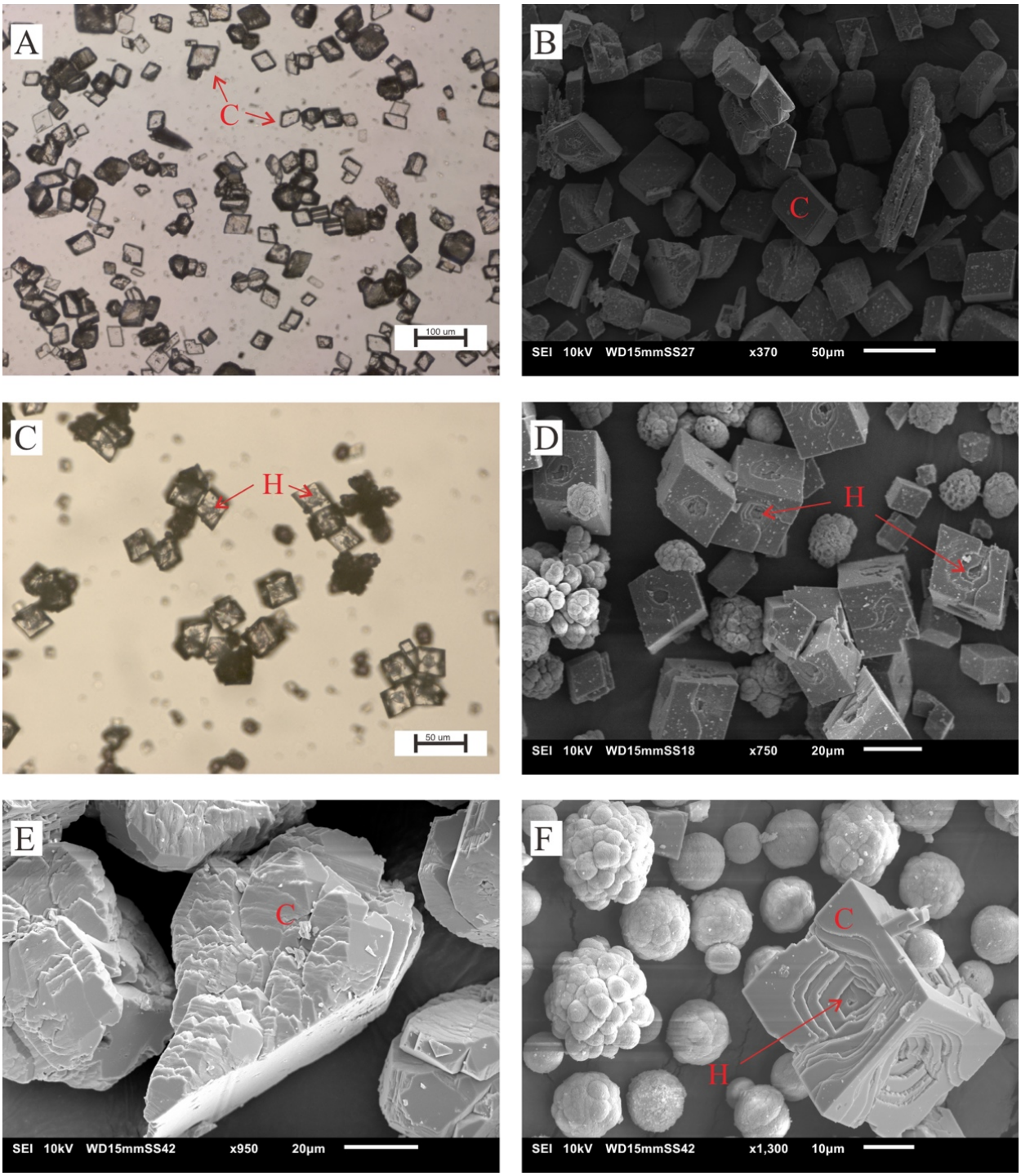


Figure 4.5 Single polarization (-) and SEM photos showing the morphology of calcites (C) under microscopes.

A-B show 50FeA calcites show rhombohedral habit with smooth surfaces. C-D show 25FeT calcites with hoppers (H) on the surfaces. E. 25MnP SEM photo displays the prismatic and scalenohedral calcites. F. 25MnT SEM photo shows the calcites with hoppers (H) on the surfaces.

Given the fact that the maximum differences between the Log $D_{Mn^{2+}}$ at different temperatures but similar precipitation rate is only 0.330 whereas that of Log $D_{Fe^{3+}}$ is 1.713 (Table 3.2 and 4.1), it is apparent that the influence of temperature on Mn^{2+} partitioning is negligible. Though sample 70MnA and 70MnP fall outside the trend between Log $D_{Mn^{2+}}$ and Log (rp) in Figure 4.4D, the direct comparison between Log $D_{Fe^{3+}}$ and Log $D_{Mn^{2+}}$ in Figure 4.6 suggests that and 70MnA and 70MnP are in line with the overall trend. Therefore, under a relatively coarse Log D_{Me} resolution, Mn^{2+} partitioning is a more suitable indicator of precipitation rate rather than temperature, and can be captured by Eqs (4.3):

$$\text{Log } D_{Mn^{2+}} = -0.073 \pm 0.004 \times \text{Log}(r_p) - 0.217 \pm 0.013 \quad (4.3)$$

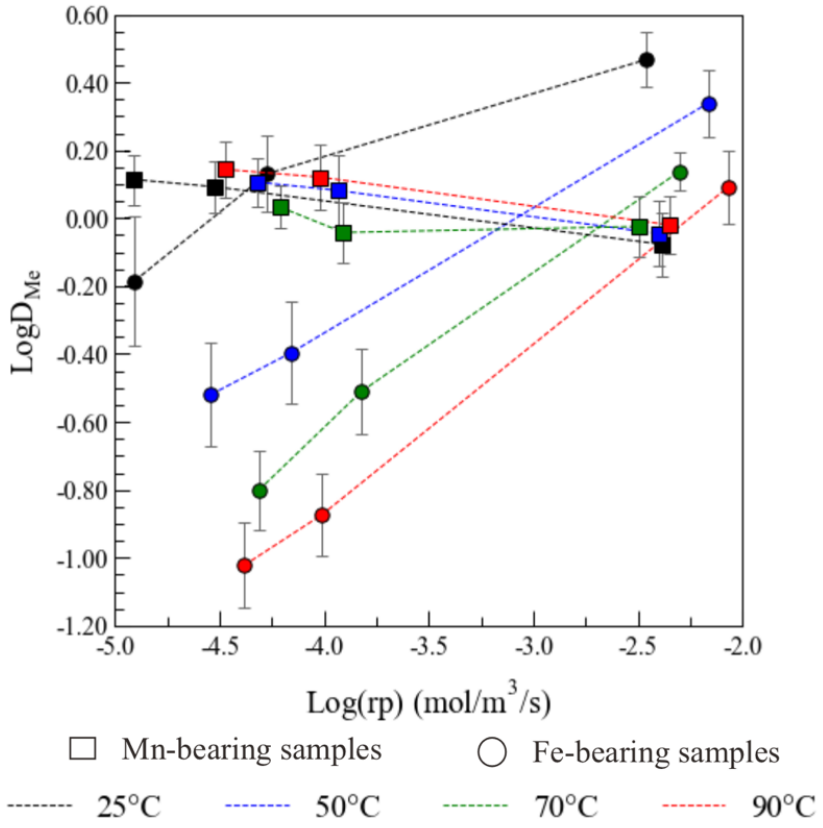


Figure 4.6 Scatter plot showing the comparison between the Log D_{Mn2+} and Log D_{Fe3+} dependence on temperature and precipitation rates.

The Log D_{Me} of Mn^{2+} varies more with precipitation rate than with temperature and can be mathematically expressed as Eqs (4.3).

In contrast to this research, Dromgoole and Walter (1990b) argued that temperature greatly influenced Mn^{2+} incorporation into calcite, with a 10 ℃ increment resulting in a ~ 0.12 decline in Log $D_{Mn^{2+}}$. Since the initial Mn/Ca molar ratio in this study is 0.14, which is one order of magnitude larger than the 0.01 Mn/Ca molar ratio in Dromgoole and Walter (1990b), the differences here are probably attributed to the Mn supply as Dromgoole and Walter (1990b) as discussed in section 4.5.2.

The relationship between temperature and trace metal incorporation has long been attributed to control temperature exercises on the $CaCO_3$ saturation level (Plummer and Busenberg, 1982; Uchikawa and Zeebe, 2012; Wynn et al., 2018). However, the saturation indexes calculated in PHREEQC indicate that the saturation level of polymorphs does not monotonically change with the temperature (Figure 4.7A and B) meaning it cannot explain the monotonic trend between the Log D_{Me} and the temperature in Figure 4.6. In other words, temperature not only influences trace metal partitioning by controlling thermodynamic properties but may also exert direct control. The direct control role was also reported by Mavromatis et al. (2022) for Mg^{2+} partitioning in aragonite, where under similar aragonite saturation index and precipitation rates, Log $Mg^{2+}_{(Aragonite)}$ increased from -4.77 at 25 °C to -4.09 at 5 °C. However, the exact mechanism behind the direct control of temperature requires further research.

4.5.4 Implications for the trace metal incorporation modelling and the use of Me/Ca in field samples

The present results indicate that under the outlined experimental settings, Fe^{3+} and Mn^{2+} partitioning in $CaCO_3$ are directly influenced by precipitation rate and temperature, especially for Fe^{3+}. This is significant as it is the first time a non-polymorph-dependent relationship has been found for precipitation mechanisms mimicking natural CO_2 degassing settings, and both Fe^{3+} and Mn^{2+} are common and important impurity ions for carbonates in natural environments (Millero et

al., 1995; GÖTte and Richter, 2009). Interestingly, Fe^{3+} is the only trivalent ion found in this study but exhibits the greatest sensitivity to both temperature and precipitation rate compared to divalent ions that have long been viewed as important environmental condition indicators, such as Mg^{2+} (Hasiuk and Lohmann, 2010; Evans and Müller, 2012) and Sr^{2+} (Hampt Andreasen and Delaney, 2000; Martin et al., 2000).

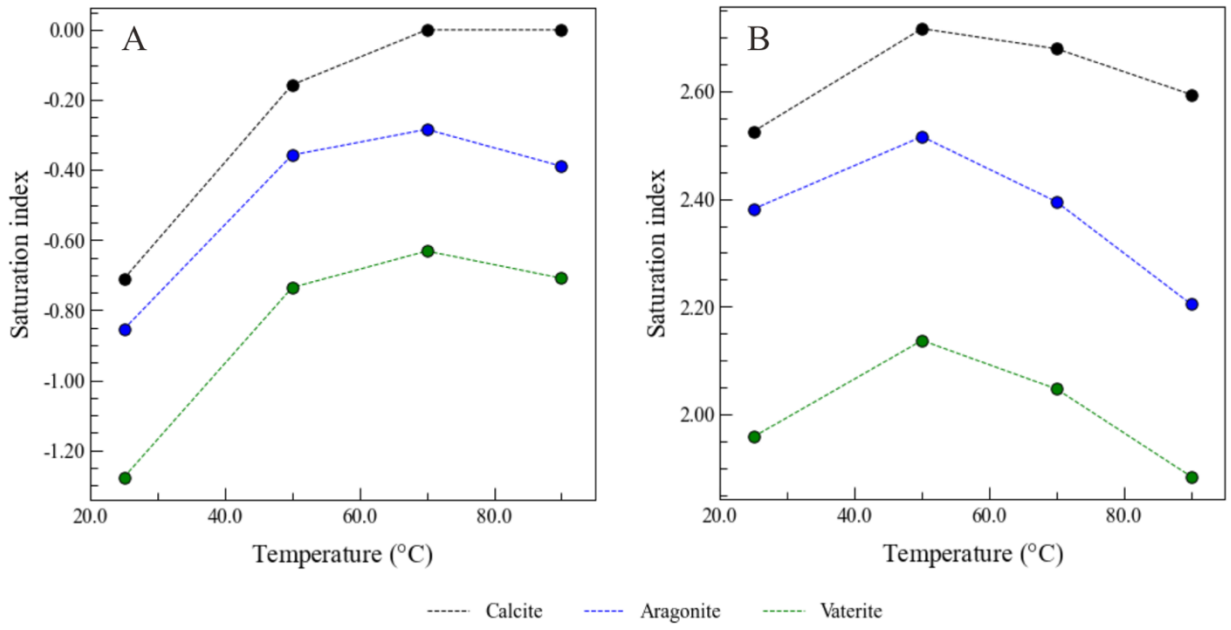


Figure 4.7 Scatter plot showing the saturation index variation with temperature increases for calcite, aragonite, and vaterite.

A. Pre-precipitation and B. End of precipitation. The saturation indexes here are calculated by PHREEQC.

Several trace metal partitioning models have been proposed to describe trace metal incorporation in $CaCO_3$ based on ideal solid-solution interactions and the ideal replacement of Ca^{2+} by divalent ions (Watson, 2004; DePaolo, 2011) such as that shown for Ba, Co, Mg, and Zn partitioning (Reeder et al., 1999; Finch and Allison, 2007). However, the model may be restricted by the complex polymorph structure of carbonates (Böttcher, 1997). The present study indicates that Fe^{3+} partitioning as a non-ideal replacement trace metal might be less affected by crystal structure and more influenced by environmental conditions which may be a route for future model research.

Though the results here are promising, the relations observed (Eqs (3)-(5)) need to be handled carefully and may not be directly applicable to natural samples for two reasons:

(1) The present study performed precipitation in deionised water without other competing ions that may influence the mechanisms observed here (Mucci, 1988; Zuddas and Mucci, 1998). For example, the presence of anions such as chloride would enhance Mn^{2+} and Zn^{2+} incorporation (Temmam et al., 2000) and the SO_4^{2-} influence the Mg^{2+} coprecipitation (Bots et al., 2011).

(2) The calculation of Log D_{Me} requires knowledge of the parent fluid composition, which is impossible to obtain for natural samples (Dromgoole and Walter, 1990b).

Therefore, the use of Me/Ca ratios is more useful for applications on field samples and has been employed extensively, such as Mg/Ca or Sr/Ca in foraminifer (Lear et al., 2000; Martin et al., 2000; Elderfield et al., 2002) and Sr/Ca in deep-sea sediments (Hampt Andreasen and Delaney, 2000). Interestingly, both Fe/Ca and Mn/Ca display a good relation with temperature and precipitation rate (Figure 4.8). Fe/Ca increases as precipitation rates increase and may also increase as temperature decreases (Figure 4.8A), whereas the Mn/Ca exhibits the opposite trend (Figure 4.8B). However, deriving a mathematical equation to describe this relationship is challenging due to its nonlinearity and the limited size of our dataset. It would be fruitful for future work to precisely describe the relationship in Figure 4.8, as it may apply to field samples to calculate paleo-precipitation rates, with temperature determined using carbonate-clumped isotopes (Anderson et al., 2021) but beyond the scope of this work.

4.6 Conclusions

The synthesis of calcium carbonate ($CaCO_3$) in this study was accomplished through CO_2 stripping. Results reveal that among the five investigated elements – Cu^{2+}, Fe^{2+}, Mg^{2+}, Mn^{2+}, Sr^{2+} – the incorporation of Fe^{3+} and Mn^{2+} are the most influenced by the average precipitation rate and temperature, showing independence from $CaCO_3$ polymorph. Log $D_{Fe^{3+}}$ increases with rising

precipitation rates but decreases with increasing temperature, whereas Log $D_{Mn^{2+}}$ exhibits the opposite trend. The precipitation rate emerges as the primary control on trace metal incorporation, overshadowing temperature, particularly for Mn^{2+} incorporation.

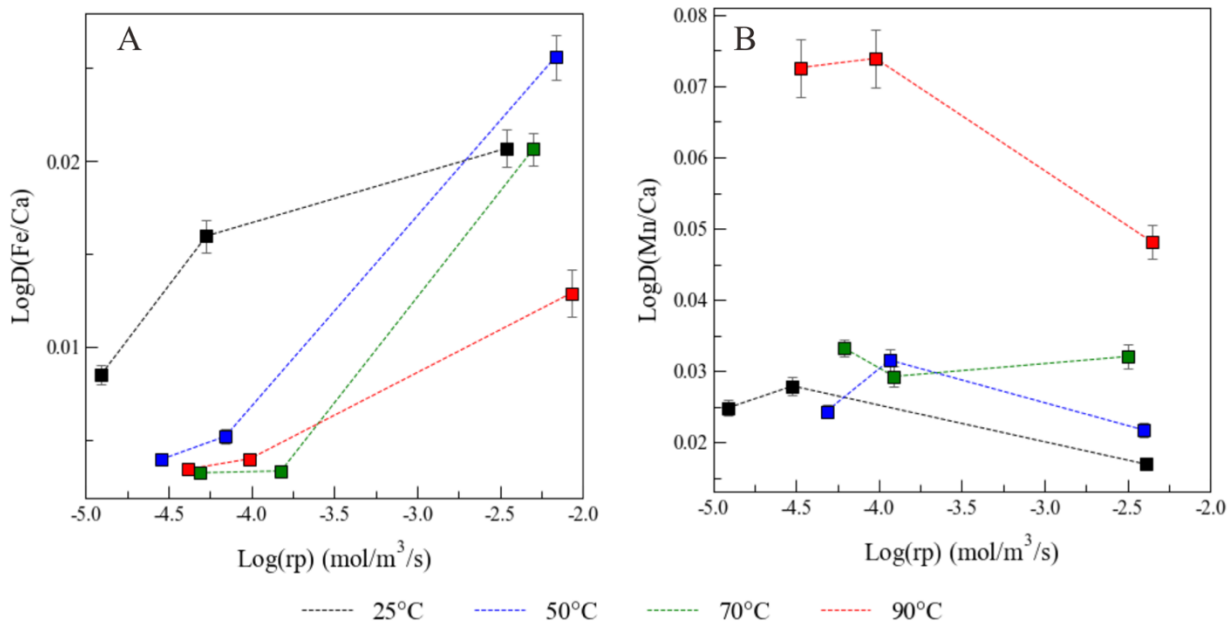


Figure 4.8. Scatter plot showing the Fe/Ca (A) and Mn/Ca (B) variation with temperature and precipitation rates.

Furthermore, the non-ideal substitution of Fe^{3+} seems to capture environmental variations better than the divalent ions offering a novel insight in trace metal partitioning model research. Although the findings hold promising applications, caution must be exercised in interpreting the observed relationships and considering the complexities of real-world scenarios. Therefore, the utilization of trace metal to calcium ratios (Fe/Ca and Mn/Ca) in field samples may prove more effective, potentially enabling the inference of ancient precipitation rates and thereby enhancing our understanding of geochemical processes.

Chapter 5

Evaluating kinetic effects in carbonate clumped isotopes (Δ_{47}) under controlled laboratory environments and first laboratory calibration to cryogenic temperatures

5.1 Abstract

Clumped isotopes (Δ_{47}) paleothermometry is a paleotemperature proxy developed two decades ago that was proven to be effective due to its independence from the parent fluid isotopic composition and the well-established correlation with temperature. However, the potential offsets in Δ_{47} caused by kinetic effects—such as changes in pH, precipitation rate, cation impurities, and calcium carbonate polymorphism—are documented but remain poorly constrained both in field and laboratory settings. To address these gaps, we conducted a systematic experiment synthesizing calcium carbonate under controlled laboratory conditions, varying temperatures from 25 to 90°C, ranging pH from 7.0 to 9.1, precipitation rates from -5.00 to -1.95 mol/m^3/s, and incorporating cation impurities (Cu^{2+}, Mg^{2+}, Mn^{2+}, Fe^{3+}, and Sr^{2+}). Besides, this study presents the first feasible method for synthesizing cryogenic $CaCO_3$ under isotopic equilibrium conditions and offers three cryogenic (< 0°C) samples. We combined our new samples with previous lab precipitates, yielding a total of 75 samples covering the temperature range from -24 to 250°C. Our results indicate that,

within the examined range, pH, precipitation rates, cation impurities, and $CaCO_3$ polymorphism do not individually cause significant Δ_{47} offsets, suggesting that any potential kinetic effects are either negligible or below the instrumental detection limit. However, we observed ~ 0.043‰ Δ_{47} offsets in samples precipitated under a complex condition—specifically, environments that combine a high volume of OH^-, the presence of cation impurities, and rapid precipitation. We interpret these offsets as resulting from a shift in the crystal growth mechanism, from stable cluster aggregation to ion-by-ion attachment, due to enhanced cation impurity dehydration under high OH^- concentrations and rapid precipitation. These findings provide valuable constraints for applying clumped isotope thermometry to natural samples (e.g. corals and travertine), which often precipitate under relatively high pH with cation impurities. Using the data deemed precipitated at equilibrium condition, we yield a Δ_{47}-T calibration across a temperature range of -15 to 250°C:

$$\Delta_{47} = 0.0386 \pm 0.0006 \times \frac{10^6}{T^2} + 0.1587 \pm 0.0055 \quad (R^2 = 0.988)$$

where T is the precipitation temperature in Kelvin (K). The reported Δ_{47}-T calibration exhibits no statistical difference from the current community calibration, but successfully extends the temperature range to the cryogenic area.

5.2 Introduction

Conventional $\delta^{18}O$ thermometry has been a foundational tool for carbonate-related research for over 70 years (Huntington and Petersen, 2023). However, its application is limited by uncertainties in evaluating the parent fluid $\delta^{18}O$ value and difficulties in identifying and quantifying kinetic effects caused by environmental parameters such as pH, precipitation rate, and fluid composition (Kim and O'Neil, 1997; Adkins et al., 2003; Kim et al., 2006; Dietzel et al., 2009). In the past two decades, Δ_{47} thermometry has emerged as a new method to extract environmental information from carbonates by examining the abundance of heavier clumped isotopologues (such as the measurement of ^{13}C-^{18}O denoted as Δ_{47}) relative to their stochastic

distribution. Unlike $\delta^{18}O$ thermometry, which relies on the heterogeneous equilibrium between carbonates and fluids (Urey, 1947), Δ_{47} thermometry is based on the homogeneous equilibrium among carbonate ions (Eiler, 2006; Eiler, 2007). This allows for the determination of carbonate formation temperature without prior knowledge of the parent fluid $\delta^{18}O$ value. Furthermore, combining Δ_{47} thermometry with conventional $\delta^{18}O$ thermometry enables back-calculation of the parent fluid $\delta^{18}O$, making Δ_{47} thermometry a superior tool for carbonate-related research.

Despite its advantages, Δ_{47} thermometry may also be affected by kinetic effects, though less is understood about these impacts compared to $\delta^{18}O$ thermometry. Quantifying and constraining kinetic effects is crucial, as most carbonates precipitate under kinetic conditions (Daëron et al., 2019). In laboratory carbonate synthetic precipitation, various research gives the Δ_{47}-temerpature (Δ_{47}-T) relationship in a wide temperature range from 0.5 to 1100℃ with merely 0.002‰ variances among different calibrations (Kluge et al., 2015; Kelson et al., 2017; Anderson et al., 2021; Fiebig et al., 2021). Previous research examined a range of pH, precipitation rate, and cation impurities suggesting kinetic effects causing negligible offsets in Δ_{47} (Tang et al., 2014; Kluge and John, 2015a). However, the *ab-initio* model work of Hill et al. (2014) and laboratory experiments such as Kluge and John (2015a) and Tripati et al. (2015) indicate that brine chemistry including pH and concentrated divalent ions can lead to observable Δ_{47} offsets. For natural samples, while many modern carbonate deposits show Δ_{47} values close to the laboratory Δ_{47}-T calibration (Ghosh et al., 2006; Tripati et al., 2010; Eiler, 2011; Grauel et al., 2013), natural carbonates are deviating from the Δ_{47}-T calibration by up to 0.1‰ on Δ_{47} (Tripati et al., 2015). Exemplary, the biologically driven kinetic effects, referred to as 'vital effects', were variously observed in bio-carbonates including both warm and cold water corals (Thiagarajan et al., 2011; Saenger et al., 2012; Spooner et al., 2016), cephalopods (Dennis et al., 2013; Davies et al., 2021), echinoderms (Davies and John, 2017, 2019), and brachiopods (Henkes et al., 2013; Bajnai et al., 2020). The high pH may cause significant kinetic effects in natural travertine sediments as demonstrated by Falk et al. (2016) and Holdsworth et al. (2022). Furthermore, the impact of polymorphism on Δ_{47}

is also debated. Theoretical studies suggest significant Δ_{47} offsets due to $CaCO_3$ polymorphism (Schauble et al., 2006; Guo et al., 2009), while lab research argues that Δ_{47} is largely determined by dissolved inorganic carbon (DIC) with minimal influence from the mineral structure (Fernandez et al., 2014; Kluge and John, 2015a; Anderson et al., 2021). Therefore, kinetic effects on Δ_{47} are variously reported and debated but lack a solid laboratory experiment examining the potential of different causes.

Another research gap is the feasibility of calibrating Δ_{47} to cryogenic temperatures (< 0℃). The current Δ_{47}-T calibration temperature ends with the lowest temperature of 0.5℃ (Anderson et al., 2021), which is sufficient for most carbonate deposits but inadequate for polar or cryogenic cave systems (Žák et al., 2013; Uwakwe et al., 2023). Previous studies successfully obtained cryogenic $CaCO_3$ precipitation down to -2℃ by freezing the $Ca(HCO_3)_2$ solution (Killawee et al., 1998; Uwakwe et al., 2023). However, this method involves large uncertainties in precipitation temperature and is probably out of isotopic equilibrium during the precipitation, so is not a valid approach to extrapolate the Δ_{47}-T calibration. A new cryogenic carbonate precipitation method needs to be established.

Here, we created a collection of lab precipitates for Δ_{47} analyses. Our strategy is to synthesise carbonates under a controlled laboratory environment with a wide range of parameters including temperature (-24 to 90℃), pH (7.0 to 9.1), precipitation rate (-5.00 to -1.95 $mol/m^3/s$), with or without cation impurities (Cu^{2+}, Mg^{2+}, Mn^{2+}, Fe^{3+}, and Sr^{2+}). The new precipitate is then analysed with existing precipitates (Kluge et al. (2015) , 25-250℃) for potential causes of kinetic effects on Δ_{47} and the deemed equilibrium precipitates were anchored to derive a Δ_{47}-T calibration covering cryogenic temperatures.

5.3 Methods and materials

In the current chapter, all three different samples XC2024 (a total of 68), CS2024 (a total of 4), and TK2015 (a total of 11) are characterized for both bulk (carbon and oxygen) and clumped isotope composition (Chapter 2 section 2.1.3). In XC2024, sample 70MgA and sample 90MgA are highly contaminated with isotope results showing $\Delta 48_{offset}$ and 49_{param} >70, so were not discussed here. The detailed sample preparation procedure (Chapter 2 section 2.2) can be found in Chapter 2. The sample IDs here are correlated to previous tables in Chapters 2, 3, and 4. The mineralogy and morphology characterization, and precipitation rate calculation of XC2024 are described in detail in Chapter 3 but will be briefly reviewed here. Similarly, the distribution coefficient of XC2024 was described in detail in Chapter 4 (section 4.4.3).

5.4 Results

5.4.1 Mineral description and ICP-MS results

XC2024 consists of 66 samples and the XRD results were published as a dataset in Cao (2024). XRD analyses confirmed that all precipitates were $CaCO_3$, including three polymorphs: calcite, aragonite, and vaterite. Most samples are composed of two polymorphs with calcite and aragonite prevailing at 25℃ and > 25℃, respectively, accounting for up to 100% (Chapter 3, Table 3.2 and Figure 3.5). Vaterite generally appears as a minor component but is widely found in NaOH titration experiments under 25℃ and can even emerge as the primary component such as in sample 25MnT(53%) and 25SrT (75%) (Chapter 3, Table 3.2 and Figure 3.5). In comparison, CS20204 consists of 3 samples which are 100% composed of calcite and TK2015 contains 9 samples with various proportions of calcite and aragonite (Kluge et al., 2015). SEM observation also confirms that the XC2024 were $CaCO_3$ and the morphology characterization varies with the precipitation method (Figure 5.1). In CO_2 degassing experiments, calcite shows rhombohedral, prismatic, or dodecahedron habits, aragonite shows acicular habits (Figure 5.1A), and vaterite exhibits spherical

or laminar habits. The calcite and aragonite morphologies display defects under NaOH Titration experiments with added salts: hoppers on the calcite surfaces and rounded and curled aragonite surfaces (Figure 5.1B).

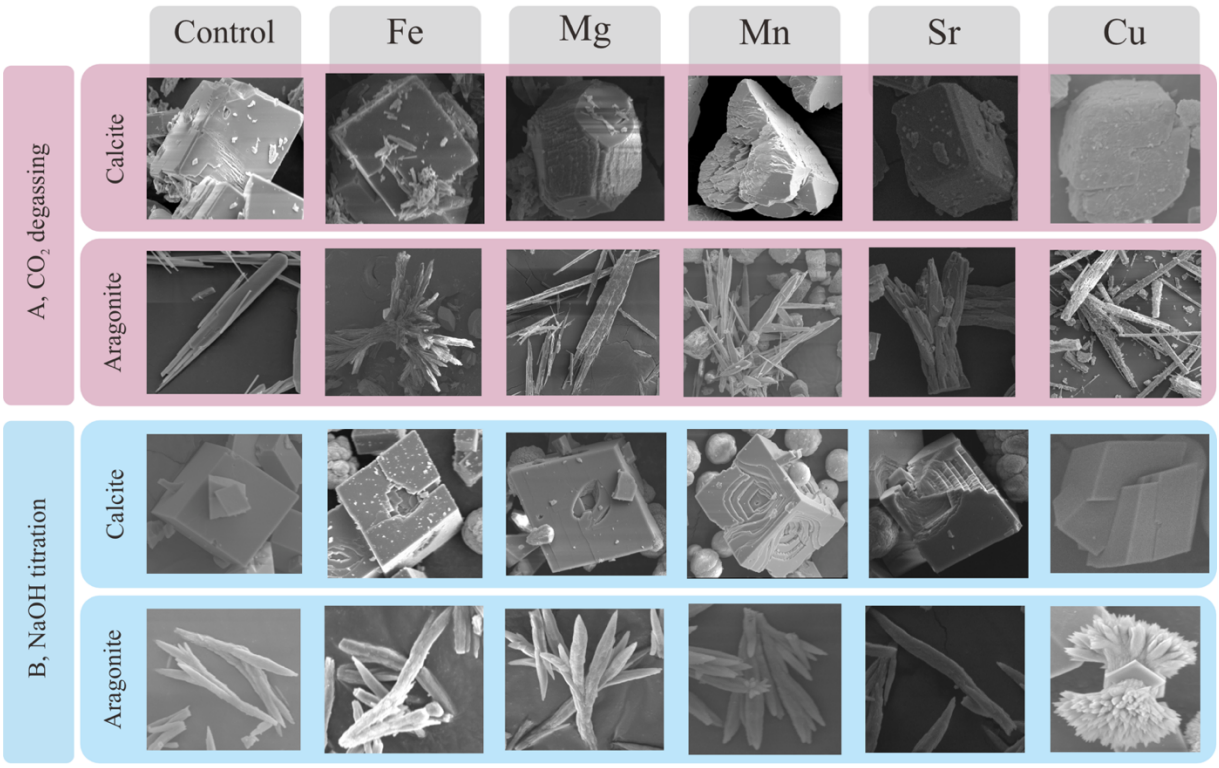


Figure 5.1 Scanning electron microscope (SEM) photos show the morphology characterization of calcites and aragonite precipitated in this study.

A. SEM photos of CO_2 degassing experiments, calcites are in rhombohedral, prismatic, or dodecahedron habits, and aragonites are in acicular habits. B SEM photos of NaOH titration experiments, calcites are in rhombohedral habits but in cation impurities-added experiments are with defects e.g. hoppers on the surfaces or nested together, and aragonites exhibit curled surfaces.

The averaged precipitation temperature, pH, and precipitation rate (Log (rp)) were calculated based on the obtained ICP-MS results of sampled solutions (Chapter 4, Table 4.1, see Chapter 2 for calculation details). The fluid temperature during the precipitation was stable with an average error of ≤ 0.3°C. The average pH of CO_2 degassing experiments ranges from 7.0 to 7.9, consistent with the log results of Kluge and John (2015a). However, the pH of NaOH titration experiments ranges from 7.2 to 9.1 due to the NaOH titration. The Log (rp) varies from -5.00 to -

4.28, -4.27 to -3.78, and -2.68 to -1.95 mol/m^3/s for passive degassing, active degassing, and NaOH titration methods respectively (Chapter 3, Table 3.2).

The Log $D_{Me/Ca}$ of the samples varies with the element and ranges from -1.601 to 0.311. The Log $D_{Fe/Ca}$, Log $D_{Mn/Ca}$, and Log $D_{Sr/Ca}$ are strongly correlated with the temperature and the Log (rp) whereas the Log $D_{Cu/Ca}$ and Log $D_{Mg/Ca}$ aren't (Chapter 4, Figure 4.3) indicating that the Fe^{3+}, Mn^{2+}, and Sr^{2+} are direct indicators of calcium carbonate precipitation rate and the Fe^{3+} uptake increase as the precipitation increases whereas the Mn^{2+} and the Sr^{2+} exhibit the opposite trend. The observed trend of Fe^{3+}, Mn^{2+}, and Sr^{2+} is analogous to the results of Lorens (1981) and Dromgoole and Walter (1990b).

5.4.2 Carbon and oxygen isotopic composition

Table 5.1 and Figure 5.2 show that the bulk isotope composition ($\delta^{13}C_{VPDB}$ and $\delta^{18}O_{VPDB}$) of samples is highly dependent on the precipitation method which is expected as the different precipitation methods used different chemicals with varying bulk isotope compositions. $\delta^{13}C_{VPDB}$ varying from -37.47 ± 0.31‰ to 2.07 ± 0.03‰ and the $\delta^{18}O_{VPDB}$ varies from -28.19 ± 0.15‰ to -6.50 ± 0.03‰. Furthermore, $\delta^{13}C_{VPDB}$ and $\delta^{18}O_{VPDB}$ of all samples negatively correlate with the temperature, consistent with previous research (Romanek et al., 1992; Kim and O'Neil, 1997).

Table 5.1 Isotopic composition and distribution coefficient of synthetic calcium carbonates in the laboratory. '-' indicates no measured data. The $\delta^{13}C_{VPDB}$, $\delta^{18}O_{VPDB}$, and $\delta^{18}O_{Fulid}$ are reported with 1SD whereas the Δ_{47} is reported with 1SE.

ID	$\delta^{13}C_{VPDB}$	$\delta^{18}O_{VPDB}$	Δ_{47}	$\delta^{18}O_{Fluid}$
XC2024				
25ControlP	-16.04 ± 0.08	-12.37 ± 0.05	0.592 ± 0.023	-10.0 ± 0.0
50ControlP	-25.47 ± 0.21	-13.48 ± 0.04	0.524 ± 0.004	-6.5 ± 0.0
70ControlP	-30.65 ± 0.15	-15.61 ± 0.08	0.493 ± 0.009	-5.3 ± 0.1
90ControlP	-34.49 ± 0.11	-16.81 ± 0.02	0.445 ± 0.007	-3.7 ± 0.0

ID	$\delta^{13}C_{VPDB}$	$\delta^{18}O_{VPDB}$	Δ_{47}	$\delta^{18}O_{Fluid}$
25CuP	-19.70 ± 0.38	-7.38 ± 0.25	0.586 ± 0.007	-5.0 ± 0.3
50CuP	-24.96 ± 0.31	-12.04 ± 0.18	0.518 ± 0.009	-5.0 ± 0.2
70CuP	-29.46 ± 0.24	-14.90 ± 0.15	0.481 ± 0.012	-4.6 ± 0.2
90CuP	-32.81 ± 0.16	-15.62 ± 0.03	0.455 ± 0.012	-2.5 ± 0.0
25FeP	-17.06 ± 0.18	-8.84 ± 0.05	0.593 ± 0.013	-6.4 ± 0.0
50FeP	-27.45 ± 0.11	-14.29 ± 0.16	0.534 ± 0.006	-7.3 ± 0.2
70FeP	-29.56 ± 0.13	-16.74 ± 0.16	0.499 ± 0.016	-6.5 ± 0.2
90FeP	-33.37 ± 0.31	-16.47 ± 0.24	0.458 ± 0.022	-3.3 ± 0.2
25MgP	-17.03 ± 0.08	-11.42 ± 0.16	0.593 ± 0.016	-9.0 ± 0.2
50MgP	-26.67 ± 1.09	-13.03 ± 0.38	0.539 ± 0.014	-6.0 ± 0.4
70MgP	-29.19 ± 0.42	-15.73 ± 0.15	0.503 ± 0.019	-5.4 ± 0.1
90MgP	-33.21 ± 0.50	-16.36 ± 0.14	0.469 ± 0.018	-3.2 ± 0.1
25MnP	-22.52 ± 0.05	-10.28 ± 0.19	0.595 ± 0.009	-7.9 ± 0.2
50MnP	-26.74 ± 0.18	-13.40 ± 0.04	0.521 ± 0.004	-6.4 ± 0.0
70MnP	-30.78 ± 0.16	-17.03 ± 0.07	0.497 ± 0.011	-6.8 ± 0.1
90MnP	-34.45 ± 0.22	-17.18 ± 0.20	0.463 ± 0.005	-4.0 ± 0.2
25ControlA	-10.94 ± 0.11	-12.71 ± 0.17	0.589 ± 0.010	-10.3 ± 0.2
50ControlA	-20.46 ± 0.11	-12.48 ± 0.11	0.534 ± 0.015	-5.6 ± 0.1
70ControlA	-28.70 ± 0.32	-15.11 ± 0.22	0.481 ± 0.022	-5.1 ± 0.2
90ControlA	-30.54 ± 0.40	-15.99 ± 0.25	0.457 ± 0.023	-3.3 ± 0.2
25CuA	-15.10 ± 0.48	-7.96 ± 0.28	0.591 ± 0.012	-5.5 ± 0.3
50CuA	-21.94 ± 0.14	-13.34 ± 0.16	0.519 ± 0.029	-6.2 ± 0.2
70CuA	-23.86 ± 0.08	-15.70 ± 0.15	0.479 ± 0.011	-5.4 ± 0.2
90CuA	-30.51 ± 0.41	-16.96 ± 0.30	0.459 ± 0.014	-4.3 ± 0.3

ID	$\delta^{13}C_{VPDB}$	$\delta^{18}O_{VPDB}$	Δ_{47}	$\delta^{18}O_{Fluid}$
25FeA	-24.50 ± 0.14	-11.73 ± 0.20	0.601 ± 0.018	-9.3 ± 0.2
50FeA	-27.92 ± 0.19	-13.15 ± 0.16	0.526 ± 0.024	-6.2 ± 0.2
70FeA	-30.07 ± 0.25	-15.40 ± 0.14	0.496 ± 0.016	-5.4 ± 0.1
90FeA	-31.94 ± 0.20	-17.35 ± 0.14	0.446 ± 0.011	-4.7 ± 0.1
25MgA	-14.48 ± 0.14	-11.62 ± 0.19	0.590 ± 0.008	-9.2 ± 0.2
50MgA	-21.70 ± 0.19	-12.84 ± 0.09	0.516 ± 0.019	-5.7 ± 0.1
25MnA	-25.07 ± 0.22	-11.08 ± 0.13	0.586 ± 0.003	-8.7 ± 0.1
50MnA	-28.15 ± 0.26	-12.47 ± 0.13	0.525 ± 0.006	-5.6 ± 0.1
70MnA	-28.97 ± 0.22	-14.71 ± 0.07	0.481 ± 0.029	-4.7 ± 0.1
90MnA	-31.18 ± 0.35	-18.06 ± 0.35	0.452 ± 0.012	-5.4 ± 0.4
25SrA	-23.18 ± 0.23	-10.52 ± 0.38	0.583 ± 0.007	-8.1 ± 0.4
50SrA	-27.31 ± 0.08	-16.72 ± 0.13	0.542 ± 0.006	-9.8 ± 0.1
70SrA	-30.67 ± 0.23	-15.87 ± 0.16	0.496 ± 0.005	-5.9 ± 0.2
90SrA	-32.33 ± 0.18	-16.29 ± 0.13	0.456 ± 0.008	-3.7 ± 0.1
25ControlT	-35.02 ± 0.16	-13.56 ± 0.28	0.593 ± 0.018	-11.1 ± 0.3
50ControlT	-36.03 ± 0.31	-14.59 ± 0.05	0.519 ± 0.009	-7.7 ± 0.1
70ControlT	-35.83 ± 0.37	-15.44 ± 0.07	0.491 ± 0.005	-5.6 ± 0.1
90ControlT	-35.99 ± 0.22	-15.58 ± 0.11	0.451 ± 0.007	-3.2 ± 0.1
25CuT	-36.94 ± 0.11	-16.56 ± 0.30	0.663 ± 0.006	-14.2 ± 0.3
50CuT	-35.75 ± 0.61	-15.90 ± 0.25	0.594 ± 0.019	-9.1 ± 0.3
70CuT	-35.91 ± 0.28	-16.18 ± 0.18	0.549 ± 0.011	-6.5 ± 0.2
90CuT	-36.40 ± 0.44	-15.92 ± 0.05	0.540 ± 0.008	-3.7 ± 0.0
25FeT	-37.19 ± 0.26	-16.16 ± 0.11	0.644 ± 0.009	-13.7 ± 0.1
50FeT	-35.13 ± 0.30	-14.60 ± 0.20	0.564 ± 0.023	-7.8 ± 0.2

ID	$\delta^{13}C_{VPDB}$	$\delta^{18}O_{VPDB}$	Δ_{47}	$\delta^{18}O_{Fluid}$
70FeT	-36.38 ± 0.14	-15.75 ± 0.10	0.536 ± 0.011	-6.1 ± 0.1
90FeT	-37.42 ± 0.16	-15.82 ± 0.09	0.490 ± 0.011	-3.7 ± 0.1
25MgT	-36.15 ± 0.34	-16.25 ± 0.24	0.629 ± 0.019	-13.8 ± 0.2
50MgT	-36.83 ± 0.15	-16.76 ± 0.26	0.569 ± 0.012	-10.0 ± 0.3
70MgT	-36.07 ± 0.14	-16.47 ± 0.14	0.550 ± 0.024	-6.6 ± 0.1
90MgT	-37.12 ± 0.05	-17.08 ± 0.15	0.513 ± 0.013	-5.0 ± 0.2
25MnT	-35.66 ± 1.30	-12.94 ± 0.45	0.668 ± 0.006	-10.5 ± 0.4
50MnT	-35.75 ± 0.61	-15.18 ± 0.10	0.598 ± 0.002	-8.3 ± 0.1
70MnT	-36.03 ± 0.16	-16.26 ± 0.63	0.553 ± 0.004	-6.5 ± 0.6
90MnT	-36.44 ± 0.23	-15.67 ± 0.06	0.518 ± 0.010	-3.5 ± 0.1
25SrT	-35.44 ± 0.30	-13.78 ± 0.16	0.655 ± 0.011	-11.3 ± 0.2
50SrT	-34.98 ± 0.28	-14.99 ± 0.33	0.603 ± 0.022	-8.1 ± 0.3
70SrT	-36.61 ± 0.37	-15.81 ± 0.28	0.531 ± 0.012	-6.0 ± 0.3
90SrT	-37.47 ± 0.31	-16.62 ± 0.11	0.478 ± 0.004	-4.5 ± 0.1
CS2024				
-10ControlCS	-34.99 ± 0.20	-19.99 ± 0.09	0.714 ± 0.031	-25.5 ± 0.1
-15ControlCS	-33.33 ± 0.09	-18.85 ± 0.04	0.735 ± 0.008	-25.7 ± 0.0
-24ControlCS	-26.89 ± 0.26	0.30 ± 0.11	0.820 ± 0.011	-9.2 ± 0.1
TK2015				
No-1	-28.25 ± 0.06	-13.86 ± 0.05	0.542 ± 0.014	-6.9 ± 0.1
No-2	-23.25 ± 0.21	-16.54 ± 0.07	0.476 ± 0.015	-6.3 ± 0.1
No-3	-26.22 ± 0.19	-17.27 ± 0.04	0.471 ± 0.014	-5.6 ± 0.1
No-4	-31.05 ± 0.18	-19.81 ± 0.25	0.457 ± 0.019	-6.6 ± 0.2
HT-1	2.07 ± 0.03	-6.50 ± 0.03	0.601 ± 0.003	-4.1 ± 0.2

ID	$\delta^{13}C_{VPDB}$	$\delta^{18}O_{VPDB}$	Δ_{47}	$\delta^{18}O_{Fluid}$
HT-2	-1.45 ± 0.03	-21.11 ± 0.09	0.399 ± 0.018	-3.7 ± 0.2
HT-3	-1.97 ± 0.03	-21.04 ± 0.12	0.375 ± 0.014	-3.7 ± 0.2
HT-4	-2.29 ± 0.07	-21.27 ± 0.09	0.352 ± 0.010	1.1 ± 0.1
HT-5	-2.76 ± 0.04	-28.19 ± 0.15	0.295 ± 0.014	-0.2 ± 0.2

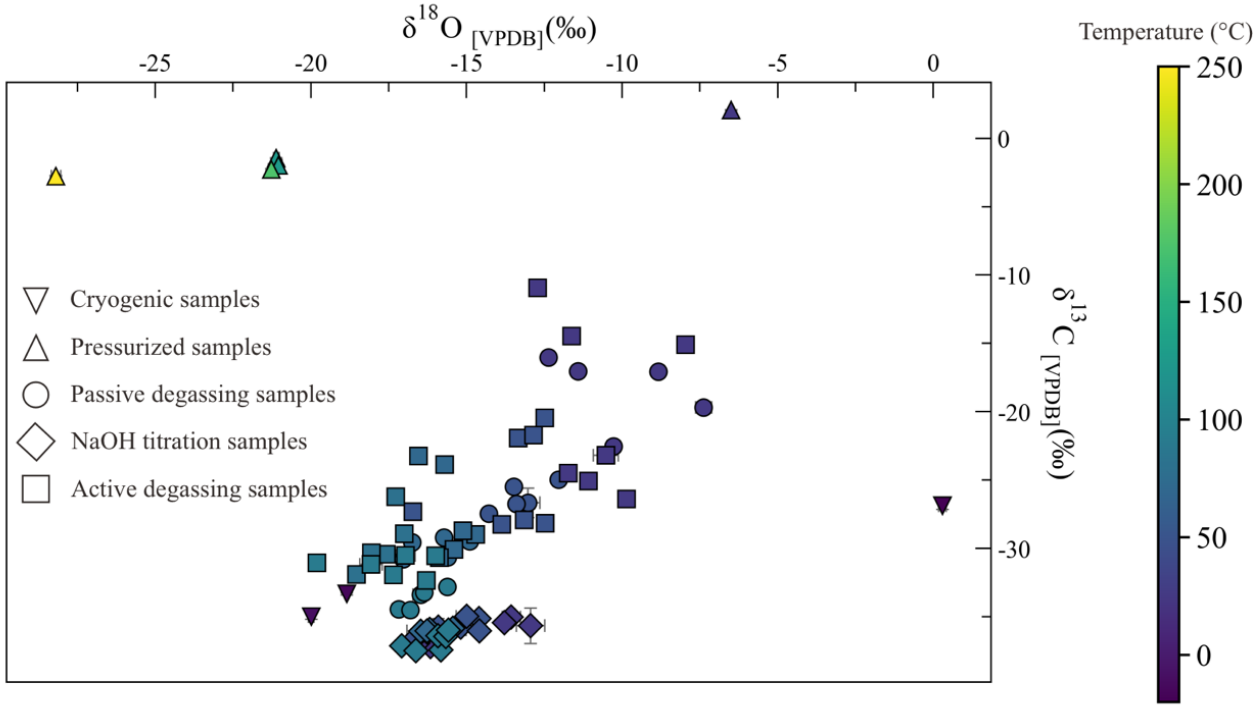


Figure 5.2 Scatter plot shows the bulk isotope composition of the samples in this study.

The shape indicates different sample types and the colour represents precipitation temperature. The bulk isotope composition is highly dependent on the precipitation method and within each method, the bulk composition value increases as the temperature decreases.

The Δ_{47} of samples vary between 0.295 ± 0.014‰ (1 SE) and 0.820 ± 0.011‰ (1 SE), covering a wide range of precipitation temperatures from -24 to 250℃ (Table 5.1). Statistically, the CO_2 degassing (both passive and active) of XC2024, CS2024 and TK2015 exhibit slight deviations from the Δ_{47}-T, with most samples falling into a 95 % confidence interval with an R^2 of 0.985 (Figure 5.3A). This confirms the viability of the Anderson et al. (2021) calibration. For these three kinds of samples, repeated experiments at the same temperature but with different Log (rp) and cation impurities led to an average offset of merely 0.002‰ from the calibration curve (Figure 5.3B). These results validate the data reproducibility of the instrument and indicate no measurable offsets on Δ_{47}, or alternatively, these offsets may be compensated. Contrary to the other samples, the NaOH titration samples of XC2024 exhibit a significant shift from the Δ_{47}-T calibration with an R^2 of 0.806 (Figure 5.3A), and the averaged offset from the calibration curve reaches 0.043‰ (Figure 5.3B), which is much larger than the 95% confidence interval of the Δ_{47}-T calibration. This indicates that the kinetic effects or polymorphism influences exist and cause the excessive clumping of ^{13}C –^{18}O.

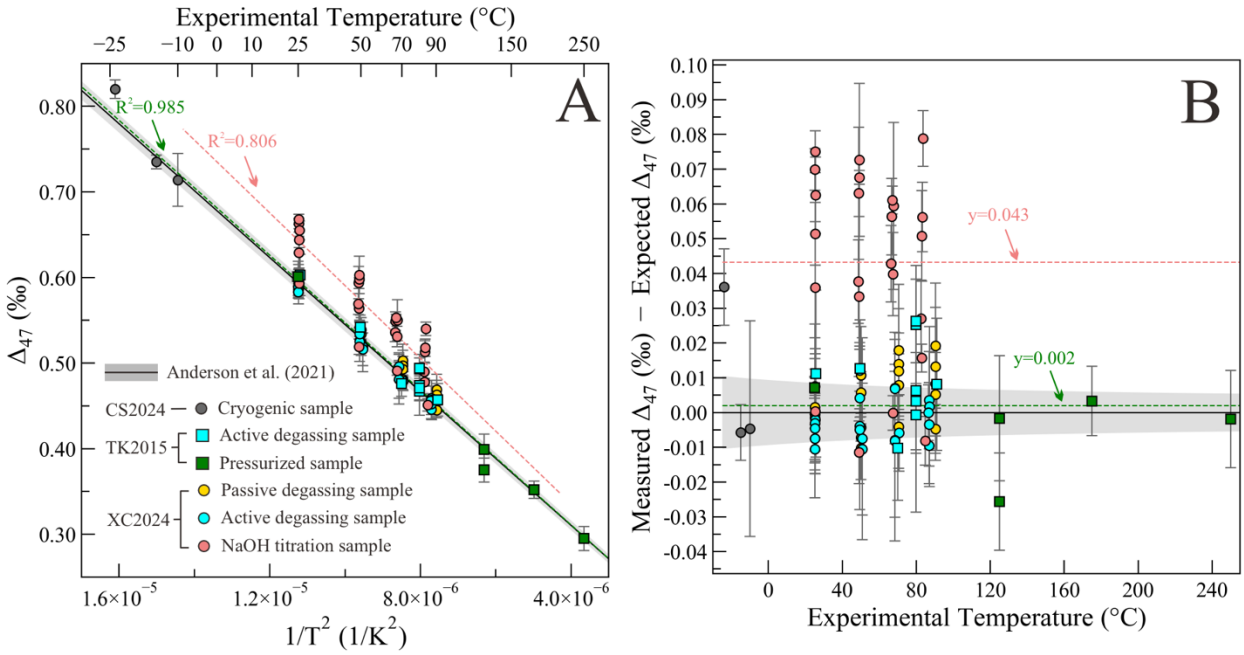


Figure 5.3 Plots show the relative relation between the current community clumped isotope calibration and the samples in this study.

A. Scatter plot shows the relation between clumped isotope (Δ_{47}) and the experimental temperature. Most samples fall on the calibration line with an R^2 of 0.985 (green dashed line for all samples except NaOH titration samples) but the NaOH titration samples deviate significantly from the calibration with an R^2 of 0.806 (red dashed line). B. Scatter plot shows The differences between measured Δ_{47} and the expected Δ_{47}, which vary with the experimental temperature. The green dashed line is the average value (0.043‰) for all samples except NaOH titration samples and the red dashed line is the average value (0.002‰) for NaOH titration samples. For both A and B, the error bar of Δ_{47} represents 1SE. The Δ_{47}-T calibration is from Anderson et al. (2021) and the 95% confidence interval is given as the grey-shaded area.

The back-calculated $\delta^{18}O_{Fluid}$ values are calculated using the experimental temperature and yield a range from -27.1 ± 0.2‰ to 1.1 ± 0.1‰ (Table 5.1). Except for CS2024, all the other CO_2 degassing samples (both XC2024 and TK2015) show no significant trend with temperature (Figure 5.4, $R^2 = 0.536$) and give an average $\delta^{18}O_{Fluid}$ of -5.66‰. This value is close to the annual $\delta^{18}O_{Fluid}$ of surface water (-6 to -7‰) in London City (Darling et al., 2003) suggesting no kinetic effects occurred during the. However, a strong positive correlation is observed between the $\delta^{18}O_{Fluid}$ of NaOH titration samples and the temperature with an R^2 value of 0.920 (Figure 5.4), implying the existence of kinetic effects (Kluge and John, 2015a; Herlambang and John, 2021). CS2024 show much lower $\delta^{18}O_{Fluid}$ (~ -25‰) due to the heavy bubbling of cylinder CO_2.

5.5 Discussions

The identified kinetic effects in Figure 5.3 and 5.4 attracted the most attention. Compared to the other experiments, the NaOH titration samples of XC2024 differ in several aspects including polymorphism composition, solution pH, precipitation rate, and the added cation impurities. To interpret the kinetic effects, our strategy is to discuss the possible causes one by one and finally reach the most possible answer.

5.5.1 Effects of polymorphism on ^{13}C–^{18}O clumping

Theoretically, the ^{13}C–^{18}O partitioning in calcium carbonate is polymorph-dependent as mineral structures vary in their ability to uptake the larger ionic group (Schauble et al., 2006; Huntington et al., 2009). For example, under the same precipitation temperature, the Δ_{47} of

aragonite is slightly higher than that of the calcite. NaOH titration samples are mostly composed of aragonite, with an average proportion of 65%, significantly higher than other samples: 46% for degassing samples of XC2024, < 1% for CS2024, and 13% for TK2015 (Chapter 3, Table 3.2 and Figure 3.5). Thus, polymorphism appears to be a plausible explanation for the elevated Δ_{47} observed in Figure 5.3. However, further investigation refutes this hypothesis.

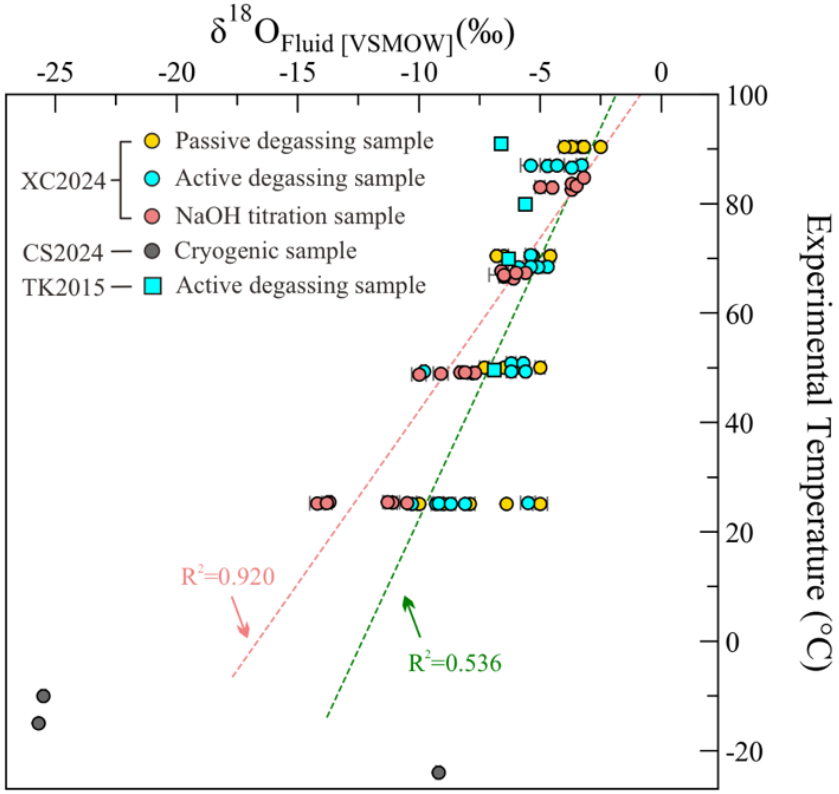


Figure 5.4 Scatter plot shows the correlation between the $\delta^{18}O_{Fluid}$ and the experimental temperature of XC2024 and CS2024.

Active degassing, and passive degassing samples in this study and the passive degassing samples of Kluge give a regression with $R^2 = 0.536$ (green dashed line) suggesting no significant kinetic effects. However, the NaOH titration samples give a regression with $R^2 = 0.920$ (red dashed line) indicating kinetic effects exist in these samples.

The experiments where $CuCl_2$ was added are characterized by a high content of aragonite (Chapter 3, Table 3.2 and Figure 3.5) and show that both the passive and active degassing precipitates yield more aragonite (92% on average) than NaOH titration experiments (61% on average). Despite this, in the $CuCl_2$-added experiments, NaOH titration samples still deviate from

the Δ_{47}-T calibration, whereas both the passive and active degassing samples do not (Figure 5.5). Similar conflicts - low aragonite proportion but elevated Δ_{47} value - are observed when comparing 90MgP and 90MgT, and 25FeP and 25FeT. Although the Control group (no added salt) samples in NaOH titration experiments consist of more aragonite (67%) than those under CO_2 degassing (50%), all samples' Δ_{47} values are within the 95% confidence interval of the Δ_{47}-T calibration, with an average offset of -0.005‰ (Figure 5.5). Besides, no statistical trend is observed between the aragonite/calcite ratio and the Δ_{47} offset from the Δ_{47}-T calibration (Figure 5.6).

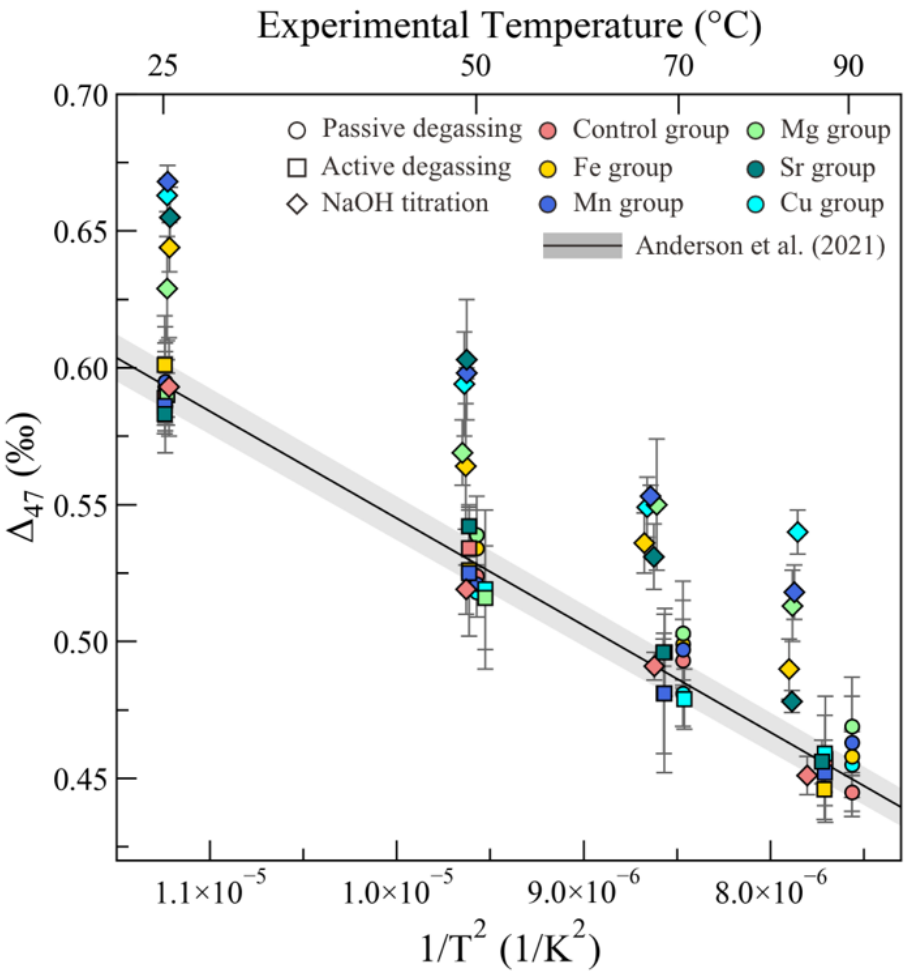


Figure 5.5 Scatter plot shows the relation between clumped isotope (Δ_{47}) and the temperature of active degassing, passive degassing, and NaOH titration samples in this study.

The colour represents different cation impurities and the shape indicates the different precipitation methods. All NaOH titration samples except the Control group exhibit a strong deviation from the Δ_{47}-T calibration of Anderson et al. (2021).

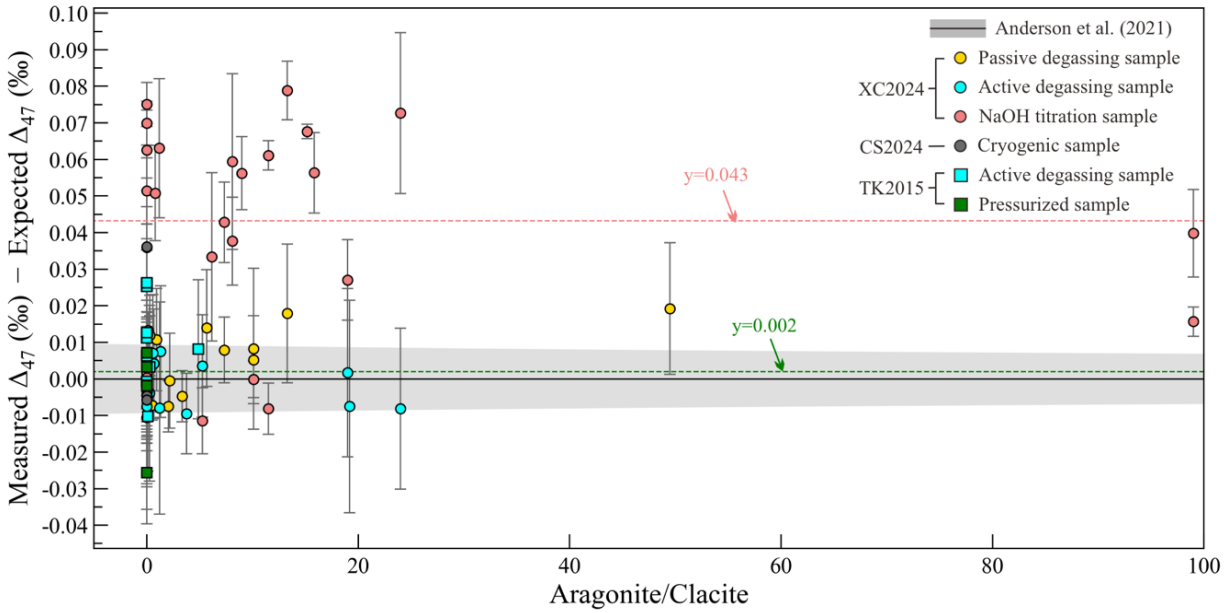


Figure 5.6 Scatter plot shows the differences between measured Δ_{47} and the expected Δ_{47}, which vary with the Aragonite to calcite ratio.

The error bar is the 1SE of Δ_{47} and the black line represents that the measured Δ_{47} is equal to the expected Δ_{47} of which the 95% confidence interval is given as the grey shaded area. The green dashed line is the average value for all samples except NaOH titration samples and the red dashed line is the average value for NaOH titration samples.

By directly comparing the single-phase (100% calcite or aragonite) samples exhibiting no kinetic effects, Figure 5.7 shows that both $\Delta_{47(Calcite)}$-T calibration (Eqs(5.1)) and $\Delta_{47(Aragontie)}$-T calibration (Eqs (5.2)) are parallel to the current Δ_{47}-T calibration, and the slopes and the intercepts are within the error range.

$$\Delta_{47(Calcite)} = 0.0399 \times \frac{10^6}{T^2} + 0.145 \quad (R^2 = 0.994) \tag{5.1}$$

$$\Delta_{47(Aragonite)} = 0.0400 \times \frac{10^6}{T^2} + 0.140 \quad (R^2 = 0.996) \tag{5.2}$$

The similarity between the pure phase regression implies that the Δ_{47} difference at 25℃ between the calcite and aragonite is less than 0.010‰. Interestingly, the calcite regression is slightly higher than the aragonite regression, contrary to the theoretical calculation of Guo et al. (2009) but similar to the laboratory results of Henkes et al. (2013) and Eagle et al. (2013). While

studies differ on the exact clumping differences between calcite and aragonite, they agree that these differences are insignificant (Henkes et al., 2013; Kluge and John, 2015a). Although the current data set is limited in evaluating the vaterite influence on Δ_{47} value, research by Kluge and John (2015b) revealed that the vaterite-regression is almost the same as the calcite-regression by analyzing synthetic samples that are composed of more than 90% vaterite. Therefore, both the results here and the literature data suggest that $CaCO_3$ polymorphism does not cause significant impacts on ^{13}C–^{18}O clumping, resulting in negligible Δ_{47} offsets.

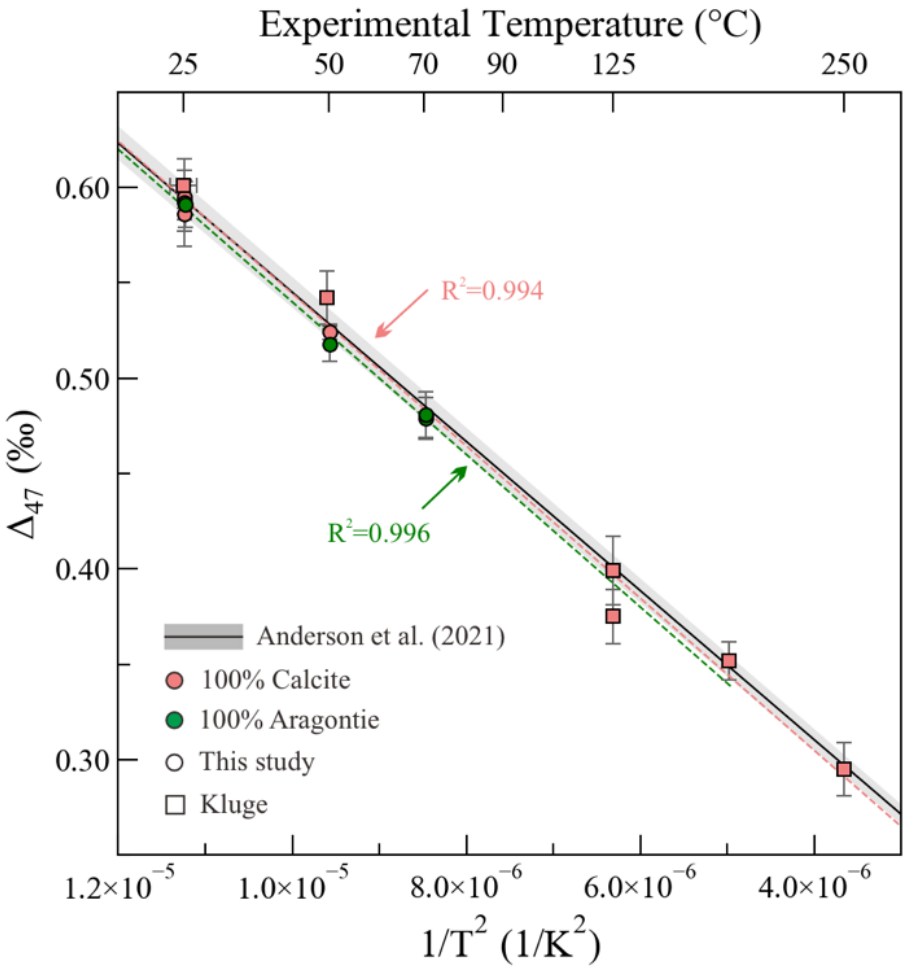


Figure 5.7 A Scatter plot shows the Δ_{47}-T regression for samples exhibiting no kinetic effects and composed of only one phase.

The red dashed line is for 100% calcite samples with a slope of 0.040 and an R^2 of 0.994, and the green dashed line is for 100% aragonite samples with a slope of 0.040 and an R^2 of 0.996. Both lines are very close to the Δ_{47}-T calibration of Anderson et al. (2021).

5.5.2 Effects of pH and Log (rp) on $^{13}C–^{18}O$ clumping

The titrated NaOH not only accelerate the $CaCO_3$ precipitation but also dramatically changes the pH, which affects the DIC speciation (Adkins et al., 2003; Dietzel et al., 2009). The Log (rp) and pH may thus result in the kinetic effects observed for NaOH titration samples.

We investigated the effect of pH for the NaOH titration experiments on $^{13}C–^{18}O$ clumping relative to the active degassing experiments. Although the elevated pH seems to increase the Δ_{47} offset (Figure 5.8A), the overlap pH range (7.2-7.9) between the active degassing experiments and NaOH titration experiments rejects the possibility of pH impacts. Some NaOH titration samples, such as 70FeT (pH = 7.2) and 90MnT (pH = 7.5), were precipitated under a similar pH range as active degassing samples, yet they still show clear offsets in Δ_{47}. A potential model could be that when NaOH drops enter the solution, precipitates form immediately around the drops, resulting in a much higher actual precipitation pH than the recorded solution pH. However, the Control group of NaOH titration experiments (25, 50, 70, and 90ControlT in Table 5.1) exhibited only -0.005‰ offset in Δ_{47} similar to the other control group samples (Figure 5.5 and Figure 5.8A). Thus, the momentary pH influence can be safely excluded. Uchikawa and Zeebe (2012) indicates that in pure water, DIC speciation is dominated by HCO_3^- in the pH range of 7.7-9.0 and changes slightly with the pH variation. Therefore, it is unlikely that the pH range reported in this study (7.0-9.0) will dramatically influence the DIC speciation causing the Δ_{47} offsets. Nevertheless, it is still possible that very high (pH > 9.5) can cause Δ_{47} offsets (Tang et al., 2014; Huntington and Petersen, 2023) as suggested by the natural travertine precipitates (pH >10) (Falk et al., 2016; Holdsworth et al., 2022).

Similarly, the potential kinetic effect caused by Log (rp) on Δ_{47} is hard to demonstrate despite a significant positive correlation between the Δ_{47} offsets and the Log (rp) (Figure 5.8B). Again, the Control group samples exhibit nearly no Δ_{47} offsets despite very high Log (rp), implying Log (rp) is not the key to the kinetic effects observed (Figure 5.8B). We note that instead

of producing $CaCO_3$ by degassing CO_2 from the solution of $Ca(HCO_3)_2$, the NaOH titration experiments chemically experience no CO_2 fractionation, and thus should be easier to keep close to equilibration state than the passive and active degassing experiments. Watkins and Hunt (2015) also suggests that the mineral Δ_{47} composition of rapid-growth carbonates is nearly equal to that of solution DIC with < 0.01‰ difference. Therefore, the rapid precipitation is not responsible for the excessive ^{13}C–^{18}O clumping in NaOH titration samples.

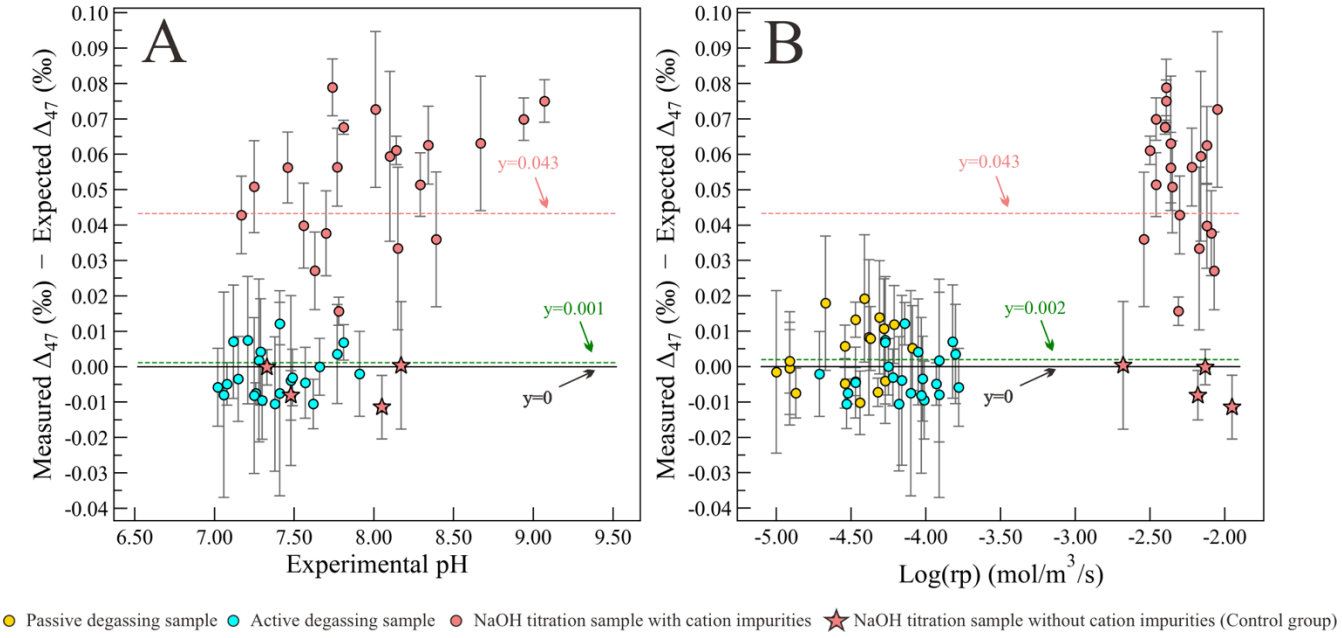


Figure 5.8 Scatter plots show the differences between measured Δ_{47} and the expected Δ_{47} of XC2024.

Variation with A. experimental pH and B. precipitation rate (Log (rp)). The green dashed line is the average value for (active) and passive degassing samples and the red dashed line is the average value for NaOH titration samples. The Control group samples precipitated using NaOH titration (star shape) show higher precipitation pH and rate but close to y = 0 meaning that these samples show negligible Δ_{47} offsets.

5.5.3 Effects of cation impurities on ^{13}C–^{18}O clumping

Given that the effects from polymorphism, pH, and Log (rp) caused kinetic effects can be discarded, and the observed Δ_{47} offsets come clearly and systematically for NaOH titration samples with added cation impurities and irrespective of the cation species (Figure 5.9), the primary mechanism contributing to excessive clumping of ^{13}C–^{18}O appears to be the incorporation

of cation impurities. Figure 5.9 illustrates how variations in Δ_{47} offset correlate with changes in Log $D_{Me/Ca}$ for different cation impurities. While Log $D_{Fe/Ca}$ and Log $D_{Sr/Ca}$ show a positive correlation with Δ_{47} offsets, Log $D_{Mn/Ca}$ exhibits an opposite trend, and Log $D_{Mg/Ca}$ and Log $D_{Cu/Ca}$ show no significant trend. Similar results were obtained when analyzing the relationship between Δ_{47} offset and absolute trace metal/calcium (Me/Ca) in solids (Figure 5.10), indicating that neither Log $D_{Me/Ca}$ nor Me/Ca induces the observed kinetic effects. We, therefore, suspect that the kinetic effects are caused by the way ionic impurities are incorporated rather than their concentration.

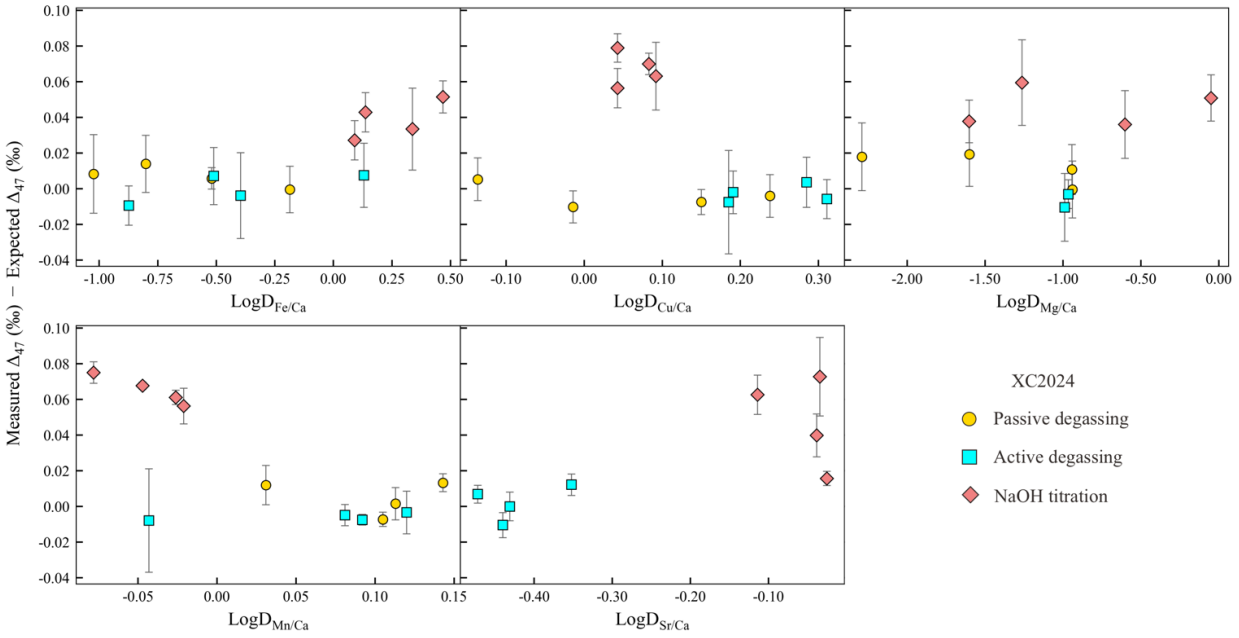


Figure 5.9 Scatter plots show the differences between measured Δ_{47} and the expected Δ_{47} vary with the distribution coefficient.

The Δ_{47} offset exhibits a positive correlation with the $LogD_{(Me/Ca)}$ of Fe and Sr but a negative correlation to the Mn and no relation is found for Mg and Cu.

Traditionally, the $CaCO_3$ lattice growth pathway is viewed as occurring through simple ion-by-ion attachment at crystal growing sites (kink sites) governing the ion attachment efficiency and the phase precipitation kinetics (Nielsen et al., 2013) (Figure 5.11). However, there are growing research results suggesting the ion-by-ion model is inadequate to account for the whole process of $CaCO_3$ precipitation (Ruiz-Agudo et al., 2011; Putnis et al., 2021; Zhang and Wang,

2024) and the stable clusters (e.g. $CaCO_3^0$) in the solution play an important role in precipitation (Nilsson and Sternbeck, 1999; Gebauer et al., 2008; Putnis et al., 2021). The stable clusters aggregation pathway (Figure 5.11), thus, is proposed as crucial and its relative contribution increases with the saturation state (Putnis et al., 2021). Moreover, summarizing the work of Ruiz-Agudo et al. (2011) and Zhang and Wang (2024), under environments with pH < 8.5 and high $CaCO_3$ saturation state, the ion-by-ion pathway is likely limited due to the strong hydration of Ca^{2+}, which hampers its attachment to kink sites (Figure 5.11).

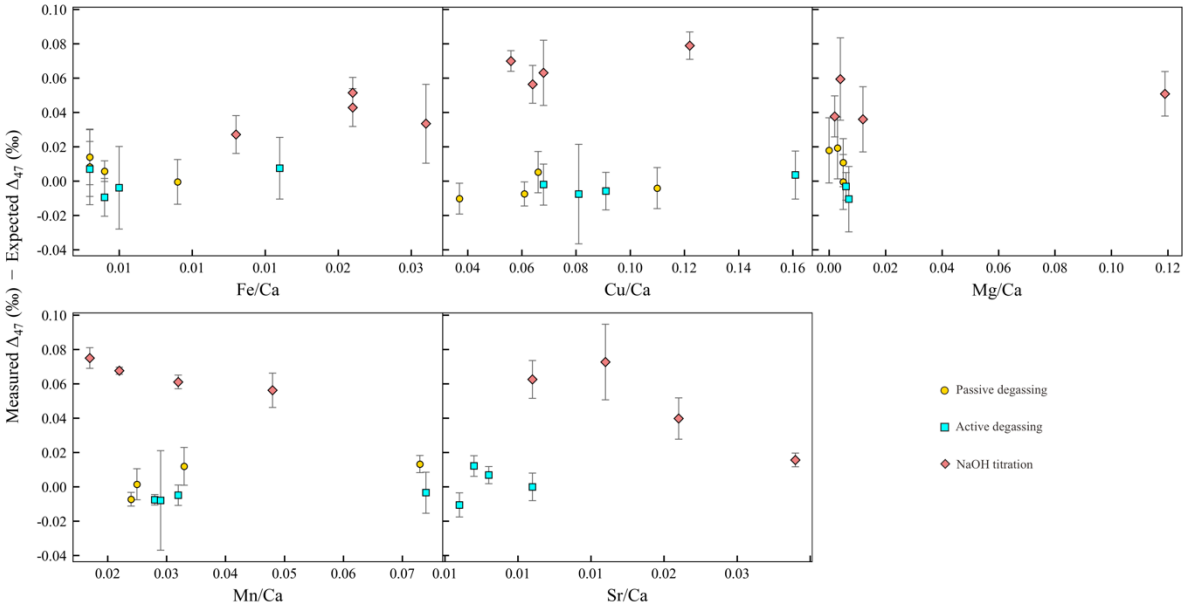


Figure 5.10 Scatter plots show the differences between the measured Δ_{47} and the expected Δ_{47} vary with the Me/Ca. The Δ_{47} offset exhibits a positive correlation with the Me/Ca of Fe and Sr but a negative correlation to the Mn and no relation is found for Mg and Cu

Furthermore, the ionic impurities incorporation into $CaCO_3$ are also proposed as two different pathways (Figure 5.11): ideal replacement of Ca^{2+} on the lattice or physical entrapment by the lattice (Lakshtanov and Stipp, 2007; Thien et al., 2014). Unlike the physical entrapment causing no influence on the kink sites, due to the differences in ionic radius and coordination number of each cation (Dietzel, 2011), the substitution of Ca^{2+} by cation impurities introduces defects on the lattice resulting in 'spoiled' kink sites. The 'spoiled' kink site constructs the lattice

uniquely by preferentially accepting the ionic impurities and influencing the distance between ions. Obviously, the ideal replacement pathway is limited by the available substitution sites (Ca^{2+}) and impurities ions and predominates when crystal growth is governed by the ion-by-ion pathway. In stable cluster-dominated environments, such as the CO_2 degassing experiments with high $CaCO_3$ saturation states and pH ranging from 7.0 to 7.9, physical entrapment likely governs ionic impurity coprecipitation.

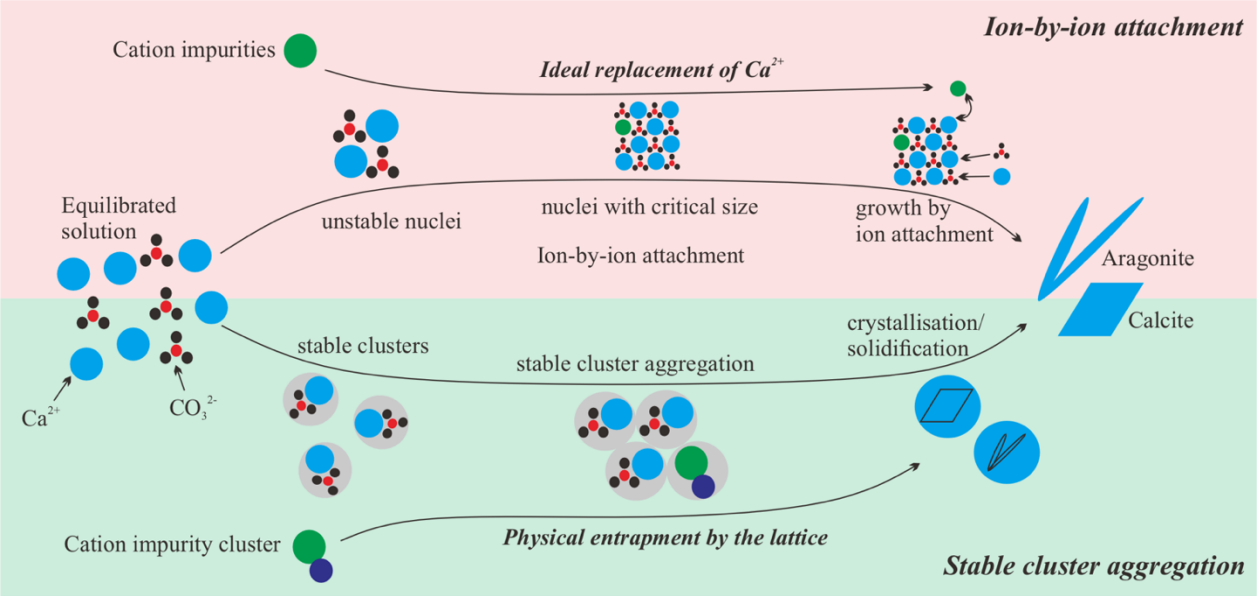


Figure 5.11 Schematic of the calcium carbonate growth pathways and the cation impurities incorporation pathways which is inspired and modified from Putnis et al. (2021).

Conversely, NaOH titration introduces a momentary high volume of OH^- ions, enhancing the dehydration of both Ca^{2+} and cation impurities, promoting ion-by-ion attachment pathway and ideal Ca^{2+} substitution by cation impurities (Tripati et al., 2015). SEM observations (Figure 5.1) provide direct evidence supporting this argument: calcites affected by kinetic effects exhibit hopper-like surface structures or nested formations, indicating "spoiled" kink sites during crystal growth (Figure 5.1B, calcite) whereas the other samples including CO_2 degassing experiments and the Control group of NaOH titration (Figure 5.1A, calcite) do not. The rapid precipitation may further prompt the Ca^{2+} replacement as it favours the ion attachment as demonstrated by the Growth Entrapment Model (GEM) of Watson (2004). Thus, under conditions of high OH^-

concentration and rapid precipitation rates, cation impurity incorporation into $CaCO_3$ is primarily through Ca^{2+} substitution, likely contributing to the observed excessive ^{13}C-^{18}O clumping.

At the same temperature and in equilibrium state, the ^{13}C-^{18}O clumping decreases in the sequence of $CO_{(aq)}$, H_2CO_3, HCO_3^-, $CaCO_3^0$, and CO_3^{2-} (Hill et al., 2014; Tripati et al., 2015). Constructed by the equilibrated stable clusters ($CaCO_3^0$), the CO_2 degassing experiments are of course close to the equilibration with indistinguishable offsets in Δ_{47}. However, for NaOH titration samples, excessively dehydrated cations necessitate more HCO_3^- for deprotonation and complexation. The equilibrium constant governing this process for cation impurities differs from that of Ca^{2+}, potentially shifting the ^{13}C-^{18}O clumping equilibrium towards CO_3^{2-}, aligning its clumping behaviour more closely with that of HCO_3^-. Δ_{47} signals of NaOH titration samples with added salt, thereby, recording the broken equilibrium state. There may also be other complexion processes that are poorly understood and contribute to this process (Tripati et al., 2015). The Control group in NaOH titration experiments, unaffected by this pathway switch, likely results from the nearly equal constants of Ca^{2+} complexation with CO_3^{2-} in forming $CaCO_3^0$ and directly on the crystal surface (Ruiz-Agudo et al., 2011).

A challenge to this hypothesis arises from the fact that completely substituted carbonate minerals such as dolomite and siderite exhibit indistinguishable Δ_{47}-T calibrations from calcite (Schauble et al., 2006; Fernandez et al., 2014). However, this is because they are precipitated at an equilibrium state mainly through the stable clusters aggregation pathway and thus don't influence the ^{13}C-^{18}O clumping equilibrium. The finding also implies that as long as the carbonate system reaches isotopic equilibrium without experiencing changes in crystallization pathways, cation impurities exert negligible effects on Δ_{47}-T calibration. We suggest that the kinetic effects observed in some samples in our study are the result of the combined effect of the presence of impurities ions, excessive OH^-, and the rapid growth rate. Since the ionic impurities incorporation can be influenced by the initial Me/Ca in the solution (Dromgoole and Walter, 1990b), we suspect that there may also be a threshold on Me/Ca to cause the kinetic effect.

This is the first time that this effect has been experimentally identified and probably the answer to why some natural carbonate deposit precipitation temperatures were underestimated. Adkins et al. (2003) demonstrated that a pH gradient existed outside the coral cells with higher pH near the coral cells, thus the relatively concentrated OH^- near the coral cell may cause CO_2 hydroxylation resulting in the enrichment of Δ_{47}. Since then, Figure 5.12 exhibiting the Δ_{47} offsets vs $\delta^{18}O_{Fluid}$ offsets has been widely used to explain the possible causes of kinetic effects (Thiagarajan et al., 2011; Saenger et al., 2012; Tripati et al., 2015; Spooner et al., 2016; Davies and John, 2019), and Thiagarajan et al. (2011), Saenger et al. (2012), and Spooner et al. (2016) suggest that CO_2 hydroxylation is the main cause for their coral dataset. However, our dataset indicates that CO_2 hydroxylation may not be the only feasible hypothesis and the dehydration of cation impurities near the coral cell can contribute to the excessive clumping of ^{13}C-^{18}O. Falk et al. (2016) and Holdsworth et al. (2022) attributed the enriched Δ_{47} in travertine deposits to the high pH (>10), given the similarity between Me/Ca in their research (0.01-0.07) and this study (0.01-0.04), we suspect the Δ_{47} offsets are also caused by the dehydration of cation impurities in high pH solution with concentrated OH^- (Figure 5.12). Beyond these considerations, within the examined pH range (7.0-9.1), temperature variations (25-90℃), precipitation rates (-5.00 to -1.95 $mol/m^3/s$), and the diversity of cations and their concentrations in different precipitation methods collectively suggest that the Δ_{47}-T calibration for calcium carbonate is broadly applicable across various scenarios.

5.5.4 Extension of Δ_{47}-T calibration to cryogenic temperature

The CS2024 align closely with the current Δ_{47}-T calibration (Figure 5.3). Except for the -24℃ sample, which falls outside the 95% confidence interval, the -10℃ and -15℃ samples are well within this interval. We further investigate whether these samples were precipitated under isotopic equilibrium. The -10℃ and -15℃ samples exhibit a similar bulk isotope composition and $\delta^{18}O_{Fluid}$, whereas the -24℃ sample differs a lot by higher values in both the bulk isotope

composition and the $\delta^{18}O_{Fluid}$ (Figure 5.2 and 5.4). Given that the sole carbon source during precipitation is cylinder CO_2, which is theoretically lighter than the solids, the heavier carbon isotope signal observed in the -24°C sample suggests either greater CO_2 fractionation due to rapid precipitation or a heavier carbon isotope signal in the parent fluid DIC due to shorter CO_2 bubbling time. As discussed before, once the solution reaches isotopic equilibrium, the Δ_{47} is not influenced by changes in precipitation rate, indicating greater CO_2 fractionation is not likely the case here. We, thereby, propose that the isotopic composition of the parent fluid DIC is the determining factor here.

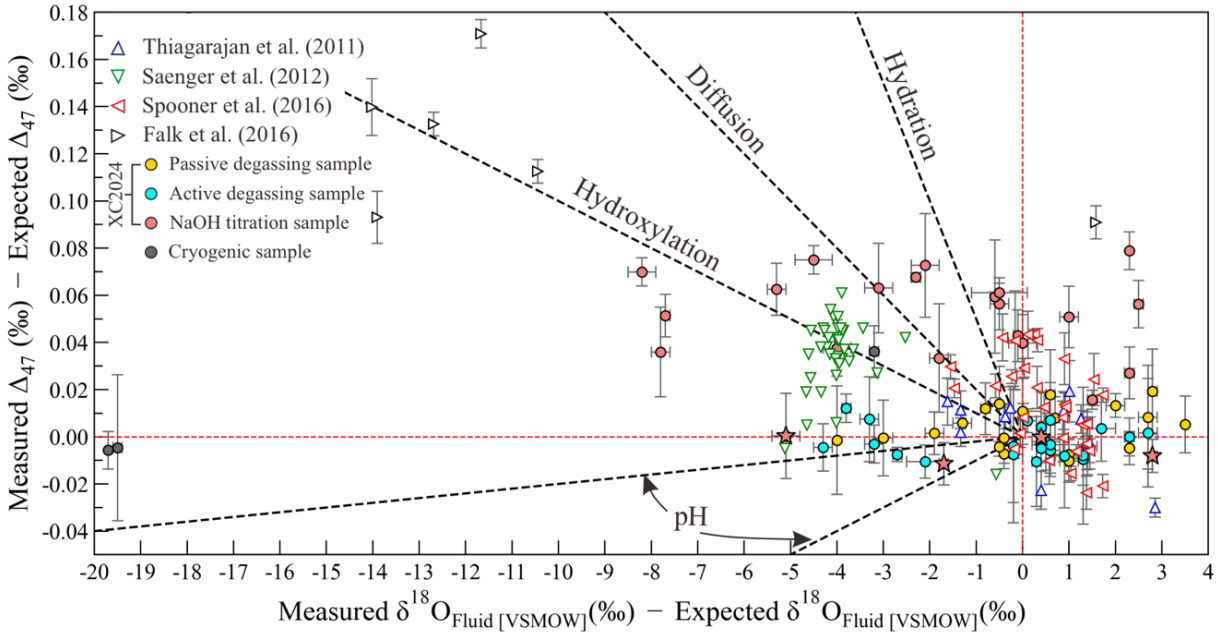


Figure 5.12 Deviations of the measured coral Δ_{47} and $\delta^{18}O_{Fluid}$ from the expected equilibrium values for different studies.

The y-error bar is 1 SE and the x-error bar is 1 SD. Dashed lines show the modelled trajectories of hydration/hydroxylation kinetic effects (slope = -0.05/-0.01), diffusive effects (slope = -0.02) and equilibrium precipitation at varying pH (slope from 0.002 to 0.01) defined in Spooner et al. (2016). The data of Thiagarajan et al. (2011) and Saenger et al. (2012) are reprocessed by Spooner et al. (2016) and all literature data are provided in supplementary materials.

Cryogenic sample precipitation involves the transformation from $CaCl_2$ to $CaCO_3$, then to $Ca(HCO_3)_2$, and finally back to $CaCO_3$ (Chapter 2, Figure 2.7B). The initially formed $CaCO_3$ is

the product of $CaCl_2$ the H_2CO_3 which records heavier isotopic signals than HCO_3^- and CO_3^{2-} (Hill et al., 2014; Tripati et al., 2015). The final precipitates probably record heavier Δ_{47} if the CO_2 bubbling time is not long enough to convert all $CaCO_3$ to $Ca(HCO_3)_2$. This confirms that the -24℃ sample was precipitated out of isotopic equilibrium whereas the -10℃ and -15℃ samples were precipitated at equilibrium. Consequently, we consider the current cryogenic sample synthesis procedures more suitable for Δ_{47} research compared to the freezing $Ca(HCO_3)_2$ solution method in previous studies (Killawee et al., 1998; Uwakwe et al., 2023), owing to its lower precipitation temperature and the ability in isotopic equilibrium precipitation.

Based on all the measurements from this study that were considered at equilibrium, we propose the following equation for temperatures ranging from -15 to 250℃ (Figure 5.13):

$$\Delta_{47} = 0.0386 \pm 0.0006 \times \frac{10^6}{T^2} + 0.1587 \pm 0.0055 \quad (R^2 = 0.988) \tag{5.3}$$

Compared to the current two Δ_{47}-T calibrations (Anderson et al., 2021; Fiebig et al., 2021), the Eqs (5.3) deviate by only 0.0009‰ and 0.0023‰ at 25℃ from Anderson et al. (2021) (0.5-1100℃) and Fiebig et al. (2021) (8-1100℃), respectively (Figure 5.14). The good consistency of Δ_{47}-T calibrations is attributed to the standard data reduction procedures developed and widely used by the clumped isotope community including using (1) parameters summarized and recommended by Daëron et al. (2016); (2) the pressure baseline correction (Bernasconi et al., 2013); (3) the new I-CDES reference frame (Bernasconi et al., 2021); (4) the ability to easily (re) process data consistently with Easotope (John and Bowen, 2016). These community procedures reduce inter-lab discrepancies caused by different sample preparation methods and instrument types, and thus greatly improve and ensure data comparability and reproducibility.

5.6 Conclusions

In the present contribution, we generated a comprehensive dataset including Δ_{47} values alongside polymorphism data (calcite, aragonite, and vaterite), pH (7.0 to 9.1), precipitation rate (-5.00 to -1.95 mol/m^3/s), and different cation impurities (Cu^{2+}, Mg^{2+}, Mn^{2+}, Fe^{3+}, and Sr^{2+}) by precipitating calcium carbonates under carefully controlled laboratory conditions. This rich dataset enables a systematic exploration of potential kinetic effects influenced by these controlled parameters.

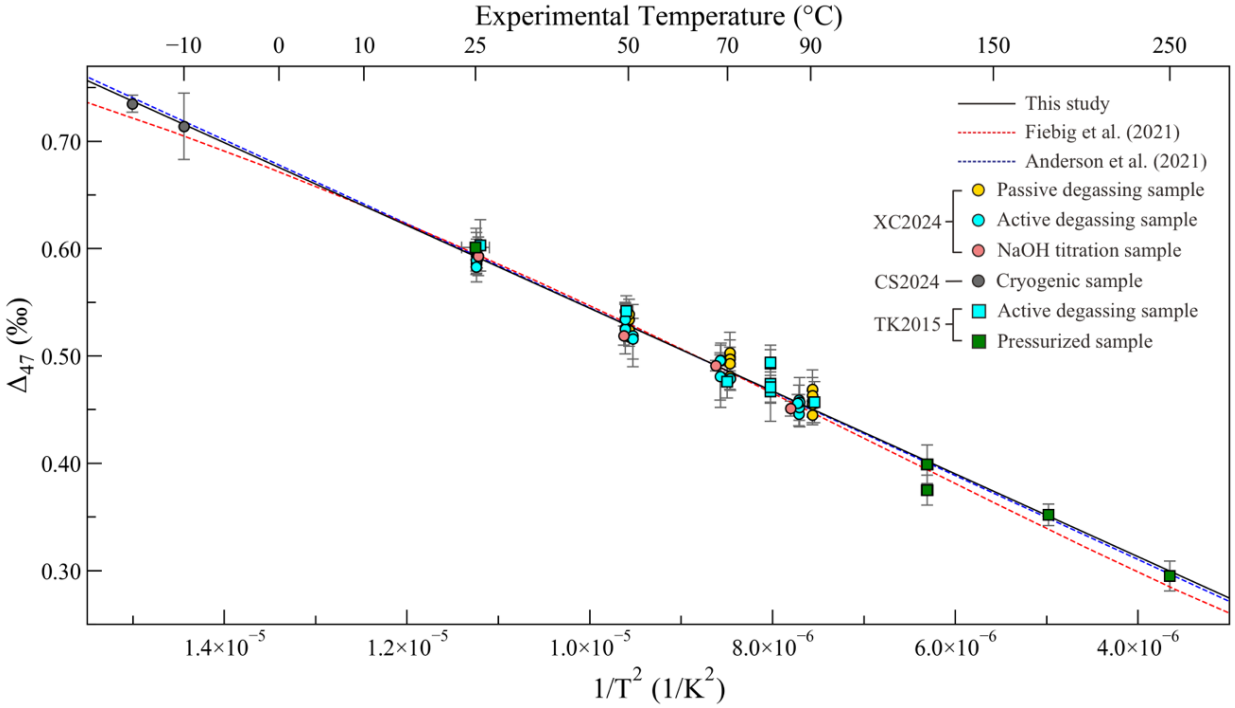


Figure 5.13 The scatter plot shows the relation between clumped isotope (Δ_{47}) and the temperature of isotopic equilibrated samples measured in this study.

The error bar of Δ_{47} represents 1SE. The blue and red dashed lines are the Δ_{47}-T calibration of Anderson et al. (2021) and Fiebig et al. (2021) respectively.

Across the experimental parameters and ranges tested, except for the NaOH titration experiments with additional salt, Δ_{47} values of samples precipitated at the same temperature are nearly identical. This indicates that individual variations in pH, precipitation rate, and cation impurities do not individually cause measurable offsets in Δ_{47}. Additionally, the analysis of

$\Delta_{47(Caclite)}$-T and $\Delta_{47\ (Aragontie)}$-T calibration suggests that polymorphism also does not significantly impact Δ_{47} values.

However, NaOH titration experiments with additional salt show a notable deviation from the current Δ_{47}-T calibration, exhibiting an average Δ_{47} offset of 0.043‰. We propose that these kinetic effects result from the combined influence of a high concentration of OH^-, available cation impurities, and rapid precipitation. The abundance of OH^- accelerates the dehydration of cations, releasing more free cations and shifting the $CaCO_3$ crystal growth pathway from one dominated by stable cluster aggregation to ion-by-ion attachment. This process promotes the incorporation of cation impurities via the ideal replacement of Ca^{2+}. Since cation impurities display different complexation constants with ^{13}C–^{18}O clumping compared to Ca^{2+}, this leads to excessive clumping of ^{13}C–^{18}O and higher Δ_{47} values. This experimental revelation represents the first identification of such effects.

Synthetic cryogenic samples produced down to -15°C confirm well to the current Δ_{47}-T calibration, effectively extending the calibration range below freezing temperatures. This study therefore introduces a viable method for precipitating $CaCO_3$ in cryogenic environments while maintaining isotopic equilibrium. This finding holds potential implications for carbonate-related research in polar and cryogenic cave systems. The resulting Δ_{47}-T calibration is provided as Eqs (5.3), offering a new tool for such environments and expanding our understanding of carbonate precipitation dynamics under extreme cold conditions.

Chapter 6

Conclusions and future research directions

This chapter presents the conclusions and key findings of this research project, alongside, unresolved issues, and recommendations for future work. The chapter begins with a summary of the thesis as a whole, highlighting the contributions to the field through the findings of this research. Following this, the current limitations of this work are identified, and suggestions for potential future research are outlined.

6.1 Conclusions

6.1.1 Overall findings

To address the concern of potential kinetic effects in clumped isotopes and validate the novel proxy the novel combined proxy – the pairing of clumped isotope and trace metal concentration – in identifying the kinetic effects, a comprehensive dataset was prepared through the synthesis of calcium carbonates under controlled laboratory conditions. The dataset was precipitated under a large range of key parameters: temperature (-24 to 90 ℃ to) polymorphism data (calcite, aragonite, and vaterite), pH (7.0 to 9.1), precipitation rate (-5.00 to -1.95 mol/m^3/s), and different cation impurities (Cu^{2+}, Mg^{2+}, Mn^{2+}, Fe^{3+}, and Sr^{2+}).

Chapter 3, by characterizing the polymorph composition of calcium carbonates and its control parameters, provides the general mineralogy background of the synthesised calcium carbonates. Chapter 4 systematically quantified the partitioning of five different trace metals from parent fluids to the precipitates providing mathematical links between the distribution coefficient

and the temperatures and precipitation rates. Based on the results of Chapter 3 and Chapter 4, Chapter 5 analyses the potential kinetic effects on clumped isotopes caused by the polymorphism and the precipitation rate along with other controlled parameters including the pH and trace metal partitioning. Though the trace metals partitioning in calcium carbonates is precipitation rate related, the high precipitation rate in this study didn't cause observable kinetic effects on the clumped isotope. Therefore, the novel combined proxy – the pairing of clumped isotope and trace metal concentration – may not be widely applicable to natural samples. Except for this main conclusion answering the initial aim of the project, this PhD work obtains new insights into the domain of calcium carbonates polymorphism, trace metal partitioning, and clumped isotope fractionation during the calcium carbonate precipitation. The detailed findings in each research chapter are summarized in the next section.

6.1.2 Main findings in research chapters

1. What controls calcium carbonate polymorphism?

In Chapter 3 we demonstrated that temperature and the coupling of temperature and high precipitation rates (HTc- Log (rp)), serve as the primary control on $CaCO_3$ polymorph formation. This is followed by ionic impurities as a secondary control and precipitation rates as a tertiary influence. Temperature influences polymorphism through two distinct patterns. In Pattern 1, calcite predominates at 25°C, while aragonite becomes increasingly prevalent at temperatures above 25°C. In Pattern 2, the relationship between temperature and aragonite proportion can exhibit two trends: one where aragonite proportion increases with temperature (Tr1), and another where aragonite proportion rebounds at higher temperatures (Tr2). Ionic impurities influence $CaCO_3$ morphologies through two primary mechanisms: kink site blocking (ion attachment) and dissolution (ion detachment), both of which are constrained by the precipitation rate. Under high precipitation rates, kink site blocking is the dominant mechanism, whereas dissolution prevails under lower precipitation rates. The speciation of ionic impurities plays a critical role in polymorph

precipitation. Free ion-dominated speciation (e.g., Mn^{2+}, Sr^{2+}) favours calcite precipitation, with this effect likely modulated by the concentration of ionic impurities. Additionally, the presence of Na^{+} and Sr^{2+} ions may retard the transformation of vaterite into calcite. The aragonite and vaterite (Ar+V) system is thermodynamically unstable at temperatures above 25°C, favouring the transformation of vaterite into calcite.

2. Trace metal partitioning into calcium carbonate polymorph mixture through CO_2 degassing as a function of precipitation temperature and rate.

Chapter 4 results demonstrate that among the five investigated elements—Cu^{2+}, Fe^{3+}, Mg^{2+}, Mn^{2+}, and Sr^{2+}—the incorporation of Fe^{3+} and Mn^{2+} is most influenced by the average precipitation rate and temperature, showing independence from $CaCO_3$ polymorph. Specifically, Log D(Fe^{3+}) increases with rising precipitation rates but decreases with increasing temperature, whereas Log D(Mn^{2+}) exhibits the opposite trend:

$$\text{Log } D_{Fe^{3+}} = 0.363 \pm 0.010 \times \text{Log}(r_p) - 0.015 \pm 0.0004 \times Tc + 1.885 \pm 0.048$$

$$\text{Log } D_{Mn^{2+}} = -0.077 \pm 0.004 \times \text{Log}(r_p) + 0.001 \pm 0.0001 \times Tc - 0.285 \pm 0.016$$

The precipitation rate emerges as the primary control on trace metal incorporation, particularly for Mn^{2+}, overshadowing the influence of temperature.

3. Clumped isotope kinetic effects identification and possible explanation.

In Chapter 4 through the analysis of the whole dataset, we conclude that under the current experimental setting and the instrumental detection limit, excluding the NaOH titration experiments with additional salt, variations in calcium carbonate polymorphism, pH, precipitation rate, and cation impurities do not individually cause measurable offsets in Δ_{47}. For the NaOH titration experiments with additional salt, the Δ_{47} offsets observed were interpreted as the result of the combined influence of high OH^- concentration, available cation impurities, and rapid

precipitation. The abundance of OH^- accelerates the dehydration of cations, releasing more free cations and shifting the $CaCO_3$ crystal growth pathway from stable cluster aggregation to ion-by-ion attachment. This process promotes the incorporation of cation impurities via the ideal replacement of Ca^{2+}. Since cation impurities exhibit different complexation constants with ^{13}C–^{18}O clumping compared to Ca^{2+}, this leads to excessive clumping of ^{13}C–^{18}O and higher Δ_{47} values. This experimental revelation represents the first identification of such effects.

This study introduces a viable method for precipitating $CaCO_3$ in cryogenic environments while maintaining isotopic equilibrium. Using the synthetic cryogenic samples and under the assistance of TK2015 we yield an extended Δ_{47}-T calibration under the temperature from -15 to 250℃ which is provided as:

$$\Delta_{47} = 0.0386 \pm 0.0006 \times \frac{10^6}{T^2} + 0.1587 \pm 0.0055 \quad (R^2 = 0.988)$$

6.2 Further work

Chapter 3 addressed the objective proposed but also faced some challenges. We designate the cation impurities as the secondary control parameter compared to temperature. However, the cation impurities investigated in this study as well as their concentration are limited. Some common trace metals in seawater such as Zn and Al, and non-metal elements like S and P may have different influences on the calcium carbonate polymorphism. Furthermore, the ionic strength, an important parameter in influencing the ion activity can be a potential pivotal parameter in the polymorph formation and needs to be figured out in the future.

Though findings in Chapter 4 hold promising applications, caution must be exercised in interpreting the observed relationships and considering the complexities of real-world scenarios. Given that most natural carbonate sediments' parent fluids properties (such as the trace metal to calcium ratio) are impossible to obtain, the utilization of trace metal to calcium ratios (Fe/Ca and

Mn/Ca) in field samples may prove more effective, potentially enabling the inference of ancient precipitation rates and thereby enhancing our understanding of geochemical processes. This requires more laboratory work in the laboratory to establish a high-precision pattern for the relation between the trace metal type, concentration, temperature, and precipitation rate.

Chapter 5 identified the first kinetic effects caused by the dehydration of cation impurities. However, the current study didn't find a good tool to constrain it through the Δ_{47} and trace metal distribution coefficient. This is mainly due to the limited trace metal concentration examined. Further research could try to repeat similar experiments as here but with different concentrations which may give us a relation between the trace metal concentration and Δ_{47} offsets thus helping us to constrain the offsets. Another potential method is to use the dual clumped isotope (Δ_{47}- Δ_{48}), the most advanced and reliable kinetic effects indicator currently. Thus, future work may apply dual clumped isotopes on precipitates like this study and elevate the relation between the kinetic effects degree and the dual clumped isotope offset.

To put it in a nutshell, this PhD work examined the potential causes of clumped isotope kinetic effects during calcium carbonate precipitation, based on which the future work may further explore the influences of other parameters (e.g. ionic strength) that were not covered in this study or employ other techniques (e.g. Δ_{48}) to examined the conclusions here.

Appendices

Appendix Table 1 ICP-MS Result

Name	Sample Number	Sample Time	Duriation	Ca	Ca error
25ControlP	0	30/09/2022	0.00	345022.73	5058.4906
25ControlP	1	01/10/2022	25.92	335534.26	5052.9299
25ControlP	2	02/10/2022	56.68	338874.06	5325.4892
25ControlP	3	03/10/2022	79.13	334740.21	12607.689
25ControlP	4	04/10/2022	105.12	296600.09	9092.3537
25ControlP	5	05/10/2022	127.28	272731.91	13759.28
25ControlP	6	06/10/2022	150.90	229513.75	3319.2173
25ControlP	9	09/10/2022	228.90	131696.84	2052.7045
25ControlP	12	12/10/2022	295.83	89827.374	2459.3717
25ControlP	15	15/10/2022	369.28	74134.032	5744.5629
25ControlP	19	19/10/2022	461.48	54488.91	1750.361
25ControlP	22	22/10/2022	534.63	40942.608	1855.0065
25ControlP	26	26/10/2022	636.90	36344.154	3578.6972
25ControlP	35	08/11/2022	941.52	29448.972	744.10533
50 ControlP	0	2023/1/20 09:40	0.00	348744.61	7050.0333
50 ControlP	1	2023/1/20 16:50	7.17	358453.54	4888.1779
50 ControlP	2	2023/1/22 14:30	52.83	132813.83	6950.6806
50 ControlP	3	2023/1/23 12:00	74.33	96410.916	5895.5198
50 ControlP	4	2023/1/23 18:30	80.83	87711.54	1850.7226
50 ControlP	5	2023/1/24 18:45	105.08	60635.61	1939.9504
50 ControlP	8	2023/1/27 19:00	177.33	32426.436	730.14397
50 ControlP	11	2023/1/30 18:50	249.17	24914.232	1869.7572
50 ControlP	15	2023/2/3 19:00	345.33	13367.676	914.26785
50 ControlP	18	2023/2/7 20:15	442.58	14993.412	1117.005
70 ControlP	0	2023/2/20 09:30	0.00	197496.94	8245.7507
70 ControlP	1	2023/2/20 19:35	10.08	182452.87	9043.0003
70 ControlP	2	2023/2/21 10:00	24.50	75368.16	3111.0253
70 ControlP	3	2023/2/21 21:30	36.00	54856.326	1297.0177
70 ControlP	4	2023/2/22 09:05	47.58	38415.72	3279.5824
70 ControlP	7	2023/2/23 21:00	83.50	20340.726	237.56462

Name	Sample Number	Sample Time	Duriation	Ca	Ca error
70 ControlP	10	2023/2/25 19:00	129.50	11017.272	249.46727
70 ControlP	12	2023/3/1 17:40	224.17	7491.624	1329.6903
90 ControlP	0	2023/3/17 16:00	0.00	120894.48	789.53422
90 ControlP	1	2023/3/17 21:23	5.38	122511.06	1496.6848
90 ControlP	2	2023/3/18 13:00	21.00	49993.02	2693.7271
90 ControlP	3	2023/3/18 20:00	28.00	38415.636	1131.6601
90 ControlP	4	2023/3/19 13:15	45.25	22328.838	2640.4402
90 ControlP	5	2023/3/19 21:15	53.25	16246.986	1725.0309
90 ControlP	8	2023/3/21 20:15	100.25	6473.208	1436.2021
90 ControlP	11	2023/3/26 17:00	217.00	2526.594	3365.462
25 ControlA	0	2023/1/25 13:00	0.00	332709.72	3019.6275
25 ControlA	1	2023/1/25 19:00	6.00	328223.99	7604.1007
25 ControlA	2	2023/1/26 09:30	20.50	207312.46	2497.1359
25 ControlA	3	2023/1/26 19:00	30.00	151098.53	9256.3986
25 ControlA	4	2023/1/27 09:20	44.33	89768.742	3184.7915
25 ControlA	5	2023/1/27 19:00	54.00	76984.488	2286.1003
25 ControlA	6	2023/1/28 13:00	72.00	53014.92	135.57457
25 ControlA	7	2023/1/29 16:50	99.83	40771.248	1435.3339
25 ControlA	8	2023/1/30 18:50	125.83	33934.74	2033.0585
25 ControlA	9	2023/1/31 18:50	149.83	31995.474	1288.8972
50 ControlA	0	2023/2/6 11:20	0.00	334887.5	10410.946
50 ControlA	2	2023/2/6 19:15	7.92	280202.37	10729.793
50 ControlA	3	2023/2/7 10:00	22.67	42426.678	2202.202
50 ControlA	4	2023/2/7 20:15	32.92	30761.43	1043.5974
50 ControlA	5	2023/2/8 09:15	45.92	22931.202	2988.4032
50 ControlA	6	2023/2/8 19:20	56.00	17187.072	581.67452
50 ControlA	7	2023/2/9 10:00	70.67	9900.786	498.54846
50 ControlA	8	2023/2/9 19:15	79.92	10723.398	1343.6544
50 ControlA	9	2023/2/10 09:45	94.42	11663.526	962.1049
70 ControlA	0	2023/2/21 21:30	0.00	180673.5	998.76245
70 ControlA	1	2023/2/22 09:05	11.58	22857.618	207.8597
70 ControlA	2	2023/2/22 21:30	24.00	7256.634	1828.2684
70 ControlA	3	2023/2/23 08:40	35.17	6492.822	415.33331
70 ControlA	4	2023/2/23 21:00	47.50	6022.674	155.45112
70 ControlA	5	2023/2/24 10:10	60.67	6933.528	3672.1847
70 ControlA	6	2023/2/24 18:10	68.67	9489.48	1578.9199
70 ControlA	7	2023/2/25 19:00	93.50	10116.246	644.49566
90 ControlA	0	2023/3/18 16:00	0.00	118969.12	1587.9749
90 ControlA	1	2023/3/18 20:00	4.00	27764.436	869.59718

Name	Sample Number	Sample Time	Duriation	Ca	Ca error
90 ControlA	2	2023/3/19 13:15	21.25	5670.084	508.95621
90 ControlA	3	2023/3/19 22:15	30.25	4436.124	1800.9377
90 ControlA	4	2023/3/20 10:00	42.00	4965.03	155.43526
90 ControlA	5	2023/3/20 20:45	52.75	3261.048	166.10363
90 ControlA	6	2023/3/21 16:20	72.33	4142.418	166.25212
25 ControlT	1	2023/5/27 15:48	0.00	179010.05	1764.0802
25 ControlT	3	2023/5/27 15:54	0.10	187053.31	1292.7153
25 ControlT	4	2023/5/27 16:02	0.23	185986.56	3223.8159
25 ControlT	5	2023/5/27 16:12	0.40	192564.04	1517.6239
25 ControlT	6	2023/5/27 16:21	0.55	197212.71	3706.0123
25 ControlT	7	2023/5/27 16:30	0.70	203227.53	1239.4057
25 ControlT	8	2023/5/27 16:40	0.87	171780.08	550.65516
25 ControlT	9	2023/5/27 16:50	1.03	94828.28	1611.9562
25 ControlT	10	2023/5/27 16:58	1.17	50721.544	799.45048
25 ControlT	11	2023/5/27 17:06	1.30	42288.515	994.57376
25 ControlT	12	2023/5/27 17:16	1.47	39587.134	428.39357
25 ControlT	13	2023/5/27 17:24	1.60	40695.497	141.5741
50 ControlT	0	2023/6/9 15:08	0.00	229190.64	7053.8974
50 ControlT	2	2023/6/9 15:18	0.17	228940.49	10121.006
50 ControlT	3	2023/6/9 15:26	0.30	232572.27	7653.2328
50 ControlT	4	2023/6/9 15:34	0.43	225117.27	4811.6479
50 ControlT	5	2023/6/9 15:42	0.57	0	2019.8061
50 ControlT	6	2023/6/9 15:48	0.67	0	1235.645
50 ControlT	7	2023/6/9 15:56	0.80	0	797.52613
70 ControlT	0	2023/6/19 14:35	0.00	213561.1	2218.4242
70 ControlT	2	2023/6/19 14:46	0.18	210238.43	10713.31
70 ControlT	3	2023/6/19 14:52	0.28	196727.33	5077.384
70 ControlT	4	2023/6/19 14:58	0.38	0	1583.4617
70 ControlT	5	2023/6/19 15:06	0.52	0	1803.2538
90 ControlT	0	2023/6/25 15:38	0.00	192037.52	3691.0974
90 ControlT	2	2023/6/25 15:46	0.13	59587.248	2514.5642
90 ControlT	3	2023/6/25 15:50	0.20	0	2562.9823
90 ControlT	4	2023/6/25 15:54	0.27	0	1117.4125
90 ControlT	5	2023/6/25 16:00	0.37	0	2522.6429
25 FeP	0	2022/10/3 17:43	0.00	404482.81	22330.579
25 FeP	1	2022/10/4 19:42	25.98	402460.29	16937.042
25 FeP	2	2022/10/5 17:52	48.15	401855.16	17859.993
25 FeP	3	2022/10/6 17:29	71.77	399358.88	19630.268
25 FeP	4	2022/10/7 16:49	95.10	403151.24	13807.124

Name	Sample Number	Sample Time	Duriation	Ca	Ca error
25 FeP	5	2022/10/8 23:43	126.00	334435.99	11789.228
25 FeP	6	2022/10/9 23:29	149.77	286649.48	10333.31
25 FeP	7	2022/10/10 17:38	167.92	247432.46	11707.288
25 FeP	9	2022/10/12 18:26	216.72	184439.39	10852.097
25 FeP	11	2022/10/14 18:09	264.43	144801.66	5999.1358
25 FeP	14	2022/10/17 17:35	335.87	111098.47	5401.409
25 FeP	17	2022/10/20 17:31	407.80	92904.126	4473.1327
25 FeP	21	2022/10/24 18:00	504.28	77207.959	3285.7524
25 FeP	25	2022/10/28 18:20	600.62	72392.44	3226.5949
25 FeP	32	2022/11/8 16:06	862.38	61099.385	2698.0616
50 FeP	0	2023/1/16 11:09	0.00	404027.48	19765.158
50 FeP	1	2023/1/16 17:44	6.58	389145.15	18108.852
50 FeP	2	2023/1/17 10:40	23.52	208597.33	8770.7541
50 FeP	3	2023/1/17 18:45	31.60	164609.81	7363.3353
50 FeP	4	2023/1/18 11:20	48.18	115459.33	6098.9866
50 FeP	5	2023/1/18 18:30	55.35	108042.09	5403.0502
50 FeP	6	2023/1/19 10:40	71.52	93092.751	3931.0442
50 FeP	7	2023/1/19 19:00	79.85	82371.107	3729.4827
50 FeP	8	2023/1/20 09:40	94.52	76706.252	3335.4931
50 FeP	11	2023/1/23 12:00	168.85	54305.955	3945.8666
50 FeP	14	2023/1/26 19:00	247.85	34439.112	678.03276
50 FeP	17	2023/1/29 16:50	317.68	28235.588	692.10185
50 FeP	20	2023/2/1 19:40	392.52	28799.05	970.51227
70 FeP	0	2023/2/16 12:50	0.00	192195.02	6362.3374
70 FeP	1	2023/2/16 19:40	6.83	153773.43	4959.9451
70 FeP	2	2023/2/17 10:35	21.75	66472.986	2387.6762
70 FeP	3	2023/2/17 20:00	31.17	55251.468	1659.0996
70 FeP	4	2023/2/18 11:20	46.50	46759.489	2551.356
70 FeP	5	2023/2/18 20:27	55.62	40842.053	857.11007
70 FeP	6	2023/2/19 16:05	75.25	35039.565	1290.4444
70 FeP	7	2023/2/19 19:57	79.12	36825.67	1697.4139
70 FeP	10	2023/2/21 10:40	117.83	30868.094	1402.1387
70 FeP	14	2023/2/27 20:00	271.17	29129.221	1206.7305
90 FeP	0	2023/3/17 16:00	0.00	135234.76	3409.8898
90 FeP	1	2023/3/17 21:23	5.38	120910.98	3314.6726
90 FeP	2	2023/3/18 13:00	21.00	53824.669	2542.3469
90 FeP	3	2023/3/18 20:00	28.00	44079.445	331.13326
90 FeP	4	2023/3/19 13:15	45.25	35293.094	582.11997
90 FeP	5	2023/3/19 21:15	53.25	32344.724	1576.3254

Name	Sample Number	Sample Time	Duriation	Ca	Ca error
90 FeP	8	2023/3/21 20:15	100.25	24231.74	1027.7817
90 FeP	11	2023/3/26 17:00	217.00	33283.879	1298.2289
25 FeA	0	2022/11/9 08:48	0.00	379691.67	10634.632
25 FeA	1	2022/11/9 14:00	5.20	369562.38	8790.5795
25 FeA	2	2022/11/9 18:43	9.92	378591.25	14078.549
25 FeA	3	2022/11/10 08:48	24.00	173689.83	6389.9553
25 FeA	4	2022/11/10 15:41	30.88	150488.93	4522.1063
25 FeA	5	2022/11/11 08:50	48.03	88104.197	2386.5373
25 FeA	6	2022/11/11 18:26	57.63	80671.58	2171.9755
25 FeA	7	2022/11/13 12:30	99.70	64852.333	313.25578
25 FeA	8	2022/11/14 16:57	128.15	56663.623	3000.4218
25 FeA	9	2022/11/15 10:58	146.17	55407.841	1197.3091
50 FeA	0	2022/11/25 13:15	0.00	314318.74	13406.954
50 FeA	1	2022/11/25 16:09	2.90	310273.92	11219.376
50 FeA	2	2022/11/25 19:31	6.27	230814.04	10191.094
50 FeA	3	2022/11/26 14:01	24.77	68629.555	2631.6091
50 FeA	4	2022/11/26 17:30	28.25	59802.055	1289.0844
50 FeA	5	2022/11/27 15:05	49.83	45991.81	1245.1112
50 FeA	6	2022/11/28 18:51	77.60	38562.066	1198.9069
50 FeA	7	2022/11/29 16:59	99.73	35691.287	1443.5712
70 FeA	0	2022/12/8 12:00	0.00	239601.65	8387.3823
70 FeA	1	2022/12/8 15:00	3.00	204752.91	6171.4182
70 FeA	2	2022/12/8 18:30	6.50	90855.076	3301.4202
70 FeA	3	2022/12/9 10:00	22.00	42850.045	695.62411
70 FeA	4	2022/12/9 18:30	30.50	36468.015	1950.4508
70 FeA	5	2022/12/10 13:00	49.00	32807.056	623.26047
70 FeA	6	2022/12/11 12:40	72.67	28697.95	220.69065
70 FeA	7	2022/12/12 09:40	93.67	27672.921	951.51554
90 FeA	0	2022/12/16 12:45	0.00	153066.71	5046.2261
90 FeA	1	2022/12/16 16:00	3.25	75323.965	2948.4858
90 FeA	2	2022/12/16 19:40	6.92	44320.195	1641.4085
90 FeA	3	2022/12/17 12:05	23.33	27512.482	800.78208
90 FeA	4	2022/12/17 16:50	28.08	27215.603	674.24248
90 FeA	5	2022/12/18 20:30	55.75	28247.175	1303.1963
90 FeA	6	2022/12/19 16:20	75.58	26474.521	1522.569
25 FeT	0	2023/6/1 12:34	0.00	327199.64	5760.1996
25 FeT	2	2023/6/1 12:55	0.35	312327.07	8600.9731
25 FeT	3	2023/6/1 13:07	0.55	314313.57	9237.9084
25 FeT	4	2023/6/1 13:17	0.72	309403.65	6155.9382

Name	Sample Number	Sample Time	Duriation	Ca	Ca error
25 FeT	5	2023/6/1 13:27	0.88	302921.62	4403.6833
25 FeT	6	2023/6/1 13:37	1.05	225908.89	3344.7575
25 FeT	7	2023/6/1 13:45	1.18	89891.067	2557.7375
25 FeT	8	2023/6/1 13:53	1.32	13314.071	112.84212
50 FeT	0	2023/6/14 16:46	0.00	281414.31	5879.0003
50 FeT	2	2023/6/14 16:56	0.17	275705	7213.9691
50 FeT	3	2023/6/14 17:04	0.30	279009.38	9245.9499
50 FeT	4	2023/6/14 17:12	0.43	269642.29	5474.4646
50 FeT	5	2023/6/14 17:20	0.57	43676.819	1578.615
50 FeT	6	2023/6/14 17:28	0.70	4828.482	269.15656
50 FeT	7	2023/6/14 17:36	0.83	2520.064	95.505074
70 FeT	0	2023/6/21 12:13	0.00	203189.97	3787.0967
70 FeT	2	2023/6/21 12:22	0.15	200222.19	3327.5989
70 FeT	3	2023/6/21 12:30	0.28	187971.09	7225.2237
70 FeT	4	2023/6/21 12:38	0.42	6412.4794	165.00458
70 FeT	5	2023/6/21 12:46	0.55	3195.3869	95.526692
70 FeT	6	2023/6/21 12:54	0.68	3017.3389	138.93416
90 FeT	0	2023/7/1 17:17	0.00	128113.58	2640.6496
90 FeT	2	2023/7/1 17:31	0.23	125897.7	2159.1645
90 FeT	3	2023/7/1 17:37	0.33	2305.208	104.19521
90 FeT	4	2023/7/1 17:44	0.45	3465.516	147.58106
90 FeT	5	2023/7/1 17:52	0.58	3293.6434	130.2224
25 MnP	0	2022/10/3 17:43	0.00	303257.11	7016.6633
25 MnP	1	2022/10/4 19:42	25.98	295834.7	9585.5927
25 MnP	2	2022/10/5 17:52	48.15	294515.21	10643.54
25 MnP	3	2022/10/6 17:29	71.77	288542.86	10130.235
25 MnP	4	2022/10/7 16:49	95.10	285625.07	12676.679
25 MnP	5	2022/10/8 23:43	126.00	246615.22	8367.2197
25 MnP	7	2022/10/10 17:38	167.92	176980.57	4201.7972
25 MnP	9	2022/10/12 18:26	216.72	121158.94	5052.1802
25 MnP	11	2022/10/14 18:09	264.43	94381.582	3770.6666
25 MnP	14	2022/10/17 17:35	335.87	66718.535	2228.3071
25 MnP	17	2022/10/20 17:31	407.80	61393.207	2246.0097
50 MnP	0	2023/1/16 11:09	0.00	317983.76	9186.3375
50 MnP	1	2023/1/16 17:44	6.58	307603.23	11646.496
50 MnP	2	2023/1/17 10:40	23.52	181600.37	4593.5655
50 MnP	3	2023/1/17 18:45	31.60	128050.05	4434.101
50 MnP	4	2023/1/18 11:20	48.18	86530.044	3745.0463
50 MnP	5	2023/1/18 18:30	55.35	75514.272	3507.8482

Name	Sample Number	Sample Time	Duriation	Ca	Ca error
50 MnP	6	2023/1/19 10:40	71.52	57762.666	1315.6461
50 MnP	7	2023/1/19 19:00	79.85	55389.62	920.3339
50 MnP	11	2023/1/23 12:00	168.85	39065.914	2986.0658
50 MnP	14	2023/1/26 19:00	247.85	32265.086	1205.1708
50 MnP	20	2023/2/1 19:40	392.52	26199.011	1307.5873
70 MnP	0	2023/2/16 12:50	0.00	213259.93	6935.3782
70 MnP	1	2023/2/16 19:40	6.83	190695.61	7397.3
70 MnP	2	2023/2/17 10:35	21.75	76312.614	2120.0267
70 MnP	3	2023/2/17 20:00	31.17	53408.958	320.25977
70 MnP	4	2023/2/18 11:20	46.50	40120.414	1096.919
70 MnP	5	2023/2/18 20:27	55.62	31577.076	523.81844
70 MnP	10	2023/2/21 10:40	117.83	22249.152	2567.8368
70 MnP	14	2023/2/27 20:00	271.17	25535.947	773.32362
90 MnP	0	2023/3/15 18:10	0.00	109774.08	2273.7227
90 MnP	1	2023/3/15 20:30	2.33	109349.2	2340.3067
90 MnP	2	2023/3/16 09:05	14.92	79586.845	2874.6591
90 MnP	3	2023/3/16 22:00	27.83	30307.781	834.38137
90 MnP	4	2023/3/17 10:45	40.58	21689.389	876.11642
90 MnP	5	2023/3/17 16:00	45.83	23285.309	1741.7189
90 MnP	6	2023/3/17 21:20	51.17	23863.904	1282.1121
90 MnP	9	2023/3/19 13:15	91.08	23577.97	1213.6908
90 MnP	12	2023/3/21 20:15	146.08	26202.099	919.41032
25 MnA	0	2022/11/9 08:48	0.00	285600.67	6809.8086
25 MnA	1	2022/11/9 14:00	5.20	275535.42	13006.808
25 MnA	2	2022/11/9 18:43	9.92	277396.22	8399.3888
25 MnA	3	2022/11/10 08:48	24.00	176487.85	5676.8837
25 MnA	4	2022/11/10 15:41	30.88	140422.09	5696.3878
25 MnA	5	2022/11/11 08:50	48.03	80825.813	3387.214
25 MnA	6	2022/11/11 18:26	57.63	65047.134	684.68362
25 MnA	7	2022/11/13 12:30	99.70	44749.754	538.46444
50 MnA	0	2022/11/25 13:15	0.00	207971.74	9534.2843
50 MnA	1	2022/11/25 16:09	2.90	205286.41	6895.7075
50 MnA	2	2022/11/25 19:31	6.27	151195.22	5872.8615
50 MnA	3	2022/11/26 14:01	24.77	40346.001	1411.2935
50 MnA	4	2022/11/26 17:30	28.25	37353.089	1742.3392
50 MnA	5	2022/11/27 15:05	49.83	32852.485	1260.655
50 MnA	6	2022/11/28 18:51	77.60	39052.401	1157.4273
70 MnA	0	2022/12/8 12:00	0.00	173305.67	7353.9556
70 MnA	1	2022/12/8 15:00	3.00	147950.92	0

Name	Sample Number	Sample Time	Duriation	Ca	Ca error
70 MnA	2	2022/12/8 18:30	6.50	54652.451	1778.6533
70 MnA	3	2022/12/9 10:00	22.00	25774.588	938.66486
70 MnA	4	2022/12/9 18:30	30.50	26723.739	3215.5983
70 MnA	5	2022/12/10 13:00	49.00	26131.509	1655.6001
90 MnA	0	2022/12/16 12:45	0.00	112664.92	4109.9573
90 MnA	1	2022/12/16 16:00	3.25	59196.741	1281.8173
90 MnA	2	2022/12/16 19:40	6.92	31302.697	1246.6513
90 MnA	3	2022/12/17 12:05	23.33	30569.258	1187.9303
90 MnA	5	2022/12/18 20:30	55.75	26888.458	830.13297
25 MnT	1	2023/5/31 20:40	0.00	250236.99	9646.0406
25 MnT	2	2023/5/31 20:52	0.21	240677.94	6739.5943
25 MnT	3	2023/5/31 21:02	0.37	244296.93	8594.5555
25 MnT	4	2023/5/31 21:13	0.56	246863.74	8931.2691
25 MnT	5	2023/5/31 21:33	0.88	247667.18	7778.4498
25 MnT	6	2023/5/31 21:35	0.92	211695.77	5846.8657
25 MnT	7	2023/5/31 21:43	1.05	141030.89	4150.7981
25 MnT	8	2023/5/31 21:55	1.25	15004.396	407.41243
50 MnT	1	2023/6/14 15:45	0.00	244468.37	9572.6111
50 MnT	2	2023/6/14 15:54	0.15	226578.95	8349.6108
50 MnT	3	2023/6/14 16:06	0.35	230894.44	5373.0835
50 MnT	4	2023/6/14 16:14	0.48	206349.5	10881.012
50 MnT	5	2023/6/14 16:22	0.62	33508.701	795.89565
50 MnT	6	2023/6/14 16:30	0.75	4196.0203	87.857038
50 MnT	7	2023/6/14 16:39	0.90	6983.3397	842.8109
70 MnT	1	2023/6/21 10:53	0.00	192971.35	6806.2031
70 MnT	2	2023/6/21 11:02	0.15	181319.72	8568.0869
70 MnT	3	2023/6/21 11:10	0.28	173615.94	6200.0152
70 MnT	4	2023/6/21 11:18	0.42	16966.807	479.77582
70 MnT	5	2023/6/21 11:26	0.55	3874.6229	341.23817
70 MnT	6	2023/6/21 11:34	0.68	3287.5291	42.812252
90 MnT	1	2023/7/1 16:44	0.00	150815.55	4651.8
90 MnT	2	2023/7/1 16:52	0.13	116811.11	5050.46
90 MnT	3	2023/7/1 16:58	0.23	3853.1923	29.679189
90 MnT	4	2023/7/1 17:04	0.33	4861.1323	252.8367
90 MnT	5	2023/7/1 17:10	0.43	4622.8586	21.422044
25 MgP	0	30/09/2022	0.00	388883.37	11233.879
25 MgP	1	01/10/2022	25.92	375719.68	12169.244
25 MgP	2	02/10/2022	56.68	373469.41	16367.304
25 MgP	3	03/10/2022	79.13	344379.47	7824.9274

Name	Sample Number	Sample Time	Duriation	Ca	Ca error
25 MgP	4	04/10/2022	105.12	292302.11	9540.7847
25 MgP	5	05/10/2022	127.28	249810.48	8513.7493
25 MgP	7	07/10/2022	174.23	167739.04	5281.2441
25 MgP	10	10/10/2022	247.05	115400.94	3987.8277
25 MgP	13	13/10/2022	319.25	88870.195	3731.2338
25 MgP	16	16/10/2022	393.03	71184.287	2380.7589
25 MgP	20	20/10/2022	486.93	48846.714	2397.3071
25 MgP	23	23/10/2022	558.00	45307.771	1245.7658
25 MgP	27	27/10/2022	654.72	40287.514	1948.5586
50 MgP	0	2023/1/18 11:20	0.00	347465.72	12253.998
50 MgP	1	2023/1/18 18:30	7.17	343350.01	10750.504
50 MgP	2	2023/1/19 10:40	23.33	214780	9044.2377
50 MgP	3	2023/1/19 19:00	31.67	164046.01	5761.1262
50 MgP	4	2023/1/20 09:40	46.33	109700.25	4284.9178
50 MgP	5	2023/1/20 16:50	53.50	94590.721	4003.9503
50 MgP	8	2023/1/24 18:45	151.42	38505.142	1207.1526
50 MgP	11	2023/1/27 19:00	223.67	30332.299	1010.211
50 MgP	14	2023/1/30 18:50	295.50	24702.356	1132.7266
70 MgP	0	2023/2/17 20:23	0.00	206670.59	5837.9625
70 MgP	2	2023/2/18 20:27	24.07	89910.296	3165.45
70 MgP	3	2023/2/19 16:05	43.70	69661.28	3003.1258
70 MgP	4	2023/2/19 19:57	47.57	42620.821	1705.5506
70 MgP	5	2023/2/20 09:30	61.12	32701.554	983.76825
70 MgP	6	2023/2/20 19:35	71.20	28740.169	1272.2243
70 MgP	9	2023/2/22 09:05	108.70	29606.625	578.69417
70 MgP	12	2023/2/24 18:00	165.62	22291.983	1157.2586
90 MgP	0	2023/3/16 22:00	0.00	138533.08	4637.9746
90 MgP	1	2023/3/17 10:45	12.75	72125.215	3404.676
90 MgP	2	2023/3/17 16:00	18.00	47440.498	2012.8473
90 MgP	3	2023/3/17 21:20	23.33	39678.749	1155.1883
90 MgP	4	2023/3/18 13:00	39.00	22134.234	669.36025
90 MgP	5	2023/3/18 20:00	46.00	21857.257	808.16254
90 MgP	7	2023/3/19 22:15	72.25	15403.567	360.44502
90 MgP	11	2023/3/24 17:41	187.68	15195.834	797.70277
25 MgA	0	2022/7/1 14:46	0.00	291453.35	31078.828
25 MgA	1	2022/7/1 19:46	5.00	277355.26	3899.6687
25 MgA	2	2022/7/1 21:36	6.83	278701.01	8976.992
25 MgA	3	2022/7/1 23:35	8.82	219041.31	18778.834
25 MgA	4	2022/7/2 10:22	19.60	107806.33	5301.5104

Name	Sample Number	Sample Time	Duriation	Ca	Ca error
25 MgA	5	2022/7/2 13:55	23.15	81397.415	7475.867
25 MgA	6	2022/7/2 21:08	30.37	67244.345	126.98795
25 MgA	7	2022/7/3 12:16	45.50	41057.941	2538.0333
25 MgA	8	2022/7/3 17:25	50.65	42232.919	4790.7427
25 MgA	9	2022/7/4 10:26	67.67	38633.311	7360.8191
25 MgA	10	2022/7/4 18:15	75.48	35176.67	2528.5142
25 MgA	11	2022/7/5 09:42	90.93	37747.897	0
25 MgA	12	2022/7/5 18:04	99.30	25990.868	584.5043
25 MgA	13	2022/7/6 13:14	118.47	34634.659	2642.5585
25 MgA	14	2022/7/6 17:16	122.50	31182.4	9424.7528
25 MgA	15	2022/7/7 10:59	140.22	29851.538	426.84055
25 MgA	16	2022/7/7 18:50	148.07	32576.141	5767.679
50 MgA	0	12/07/2022	0.00	189125.42	6791.0551
50 MgA	1	13/07/2022	14.49	41277.38	9765.6506
50 MgA	2	13/07/2022	18.81	37506.927	2269.0479
50 MgA	3	13/07/2022	25.13	28100.877	8397.9832
50 MgA	4	14/07/2022	36.56	19434.565	2477.7851
50 MgA	5	14/07/2022	40.45	23068.057	706.70051
50 MgA	6	14/07/2022	45.97	26412.152	3268.0015
50 MgA	7	15/07/2022	62.53	18782.169	711.49992
50 MgA	8	15/07/2022	70.22	26845.317	13571.392
50 MgA	9	16/07/2022	89.24	19199.947	4680.9081
50 MgA	10	16/07/2022	95.05	19008.755	4885.7617
50 MgA	11	17/07/2022	116.05	17447.345	0
50 MgA	12	18/07/2022	137.56	20127.369	10222.411
50 MgA	end	20/07/2022	182.68	25134.426	16786.932
70 MgA	0	23/07/2022	0.00	197383.2	38149.708
70 MgA	1	23/07/2022	3.59	128960.26	27402.124
70 MgA	2	24/07/2022	24.34	10979.517	0
70 MgA	3	25/07/2022	42.44	14344.822	5762.5667
70 MgA	4	25/07/2022	50.47	11753.928	10035.606
70 MgA	5	26/07/2022	65.73	9323.7067	4725.8332
70 MgA	6	26/07/2022	73.39	5560.0072	5310.2925
70 MgA	7	27/07/2022	89.96	5682.0369	3072.5179
70 MgA	8	27/07/2022	97.68	9650.5981	6345.3997
70 MgA	9	28/07/2022	112.62	13786.185	1176.1103
70 MgA	10	28/07/2022	121.24	23507.53	12314.549
70 MgA	11	29/07/2022	138.76	4861.8073	0
70 MgA	13	29/07/2022	143.20	8440.5974	1445.9024

Name	Sample Number	Sample Time	Duriation	Ca	Ca error
90 MgA	0	2022/10/14 23:04	0.00	119847.63	3529.1926
90 MgA	1	2022/10/15 12:38	13.57	26874.6	735.0385
90 MgA	2	2022/10/15 20:01	20.95	25865.2	1248.6238
90 MgA	3	2022/10/16 19:38	44.57	25462.686	1300.2934
90 MgA	4	2022/10/17 17:35	66.52	28258.114	1014.5839
90 MgA	5	2022/10/18 18:21	91.28	29493.943	1052.7449
90 MgA	6	2022/10/19 16:05	113.02	32899.743	1508.386
90 MgA	7	2022/10/20 17:31	138.45	34626.229	1106.6151
25 MgT	1	2023/5/28 16:21	0.00	378796.94	8536.5444
25 MgT	2	2023/5/28 16:32	0.19	377702.2	10604.778
25 MgT	3	2023/5/28 16:42	0.35	366747.54	14767.512
25 MgT	4	2023/5/28 16:52	0.52	365080.21	11807.869
25 MgT	6	2023/5/28 17:18	0.96	241323.09	6970.8289
25 MgT	7	2023/5/28 17:33	1.20	25655.054	1077.2798
25 MgT	8	2023/5/28 17:44	1.39	10964.137	108.49705
50 MgT	1	2023/6/9 16:41	0.00	327055.44	6480.3311
50 MgT	2	2023/6/9 16:53	0.20	311647.89	9931.9574
50 MgT	3	2023/6/9 17:03	0.37	308873.48	7427.4721
50 MgT	4	2023/6/9 17:11	0.50	176239.55	5721.2716
50 MgT	5	2023/6/9 17:19	0.63	4155.0851	53.219759
50 MgT	6	2023/6/9 17:25	0.73	335.49086	153.6339
50 MgT	7	2023/6/9 17:31	0.83	2300.6529	297.64665
70 MgT	1	2023/6/19 13:46	0.00	279715.67	8838.8967
70 MgT	2	2023/6/19 13:54	0.13	276604.75	8850.2423
70 MgT	3	2023/6/19 14:02	0.27	53223.329	2152.5158
70 MgT	4	2023/6/19 14:10	0.40	7435.9497	333.09289
70 MgT	5	2023/6/19 14:16	0.50	6879.886	352.76181
90 MgT	1	2023/7/2 14:00	0.00	152002.3	1223.936
90 MgT	2	2023/7/2 14:07	0.12	147236.71	3538.9218
90 MgT	3	2023/7/2 14:13	0.22	11680.12	90.381783
90 MgT	4	2023/7/2 14:19	0.32	6956.5591	63.273733
90 MgT	5	2023/7/2 14:26	0.43	8554.4666	334.4407
25 CuP	0	2022/10/6 17:19	0.00	455487.4	7787.3184
25 CuP	1	2022/10/7 16:49	23.50	459421.83	8198.2879
25 CuP	2	2022/10/8 23:43	54.40	469085.69	13045.095
25 CuP	3	2022/10/9 23:29	78.17	491650.45	17417.57
25 CuP	4	2022/10/10 17:38	96.32	482983.12	13713.195
25 CuP	5	2022/10/11 22:26	125.12	482534.98	11783.064
25 CuP	6	2022/10/12 18:26	145.12	488836.28	8168.0846

Name	Sample Number	Sample Time	Duriation	Ca	Ca error
25 CuP	7	2022/10/13 17:50	168.52	496980.54	4865.4488
25 CuP	9	2022/10/15 19:52	218.55	512175.3	7179.6741
25 CuP	11	2022/10/17 17:35	264.27	502809.97	6987.5333
25 CuP	13	2022/10/19 16:05	310.77	338724.2	7906.8786
25 CuP	16	2022/10/22 17:13	383.90	273298.28	10266.509
25 CuP	19	2022/10/25 16:12	454.88	238100.56	16119.583
25 CuP	22	2022/10/28 18:20	529.02	214977.17	12995.995
25 CuP	25	2022/10/31 17:47	600.47	193397.57	5433.9862
25 CuP	30	2022/11/8 16:06	790.78	170757.68	639.86776
50 CuP	0	2023/1/18 11:20	0.00	580454.45	6679.712
50 CuP	1	2023/1/18 18:30	7.17	593633.84	17066.591
50 CuP	2	2023/1/19 10:40	23.33	596025.15	3950.3132
50 CuP	3	2023/1/19 19:00	31.67	598965.28	28136.147
50 CuP	4	2023/1/20 09:40	46.33	536537.06	11823.453
50 CuP	5	2023/1/20 16:50	53.50	506046.45	422.52034
50 CuP	6	2023/1/22 14:30	99.17	262171.69	9578.6357
50 CuP	7	2023/1/23 12:00	120.67	218884.68	10825.558
50 CuP	10	2023/1/26 19:00	199.67	197230.32	5910.0852
50 CuP	13	2023/1/29 16:50	269.50	176697.65	4585.697
50 CuP	15	2023/1/31 11:00	311.67	174980.15	1103.5546
50 CuP	19	2023/2/5 14:20	435.00	151586.78	4834.7935
70 CuP	0	2023/2/17 20:23	0.00	464727.77	4647.5732
70 CuP	1	2023/2/18 11:20	14.95	321794.72	4274.5034
70 CuP	2	2023/2/18 20:27	24.07	303371.29	5440.6786
70 CuP	3	2023/2/19 16:05	43.70	177394.35	3845.9646
70 CuP	4	2023/2/19 19:57	47.57	213732.16	5556.2758
70 CuP	5	2023/2/20 09:30	61.12	195338.64	9613.375
70 CuP	6	2023/2/20 19:35	71.20	194044.7	9071.3943
70 CuP	7	2023/2/21 10:00	85.62	179153.27	7151.8767
70 CuP	10	2023/2/22 21:30	121.12	169994.62	1006.3932
70 CuP	14	2023/3/1 17:40	285.28	168882.92	2604.7353
90 CuP	0	2023/3/16 22:00	0.00	369399.49	9846.3856
90 CuP	1	2023/3/17 10:45	12.75	365964.14	17546.962
90 CuP	2	2023/3/17 16:00	18.00	262992.83	6136.3242
90 CuP	3	2023/3/17 21:20	23.33	219357.52	10128.422
90 CuP	4	2023/3/18 13:00	39.00	185433.19	8540.9053
90 CuP	5	2023/3/18 20:00	46.00	184039.42	4325.2157
90 CuP	6	2023/3/19 13:15	63.25	162129.91	402.11984
90 CuP	9	2023/3/21 20:15	118.25	169762.4	6697.6533

Name	Sample Number	Sample Time	Duriation	Ca	Ca error
25 CuA	0	2022/7/1 14:46	0.00	285687.99	13834.689
25 CuA	1	2022/7/1 19:46	5.00	273348.78	18452.359
25 CuA	2	2022/7/1 21:36	6.83	271843.67	25212.654
25 CuA	3	2022/7/1 23:35	8.82	275174.12	30462.819
25 CuA	4	2022/7/2 10:22	19.60	296024.82	8422.1843
25 CuA	5	2022/7/2 13:55	23.15	286770.07	19340.088
25 CuA	6	2022/7/2 21:08	30.37	204625.23	32225.509
25 CuA	7	2022/7/3 12:16	45.50	139804.88	4553.5359
25 CuA	8	2022/7/3 17:25	50.65	135362.18	18962.012
25 CuA	9	2022/7/4 10:26	67.67	96211.833	516.96373
25 CuA	10	2022/7/4 18:15	75.48	89641.394	8840.6928
25 CuA	11	2022/7/5 09:42	90.93	64143.983	0
25 CuA	12	2022/7/5 18:04	99.30	57995.538	677.69321
25 CuA	13	2022/7/6 13:14	118.47	55830.629	2945.683
25 CuA	14	2022/7/6 17:16	122.50	51767.178	1703.2762
25 CuA	15	2022/7/7 10:59	140.22	42459.316	2042.108
25 CuA	16	2022/7/7 18:50	148.07	42872.17	6095.3692
50 CuA	0	12/07/2022	0.00	230274.48	32741.84
50 CuA	1	13/07/2022	14.49	42553.176	9895.6244
50 CuA	2	13/07/2022	18.81	35605.334	5424.7011
50 CuA	3	13/07/2022	25.13	32782.452	1347.5412
50 CuA	4	14/07/2022	36.56	24922.091	2068.3301
50 CuA	5	14/07/2022	40.45	22625.908	6504.7539
50 CuA	6	14/07/2022	45.97	19337.897	4325.3592
50 CuA	7	15/07/2022	62.53	16411.36	3149.1536
50 CuA	8	15/07/2022	70.22	17918.65	2131.4716
50 CuA	9	16/07/2022	89.24	21453.751	3721.0001
50 CuA	10	16/07/2022	95.05	16484.415	4651.2479
50 CuA	11	17/07/2022	116.05	13803.795	0
50 CuA	12	18/07/2022	137.56	23145.376	8725.4701
50 CuA	end	20/07/2022	182.68	19193.332	1335.0712
70 CuA	0	23/07/2022	0.00	214828.27	25311.609
70 CuA	1	23/07/2022	3.59	80956.507	1782.4196
70 CuA	2	24/07/2022	24.34	36182.823	13855.884
70 CuA	3	25/07/2022	42.44	30374.749	2260.5285
70 CuA	4	25/07/2022	50.47	24117.716	3746.0519
70 CuA	5	26/07/2022	65.73	24027.602	4005.0076
70 CuA	6	26/07/2022	73.39	24546.342	2233.8649
70 CuA	7	27/07/2022	89.96	16419.755	693.80072

Name	Sample Number	Sample Time	Duriation	Ca	Ca error
70 CuA	8	27/07/2022	97.68	24266.128	906.41185
70 CuA	9	28/07/2022	112.62	17552.356	4348.2453
70 CuA	10	28/07/2022	121.24	12681.132	161.66375
70 CuA	11	29/07/2022	138.76	4251.5127	0
70 CuA	13	29/07/2022	143.20	18867.56	190.86411
90 CuA	0	2022/10/14 23:04	0.00	370320.8	12540.428
90 CuA	1	2022/10/15 12:38	13.57	197471.06	7381.7681
90 CuA	2	2022/10/15 20:01	20.95	181824.43	8921.2935
90 CuA	3	2022/10/16 19:38	44.57	169928.01	6617.7798
90 CuA	4	2022/10/17 17:35	66.52	185881.21	4233.1921
90 CuA	5	2022/10/18 18:21	91.28	183467.21	5279.3932
90 CuA	6	2022/10/19 16:05	113.02	196185.15	6514.4748
90 CuA	7	2022/10/20 17:31	138.45	199619.83	8122.1162
25 CuT	1	2023/6/4 16:55	0.00	323586.82	9152.653
25 CuT	2	2023/6/4 17:15	0.33	332890.87	16648.296
25 CuT	3	2023/6/4 17:27	0.53	333545.69	10586.182
25 CuT	4	2023/6/4 17:37	0.70	313173.17	8195.7523
25 CuT	5	2023/6/4 17:47	0.87	266353.21	1056.4939
25 CuT	6	2023/6/4 17:57	1.03	120322.4	3301.4618
25 CuT	7	2023/6/4 18:09	1.23	56955.192	1407.6785
50 CuT	1	2023/6/17 15:13	0.00	317761.71	9367.8723
50 CuT	2	2023/6/17 15:22	0.15	297148.32	13550.72
50 CuT	3	2023/6/17 15:30	0.28	304690.72	7933.6908
50 CuT	4	2023/6/17 15:39	0.43	287089.99	4300.0343
50 CuT	5	2023/6/17 15:48	0.58	187150.66	3709.8667
50 CuT	6	2023/6/17 15:56	0.72	30881.55	3400.922
50 CuT	7	2023/6/17 16:05	0.87	22820.784	1688.8043
70 CuT	1	2023/6/23 13:56	0.00	266668.96	14221.654
70 CuT	2	2023/6/23 14:05	0.15	255823.13	6338.6411
70 CuT	3	2023/6/23 14:13	0.28	216818.53	7097.937
70 CuT	4	2023/6/23 14:21	0.42	24711.414	1407.4706
70 CuT	5	2023/6/23 14:29	0.55	24064.614	1336.9961
70 CuT	6	2023/6/23 14:35	0.65	27730.248	857.98019
90 CuT	1	2023/6/25 16:10	0.00	192875.26	4692.4538
90 CuT	2	2023/6/25 16:18	0.13	159774.3	4848.9587
90 CuT	3	2023/6/25 16:26	0.27	35459.34	5207.3917
90 CuT	4	2023/6/25 16:32	0.37	34190.478	2839.8556
90 CuT	5	2023/6/25 16:36	0.43	35707.896	5240.9542
25 SrA	0	2023/1/25 13:00	0.00	443329.37	13376.526

Name	Sample Number	Sample Time	Duriation	Ca	Ca error
25 SrA	1	2023/1/25 19:00	6.00	437242.94	15748.46
25 SrA	2	2023/1/26 09:30	20.50	374471.37	14990.446
25 SrA	3	2023/1/26 19:00	30.00	290434.66	9129.5254
25 SrA	4	2023/1/27 09:20	44.33	246388.37	9111.0394
25 SrA	5	2023/1/27 19:00	54.00	172148.83	6659.5578
25 SrA	6	2023/1/28 13:00	72.00	183474.97	9063.927
25 SrA	7	2023/1/29 16:50	99.83	160361.2	3861.6856
25 SrA	9	2023/1/31 18:50	149.83	141212.4	6690.8666
50 SrA	1	2023/2/6 11:20	0.00	423762.09	10798.672
50 SrA	2	2023/2/6 19:15	7.92	380962.57	7710.9696
50 SrA	3	2023/2/7 10:00	22.67	158458.31	3906.7418
50 SrA	4	2023/2/7 20:15	32.92	137149.43	4000.3913
50 SrA	5	2023/2/8 09:15	45.92	118053.51	4018.0056
50 SrA	6	2023/2/8 19:20	56.00	106151.29	2667.2624
50 SrA	7	2023/2/9 10:00	70.67	106100.2	2393.4514
50 SrA	8	2023/2/9 19:15	79.92	97732.914	6034.4695
50 SrA	9	2023/2/10 09:45	94.42	95206.8	3328.5887
70 SrA	0	2023/2/21 21:30	0.00	348467.26	8455.5951
70 SrA	1	2023/2/22 09:05	11.58	171603.11	5485.77
70 SrA	2	2023/2/22 21:30	24.00	126649.37	2315.9239
70 SrA	3	2023/2/23 08:40	35.17	113796.29	3338.4839
70 SrA	4	2023/2/23 21:00	47.50	105223.23	2645.1256
70 SrA	5	2023/2/24 10:10	60.67	109342.06	1969.0078
70 SrA	7	2023/2/25 19:00	93.50	86583.543	2629.2804
90 SrA	0	2023/3/18 16:00	0.00	200345.49	7815.5994
90 SrA	1	2023/3/18 20:00	4.00	142085.71	4630.9844
90 SrA	2	2023/3/19 13:15	21.25	95904.057	3999.9146
90 SrA	3	2023/3/19 22:15	30.25	92226.371	2550.2825
90 SrA	4	2023/3/20 10:00	42.00	92426.971	2640.5211
25 SrT	1	2023/6/4 15:30	0.00	438456.86	14904.977
25 SrT	2	2023/6/4 15:45	0.25	427863.8	11540.594
25 SrT	3	2023/6/4 16:03	0.55	420712.49	13138.96
25 SrT	4	2023/6/4 16:11	0.68	413008.14	16042.05
25 SrT	5	2023/6/4 16:25	0.92	27406.771	1267.7414
25 SrT	6	2023/6/4 16:32	1.03	23478.714	1043.616
25 SrT	7	2023/6/4 16:40	1.17	18990.343	676.08704
50 SrT	1	2023/6/17 14:00	0.00	372395.54	18446.47
50 SrT	2	2023/6/17 14:11	0.18	369585.54	10234.334
50 SrT	3	2023/6/17 14:22	0.37	362221.69	7254.7384

Name	Sample Number	Sample Time	Duriation	Ca	Ca error
50 SrT	4	2023/6/17 14:32	0.53	115602.2	3497.5272
50 SrT	5	2023/6/17 14:39	0.65	5806.5714	210.439
50 SrT	6	2023/6/17 14:48	0.80	1565.8	150.2909
70 SrT	1	2023/6/23 12:50	0.00	281576.51	10028.168
70 SrT	2	2023/6/23 13:00	0.17	279703.69	7901.9478
70 SrT	3	2023/6/23 13:07	0.28	241717.71	11167.797
70 SrT	4	2023/6/23 13:15	0.42	7373.5714	531.09498
70 SrT	5	2023/6/23 13:23	0.55	0	398.61985
70 SrT	6	2023/6/23 13:31	0.68	863.02857	143.58308
90 SrT	1	2023/7/2 14:34	0.00	191873.11	5675.4794
90 SrT	2	2023/7/2 14:39	0.08	158812.2	6000.7326
90 SrT	3	2023/7/2 14:45	0.18	25067.2	875.34331
90 SrT	4	2023/7/2 14:50	0.27	0	234.95854
90 SrT	5	2023/7/2 14:54	0.33	0	288.87798

Bibliography

Adkins, J.F., Boyle, E.A., Curry, W.B., Lutringer, A., 2003. Stable isotopes in deep-sea corals and a new mechanism for "vital effects". Geochim. Cosmochim. Acta 67, 1129-1143.
Alvarez, C.C., Quitté, G., Schott, J., Oelkers, E.H., 2021. Nickel isotope fractionation as a function of carbonate growth rate during Ni coprecipitation with calcite. Geochim. Cosmochim. Acta 299, 184-198.
Anderson, N.T., Kelson, J.R., Kele, S., Daëron, M., Bonifacie, M., Horita, J., Mackey, T.J., John, C.M., Kluge, T., Petschnig, P., Jost, A.B., Huntington, K.W., Bernasconi, S.M., Bergmann, K.D., 2021. A Unified Clumped Isotope Thermometer Calibration (0.5–1,100°C) Using Carbonate-Based Standardization. Geophys. Res. Lett. 48, e2020GL092069.
Assonov, S.S., Brenninkmeijer, C.A., 2003. A redetermination of absolute values for 17RVPDB-CO2 and 17RVSMOW. Rapid Commun. Mass Spectrom. 17, 1017-1029.
Bajnai, D., Guo, W., Spötl, C., Coplen, T.B., Methner, K., Löffler, N., Krsnik, E., Gischler, E., Hansen, M., Henkel, D., Price, G.D., Raddatz, J., Scholz, D., Fiebig, J., 2020. Dual clumped isotope thermometry resolves kinetic biases in carbonate formation temperatures. Nature Communications 11, 4005.
Beck, W.C., Grossman, E.L., Morse, J.W., 2005. Experimental studies of oxygen isotope fractionation in the carbonic acid system at 15°, 25°, and 40°C. Geochim. Cosmochim. Acta 69, 3493-3503.
Becker, R., Döring, W., 1935. Kinetische Behandlung der Keimbildung in übersättigten Dämpfen. Annalen der Physik 416, 719-752.
Bernasconi, S.M., Daëron, M., Bergmann, K.D., Bonifacie, M., Meckler, A.N., Affek, H.P., Anderson, N., Bajnai, D., Barkan, E., Beverly, E., Blamart, D., Burgener, L., Calmels, D., Chaduteau, C., Clog, M., Davidheiser-Kroll, B., Davies, A., Dux, F., Eiler, J., Elliott, B., Fetrow, A.C., Fiebig, J., Goldberg, S., Hermoso, M., Huntington, K.W., Hyland, E., Ingalls, M., Jaggi, M., John, C.M., Jost, A.B., Katz, S., Kelson, J., Kluge, T., Kocken, I.J., Laskar, A., Leutert, T.J., Liang, D., Lucarelli, J., Mackey, T.J., Mangenot, X., Meinicke, N., Modestou, S.E., Müller, I.A., Murray, S., Neary, A., Packard, N., Passey, B.H., Pelletier, E., Petersen, S., Piasecki, A., Schauer, A., Snell, K.E., Swart, P.K., Tripati, A., Upadhyay, D., Vennemann, T., Winkelstern, I., Yarian, D., Yoshida, N., Zhang, N., Ziegler, M., 2021. InterCarb: A community effort to improve inter-laboratory standardization of the carbonate clumped isotope thermometer using carbonate standards. Geochem. Geophys. Geosyst. n/a, e2020GC009588.
Bernasconi, S.M., Hu, B., Wacker, U., Fiebig, J., Breitenbach, S.F.M., Rutz, T., 2013. Background effects on Faraday collectors in gas-source mass spectrometry and implications for clumped isotope measurements. Rapid Commun. Mass Spectrom. 27, 603-612.
Bigeleisen, J., 1955. Statistical Mechanics of Isotopic Systems with Small Quantum Corrections. I. General Considerations and the Rule of the Geometric Mean. The Journal of Chemical Physics 23, 2264-2267.

Blue, C.R., Giuffre, A., Mergelsberg, S., Han, N., De Yoreo, J.J., Dove, P.M., 2017. Chemical and physical controls on the transformation of amorphous calcium carbonate into crystalline CaCO3 polymorphs. Geochim. Cosmochim. Acta 196, 179-196.
Bots, P., Benning, L.G., Rickaby, R.E.M., Shaw, S., 2011. The role of SO4 in the switch from calcite to aragonite seas. Geology 39, 331-334.
Böttcher, M.E., 1997. Comment on "solid solution partitioning of Sr2+, Ba2+, and Cd2+ to calcite" by A. J. Tesoriero and J. F. Pankow. Geochim. Cosmochim. Acta 61, 661-662.
Brand, W.A., Assonov, S.S., Coplen, T.B., 2010. Correction for the 17O interference in δ(13C) measurements when analyzing CO2 with stable isotope mass spectrometry (IUPAC Technical Report). Pure and Applied Chemistry 82, 1719-1733.
Bretti, C., Foti, C., Sammartano, S., 2004. A new approach in the use of SIT in determining the dependence on ionic strength of activity coefficients. Application to some chloride salts of interest in the speciation of natural fluids. Chemical Speciation & Bioavailability 16, 105-110.
Burton, E.A., Walter, L.M., 1991. The effects of PCO2 and temperature on magnesium incorporation in calcite in seawater and MgCl2-CaCl2 solutions. Geochim. Cosmochim. Acta 55, 777-785.
Busenberg, E., Niel Plummer, L., 1985. Kinetic and thermodynamic factors controlling the distribution of SO32− and Na+ in calcites and selected aragonites. Geochim. Cosmochim. Acta 49, 713-725.
Cao, X., 2024. Formation of carbonate polymorphs under controlled laboratory conditions: Relative control of temperature, precipitation rate and ionic impurities, V5 ed. Mendeley Data.
Cao, X., Zhong, D., Liu, J., Sun, H., Song, Z., Cao, T., Wang, F., Gong, S., 2020. Coupling between Diagenetic Environment and Porosity Evolution—A Quantitative Study of the Zhuhai Formation in the Huizhou Sag, Pearl River Mouth Basin, South China Sea, Minerals.
Chen, J., Xiang, L., 2009. Controllable synthesis of calcium carbonate polymorphs at different temperatures. Powder Technol. 189, 64-69.
Cherkas, O., Beuvier, T., Zontone, F., Chushkin, Y., Demoulin, L., Rousseau, A., Gibaud, A., 2018. On the kinetics of phase transformations of dried porous vaterite particles immersed in deionized and tap water. Adv. Powder Technol. 29, 2872-2880.
Chuang, C., 1987. The analysis of a titration study. Stat. Med. 6, 583-590.
Coplen, T.B., Kendall, C., Hopple, J., 1983. Comparison of stable isotope reference samples. Nature 302, 236-238.
Curl, R.L., 1962. The aragonite-calcite problem. Bulletin of the National Speleological Society 24, 57-73.
D'Autry, W., Wolfs, K., Yarramraju, S., Schepdael, A.V., Hoogmartens, J., Adams, E., 2010. Characterization and Improvement of Signal Drift Associated with Electron Ionization Quadrupole Mass Spectrometry. Anal. Chem. 82, 6480-6486.
Daëron, M., Blamart, D., Peral, M., Affek, H.P., 2016. Absolute isotopic abundance ratios and the accuracy of Δ47 measurements. Chem. Geol. 442, 83-96.
Daëron, M., Drysdale, R.N., Peral, M., Huyghe, D., Blamart, D., Coplen, T.B., Lartaud, F., Zanchetta, G., 2019. Most Earth-surface calcites precipitate out of isotopic equilibrium. Nature Communications 10, 429.
Darling, W.G., Bath, A.H., Talbot, J.C., 2003. The O and H stable isotope composition of freshwaters in the British Isles. 2. Surface waters and groundwater. Hydrol. Earth Syst. Sci. 7, 183-195.

Davies, A.J., Davis, S., John, C.M., 2021. Evidence of taxonomic non-equilibrium effects in the clumped isotope composition of modern cephalopod carbonate. Chem. Geol. 578, 120317.
Davies, A.J., John, C.M., 2017. Reducing contamination parameters for clumped isotope analysis: The effect of lowering Porapak™ Q trap temperature to below –50°C. Rapid Commun. Mass Spectrom. 31, 1313-1323.
Davies, A.J., John, C.M., 2019. The clumped (13C18O) isotope composition of echinoid calcite: Further evidence for "vital effects" in the clumped isotope proxy. Geochim. Cosmochim. Acta 245, 172-189.
Davies, C., 1962. Ion association.,(Butterworths: London). Ion association. Butterworths, London., -.
Davis, K.J., Dove, P.M., De Yoreo, J.J., 2000a. The Role of Mg2+ as an Impurity in Calcite Growth. Science 290, 1134-1137.
Davis, K.J., Dove, P.M., Yoreo, J.J.D., 2000b. Resolving the Control of Magnesium on Calcite Growth: Thermodynamic and Kinetic Consequences of Impurity Incorporation for Biomineral Formation. MRS Proceedings 620, M9.5.1.
De Choudens-Sánchez, V., González, L.A., 2009. Calcite and Aragonite Precipitation Under Controlled Instantaneous Supersaturation: Elucidating the Role of CaCO3 Saturation State and Mg/Ca Ratio on Calcium Carbonate Polymorphism. Journal of Sedimentary Research 79, 363-376.
De Villiers, S., Nelson, B.K., Chivas, A.R., 1995. Biological Controls on Coral Sr/Ca and δ¹⁸O Reconstructions of Sea Surface Temperatures. Science 269, 1247.
Debye, P., Hückel, E., 1923. Zur Theorie Der Elektrolyte. I. Gefrierpunktserniedrigung Und Verwandte Erscheinungen. Phys. Zeitschrift 24, 185-206.
Dennis, K.J., Affek, H.P., Passey, B.H., Schrag, D.P., Eiler, J.M., 2011. Defining an absolute reference frame for 'clumped' isotope studies of CO2. Geochim. Cosmochim. Acta 75, 7117-7131.
Dennis, K.J., Cochran, J.K., Landman, N.H., Schrag, D.P., 2013. The climate of the Late Cretaceous: New insights from the application of the carbonate clumped isotope thermometer to Western Interior Seaway macrofossil. Earth. Planet. Sci. Lett. 362, 51-65.
DePaolo, D.J., 2011. Surface kinetic model for isotopic and trace element fractionation during precipitation of calcite from aqueous solutions. Geochim. Cosmochim. Acta 75, 1039-1056.
Dietzel, M., 2011. Carbonates, in: Reitner, J., Thiel, V. (Eds.), Encyclopedia of Geobiology. Springer Netherlands, Dordrecht, pp. 261-266.
Dietzel, M., Gussone, N., Eisenhauer, A., 2004. Co-precipitation of Sr2+ and Ba2+ with aragonite by membrane diffusion of CO2 between 10 and 50 °C. Chem. Geol. 203, 139-151.
Dietzel, M., Tang, J., Leis, A., Köhler, S.J., 2009. Oxygen isotopic fractionation during inorganic calcite precipitation — Effects of temperature, precipitation rate and pH. Chemical Geology 268, 107-115.
Dietzel, M., Usdowski, E., 1996. Coprecipitation of Ni2+, Co2+, and Mn2+ with galena and covellite, and of Sr2+ with calcite during crystallization via diffusion of H2S and C02 through polyethylene at 20°C: Power law and Nernst law control of trace element partitioning. Chem. Geol. 131, 55-65.
Dromgoole, E.L., Walter, L.M., 1990a. Inhibition of calcite growth rates by Mn2+ in CaCl2 solutions at 10, 25, and 50°C. Geochim. Cosmochim. Acta 54, 2991-3000.
Dromgoole, E.L., Walter, L.M., 1990b. Iron and manganese incorporation into calcite: Effects of growth kinetics, temperature and solution chemistry. Chem. Geol. 81, 311-336.
Eagle, R.A., Eiler, J.M., Tripati, A.K., Ries, J.B., Freitas, P.S., Hiebenthal, C., Wanamaker Jr, A.D., Taviani, M., Elliot, M., Marenssi, S., Nakamura, K., Ramirez, P., Roy, K., 2013. The

influence of temperature and seawater carbonate saturation state on ¹³C–¹⁸O bond ordering in bivalve mollusks. Biogeosciences 10, 4591-4606.
Eiler, J.M., 2006. 'Clumped' isotope geochemistry. Geochim. Cosmochim. Acta 70, A156.
Eiler, J.M., 2007. "Clumped-isotope" geochemistry—The study of naturally-occurring, multiply-substituted isotopologues. Earth. Planet. Sci. Lett. 262, 309-327.
Eiler, J.M., 2011. Paleoclimate reconstruction using carbonate clumped isotope thermometry. Quaternary Science Reviews 30, 3575-3588.
Eiler, J.M., Clog, M., Magyar, P., Piasecki, A., Sessions, A., Stolper, D., Deerberg, M., Schlueter, H.-J., Schwieters, J., 2013. A high-resolution gas-source isotope ratio mass spectrometer. Int. J. Mass spectrom. 335, 45-56.
Eiler, J.M., Schauble, E., 2004. 18O13C16O in Earth's atmosphere. Geochim. Cosmochim. Acta 68, 4767-4777.
Elderfield, H., Vautravers, M., Cooper, M., 2002. The relationship between shell size and Mg/Ca, Sr/Ca, δ18O, and δ13C of species of planktonic foraminifera. Geochem. Geophys. Geosyst. 3, 1-13.
Elhadj, S., Salter, E.A., Wierzbicki, A., De Yoreo, J.J., Han, N., Dove, P.M., 2006. Peptide Controls on Calcite Mineralization: Polyaspartate Chain Length Affects Growth Kinetics and Acts as a Stereochemical Switch on Morphology. Crystal Growth & Design 6, 197-201.
Evans, D., Müller, W., 2012. Deep time foraminifera Mg/Ca paleothermometry: Nonlinear correction for secular change in seawater Mg/Ca. Paleoceanography 27, np-n/a.
Falk, E.S., Guo, W., Paukert, A.N., Matter, J.M., Mervine, E.M., Kelemen, P.B., 2016. Controls on the stable isotope compositions of travertine from hyperalkaline springs in Oman: Insights from clumped isotope measurements. Geochim. Cosmochim. Acta 192, 1-28.
Fernandez, A., Tang, J., Rosenheim, B.E., 2014. Siderite 'clumped' isotope thermometry: A new paleoclimate proxy for humid continental environments. Geochim. Cosmochim. Acta 126, 411-421.
Fernández-Díaz, L., Putnis, A., Prieto, M., Putnis, C.V., 1996. The role of magnesium in the crystallization of calcite and aragonite in a porous medium. Journal of Sedimentary Research 66, 482-491.
Fiebig, J., Daëron, M., Bernecker, M., Guo, W., Schneider, G., Boch, R., Bernasconi, S.M., Jautzy, J., Dietzel, M., 2021. Calibration of the dual clumped isotope thermometer for carbonates. Geochim. Cosmochim. Acta 312, 235-256.
Finch, A.A., Allison, N., 2007. Coordination of Sr and Mg in calcite and aragonite. Mineralogical Magazine 71, 539-552.
Friedman, I., O'Neil, J.R., 1977. Compilation of stable isotope fractionation factors of geochemical interest, Professional Paper, - ed.
Friend, A.S., Kamalesh, M., Schellhase, E., Eckert, G.J., Evans, T.S., 2009. Effect of time to titration to maximum dose of statins on cardiovascular outcomes: a retrospective analysis in high-risk patients. Am. J. Cardiovasc. Drugs 9, 103-107.
Füger, A., Konrad, F., Leis, A., Dietzel, M., Mavromatis, V., 2019. Effect of growth rate and pH on lithium incorporation in calcite. Geochim. Cosmochim. Acta 248, 14-24.
Gabitov, R.I., Gaetani, G.A., Watson, E.B., Cohen, A.L., Ehrlich, H.L., 2008. Experimental determination of growth rate effect on U6+ and Mg2+ partitioning between aragonite and fluid at elevated U6+ concentration. Geochim. Cosmochim. Acta 72, 4058-4068.
Gabitov, R.I., Watson, E.B., 2006. Partitioning of strontium between calcite and fluid. Geochem. Geophys. Geosyst. 7.

Gabitov, R.I., Watson, E.B., Sadekov, A., 2012. Oxygen isotope fractionation between calcite and fluid as a function of growth rate and temperature: An in situ study. Chem. Geol. 306-307, 92-102.
Gebauer, D., V?lkel, A., C?lfen, H., 2008. Stable Prenucleation Calcium Carbonate Clusters. Science 322, 1819-1822.
Ghosh, P., Adkins, J., Affek, H., Balta, B., Guo, W., Schauble, E.A., Schrag, D., Eiler, J.M., 2006. 13C–18O bonds in carbonate minerals: A new kind of paleothermometer. Geochim. Cosmochim. Acta 70, 1439-1456.
Goetschl, K.E., Purgstaller, B., Dietzel, M., Mavromatis, V., 2019. Effect of sulfate on magnesium incorporation in low-magnesium calcite. Geochim. Cosmochim. Acta 265, 505-519.
Goto, M., 1961. Some mineralo-chemical problems concerning calcite and aragonite, with special reference to the genesis of aragonite. Journal of the Faculty of Science, Hokkaido University. Series 4, Geology and mineralogy 10, 571-640.
GÖTte, T., Richter, D.K., 2009. Quantitative aspects of Mn-activated cathodoluminescence of natural and synthetic aragonite. Sedimentology 56, 483-492.
Grauel, A.-L., Schmid, T.W., Hu, B., Bergami, C., Capotondi, L., Zhou, L., Bernasconi, S.M., 2013. Calibration and application of the 'clumped isotope' thermometer to foraminifera for high-resolution climate reconstructions. Geochim. Cosmochim. Acta 108, 125-140.
Guggenheim, E.A., Turgeon, J.C., 1955. Specific interaction of ions. Transactions of the Faraday Society 51, 747-761.
Guo, W., Mosenfelder, J.L., Goddard, W.A., Eiler, J.M., 2009. Isotopic fractionations associated with phosphoric acid digestion of carbonate minerals: Insights from first-principles theoretical modeling and clumped isotope measurements. Geochim. Cosmochim. Acta 73, 7203-7225.
Hampt Andreasen, G., Delaney, M.L., 2000. Bulk calcite size fraction distribution and Sr/Ca composition for deep-sea sediments at selected age horizons. Mar. Geol. 169, 185-205.
Hartman, P., 1973. Crystal growth: an introduction, in: Hartman, P. (Ed.). North-Holland Pub. Co.;, Amsterdam.
Hasiuk, F.J., Lohmann, K.C., 2010. Application of calcite Mg partitioning functions to the reconstruction of paleocean Mg/Ca. Geochim. Cosmochim. Acta 74, 6751-6763.
Hasse, B., Ehrenberg, H., Marxen, J.C., Becker, W., Epple, M., 2000. Calcium Carbonate Modifications in the Mineralized Shell of the Freshwater Snail Biomphalaria glabrata. Chemistry – A European Journal 6, 3679-3685.
Henderson, L.M., Kracek, F.C., 1927. THE FRACTIONAL PRECIPITATION OF BARIUM AND RADIUM CHROMATES1. Journal of the American Chemical Society 49, 738-749.
Henkes, G.A., Passey, B.H., Wanamaker, A.D., Grossman, E.L., Ambrose, W.G., Carroll, M.L., 2013. Carbonate clumped isotope compositions of modern marine mollusk and brachiopod shells. Geochim. Cosmochim. Acta 106, 307-325.
Herlambang, A., John, C.M., 2021. Combining clumped isotope and trace element analysis to constrain potential kinetic effects in calcite. Geochim. Cosmochim. Acta https://doi.org/10.1016/j.gca.2020.12.024.
Hill, P.S., Tripati, A.K., Schauble, E.A., 2014. Theoretical constraints on the effects of pH, salinity, and temperature on clumped isotope signatures of dissolved inorganic carbon species and precipitating carbonate minerals. Geochim. Cosmochim. Acta 125, 610-652.
Holdsworth, C., MacDonald, J., John, C., 2022. Non-Linear Clumped Isotopes from DIC Endmember Mixing and Kinetic Isotope Fractionation in High pH Anthropogenic Tufa, Minerals.
Horn, D., Rieger, J., 2001. Organic Nanoparticles in the Aqueous Phase—Theory, Experiment, and Use. Angew. Chem. Int. Ed. 40, 4330-4361.

Huang, Y., Fairchild, I.J., 2001. Partitioning of Sr2+ and Mg2+ into calcite under karst-analogue experimental conditions. Geochim. Cosmochim. Acta 65, 47-62.
Huntington, K.W., Budd, D.A., Wernicke, B.P., Eiler, J.M., 2011. Use of Clumped-Isotope Thermometry To Constrain the Crystallization Temperature of Diagenetic Calcite. Journal of Sedimentary Research 81, 656-669.
Huntington, K.W., Eiler, J.M., Affek, H.P., Guo, W., Bonifacie, M., Yeung, L.Y., Thiagarajan, N., Passey, B., Tripati, A., Daëron, M., Came, R., 2009. Methods and limitations of 'clumped' CO2 isotope (Δ47) analysis by gas-source isotope ratio mass spectrometry. J. Mass Spectrom. 44, 1318-1329.
Huntington, K.W., Petersen, S.V., 2023. Frontiers of Carbonate Clumped Isotope Thermometry. Annual Review of Earth and Planetary Sciences 51, 611-641.
Immenhauser, A., Nägler, T.F., Steuber, T., Hippler, D., 2005. A critical assessment of mollusk 18O/16O, Mg/Ca, and 44Ca/40Ca ratios as proxies for Cretaceous seawater temperature seasonality. Palaeogeography, Palaeoclimatology, Palaeoecology 215, 221-237.
Jiménez-López, C., Caballero, E., Huertas, F.J., Romanek, C.S., 2001. Chemical, mineralogical and isotope behavior, and phase transformation during the precipitation of calcium carbonate minerals from intermediate ionic solution at 25°C. Geochim. Cosmochim. Acta 65, 3219-3231.
Jiménez-López, C., Romanek, C.S., Huertas, F.J., Ohmoto, H., Caballero, E., 2004. Oxygen isotope fractionation in synthetic magnesian calcite 1 1Associate editor: D. R. Cole. Geochim. Cosmochim. Acta 68, 3367-3377.
John, C.M., Bowen, D., 2016. Community software for challenging isotope analysis: First applications of 'Easotope' to clumped isotopes. Rapid Commun. Mass Spectrom. 30, 2285-2300.
John, C.M., Davis, S., 2015. A Review of the Performance of the "Imperial Batch EXtraction" (IBEX) Device for Clumped Isotope Analysis. Scholar Commons.
Jones, B., 2017. Review of calcium carbonate polymorph precipitation in spring systems. Sedimentary Geology 353, 64-75.
Jones, B., Peng, X., 2014. Hot spring deposits on a cliff face: A case study from Jifei, Yunnan Province, China. Sedimentary Geology 302, 1-28.
Kawano, M., Obokata, S., 2007. Effects of Cyanobacteria on Precipitation Rate and Polymorphism of CaCO3Minerals in Hot Spring Water. Journal of the Clay Science Society of Japan (in Japanese) 46, 156-168.
Kelson, J.R., Huntington, K.W., Schauer, A.J., Saenger, C., Lechler, A.R., 2017. Toward a universal carbonate clumped isotope calibration: Diverse synthesis and preparatory methods suggest a single temperature relationship. Geochim. Cosmochim. Acta 197, 104-131.
Killawee, J.A., Fairchild, I.J., Tison, J.L., Janssens, L., Lorrain, R., 1998. Segregation of solutes and gases in experimental freezing of dilute solutions: implications for natural glacial systems. Geochim. Cosmochim. Acta 62, 3637-3655.
Kim, S.-T., Hillaire-Marcel, C., Mucci, A., 2006. Mechanisms of equilibrium and kinetic oxygen isotope effects in synthetic aragonite at 25°C. Geochim. Cosmochim. Acta 70, 5790-5801.
Kim, S.-T., O'Neil, J.R., 1997. Equilibrium and nonequilibrium oxygen isotope effects in synthetic carbonates. Geochim. Cosmochim. Acta 61, 3461-3475.
Kim, S.-T., O'Neil, J.R., Hillaire-Marcel, C., Mucci, A., 2007. Oxygen isotope fractionation between synthetic aragonite and water: Influence of temperature and Mg2+ concentration. Geochim. Cosmochim. Acta 71, 4704-4715.
Kitano, Y., 1962a. The Behavior of Various Inorganic Ions in the Separation of Calcium Carbonate from a Bicarbonate Solution. Bull. Chem. Soc. Jpn. 35, 1973-1980.

Kitano, Y., 1962b. A Study of the Polymorphic Formation of Calcium Carbonate in Thermal Springs with an Emphasis on the Effect of Temperature. Bull. Chem. Soc. Jpn. 35, 1980-1985.
Kluge, T., John, C.M., 2015a. Effects of brine chemistry and polymorphism on clumped isotopes revealed by laboratory precipitation of mono- and multiphase calcium carbonates. Geochim. Cosmochim. Acta 160, 155-168.
Kluge, T., John, C.M., 2015b. Technical Note: A simple method for vaterite precipitation for isotopic studies: implications for bulk and clumped isotope analysis. Biogeosciences 12, 3289-3299.
Kluge, T., John, C.M., Jourdan, A.-L., Davis, S., Crawshaw, J., 2015. Laboratory calibration of the calcium carbonate clumped isotope thermometer in the 25–250°C temperature range. Geochim. Cosmochim. Acta 157, 213-227.
Knight, A.W., Harvey, J.A., Shohel, M., Lu, P., Cummings, D., Ilgen, A.G., 2023. The combined effects of Mg2+ and Sr2+ incorporation during CaCO3 precipitation and crystal growth. Geochim. Cosmochim. Acta 345, 16-33.
Lakshtanov, L.Z., Stipp, S.L.S., 2007. Experimental study of nickel(II) interaction with calcite: Adsorption and coprecipitation. Geochim. Cosmochim. Acta 71, 3686-3697.
Lam, R.S.K., Charnock, J.M., Lennie, A., Meldrum, F.C., 2007. Synthesis-dependant structural variations in amorphous calcium carbonate. CrystEngComm 9, 1226-1236.
Lear, C.H., Elderfield, H., Wilson, P.A., 2000. Cenozoic Deep-Sea Temperatures and Global Ice Volumes from Mg/Ca in Benthic Foraminiferal Calcite. Science 287, 269-272.
Lewis, G.N., 1907. Outlines of a New System of Thermodynamic Chemistry. Proceedings of the American Academy of Arts and Sciences 43, 259-293.
Lorens, R.B., 1981. Sr, Cd, Mn and Co distribution coefficients in calcite as a function of calcite precipitation rate. Geochim. Cosmochim. Acta 45, 553-561.
Marriott, C.S., Henderson, G.M., Belshaw, N.S., Tudhope, A.W., 2004. Temperature dependence of δ7Li, δ44Ca and Li/Ca during growth of calcium carbonate. Earth. Planet. Sci. Lett. 222, 615-624.
Martin, P.A., Lea, D.W., Mashiotta, T.A., Papenfuss, T., Sarnthein, M., 2000. Variation of foraminiferal Sr/Ca over Quaternary glacial-interglacial cycles: Evidence for changes in mean ocean Sr/Ca? Geochem. Geophys. Geosyst. 1.
Mason, B.H., 1966. Principles of Geochemistry. Wiley.
Matsumoto, M., Fukunaga, T., Onoe, K., 2010. Polymorph control of calcium carbonate by reactive crystallization using microbubble technique. Chem. Eng. Res. Des. 88, 1624-1630.
Mavromatis, V., Brazier, J.-M., Goetschl, K.E., 2022. Controls of temperature and mineral growth rate on Mg incorporation in aragonite. Geochim. Cosmochim. Acta 317, 53-64.
Mavromatis, V., Gautier, Q., Bosc, O., Schott, J., 2013. Kinetics of Mg partition and Mg stable isotope fractionation during its incorporation in calcite. Geochim. Cosmochim. Acta 114, 188-203.
Mavromatis, V., Goetschl, K.E., Grengg, C., Konrad, F., Purgstaller, B., Dietzel, M., 2018. Barium partitioning in calcite and aragonite as a function of growth rate. Geochim. Cosmochim. Acta 237, 65-78.
Mavromatis, V., González, A.G., Dietzel, M., Schott, J., 2019. Zinc isotope fractionation during the inorganic precipitation of calcite – Towards a new pH proxy. Geochim. Cosmochim. Acta 244, 99-112.
Mavromatis, V., Montouillout, V., Noireaux, J., Gaillardet, J., Schott, J., 2015. Characterization of boron incorporation and speciation in calcite and aragonite from co-precipitation experiments

under controlled pH, temperature and precipitation rate. Geochim. Cosmochim. Acta 150, 299-313.
Meldrum, F.C., 2003. Calcium carbonate in biomineralisation and biomimetic chemistry. Int. Mater. Rev. 48, 187-224.
Meyer, H.J., 1984. The influence of impurities on the growth rate of calcite. J. Cryst. Growth 66, 639-646.
Millero, F.J., Yao, W., Aicher, J., 1995. The speciation of Fe(II) and Fe(III) in natural waters. Mar. Chem. 50, 21-39.
Mills, J.V., Barnhart, H.A., DePaolo, D.J., Lammers, L.N., 2022. New insights into Mn2+ and Mg2+ inhibition of calcite growth. Geochim. Cosmochim. Acta 334, 338-367.
Molnár, Z., Pekker, P., Dódony, I., Pósfai, M., 2021. Clay minerals affect calcium (magnesium) carbonate precipitation and aging. Earth. Planet. Sci. Lett. 567, 116971.
Montagna, P., McCulloch, M., Douville, E., López Correa, M., Trotter, J., Rodolfo-Metalpa, R., Dissard, D., Ferrier-Pagès, C., Frank, N., Freiwald, A., Goldstein, S., Mazzoli, C., Reynaud, S., Rüggeberg, A., Russo, S., Taviani, M., 2014. Li/Mg systematics in scleractinian corals: Calibration of the thermometer. Geochim. Cosmochim. Acta 132, 288-310.
Morse, J.W., Bender, M.L., 1990. Partition coefficients in calcite: Examination of factors influencing the validity of experimental results and their application to natural systems. Chem. Geol. 82, 265-277.
Mucci, A., 1988. Manganese uptake during calcite precipitation from seawater: Conditions leading to the formation of a pseudokutnahorite. Geochim. Cosmochim. Acta 52, 1859-1868.
Mucci, A., Morse, J.W., 1983. The incorporation of Mg2+ and Sr2+ into calcite overgrowths: influences of growth rate and solution composition. Geochim. Cosmochim. Acta 47, 217-233.
Müller, I.A., Violay, M.E.S., Storck, J.-C., Fernandez, A., van Dijk, J., Madonna, C., Bernasconi, S.M., 2017. Clumped isotope fractionation during phosphoric acid digestion of carbonates at 70°C. Chem. Geol. 449, 1-14.
Müller, W.E.G., Neufurth, M., Huang, J., Wang, K., Feng, Q., Schröder, H.C., Diehl-Seifert, B., Muñoz-Espí, R., Wang, X., 2015. Nonenzymatic Transformation of Amorphous CaCO3 into Calcium Phosphate Mineral after Exposure to Sodium Phosphate in Vitro: Implications for in Vivo Hydroxyapatite Bone Formation. Chembiochem 16, 1323-1332.
Navrotsky, A., 2004. Energetic clues to pathways to biomineralization: Precursors, clusters, and nanoparticles. Proceedings of the National Academy of Sciences 101, 12096-12101.
Nielsen, L.C., De Yoreo, J.J., DePaolo, D.J., 2013. General model for calcite growth kinetics in the presence of impurity ions. Geochim. Cosmochim. Acta 115, 100-114.
Nielsen, M.R., Sand, K.K., Rodriguez-Blanco, J.D., Bovet, N., Generosi, J., Dalby, K.N., Stipp, S.L.S., 2016. Inhibition of Calcite Growth: Combined Effects of Mg2+ and SO42–. Crystal Growth & Design 16, 6199-6207.
Nilsson, Ö., Sternbeck, J., 1999. A mechanistic model for calcite crystal growth using surface speciation. Geochim. Cosmochim. Acta 63, 217-225.
Nishiyama, R., Munemoto, T., Fukushi, K., 2013. Formation condition of monohydrocalcite from CaCl2–MgCl2–Na2CO3 solutions. Geochim. Cosmochim. Acta 100, 217-231.
O'Neil, J.R., Clayton, R.N., Mayeda, T.K., 1969. Oxygen Isotope Fractionation in Divalent Metal Carbonates. The Journal of Chemical Physics 51, 5547-5558.
Ogino, T., Suzuki, T., Sawada, K., 1990. The rate and mechanism of polymorphic transformation of calcium carbonate in water. J. Cryst. Growth 100, 159-167.

Oomori, T., Kaneshima, H., Maezato, Y., Kitano, Y., 1987. Distribution coefficient of Mg2+ ions between calcite and solution at 10–50°C. Mar. Chem. 20, 327-336.
Paquette, J., Vali, H., Mucci, A., 1996. TEM study of Pt-C replicas of calcite overgrowths precipitated from electrolyte solutions. Geochim. Cosmochim. Acta 60, 4689-4699.
Parkhurst, D.L., Appelo, C., 2013. Description of input and examples for PHREEQC version 3—a computer program for speciation, batch-reaction, one-dimensional transport, and inverse geochemical calculations. US geological survey techniques and methods 6, 497.
Parsiegla, K.I., Katz, J.L., 1999. Calcite growth inhibition by copper(II): I.Effect of supersaturation. J. Cryst. Growth 200, 213-226.
Pingitore, N.E., Eastman, M.P., Sandidge, M., Oden, K., Freiha, B., 1988. The coprecipitation of manganese(II) with calcite: an experimental study. Mar. Chem. 25, 107-120.
Pitzer, K.S., Press, C., 1991. Activity coefficients in electrolyte solutions. CRC press Boca Raton, FL.
Plummer, L.N., Busenberg, E., 1982. The solubilities of calcite, aragonite and vaterite in CO2-H2O solutions between 0 and 90°C, and an evaluation of the aqueous model for the system CaCO3-CO2-H2O. Geochim. Cosmochim. Acta 46, 1011-1040.
Politi, Y., Levi-Kalisman, Y., Raz, S., Wilt, F., Addadi, L., Weiner, S., Sagi, I., 2006. Structural Characterization of the Transient Amorphous Calcium Carbonate Precursor Phase in Sea Urchin Embryos. Adv. Funct. Mater. 16, 1289-1298.
Putnis, C.V., Wang, L., Ruiz-Agudo, E., Ruiz-Agudo, C., Renard, F., 2021. Crystallization via Nonclassical Pathways: Nanoscale Imaging of Mineral Surfaces, Crystallization via Nonclassical Pathways Volume 2: Aggregation, Biomineralization, Imaging & Application. American Chemical Society, pp. 1-35.
Reeder, R.J., Lamble, G.M., Northrup, P.A., 1999. XAFS study of the coordination and local relaxation around Co2+, Zn2+, Pb2+, and Ba2+ trace elements in calcite. Am. Mineral. 84, 1049-1060.
Rimstidt, J.D., Balog, A., Webb, J., 1998. Distribution of trace elements between carbonate minerals and aqueous solutions. Geochim. Cosmochim. Acta 62, 1851-1863.
Rodriguez-Blanco, J.D., Shaw, S., Bots, P., Roncal-Herrero, T., Benning, L.G., 2012. The role of pH and Mg on the stability and crystallization of amorphous calcium carbonate. J. Alloys Compd. 536, S477-S479.
Rodriguez-Cruz, S.E., Jockusch, R.A., Williams, E.R., 1999. Hydration energies and structures of alkaline earth metal ions, M2+(H2O)n, n = 5-7, M = Mg, Ca, Sr, and Ba. J. Am. Chem. Soc. 121, 8898-8906.
Romanek, C.S., Grossman, E.L., Morse, J.W., 1992. Carbon isotopic fractionation in synthetic aragonite and calcite: Effects of temperature and precipitation rate. Geochim. Cosmochim. Acta 56, 419-430.
Ropp, R.C., 2013. Chapter 2 - Group 17 (H, F, Cl, Br, I) Alkaline Earth Compounds, in: Ropp, R.C. (Ed.), Encyclopedia of the Alkaline Earth Compounds. Elsevier, Amsterdam, pp. 25-104.
Rosa, S., Lundager Madsen, H.E., 2011. Kinetics of mass crystallization of calcium carbonate at 25, 30 and 37°C. J. Cryst. Growth 318, 99-102.
Rose, G., 1837. Ueber die Bildung des Kalkspaths und Arragonits. Annalen der Physik 118, 353-367.
Rose, G., 1860. Ueber die Umstände, unter denen der kohlensaure Kalk sich in seinen heteromorphen Zuständen, als Kalkspath, Aragonit und Kreide abscheidet. Annalen der Physik 187, 156-165.

Rowling, J., 2004. Studies on aragonite and its occurrence in caves, including New South Wales caves. Journal and proceedings of the Royal Society of New South Wales 137, 123-149.
Ruiz-Agudo, E., Putnis, C.V., Rodriguez-Navarro, C., Putnis, A., 2011. Effect of pH on calcite growth at constant aCa2+/aCO32- ratio and supersaturation. Geochim. Cosmochim. Acta 75, 284-296.
Sadekov, A.Y., Eggins, S.M., Klinkhammer, G.P., Rosenthal, Y., 2010. Effects of seafloor and laboratory dissolution on the Mg/Ca composition of Globigerinoides sacculifer and Orbulina universa tests — A laser ablation ICPMS microanalysis perspective. Earth. Planet. Sci. Lett. 292, 312-324.
Saenger, C., Affek, H.P., Felis, T., Thiagarajan, N., Lough, J.M., Holcomb, M., 2012. Carbonate clumped isotope variability in shallow water corals: Temperature dependence and growth-related vital effects. Geochim. Cosmochim. Acta 99, 224-242.
Saldi, G.D., Jordan, G., Schott, J., Oelkers, E.H., 2009. Magnesite growth rates as a function of temperature and saturation state. Geochim. Cosmochim. Acta 73, 5646-5657.
Sarkar, A., Mahapatra, S., 2010. Synthesis of All Crystalline Phases of Anhydrous Calcium Carbonate. Crystal Growth & Design 10, 2129-2135.
Schauble, E.A., Ghosh, P., Eiler, J.M., 2006. Preferential formation of 13C–18O bonds in carbonate minerals, estimated using first-principles lattice dynamics. Geochim. Cosmochim. Acta 70, 2510-2529.
Siegel, F.R., Reams, M.W., 1966. TEMPERATURE EFFECT ON PRECIPITATION OF CALCIUM CARBONATE FROM CALCIUM BICARBONATE SOLUTIONS AND ITS APPLICATION TO CAVERN ENVIRONMENTS. Sedimentology 7, 241-248.
Simon, N., Urien, S., Riou, B., Lechat, P., Aubrun, F., 2009. Intravenous morphine titration in immediate postoperative pain management: Population kinetic–pharmacodynamic and logistic regression analysis. PAIN® 144, 139-146.
Spooner, P.T., Guo, W., Robinson, L.F., Thiagarajan, N., Hendry, K.R., Rosenheim, B.E., Leng, M.J., 2016. Clumped isotope composition of cold-water corals: A role for vital effects? Geochim. Cosmochim. Acta 179, 123-141.
Stamou Jr, M., Intzes Jr, S., Lamprianidou, E., Papoutselis, M.K., Bezirgiannidou, Z., Nakou, E., Kartasis, Z., Vrachiolias, G., Bazntiara, I., Kotsianidis, I., 2018. Longer duration and proper titration of low molecular weight heparin (LMWH), are independent factors for successful pregnancy outcome. retrospective analysis from a single center. Blood 132, 5065.
Suganuma, I., 1928. ON THE CONSTITUENTS AND GENESIS OF A FEW MINERALS PRODUCED FROM HOT SPRINGS AND THEIR VICINITIES IN JAPAN. III. CALCIUM CARBONATE MINERALS DEPOSITED FROM EFFERVESCENT SPRINGS. Bull. Chem. Soc. Jpn. 3, 87-89.
Sun, W., Jayaraman, S., Chen, W., Persson, K.A., Ceder, G., 2015. Nucleation of metastable aragonite CaCO3 in seawater. Proceedings of the National Academy of Sciences 112, 3199-3204.
Tai, C.Y., Chen, F.B., 1998. Polymorphism of CaCO3, precipitated in a constant-composition environment. AIChE Journal 44, 1790-1798.
Tai, C.Y., Chen, P.C., 1995. Nucleation, agglomeration and crystal morphology of calcium carbonate. Aiche Journal 41, 68-77.
Tang, J., Dietzel, M., Fernandez, A., Tripati, A.K., Rosenheim, B.E., 2014. Evaluation of kinetic effects on clumped isotope fractionation (Δ47) during inorganic calcite precipitation. Geochim. Cosmochim. Acta 134, 120-136.

Tang, J., Köhler, S.J., Dietzel, M., 2008. Sr2+/Ca2+ and 44Ca/40Ca fractionation during inorganic calcite formation: I. Sr incorporation. Geochim. Cosmochim. Acta 72, 3718-3732.
Tarutani, T., Clayton, R.N., Mayeda, T.K., 1969. The effect of polymorphism and magnesium substitution on oxygen isotope fractionation between calcium carbonate and water. Geochim. Cosmochim. Acta 33, 987-996.
Temmam, M., Paquette, J., Vali, H., 2000. Mn and Zn incorporation into calcite as a function of chloride aqueous concentration. Geochim. Cosmochim. Acta 64, 2417-2430.
Teng, H.H., Dove, P.M., De Yoreo, J.J., 2000. Kinetics of calcite growth: surface processes and relationships to macroscopic rate laws. Geochim. Cosmochim. Acta 64, 2255-2266.
Tesoriero, A.J., Pankow, J.F., 1996. Solid solution partitioning of Sr2+, Ba2+, and Cd2+ to calcite. Geochim. Cosmochim. Acta 60, 1053-1063.
Thiagarajan, N., Adkins, J., Eiler, J., 2011. Carbonate clumped isotope thermometry of deep-sea corals and implications for vital effects. Geochim. Cosmochim. Acta 75, 4416-4425.
Thien, B.M.J., Kulik, D.A., Curti, E., 2014. A unified approach to model uptake kinetics of trace elements in complex aqueous – solid solution systems. Appl. Geochem. 41, 135-150.
Tripati, A.K., Eagle, R.A., Thiagarajan, N., Gagnon, A.C., Bauch, H., Halloran, P.R., Eiler, J.M., 2010. 13C–18O isotope signatures and 'clumped isotope' thermometry in foraminifera and coccoliths. Geochim. Cosmochim. Acta 74, 5697-5717.
Tripati, A.K., Hill, P.S., Eagle, R.A., Mosenfelder, J.L., Tang, J., Schauble, E.A., Eiler, J.M., Zeebe, R.E., Uchikawa, J., Coplen, T.B., Ries, J.B., Henry, D., 2015. Beyond temperature: Clumped isotope signatures in dissolved inorganic carbon species and the influence of solution chemistry on carbonate mineral composition. Geochim. Cosmochim. Acta 166, 344-371.
Truesdell, A.H., Jones, B.F., Survey, G., 1973. WATEQ: A Computer Program for Calculating Chemical Equilibria of Natural Waters. U.S. Department of the Interior, Geological Survey.
Turnbull, A.G., 1973. A thermochemical study of vaterite. Geochim. Cosmochim. Acta 37, 1593-1601.
Uchikawa, J., Zeebe, R.E., 2012. The effect of carbonic anhydrase on the kinetics and equilibrium of the oxygen isotope exchange in the CO2–H2O system: Implications for δ18O vital effects in biogenic carbonates. Geochim. Cosmochim. Acta 95, 15-34.
Urey, H.C., 1947. The thermodynamic properties of isotopic substances. Journal of the Chemical Society (Resumed) 10.1039/JR9470000562, 562-581.
Uwakwe, O.C., Riechelmann, S., Hoffmann, R., Spötl, C., Jantschke, A., Hansen, M., Immenhauser, A., 2023. Experimental precipitation of cryogenic carbonate. Chem. Geol. 635, 121615.
Veizer, J., 1983. Trace elements and isotopes in sedimentary carbonates. Reviews in Mineralogy & Geochemistry 11, 265-299.
Voigt, M., Mavromatis, V., Oelkers, E.H., 2017. The experimental determination of REE partition coefficients in the water-calcite system. Chem. Geol. 462, 30-43.
Wada, N., Yamashita, K., Umegaki, T., 1995. Effects of divalent cations upon nucleation, growth and transformation of calcium carbonate polymorphs under conditions of double diffusion. J. Cryst. Growth 148, 297-304.
Wang, X., Schröder, H.C., Müller, W.E.G., 2014. Enzyme-based biosilica and biocalcite: biomaterials for the future in regenerative medicine. Trends Biotechnol. 32, 441-447.
Wang, Z., Schauble, E.A., Eiler, J.M., 2004. Equilibrium thermodynamics of multiply substituted isotopologues of molecular gases. Geochim. Cosmochim. Acta 68, 4779-4797.

Watkins, J.M., Hunt, J.D., 2015. A process-based model for non-equilibrium clumped isotope effects in carbonates. Earth. Planet. Sci. Lett. 432, 152-165.
Watson, E.B., 2004. A conceptual model for near-surface kinetic controls on the trace-element and stable isotope composition of abiogenic calcite crystals11Associate editor: R.H. Byrne. Geochim. Cosmochim. Acta 68, 1473-1488.
Weiss, C.A., Torres-Cancel, K., Moser, R., Chandler, M.Q., Malone, P.G., 2014. Influence of Temperature on Calcium Carbonate Polymorph formed from Ammonium Carbonate and Calcium Acetate. jnsm.
Weremeichik, J.M., Gabitov, R.I., Thien, B.M.J., Sadekov, A., 2017. The effect of growth rate on uranium partitioning between individual calcite crystals and fluid. Chem. Geol. 450, 145-153.
White, A.F., 1977. Sodium and potassium coprecipitation in aragonite. Geochim. Cosmochim. Acta 41, 613-625.
Wynn, P.M., Fairchild, I.J., Borsato, A., Spötl, C., Hartland, A., Baker, A., Frisia, S., Baldini, J.U.L., 2018. Sulphate partitioning into calcite: Experimental verification of pH control and application to seasonality in speleothems. Geochim. Cosmochim. Acta 226, 69-83.
Yagi, H., Iwazawa, A., Sonobe, R., Matsubara, T., Hikita, H., 1984. Crystallization of calcium carbonate accompanying chemical absorption. Industrial & Engineering Chemistry Fundamentals 23, 153-158.
Žák, K., Orvošová, M., Filippi, M., Vlček, L., Onac, B.P., Perşoiu, A., Rohovec, J., Světlík, I., 2013. Cryogenic Cave Pearls In the Periglacial Zones of Ice Caves. Journal of Sedimentary Research 83, 207-220.
Zeebe, R.E., 1999. An explanation of the effect of seawater carbonate concentration on foraminiferal oxygen isotopes. Geochim. Cosmochim. Acta 63, 2001-2007.
Zhang, J., Nancollas, G.H., 1998. Kink Density and Rate of Step Movement during Growth and Dissolution of anABCrystal in a Nonstoichiometric Solution. Journal of Colloid and Interface Science 200, 131-145.
Zhang, Y., Dawe, R.A., 2000. Influence of Mg2+ on the kinetics of calcite precipitation and calcite crystal morphology. Chem. Geol. 163, 129-138.
Zhang, Z., Wang, J., 2024. Quantification of classical and non-classical crystallization pathways in calcite precipitation. Earth. Planet. Sci. Lett. 636, 118712.
Zhang, Z., Xie, Y., Xu, X., Pan, H., Tang, R., 2012. Transformation of amorphous calcium carbonate into aragonite. J. Cryst. Growth 343, 62-67.
Zuddas, P., Mucci, A., 1998. Kinetics of Calcite Precipitation from Seawater: II. The Influence of the Ionic Strength. Geochim. Cosmochim. Acta 62, 757-766.